

A COMPARATIVE STUDY OF GLACIOVOLCANIC PALAGONITIZATION OF
THOLEIITIC AND ALKALINE SIDEROMELANE IN HELGAFELL, ICELAND AND
WELLS GRAY-CLEARWATER VOLCANIC FIELD, BC, CANADA

by

Erica A. Massey

B.Sc., The University of British Columbia, 2014

A THESIS SUBMITTED IN PARTIAL FULFILLMENT OF
THE REQUIREMENTS FOR THE DEGREE OF

MASTER OF SCIENCE

in

The College of Graduate Studies

(Earth & Environmental Science)

THE UNIVERSITY OF BRITISH COLUMBIA

(Okanagan)

April 2017

© Erica A. Massey, 2017

Examination Committee

The undersigned certify that they have read, and recommend to the College of Graduate Studies for acceptance, a thesis entitled:

A comparative study of glaciovolcanic palagonitization of tholeiitic and alkaline sideromelane in Helgafell, Iceland and Wells Gray-Clearwater Volcanic Field, BC, Canada.

Submitted by **Erica A. Massey** in partial fulfilment of the requirements of the degree of Master of Science.

Supervisor, Professor: **Dr. John D. Greenough**

Co-Supervisor, Professor: **Dr. Benjamin R. Edwards**

Supervisory Committee Member, Professor: **Dr. Kyle P. Larson**

University Examiner, Professor: **Dr. Susan J. Murch**

Neutral Chair, Professor: **Dr. Murray Neuman**

Date Submitted to Graduate Studies: April 26, 2017

Abstract

Pleistocene glaciovolcanic eruptions occurred frequently beneath continental-scale ice sheets producing vitric, fragmental volcanic deposits in Helgafell, Iceland (tholeiitic basalt) and Wells Gray, BC, Canada (alkali olivine basalt). They are highly susceptible to hydrothermal alteration that transforms sideromelane (basaltic volcanic glass) into palagonite (early amorphous material) and secondary minerals (i.e. zeolites, clays and sulfides). Compositional controls, mass transfer and geochemical-textural relationships are investigated by optical microscopy and analyses of major (12) and trace (32) elements in glass-palagonite pairs by Electron Microprobe Analysis (EMPA), Laser Ablation Inductively Coupled Plasma Mass Spectrometry (LA-ICP-MS), and geochemical modelling. Helgafell's thinner (6-10 μm vs. 10-20 μm) palagonite rims demarcate highly vesicular (30.2% vs. 4.9%) sideromelane that has more secondary minerals (1.4% vs. 0.5%) than Wells Gray's microlite-rich (12.3% vs. 0.1%) sideromelane. The thicknesses of palagonite rims are similar whether the sideromelane is unaltered or completely altered.

Multi-dimensional scaling confirms that sideromelane composition, reflecting igneous processes, strongly controls the chemistry of palagonite. A comparison of element behavior in the palagonite from both localities reveals a tendency for water-soluble cations (Cl, K, Na, Rb, Cu, Mn, P) to correlate with water concentrations. Plots of element ratios (Nb/Y vs La/Nd; Sc/Ta vs Zr/Th) calculated from "immobile" elements show that palagonite from Wells Gray and Helgafell are distinct, and have ratios that are similar to sideromelane that produced the palagonite. Thus some palagonite compositions reflect primary magma compositions based on immobile elements. Gresens' mass transfer calculations confirm minimal movement of these elements during palagonitization. However, the same calculations reveal a pattern of Cu, Cl, Ni, Rb and U addition and Na, Ca, Mg, P, V and Mn removal that is similar at both localities.

Microprobe traverses identified eight prominent trends across the glass-palagonite interface and palagonite rim, which do not appear to be controlled by sideromelane composition. Several element concentrations decrease in palagonite, including Si (by ~3-10%), Al, Ca and Na, while Ti, Fe and Mg concentrations increase. Locally, the palagonite has an inner Ti-rich zone. The gradual increase in Mg across the palagonite rim may be indicative of changes in solubility and pH.

Preface

The sites chosen in Iceland and British Columbia to sample and analyze for this thesis were at the suggestion of co-supervisor, Dr. Benjamin Edwards. Sample collection, cutting and preparation was completed by the author. Stephen Wood at the University of Western Ontario cut the thin sections. Standards used during the SEM-EDS and EMPA-WDS analyses were provided by both the Smithsonian and Micro-Analysis Consultants Ltd. Data presented within this work arose from observations and analyses conducted primarily by the author with the exception of LA-ICP-MS analyses, carried out at the University of Toronto by Dr. John Greenough. Data reduction, data-set compilation and statistical interpretation was completed by the author. Photomicrographs and high-magnification imaging from the SEM and EMPA of thin sections were analyzed, collected, organized and interpreted by the author, with assistance from David Arkininstall in SEM and EMPA work.

Table of Contents

Examination Committee	ii
Abstract.....	iii
Preface.....	iv
Table of Contents	v
List of Tables	ix
List of Figures.....	x
List of Equations	xiii
List of Abbreviations	xiv
Acknowledgements	xv
Dedication	xvii
Chapter 1: Introduction	1
Chapter 2: Literature Review of Palagonite (1846 – 2016).....	6
2.1 What is Palagonite?	6
2.1.1 Minerals Associated with Palagonite	7
2.1.2 Textures of Palagonite	7
2.2 Palagonite – Key Historical Studies	9
2.3 How Does Palagonite Form?.....	13
2.3.1 Environments of Formation.....	13
2.3.2 Eruption Progression	13
2.3.3 Chemical Controls and Processes of Palagonitization	15
2.3.3.1 Thorseth et al. (1991).....	15
2.3.3.2 Pauly et al. (2011).....	17
2.3.3.3 Isovolumetric Assumption and Density.....	18
2.3.3.4 Determining Element Mobility and Calculating Mass Balance	19
2.3.3.5 Assessment of Element Gains and Losses.....	21
2.3.3.6 High-Aluminum vs. Low-Aluminum Palagonite	22
2.3.4 Water in Palagonitization	23
2.3.5 Controls on Palagonitization from Atomic Structure	23
2.3.6 Temperature.....	24
2.3.7 Porosity	26
2.3.8 Stages of Palagonitization	26

2.3.9 Thermodynamics and Kinetic Considerations.....	28
2.4 Summary	29
2.5 Outstanding Issues.....	29
Chapter 3: Site Description.....	30
3.1 Helgafell, Reykjanes Peninsula, SW Iceland.....	30
3.2 Wells Gray-Clearwater Volcanic Field, Clearwater, BC, Canada.....	35
Chapter 4: Methodology.....	42
4.1 Sample Preparation	42
4.2 Photomicrographs and Images	42
4.3 Analytical Methods.....	44
4.3.1 Polarizing Light Microscopy	44
4.3.2 Scanning Electron Microscope – Energy Dispersive Spectroscopy.....	44
4.3.3 Electron Microprobe Analysis.....	45
4.3.4 Laser Ablation Inductively Coupled Plasma Mass Spectrometry	46
4.3.5 Precision and Accuracy from Reference Materials	47
4.4 Statistical Methods.....	47
4.4.1 Multi-Dimensional Scaling.....	48
4.4.2 Gresens’ Isocon Diagrams and Mass Balance.....	48
4.4.2.1 Mathematical Assumptions for Water in Data Sets for Mass Balance.....	49
Chapter 5: Results.....	51
5.1 Petrography: Modal Proportions, Textures, and Secondary Minerals	51
5.1.1 Wells Gray, British Columbia, Canada	52
5.1.2 Helgafell, Iceland.....	54
5.1.3 Comparison Between Sites	55
5.1.4 Unique Textures	58
5.1.5 Secondary Minerals	66
5.2 Major and Trace Element Geochemistry of Sideromelane and Palagonite	70
5.2.1 Water in Palagonite	76
5.2.2 Geochemical Variation	77
5.2.3 Multi-Dimensional Scaling (MDS) Statistics.....	84
5.2.4 Microprobe Traverses and Element Maps.....	90
5.2.5 Mass Balance Calculations	95
Chapter 6: Discussion.....	105

6.1 Sideromelane Compositions.....	105
6.2 Relict Sideromelane Signatures in Palagonite	106
6.3 Geochemistry of Palagonite Formation	108
6.4 Element Addition and Removal Based on Gresens Calculations	109
6.5 The Aqueous Environment of Sideromelane and Palagonite	111
6.6 Microprobe Traverses	113
6.6.1 Helgafell and Wells Gray	113
6.6.2 Reanalysis of Subalkaline Glass-Palagonite Microprobe Traverses	116
6.7 Major and Trace Element Mass Transfer	126
6.8 Secondary Minerals: Compositional Control and Importance	127
6.9 Controlling Mechanisms	128
6.10 Palagonite Rim Thickness and Gel-Material	130
6.10.1 Palagonitization Extent and Rates	131
6.10.2 Vesicularity and Microlites	132
6.11 Unique Textures.....	133
6.12 Future Work Recommended	134
Chapter 7: Conclusions	136
References.....	139
Appendices.....	153
Appendix A Precision and Accuracy Tables	153
A.1 Major element precision and accuracy	153
A.2 Trace element precision and accuracy	154
Appendix B Data Tables	155
B.1 Modal proportions (%) for Helgafell and Wells Gray	155
B.2 Sideromelane major element (normalized) data in Helgafell and Wells Gray	156
B.3 Palagonite major element (normalized) data in Helgafell Wells Gray	157
B.4 Glass-palagonite traverse for Helgafell (sample #03-2) by EMPA	158
B.5 Glass-Palagonite traverse for Wells Gray (sample #21a-2) by EMPA.....	159
B.6 Error bar calculations for ratio plots to test immobility of trace elements (Nb, Y, La, Nd, Zr, Th, Sc and Ta) in Helgafell and Wells Gray.....	160
B.7 Mass balance calculations for 32 trace elements in Helgafell and Wells Gray	161
B.8 Major element (%) mass transfer using isocon diagrams for two data sets with different assumptions for water	162

B.9 Trace element (%) mass transfer using isocon diagrams for two data sets with different assumptions for water	163
Appendix C Historical Review Summary	164
C.1 Characteristics of high-temperature vs. low-temperature alteration.....	164
C.2 Minerals and materials associated with palagonitization.....	165
C.3 Scientific analytical methods used to study palagonitization.	166

List of Tables

Table 1	Alteration characteristics of palagonite from three parent materials	16
Table 2	Density values for sideromelane, palagonite and associated tuff material	19
Table 3	Samples and matching glass-palagonite pairs analyzed by EMP and LA-ICP-MS.	42
Table 4	Standards used for calibration of the EMP	45
Table 5	Two data sets with different mathematical assumptions for water in sideromelane and palagonite.....	50
Table 6	Modal proportions of materials and features in Helgafell and Wells Gray samples..	51
Table 7	EMP data for the secondary mineral in vesicles (oxide wt.%)	69
Table 8	Sideromelane major element data for Helgafell and Wells Gray by EMP	72
Table 9	Palagonite major element data for Helgafell and Wells Gray by EMP	73
Table 10	Sideromelane trace element data for Helgafell and Wells Gray.....	74
Table 11	Palagonite trace element data for Helgafell and Wells Gray.....	75
Table 12	Estimate of variation due to precision errors for sideromelane and palagonite.....	76
Table 13	Mass balance calculations (major elements) from Gresens' isocon diagrams for each glass-palagonite pair at Helgafell and Wells Gray.....	98
Table 14	Mass balance calculations (16 of 32 trace elements detected) from Gresens' isocon diagrams for each glass-palagonite pair at Helgafell and Wells Gray..	99
Table 15	Eight prominent element trends across the glass-palagonite interface and palagonite rims in seven EMP traverses from Helgafell and Wells Gray (this study), and Pauly et al. (2011)	125

List of Figures

Figure 1	Textural studies (e.g. tunneling, zoned hemispheres) in basaltic glass	8
Figure 2	The macroenvironment of palagonitized lapilli tuff (cont.)	9
Figure 3	Lava-capped tuyas form in stages with characteristic lithofacies (cont.).....	14
Figure 4	Aging steps of palagonitization (cont.)	28
Figure 5	Helgafell, Reykjanes Peninsula, SW Iceland	31
Figure 6	NE-SW trending fissures swarms in the Reykjanes Peninsula, SW Iceland.....	32
Figure 7	Sampling at Helgafell, Reykjanes Peninsula, SW Iceland	33
Figure 8	Helgafell, Iceland: SW outcrop, fine- to moderately bedded, cemented and palagonitized lapilli tuff.	34
Figure 9	Subhorizontal, cemented palagonitized lapilli tuff with fine to coarse bedding at Helgafell.	34
Figure 10	Top of Helgafell ridge: cemented palagonitized lapilli tuff sculpted as wave- formed erosional features.	35
Figure 11	Helgafell, Iceland: remnant pillow lava embedded in cemented, palagonitized lapilli tuff	35
Figure 12	Location of the Wells Gray-Clearwater Volcanic Field, BC, Western Canada	36
Figure 13	Second Canyon, Wells Gray-Clearwater Volcanic Field in BC, Canada.....	37
Figure 14	Sampling at Second Canyon, Wells Gray-Clearwater Volcanic Field.....	39
Figure 15	Second Canyon, Wells Gray: creekside wall and cliff samples	39
Figure 16	Second Canyon, Wells Gray: dykes with quenched margins cross-cutting tuff- breccia	40
Figure 17	Second Canyon's stratigraphic column	41
Figure 18	BSE image of a Wells Gray glass-palagonite pair analysis area	44
Figure 19	Isocon diagram for one glass-palagonite pair for Gresens' mass balance calculations	50
Figure 20	Photomicrographs of sideromelane and tachylite glass, palagonite, sulfides and olivine (PPL, XPL and reflected light). Wells Gray #21a-3	53
Figure 21	Photomicrograph (XPL) of alkali olivine basaltic sideromelane at Wells Gray	54
Figure 22	Typical sideromelane grain at Helgafell (PPL)	55
Figure 23	Photomicrographs (PPL; XPL) of sideromelane grains, palagonite rims, gel- material and zeolite-like material (#09-2 Helgafell)..	56
Figure 24	Textural differences in photomicrographs (PPL): Helgafell and Wells Gray	57
Figure 25	Completely altered sideromelane with remnant palagonite rims and plagioclase lathes situated next to fresh sideromelane grains (SEM BSE image; WG #21b-3)58	
Figure 26	Fluidal or stretched glass. Helgafell #03-2 (PPL)	59
Figure 27	Concentrically zoned vesicles in a sideromelane grain. Helgafell #03-2 (PPL)	59
Figure 28	Zoned palagonite rim with a central white linear zone and a spherical texture in the inner portion of the palagonite rim that propagates into the glass. Wells Gray #21a- 2 (EMP BSE image)	60
Figure 29	Microzoned semicircular texture that propagates from the glass-palagonite interface into sideromelane grains. Helgafell #09-2 (SEM BSE image)	61
Figure 30	Zoned palagonite rim with a spherical texture at the glass-palagonite boundary. Wells Gray #21a-3 (SEM BSE image).....	62

Figure 31 Multiple, sub-parallel, linear microveins linking vesicles in sideromelane. Helgafell #11-2 (SEM BSE image).....	63
Figure 32 Multiple, sub-parallel, linear microveins in sideromelane join vesicles. Helgafell #14-2 (SEM a) BSE image and b) element map)	64
Figure 33 Photomicrograph (PPL) of a dendritic texture in sideromelane. WG #20-2	65
Figure 34 Photomicrograph (PPL) of a dendritic texture emanating away from a vesicle in sideromelane. HG #09-2.....	65
Figure 35 Photomicrographs (PPL and RL) showing sulfides (e.g. pyrite, chalcopyrite) in voids and vesicles. WG #21a-3	66
Figure 36 Photomicrographs (PPL and SEM BSE) showing material in vesicles: broken glass, palagonite rims, and minerals. WG #20-2.....	67
Figure 37 Na-rich, Al-poor zeolite-like mineral in vesicles. HG #09-2 (a) EMP BSE image and b) PPL).....	68
Figure 38 Na-rich, Al-poor zeolite-like mineral collecting in a vesicle. HG #09-2 (a) EMP BSE image and b) PPL).....	68
Figure 39 Zeolite-like mineral in a vesicle lined with an exceptionally thick, uniform material (likely smectite) separate from the palagonite rim. HG #09-2 (EMP BSE image).....	69
Figure 40 Abundant zeolite-like mineral with low Na and Al, and high H ₂ O relative to other analyses. Pitting in glass is common. HG #09-2 (EMP BSE image).....	70
Figure 41 Average estimated water content of palagonite from Helgafell and Wells Gray ...	77
Figure 42 Total alkalis-silica diagram of sideromelane from Helgafell and Wells Gray.....	78
Figure 43 Nb/Y vs. Zr/TiO ₂ diagram of sideromelane from Helgafell and Wells Gray.....	79
Figure 44 Helgafell vs. Wells Gray SiO ₂ vs. FeO diagram for glass and palagonite	80
Figure 45 Helgafell vs. Wells Gray SiO ₂ vs. TiO ₂ diagram for glass and palagonite.....	80
Figure 46 Helgafell vs. Wells Gray SiO ₂ /TiO ₂ vs. FeO/TiO ₂ diagram for glass and palagonite.	81
Figure 47 Helgafell vs. Wells Gray Al ₂ O ₃ diagram for glass and palagonite	81
Figure 48 Chondrite-normalized Helgafell and Wells Gray sideromelane	82
Figure 49 Chondrite-normalized REE's in glass and palagonite from Helgafell and Wells Gray..	82
Figure 50 Concentration of SiO ₂ plotted against Nb/Y in sideromelane.....	83
Figure 51 Concentration of SiO ₂ versus Mg# in sideromelane.	84
Figure 52 MDS plot of Helgafell and Wells Gray sideromelane and palagonite, based on major and trace element data	85
Figure 53 MDS plot of Helgafell and Wells Gray sideromelane, based on major element data.	86
Figure 54 MDS plot of Helgafell palagonite, based on major and trace element data	86
Figure 55 MDS plot of Wells Gray palagonite, based on major and trace element data.....	87
Figure 56 MDS plot comparing element behaviour in Wells Gray palagonite, based on major and trace element data.	88
Figure 57 MDS plot comparing element behaviour in Helgafell's basalt 1 palagonite, based on major and trace element data	89
Figure 58 MDS plot comparing element behaviour in Helgafell's basalt 2 palagonite, based on major and trace element data.....	89

Figure 59 MDS plot of palagonite from Helgafell (tholeiitic) and Wells Gray (alkali olivine basalt), based on major element data. A pore-lining smectite (microprobe) analysis from a tholeiitic Hawaiian basalt included for comparison.	90
Figure 60 Helgafell glass-palagonite microprobe traverse. HG #03-2 (EMP BSE image)....	92
Figure 61 Wells Gray glass-palagonite microprobe traverse. WG #21a-2 (EMP BSE image)	93
Figure 62 Wells Gray glass-palagonite microprobe traverse (shown in Figure 61) of only minor elements. WG #21a-2	94
Figure 63 Geochemical-textural zoning in a palagonite rim between two glass grains. WG #28-2 (SEM line scan and BSE image).....	94
Figure 64 Element maps of a sideromelane grain with palagonite rims on the grain's edge and in a vesicle. HG #11-2 (SEM BSE image).....	95
Figure 65 Log-ratio plots of a) Nb/Y vs. La/Nd and b) Zr/Th vs. Sc/Ta for Helgafell and Wells Gray glass and palagonite indicate the tendency to be immobile elements for isocon diagrams	96
Figure 66 Wells Gray low-H ₂ O palagonite mass change sorted from highest gain to greatest loss by the average of the four lowest water palagonite at Wells Gray (cont.)....	101
Figure 67 Wells Gray high-H ₂ O palagonite mass change shown by an average of the four highest water palagonite at Wells Gray, sorted to the same element order as Wells Gray low-H ₂ O palagonite (cont.)	102
Figure 68 Helgafell high-H ₂ O palagonite mass change shown by an average of the four highest water palagonite at Helgafell, sorted to the same element order as Wells Gray low-H ₂ O palagonite (cont.)	103
Figure 69 Helgafell low-H ₂ O palagonite mass change shown by an average of the four lowest water palagonite at Helgafell, sorted to the same element order as Wells Gray low-H ₂ O palagonite (cont.).....	104
Figure 70 Total alkali silica diagram showing glass compositions, environments, or sample type associated with seven glass-palagonite microprobe traverses from Wells Gray and Helgafell (this study), and from Pauly et al. (2011)	117
Figure 71 Kilauea, HI SOH-1 glass-palagonite microprobe traverse of subalkaline sideromelane (data from Pauly et al. (2011)) (cont.)	118
Figure 72 Hilina Bench, HI glass-palagonite microprobe traverse of subalkaline sideromelane (data from Pauly et al. (2011)) (cont.).....	119
Figure 73 Hawaii Scientific Drilling Project (HSDP) glass-palagonite microprobe traverse of subalkaline sideromelane (data from Pauly et al. (2011)) (cont.)	120
Figure 74 Palagonia, Sicily glass-palagonite microprobe traverse of subalkaline sideromelane (data from Pauly et al. (2011)) (cont.).....	121
Figure 75 Ingólfssjall, Iceland glass-palagonite microprobe traverse of sideromelane (data from Pauly et al. (2011)) (cont.).....	122
Figure 76 Palagonitization summarized as a five-step alteration process	130

List of Equations

(1) Precision:
$$\% = \frac{\text{Std Dev}}{\text{Mean}} * 100$$

(2) Accuracy:
$$\% = \frac{(\text{Mean} - \text{Standardized Reference Value})}{\text{Standardized Reference Value}} * 100$$

Standard deviation and variance are derived from the mean of the data set and measure how spread out the numbers are. The equations used are:

(3) Variance:
$$s^2 = \frac{\sum(x-\bar{x})^2}{n-1}$$

(4) Standard Deviation:
$$s = \sqrt{\frac{\sum(x-\bar{x})^2}{n-1}}$$

where s^2 = sample variance, s = standard deviation, x = each term in the data set, \sum = sum, \bar{x} = sample mean, n is the number of data points in the population.

(5) Standardized (z-scored) equation:

$$z = \frac{(x - \mu)}{\sigma}$$

where x = concentration of an element in an analysis, μ = mean, σ = standard deviation.

(6) Percent mass balance equation, using the slope from isocon diagrams (Grant, 1986):

$$\% = \frac{C^A - (C^O * \text{slope})}{C^O * \text{slope}} * 100$$

where C^A = alteration material (palagonite), C^O = parent/original material (sideromelane).

(7) Error bars for ratio plots are based on precision and determine element immobility (error bar calculation formula from Ragland, 1989):

$$q = Q * \sqrt{\left(\frac{a}{A}\right)^2 + \left(\frac{b}{B}\right)^2}$$

where q = total ratio error, Q = ratio value, a = numerator error, A = numerator value, b = denominator error, B = denominator value.

List of Abbreviations

BC	British Columbia
BDL	Below detection limit
BSE	Backscatter image
cm ³	cubic centimetres
cps	Counts per second
EMP	Electron Microprobe
EMPA-WDS	Electron Microprobe Analysis Wavelength Dispersive Spectroscopy
FILTER	Fipke Lab for Trace Element Research
G	Glass
G	gram
Ga	Billion years
HG	Helgafell
LA-ICP-MS	Laser Ablation Inductively Coupled Plasma Mass Spectrometer
μm	Micron
Ma	Million years
MDS	Multi-dimensional Scaling
P	Palagonite
ppb	Parts per billion
PPL	Plane Polarized Light
ppm	Parts per million
RL	Reflected Light
SEM-EDS	Scanning Electron Microscope Energy Dispersive Spectroscopy
Std Dev	Standard deviation
WG	Wells Gray
WGCVF	Wells Gray-Clearwater Volcanic Field
Wt.%	Weight percent
XPL	Cross Polarized Light
XRD	X-ray diffraction

Acknowledgements

I would like to acknowledge with gratitude to my supervisors Dr. John Greenough at UBC Okanagan, and Dr. Benjamin Edwards at Dickinson College, Pennsylvania, for such excellent guidance and patience throughout this project. Without each of your unique areas of expertise and assistance I would not have been able to culminate an idea into reality and complete this thesis. Thank you to John Greenough for guiding and believing in me step-by-step throughout the project at UBC Okanagan. Sincere appreciation to Ben Edwards for unwavering positive encouragement and to helpfully teach, guide, challenge and support me on any topic we discussed. Your expertise and interests in glaciovolcanism on Earth and Mars often especially inspired me to work on understanding these enigmatic materials. I acknowledge how fortunate I am for your mentorship and to have had the privilege to learn from you both.

Special acknowledgement to UBCO's Go Global Scholarship during my undergraduate degree to study at the University of Iceland in 2012-13, and especially the program coordinator, Dana Lowton, for having the insight to encourage me to choose Iceland over Scotland for the exchange opportunity. It was a life-changer! For significant scholarships, bursaries and awards I would not have been able to participate and achieve this MSc thesis, therefore special acknowledgement is given to the Natural Sciences and Engineering Research Council of Canada (NSERC), UBCO Graduate Study Fellowships, University of British Columbia Okanagan bursaries, and scholarships from the Canadian Federation of University Women (Kelowna) and the Rix Family Foundation Award in Science and Technology. Special thanks for the collaborative opportunity from UBCO's IKBSAS International Education Bursary (2015) and Magnús Tumi Guðmundsson (University of Iceland) to participate in a seafloor volcano drilling preparation project for Surtsey, off the coast of Iceland. Acknowledgement to the Geological Association of Canada for the travel grant to present this project at their annual conference in June 2016 at Whitehorse, Yukon. In July 2017, I appreciate the travel grant offer from the Mineralogical Association of Great Britain and Ireland to present at the International Clay Conference in Granada, Spain.

Special thanks to Stefán Helgi Valsson in Reykjavik, for guiding me in local Icelandic knowledge, accompanying me, lending sampling tools and outdoor gear at Helgafell (with only four hours of mid-winter sunlight!), and numerous ways that you were an encouragement. To a special colleague, Sigríður Lára Hermannsdóttir, thank you for accompanying me to

Helgafell's glaciovolcanic ridge for my second visit and sharing of Icelandic knowledge and geological terms as it enriched my research and life. For assistance in Wells Gray, BC fieldwork (including braving the black bears and zillions of mosquitos) I thank Alejandro Valasquez, Lorne Costley, and the Thompson Rivers University (TRU) Research Cabins for lodging. I would like to acknowledge my fellow colleagues in the geology faculty at UBCO for comradeship: Jaida Lamming (SK), Sudip Shrestha (Nepal), Iva Lihter (Croatia), Kumar K.C. (Nepal), Hannah Cavallin (BC), Zhen Zhang (China), Asghar Ali (Pakistan) and Shah Faisal (Pakistan). Especially Sudip and Iva, your help with formatting or software programs was invaluable. A special thank you to Alexis Shuffler for your exceptional graphic design skills for the sedimentary profile and graphic design in illustrations and figures.

Special thanks are given to David Arkinstall at UBCO's FiLTER lab (Fipke Lab for Trace Element Research) for help in SEM and EMP analysis - your patience with my samples and instrument/technical expertise was outstanding. Funding for the FiLTER lab was provided by a generous donation by Dr. Charles Fipke. C.F. Mineral Research in Kelowna was very helpful in providing carbon coating services for samples. I appreciate UBCO's Centre for Scholarly Communication, especially Amanda Brobbel, for helpful support in academic writing.

Special acknowledgement to the following professors at the University of Iceland for each guiding and influencing my professional and academic growth during my undergraduate year of exchange studies in Iceland in addition to your inspiration and support during this master's degree project: Ólafur Ingólfsson, Gudfinna Aðalgeirsdóttir, Magnús Tumi Guðmundsson, Sigrun Hreinsdottir, Páll Einarsson, Ármann Höskuldsson and Gro Birkefeldt Møller Pedersen. For your mentorship and pioneering research in this field of work, I am thankful to have met with and learned from the late Sveinn Jakobsson (Natural Museum of Iceland). I am grateful to a life-long mentor, the late Jim Rohn: your wisdom forever had a positive influence on me.

Thank you to many families and friends that have lent a helping hand or voiced encouragement. There are not enough words to truly express adequate appreciation for my parents, Wilfred and Carol, for raising me on the prairies the way you did with the belief that we are capable of anything and to work hard for it. To my dear children, Alexis, Kai and Niall, I feel that we have done this together somehow, from our adventures while living and studying in Iceland together to sitting with me at the university while I worked, and many other ways you have inspired me.

Dedication

To my dear children, Alexis, Kai and Niall. For you have taught me the most.
Thank you for your presence in all of our journeys together.

Chapter 1: Introduction

When a volcano erupts underneath a glacier, a process called glaciovolcanism (Guðmundsson et al, 1997; Smellie & Edwards, 2016;), the extremes of hot magma and cold glacial meltwater collide in an instant. Crystals have no time to form, and, as a result, volcanic glass is produced (Bonatti, 1965; Honnorez, 1972; Jakobsson & Guðmundsson, 2008; Jercinovic, et al., 1990; Moore, 1966; Peacock, 1926). If the quenched glass remains in contact with water, it begins a process of dissolution-precipitation that first forms an amorphous material, palagonite, in a rim at the edge of the glass grains, vesicles and along fractures in the glass grains (Furnes, 1984; Hay & Iijima, 1968; Pauly et al., 2011; Peacock, 1926; Staudigel & Hart, 1983; Stroncik & Schmincke, 2001, 2002; Thorseth et al., 1991). As the volcanic pile cools, it can undergo diagenetic/secondary alteration over thousands to millions of years. The palagonite further alters to form clay and zeolite minerals, Fe-oxides and other secondary minerals (Hay & Iijima, 1968; Jakobsson & Moore, 1986; Johnson & Smellie, 2007; Paque, 2016; Walton & Schiffman, 2003). The palagonite and secondary minerals act as a cement as porosity decreases and re-crystallization processes solidify the volcanic pile (Hay & Iijima, 1968; Pauly et al., 2011; Stroncik & Schmincke, 2002).

On Earth and other planets, volcanism in water-rich environments produces different ‘flavours’ of glass, depending on magma composition. For example, obsidian glass forms from rhyolite, a high-silica (~ 65-70% SiO₂) magma (Best, 2003) whereas sideromelane (isotropic) and tachylite (opaque and cryptocrystalline) glass form from basalt, a lower-silica (~ 49-50% SiO₂) magma (Taddeucci et al., 2004). Volcanic glass is non-crystalline, amorphous and thermodynamically unstable, and prefers to eventually be in a more stable crystalline form (i.e. minerals) (Best, 2003). Nature in general likes to be in a thermodynamically stable state and this applies to geological materials such as volcanic glass (Crovisier, 1985). The role of palagonitization (the alteration of basaltic volcanic glass) is an integral part of the story of the extreme environments of volcanism in water (e.g. glaciers and oceans) on Earth and maybe on Mars and other planets (Francis & Oppenheimer, 2004; Smellie & Edwards, 2016).

In the early stages of Earth’s evolution, volcanoes and oceans were prominent, so this meeting of magma and water has been important since at least 4 billion years ago (Francis & Oppenheimer, 2004; Wicander and Monroe, 2006). Today, seafloor volcanoes comprise ~80 %

of all volcanism occurring on Earth. It is estimated that 100,000 to 10 million hydrothermally active seamounts exist on the seafloor (Fisher & Wheat, 2010; Wessel, Sandwell & Kim, 2010). Most of these volcanoes occur below thousands of metres of ocean water (Fisher & Wheat, 2010). It has been said that scientists know more about outer space than the ocean floor (Fisher & Wheat, 2010; Wessel et al., 2010).

Earth's climate has cycled between glaciations and warm periods many times in its history, with the Snowball Earth hypothesis suggesting that ice covered the entire planet during the Neoproterozoic (~650 Ma) until volcanism initiated a warmer period once again (Hoffman et al., 1998; Kirschvink, 1992). Five major Ice Ages are thought to have occurred on Earth, with minor Ice Ages occurring every ~100,000 years due to eccentricity, obliquity and precession cycles in Earth's elliptical orbit around the sun, axis gyration and fluctuations, and internal feedback cycles (Abe-Ouchi, 2013).

Deglaciation during post-glacial warming periods has been associated with increased volcanism due to rapid isostatic rebound (Ingólfsson et al., 1995) and release of pressure on the underlying mantle (MacLennan et al., 2002). Therefore, environments where glaciation has repeatedly occurred in areas with active volcanism provide the conditions for increased glaciovolcanism during these periods (Ingólfsson et al., 1995). Geochemical changes in magma have also been recognized between glacial and post-glacial eruptions (MacLennan et al., 2002), further establishing glaciovolcanic deposits as important windows into Earth's climate cycles and geologic past.

During the past 2 Ma, there is evidence for at least ~ 20 glacial-interglacial periods (Wicander & Monroe, 2013) in which explosive, glaciovolcanic eruptions have occurred globally but especially in Iceland and British Columbia (Smellie & Edwards, 2016). In British Columbia, many volcanoes in the northern Cordilleran volcanic province (e.g. Mount Edziza, Hoodoo Mountain, Level Mountain, and the Tuya-Kawdy Volcanic Field), as well as the Wells Gray Volcanic Field (WGVF) and Garibaldi Belt are excellent examples of glaciovolcanism that occurred during periods of continental glaciation dating back to at least the Pleistocene (Edwards et al., 2002; Edwards & Russell, 2002; Harder & Russell, 2007; Hickson, 2000; Jercinovic, 1997; Mathews, 1947).

A subglacial eruption was not actively observed until an event in Antarctica in 1969 (Smellie & Edwards, 2016), followed by the Gjálp eruption under Europe's largest glacier,

Vatnajokull, Iceland in 1996 (Guðmundsson et al., 1997). More recently, glaciovolcanic events have been monitored and observed at Grímsvötn, Iceland (2004 and 2011), during the air traffic-stopping eruption of Eyjafjallajökull in 2010 (Oddson et al., 2016), and Veniaminof, Alaska and Tolbachik, Russia in 2013 (Smellie & Edwards, 2016). New discoveries on caldera-formation (e.g. the eruption drives caldera formation, not vice versa) at an ice-covered stratovolcano have just been published from closely-monitored subsidence of the ice cauldron above Bárðarbunga's magma chamber during its 2014-15 eruption, which propagated through a 40-km long dyke to produce voluminous lava at Holuhraun (Guðmundsson et al., 2016).

Although continental ice sheets other than in Greenland and the Antarctic are now mostly melted, glaciovolcanic events continue to produce vitric, fragmental volcanic deposits that are highly susceptible to hydrothermal alteration that partly transforms glass into palagonite (Jakobsson & Guðmundsson, 2008; Stroncik & Schmincke, 2002). Because palagonitization rates are thought to depend on temperature (Jakobsson & Moore, 1986), the preserved deposits can provide general constraints on the cooling conditions of the volcanic pile within the glacier. It is generally accepted that palagonite forms from sideromelane by an evolutionary process of dissolution-precipitation, although the mechanisms controlling the alteration are not fully understood (Furnes, 1984; Honnorez, 1981; Pauly et al., 2011; Stroncik & Schmincke, 2002).

It is important to understand palagonitization because it has a critical, controlling influence on water-rich environments, such as the chemistry of the ocean (Bonatti, 1965), lakes and rivers (Hein et al., 1979; Staudigel & Hart, 1983), and on the porosity, fluid circulation, and edifice stability of volcanoes (Pauly et al., 2011; Schiffman et al., 2000). Glaciovolcanic deposits are a useful paleoclimate proxy to interpret environments in which volcanic landforms were made (Edwards et al., 2010). In fact, 1000 miles (about 1600 km) from the southern ice cap on Mars, glaciovolcanic deposits were recently observed and NASA scientists suggest that glacial ice once covered a larger area of Mars based on these important volcanic landforms (Ackiss et al., 2016). Basaltic glass is a natural analogue for borosilicate glasses purposed as a stable storage medium for high-level nuclear waste (Crovisier et al., 1997) and altered volcanic deposits may be important today for hosting potential sources of geothermal energy (Liu et al., 2012).

The Canadian Space Agency designates palagonite as an analogue material for Mars (Cloutis et al., 2015), and it is thought to give evidence for water on Mars. Glaciovolcanic

lithologies and palagonitization processes on Earth are helping scientists to understand the alteration of the crust on Mars, and to provide evidence for future astrobiology studies (Ackiss et al., 2016, 2017; Cockell et al., 2014; Cousins et al., 2013; Quinn & Orenberg, 1993). Therefore, research on the formation of palagonite can help us interpret geochemical data for martian basalts where basaltic glass may have interacted with water, and to constrain hypotheses for the possibility of life-giving water.

Research on palagonite has shown that it can form anywhere that volcanic glass contacts water. For example, sideromelane and its alteration products can be found where magma-water interaction has occurred during eruptions on the ocean floor (Banerjee, 2006; Bonatti, 1965; Hein et al., 1979; Pauly et al., 2011) or underneath glaciers and glacial meltwater (Edwards et al., 2010; Jakobsson & Guðmundsson, 2008). Palagonitization can also occur within subaerial deposits (Furnes, 1984), or along faults in a volcanic pile or a caldera rim (Schiffman et al., 2000) due to fluid percolation.

Factors that affect palagonitization include the structure and reactive surface area of both the parent glass and secondary phases, in addition to temperature, time and fluid properties including pH (activity of H^+ ions), Eh (redox potential or activity of electrons), oxygen fugacity (partial pressure of oxygen) and ionic strength (Stroncik & Schmincke, 2002). Fluctuations in pressure gradients, permeability and porosity are also important to the geochemical processes (Pauly et al., 2011; Stroncik & Schmincke, 2002).

Although the formation of palagonite in glaciovolcanic deposits has been investigated separately in Iceland's tholeiitic systems (Pauly et al., 2011; Peacock, 1926; Stroncik & Schmincke, 2001; Thorseth et al., 1990) and British Columbia, Canada's alkali olivine basalt (AOB) deposits (Jercinovic et al., 1990), no single study has directly compared palagonite from Iceland and BC.

Stroncik and Schmincke's (2001) review on palagonite suggested that future workers systematically study palagonite from different volcanic settings and alteration environments, keeping in mind that different controlling mechanisms may occur at different times. Furnes (1978) predicted that if chemically different basaltic glasses under identical physio-chemical conditions were compared, different compositions of palagonite would result. This study tests these predictions and the hypothesis that the composition of glaciovolcanic sideromelane is the most important control on the composition and texture of palagonite. For example, is the

process isovolumetric for AOB sideromelane but not for tholeiitic? Does mass transfer differ for the two compositions? Does element mobility change depending on the sideromelane composition? Is there a unique signature of sideromelane composition in the palagonite or is palagonite composition not variable?

Many variables cannot be rigorously controlled, such as pressure (ice thickness) or post-formation temperatures and/or crustal fluids, which could impact the composition of palagonite, but this study attempts to eliminate many of them as variables. The two glaciovolcanic deposits chosen for this study are approximately the same age (Pleistocene), result from interaction between sideromelane and pure water formed by melting of overlying glaciers, and are located in an extensional tectonic setting. But the sideromelane compositions are different. Glaciovolcanic palagonite from Second Canyon in Wells Gray-Clearwater Volcanic Field, BC, Canada (alkali olivine composition) and Helgafell, Reykjanes Peninsula, SW Iceland (tholeiitic composition) were collected and examined in order to characterize pre-alteration textures and degrees of palagonitization, element mobility, and mass transfer.

Chapter 2: Literature Review of Palagonite (1846 – 2017)

Although the study of palagonite has been ongoing for more than 100 years its formation is still not well understood (Jercinovic, 1990; Pauly et al., 2011; Peacock, 1926; Stroncik & Schmincke, 2001; Thorseth et al., 1990). The purpose of this historical review is to clearly define and describe palagonite and its environments of formation, and to summarize the hypothesized physical and chemical controls on the processes of palagonitization.

2.1 What is Palagonite?

Sideromelane and palagonite were observed and named before petrographic microscopes were common, thus technological advances continue to be critical to the definition of these materials (Pauly et al., 2011; Peacock & Fuller, 1926). Palagonite was first defined as a hydrated volcanic glass and brown material (von Waltershausen, 1845) with a low refractive index (~1.46) and high water content (~18–32 wt. %; Peacock, 1926), that was associated with tuffs and subaqueous basalt. Within a few years of its discovery by von Walterhausen (~1845) in the Hyblean Mounts at Palagonia, Sicily, palagonite went from being considered a new mineral to being considered an amorphous mixture of materials consisting of altered, hydrated and oxidized glass (Penck, 1879, as cited by Honnorez, 1981). Peacock (1926) proposed the term chlorophaeite to be used for all hydrous, amorphous materials of deuteric origin such as palagonite, but this term did not take hold and palagonite has remained the term for the material that results from the alteration of basaltic glass. Palagonite is usually described as yellow-brown in colour, although Thorseth et al. (1991) found coloured zoning ranging between brown, yellow and white, depending on porosity. Thorseth et al. (1991) observed that palagonite is texturally granular and sponge-like but most studies refer to two palagonite textures: gel-palagonite (amorphous, isotropic and yellow to red-brown) in earlier stages and fibro-palagonite (darker yellow-brown, slightly anisotropic and poorly crystalline) in advanced stages, similar to Peacock's (1926) observations. Stroncik & Schmincke (2001) introduced the idea of two aging steps (step I: mix of palagonite and crystalline phases; step II: mainly crystalline) that follows the initial formation of amorphous palagonite.

Today, there is general consensus that palagonite is the first alteration material of basaltic glass (sideromelane) and is a hydrated, metastable, variably isotropic to anisotropic, yellow to

brown-coloured amorphous material that closely resembles smectite in overall chemistry (Stroncik & Schmincke, 2001).

2.1.1 Minerals Associated with Palagonite

Palagonite's mineralogy is not completely defined (Stroncik & Schmincke, 2000), although at least nineteen common minerals and substances are found in or associated with palagonite (Appendix C.1). Secondary crystalline phases form an impressive number of minerals (Appendix C.1) such as various types of clays (e.g. smectite, montmorillonite), opal, chalcedony, gypsum, halite, anhydrite, zeolites, hematite, sulfides, (e.g. pyrite, chalcopyrite), and sulfates (Bonatti, 1965; Stroncik & Schmincke, 2001). A host of temperature-dependent secondary minerals are associated with palagonite and were identified in a 181-m drill core on the volcanic island of Surtsey (off the south coast of Iceland) only twelve years after its famous 1963-67 seafloor eruption (Jakobsson, 1979), and include calcite, phillipsite, analcime, tobermorite, nontronite (from olivine), globular smectite, gypsum, halite and chabazite (Jakobsson, 1979).

Clay minerals usually fill vesicles and pores rather than forming well-defined layers, although Fe-saponite and illite interlaying were identified based on EMPA results (Jercinovic et al., 1990). Weathering products are predominantly (14–30 %) calcic zeolites, and analcime, $\text{NaAlSi}_2\text{O}_6 \cdot \text{H}_2\text{O}$, in the latest alteration stages (Jercinovic et al., 1990). Other features, such as prismatic calcite crystals in cavities and fine-grained aggregate growths on zeolites/clay substrates, have been noted in late-stage alteration (Jercinovic et al., 1990). The clay mineral tobermorite was tentatively identified from rare bundles of Ca-Si-P phases found inside vesicles (Jercinovic et al., 1990).

2.1.2 Textures of Palagonite

During early alteration, Peacock (1926) described isotropic gel-palagonite to be light yellow to red-brown, and in more advanced stages he described slightly anisotropic fibro-palagonite as darker yellow-brown in the outer part of the altered rind. Later studies (Eggleton & Keller, 1982) reported that the fibro-palagonite frequently had scattered opaque granules in its more fibrous texture, which were thought to result from the crystallization of clays, Fe-oxides and hydroxides (Moore, 1966; Stokes, 1971).

Microscopic textures of palagonite also are sometimes interpreted as of biologic origin (Banerjee et al., 2006; Fisk & McLaughlin, 2013). Microphotographs by previous workers have shown dendritic, tunneling and tubular textures propagating within basaltic glass from vesicles, fractures and grain edges, some of which are interpreted to be bioalteration textures (Banerjee et al., 2006; Fisk & McLaughlin, 2013; Furnes et al., 2008; Staudigel et al., 2008; Walton & Schiffman, 2003). Ocean drilling programs have contributed an impressive atlas of alteration textures in volcanic glass analyzed from oceanic basins (e.g. Figure 1, from Fisk & McLaughlin, 2013).

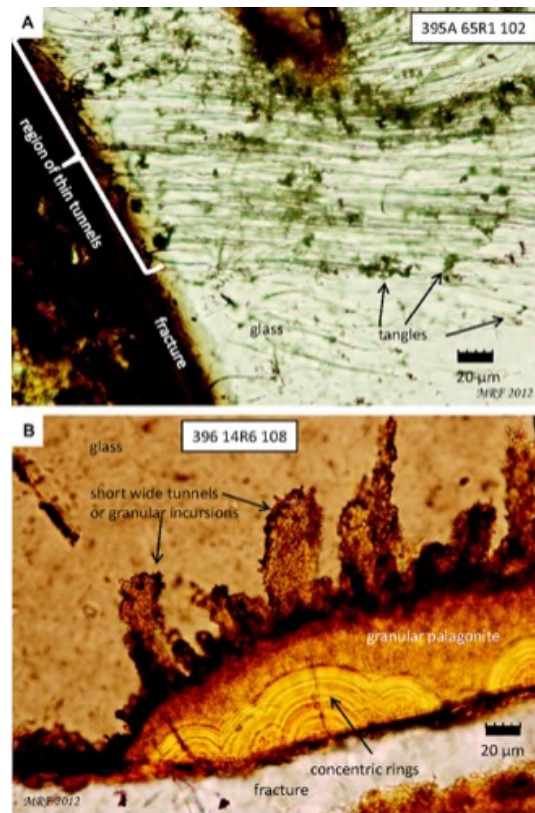


Figure 1 Textural studies reveal tunneling (possibly microbial), zoned hemispheres or concentric rings and granular shades of yellow to brown palagonite in basaltic glass (Fisk & McLaughlin, 2013, their Figure 8). Permission granted by the Geological Society of America.

The harsh habitats that microbes colonize to perform alteration of volcanic glass can support either diverse or restricted groups of microorganisms (Furnes et al., 2008) and seafloor basalts have been recognized as fungal habitats (Ivarsson, 2012), an important area for future research. The ocean crust is believed to have the largest potential for microbial habitat on Earth (Ivarsson, 2012). Banerjee et al. (2006) documented the preservation of textural and chemical biomarkers in Archean basaltic glassy rims of pillow lavas that indicate

microbially mediated alteration and colonization in 3.4 - 3.5 Ga rocks in oceanic crust and young ophiolites of the Barberton Greenstone Belt. As a result, Banerjee et al. (2006) predicts the importance of subaqueous volcanic rocks for discovering early life on Earth.

Complex chemical reactions during palagonitization gradually form extremely erosion-resistant, cemented deposits of tephra (Liu, 2012), illustrated in the macroenvironments at Helgafell, SW Iceland and Wells Gray, BC Canada (Figure 2).

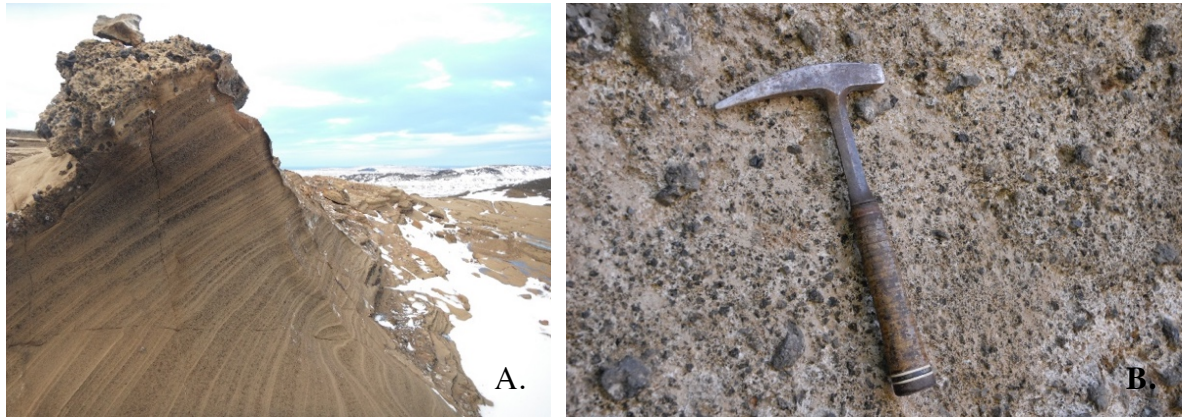


Figure 2 The macroenvironment of palagonitized lapilli tuff is erosion-resistant, cemented and can have a) fine to coarse-grained bedding (Image: Helgafell), or be b) massive (Image: Wells Gray).

2.2 Palagonite – Key Historical Studies

The term palagonite was first used by Sartorius von Waltershausen in 1846, to describe the tuff material prevalent near the village of Palagonia, located at the base of the stratovolcano, Etna, on the east coast of Sicily, Italy (Watts, 1966). The German chemist, R. Bunsen (1867), noticed the chemical similarity between palagonite and basaltic glass in Icelandic hyaloclastites (except for the addition of water in palagonite), and suggested a stoichiometric formula for palagonite to be $3(M_2O, SiO_2)Al_2O_3 \cdot 3SiO_2 \cdot 10H_2O$ (M = cation site).

The Palagonite Formation of Iceland was first described by Peacock (1926) as a broad, irregular belt trending in a SW-NE direction across Iceland that forms the highest mountains built by lavas, glacial deposits and ice. Peacock (1926) hypothesized that the formation resulted from subglacial extrusions that exceeded the restraints of the overlying ice. Peacock (1926) documented that the palagonite-tuff was almost entirely composed of highly hydrous, palagonitized glass fragments that compared closely to what he termed “explosion-tuff” from Viðey Island, Iceland. Peacock and Fuller (1926) measured and compared the refractive indices for Icelandic sideromelane (~ 1.592), palagonite (~ 1.47), and water (~ 1.33), in order to

estimate the water-content in palagonite (~28 wt. %). They determined that refractive index and water content were inversely related in palagonite, and recognized differences between gel-palagonite (isotropic) and fibrous, spherulitic palagonite (birefringent).

The MÓberg (Palagonite) Formation of Iceland was later studied further and categorized as a chronostratigraphical unit that formed in the Late Pleistocene (Kjartansson, 1960; Einarsson, 1994). MÓberg (an Icelandic term for ‘tuff mountain’) is consolidated, mafic to intermediate hyaloclastite that covers ~ 11,200 km² in Iceland’s ice-free volcanic zones (van Bemmelen & Rutten, 1955; Kjartansson, 1943). In their book, *Tablemountains of Northern Iceland*, van Bemmelen and Rutten (1955) provide an excellent description for dozens of tablemountains (now referred to as tuyas) that comprise the MÓberg (Palagonite) Formation of Iceland in the vicinity of Mývatn, northeast Iceland. Petrographically, palagonite varies from black at Blafjall and brown at Búrfell, to lighter brown at Skógarmannafjöll (van Bemmelen & Rutten, 1955).

In the 1940’s, two geologists separately described flat-topped, steep-sided volcanoes (now known as tuyas) and attributed their unusual form to subglacial volcanism (Hickson, 2000; Russell et al., 2014): G. Kjartansson, in Iceland, and W. H. Mathews, in northern British Columbia. Geologists in Iceland and Canada continued to expand their knowledge of glaciovolcanism in the 1950’s, such as in the Mount Garibaldi region of BC (Mathews, 1947) and numerous locations in Iceland (Jones, 1969). In most of these locations the occurrence of palagonite was an important aspect of the interpretation of glaciovolcanic deposits.

In his study of Quaternary basalts in Iceland, Bonatti (1965) proposed that sideromelane fragments and devitrified palagonite alter primarily in the last stages of cooling. He also examined volcanic glass from the Pacific Ocean floor, the Columbia River plateau, Iceland and the Oregon coast using X-Ray Diffraction (XRD). Bonatti (1965) concluded that palagonitization results from an attack on the more hydrated (~ 4.38% H₂O), translucent basaltic glass (sideromelane) than the opaque, nearly anhydrous (< 1.13% H₂O) basaltic glass (tachylite). In order for the catalyzing action of water to devitrify (i.e. break Si-O-Si or Si-O-Al bonds) in basaltic glass and initiate crystallization (reorganization of atoms), he suggested that 15% water is required, and up to 20-25% water is required for acidic glasses due to more Si-O and Al-O bonds. Bonatti (1965) speculated that solutions in contact with the glass are important to provide cations for new mineral formation, and he described two stages of

palagonitization: 1) the glass structure is disrupted by water molecules diffusing into its structure. The diffusion rate is very low, with an estimated diffusivity of 10^{-10} cm²/Ma years at 20° C, so devitrification also occurs slowly. 2) Si and Al tetrahedra are arranged into ordered structures as crystalline alteration products form.

Shortly thereafter, Furnes (1984) presented a microprobe study of subaerial palagonitization by means of meteoric water percolating through a deposit of glaciovolcanic olivine tholeiite pillow lavas/hyaloclastites at Mosfell, Iceland. He noticed that south-facing samples showed more advanced stages of palagonitization and claimed that Fe is the most immobile element, as its concentration varied minimally between the sideromelane and palagonite, although in later stages of alteration Fe was slightly enriched in the palagonite (Furnes, 1984).

Crovisier et al. (1987) conducted experiments wherein artificial tholeiitic glass was altered in synthetic seawater. They found that palagonitization first breaks down the cation-anion network of the glass, then causes precipitation of secondary minerals. They suggested that the growth rate of palagonite layers was linear with time, and they predicted that within the first 2×10^5 years of reaction time palagonitic layers would still not constitute a diffusional barrier to mass transfer between the bulk solution and glass (Crovisier et al., 1987). The study concluded that Ti or Fe were preferable as conserved elements in mass balance calculations (Crovisier et al., 1987).

A study of the Gulf of Alaska seamount province found that low-temperature, oxidative palagonitization of basaltic glass mobilizes Mn and other transition metals to form Mn-Fe deposits (Koski, 1988). The study suggested that palagonitization releases K, which can then form secondary phyllosilicate minerals, (e.g. phillipsite, todorokite and cryptomelane) and that the oxidation of Fe²⁺ to Fe³⁺ in palagonite lowers Eh values of the ambient pore fluids and increases the solubility of Mn²⁺ (Koski, 1988).

More recent studies by Stroncik and Schmincke (2001, 2002) and Pauly et al. (2011) sought to compare palagonitization in different environments. Two aging steps with different trends in element mobility were observed in palagonite (Stroncik & Schmincke, 2001) and increased chemical variation was restricted to earlier stages of alteration than in later stages of crystallization (Stroncik & Schmincke, 2001). They interpreted palagonitization to be at least partly controlled by the aging process and that it is independent of the alteration environment.

In a review on palagonite, Stroncik and Schmincke (2002) attribute the chemical heterogeneity of palagonite to fluid properties, e.g. composition, pH, and observed palagonitization rates to vary at a microscale (within one sample) thus independent of time. They found uncertainty from previous workers in understanding different controlling mechanisms at different stages of palagonitization and predicted that it was necessary for future studies to effectively analyze palagonite from 1) different volcanic environments, and 2) different alteration stages.

Most recently, Pauly et al. (2011) studied palagonite from five different volcanic environments (e.g. subglacial, marine phreatomagmatic, lacustrine, seafloor). They suggested that water content in palagonite and original sample porosity are related to palagonitization extent (inversely and linearly). Original sideromelane composition has a significant control on palagonitization, e.g. increased rates of dissolution in subalkaline relative to alkaline sideromelane (Pauly et al., 2011). Element behaviour estimated with isocon diagrams showed REEs to be immobile and major elements to be variable in palagonite (Pauly et al., 2011).

Extensive research has been conducted on the palagonitization of natural and artificial glasses (Anaf, 2010; Bunker & Casey, 2016; Grambow, 2011). Different corrosion processes that can transform glass have been described, such as ion exchange (forms a leached layer in glass), hydration (diffusion of water into the glass), and hydrolysis (OH^- and H_2O attack the SiO_2 -rich glass network). Grambow (2011) found glass corrosion to be dependent on its composition (since composition effects structure), in addition to surface and environmental conditions (i.e. temperature, pH, stress, strain and vapour pressure). Increased concentration of alkali ions (alkali metals: Li, Na, K, Rb, Cs, Fr) disrupts the bridging in glass structures, therefore, reducing the melting point and resistance to corrosion (Grambow, 2011). On the other hand, alkali earth cations (i.e. Be, Mg, Ca, Sr, Ba) increase the density of crosslinks in glass networks, thus, increasing resistance to corrosion (Grambow, 2011). Early phases in hydrolysis (chemical breakdown of glass dissolution by water) commonly produce a hydrated gel-phase in synthetic glass studies (Anaf, 2010; Bunker & Casey, 2016; Grambow, 2011).

Historical studies have shown variability in palagonite composition may be related to different factors, e.g. original sample porosity, water content in palagonite, sideromelane composition, but the controlling mechanisms of palagonitization remain poorly understood.

2.3 How Does Palagonite Form?

This study examines palagonite formation resulting from glaciovolcanism, therefore a description of palagonitization in this environment is warranted.

2.3.1 Environments of Formation

Palagonitization and its signature product palagonite can be found in many different environments on Earth, and possibly other planets, where the key ingredients exist: basaltic glass, water and heat. On Earth, palagonite is located where volcanoes erupt under water or below glaciers in colder climates, such as Iceland (Jakobsson & Guðmundsson, 2008), British Columbia (BC; Edwards et al., 2010; Hickson, 2000), James Ross Island, Antarctica (Johnson & Smellie, 2007), and Alaska (Koski, 1988). But palagonite also forms in warmer climates, such as Hawaii (Schiffman, 2000), the Columbia River Basalts (Peacock & Fuller, 1928), Jamaica (Raw & Matley, 1943) and the Galapagos Islands (McBirney & Howel, 1969).

Palagonite can also be found near faults in areas prone to hydrothermal alteration (Schiffman et al., 2000), where subaqueous eruptions have formed submarine or lacustrine deposits, or where phreatomagmatic eruptions have formed volcanic islands on the ocean floor, such as Hawaii or Surtsey (Jakobsson & Moore, 1986; Pauly et al., 2011).

2.3.2 Eruption Progression

Although the eruptive processes that produce distinct volcanic landforms associated with palagonitization are diverse, (e.g. submarine, seafloor, lacustrine or subglacial environments), only the classic, flat-topped, near-vertical-walled tuya will be discussed here since palagonite is closely associated with glaciovolcanic eruptive processes at Helgafell and Wells Gray.

Glaciovolcanic eruptions commonly form the classic volcanoes, termed tuyas, that are produced in stages under thick glacial ice (Figure 3) (Jakobsson & Guðmundsson, 2008; Smellie & Edwards, 2016). First, pillow lava is produced at high-pressure in water formed from ice melting at the eruption onset (Smellie & Edwards, 2016). In the second stage, an ice cauldron grows above the lava pile that continues to grow upwards, thereby producing fragmented lapilli and brecciated material due to a reduction in water pressure (Smellie & Edwards, 2016). This process allows for the expansion of gas phases and increased amounts and rates of vesiculation in an eruption that is progressively becoming more explosive and

phreatomagmatic (Smellie & Edwards, 2016). In the third stage, the edifice breaches the surface of the ice-confined, englacial lake and builds a lava cap that broadens out laterally to form a prograding delta of pillow lavas and tephra, until the eruption ends or the englacial lake drains (Smellie & Edwards, 2016).

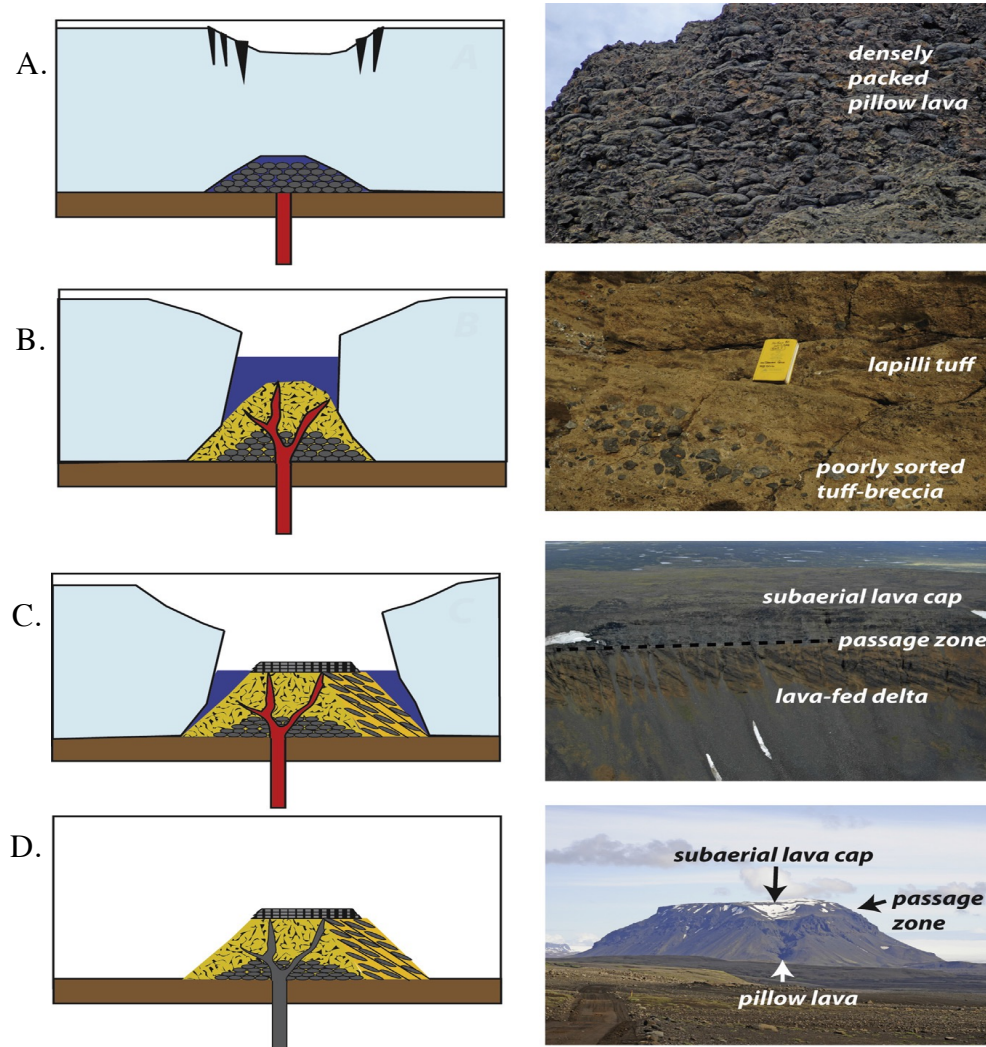


Figure 3 Lava-capped tuyas form in stages with characteristic lithofacies (from Smellie & Edwards, 2016) . (A) Effusive eruption under thick ice forms a sub-ice cavern, Pillow Ridge, BC. (B) Volatile exsolution and phreatomagmatic fragmentation produce lapilli tuff and tuff breccia, Kima' Kho tuya, BC, (C) Eruptive breach of englacial lake surface produces bedded lavas, and passage zone to subaerial lava cap, Kima' Kho tuya, (D) Removal of ice sheet leaves flat-topped tuya landform of pillow lavas and hyaloclastite, tephra, pillow breccia and subaerial lava cap, Hloðufell tuya, Iceland. (Image from: Smellie & Edwards, 2016).

The passage zone (lithofacies transitions from tuff-breccia and isolated pillow lavas to subaerial lava flows) in the delta between subaqueous and subaerial material is thought to be a useful paleoclimate proxy that provides clues to former ice thicknesses, englacial lake depth,

glaciohydraulics and ice sheet location (Russell et al., 2014). In the fourth and final stage (Figure 3), the glacial ice completely melts and leaves the landscape either by a jökulhlaup (Icelandic term for a catastrophic glacial flood), or more gradually (Smellie & Edwards, 2016). If the glaciovolcanic eruption does not breach the surface of the englacial lake, a remnant subglacial mound or ridge that is not flat-topped, but rather a rounded, pyramidal, or an elongated landform will result (Smellie & Edwards, 2016).

2.3.3 Chemical Controls and Processes of Palagonitization

The chemical controls on palagonitization include glass and solution compositions, variations in subsequent element mobility, and thermodynamic and kinetic properties.

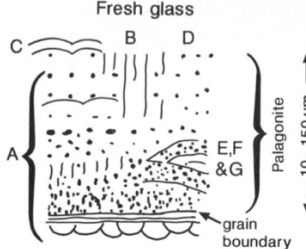
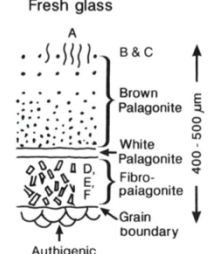
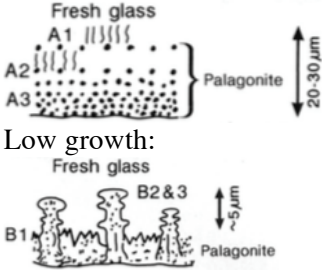
The composition of basalts vary due to the percentage of melting, depth of melting, mantle source composition and degree of differentiation prior to eruption. The active rift-zones in Iceland produce basalts of the tholeiitic series (high percent melting) compared to alkaline series basalts (low percent melting) in the off-rift volcanic zones (Sigmarsson & Steinthorsson, 2007). Basalts produced by extension in British Columbia are generally of the alkaline series (Edwards & Russell, 2000).

Two previous studies examined palagonite formed from different compositions of basaltic glass, Thorseth et al. (1991) and Pauly et al. (2011).

2.3.3.1 Thorseth et al. (1991)

Thorseth et al. (1991) examined the textures and geochemistry of palagonite from basaltic andesite, olivine tholeiite and quartz tholeiite glass (Table 1). In the basaltic andesite glass, several Fe-rich zones alternate in the palagonite (Thorseth et al., 1991). White, Fe-depleted palagonite alternates with yellow to brown palagonite, and its texture progresses from slightly granular at the glass-boundary (sharp or gradual) to very granular and porous at the edges of rims (Thorseth et al., 1991). Spherical bodies or chains of connected spheres (often extensively zoned) at the palagonite boundary grow in an outward-convex pattern into the glass grain and seem similar to palagonite but are highly variable in TiO₂ and FeO (Thorseth et al., 1991, their Figure 1A and 2A).

Table 1 Alteration characteristics of palagonite from three parent materials (Thorseth et al., 1991).

Rock Type	Chemical & Mineral Characteristics	Study Location & Water Source	Colour/Features of Palagonite	Various Alteration Characteristics
Basaltic Andesite	53-57% Silica Minerals: Olivine, augite, plagioclase	Location: Kerlingarfjöl, Iceland Highlands. Meteoric water.	 <p><i>Inner zone:</i> isotropic gel-palagonite; alteration front is white to gray. <i>Outer rim:</i> yellow-brown to dark brown palagonite.</p>	White palagonite decreases in Ti, Fe, Na, Mg, Ca, Al (relative to glass); progresses to brown Ti, Fe-rich palagonite; outer glass has spherical/hemispherical, porous Fe-, Ti-Al-rich growth.
Quartz tholeiite	48-52% Silica Minerals: Lacks olivine, abundant low-Ca pyroxene (pigeonite or hypersthene), and quartz granophyric intergrowths.	Location: Kjalarnes, West Iceland Seawater and meteoric water.	 <p><i>Inner and outer zone:</i> Slightly anisotropic yellow-brown to dark-brown fibropalagonite having smectite. <i>Central zone:</i> white palagonite.</p> <p>‘Globules’ (glass & rim). Rims: 400-500 μm thick.</p>	Sharp glass-palagonite boundary with micro-fractures. Outer rind, fibrous and Mg-enriched progressively (may be due to seawater alteration at high temp.)
Olivine tholeiite	48-52% Silica Mineralogy: olivine, plagioclase & high-Ca pyroxene; olivines can have low-Ca opx rims.	Location: Laugarvatn and Mosfell, Iceland. Meteoric water.	 <p><i>Inner zone:</i> isotropic gel-palagonite/yellow-dark brown. Between glass & palagonite: <i>white zone</i>. Rims: 5 - 25 μm thick. High growth: Low growth:</p>	Brown palagonite at outer edge of rim.

Element concentrations of white palagonite associated with basaltic andesitic glass are lower than in the parent glass except SiO_2 is higher. At the glass-palagonite boundary, FeO , TiO_2 , MgO and Na_2O in palagonite were almost completely lost and CaO , Al_2O_3 and K_2O are slightly lost (Thorseth et al., 1991).

The quartz tholeiite glass shows very thick (400–500 μm) palagonite rinds and is slightly anisotropic, which differs from typical isotropic gel-palagonite (Thorseth et al., 1991). Granular textures or microfractures are common in the glass. Globules in palagonite have a granular-porous texture, whereas zoning in fibrous-textured palagonite has sponge-like textures or fan/leaf-shaped growths of smectite (Thorseth et al., 1991).

In the olivine tholeiite glass, yellow to brown palagonite is common yet so are white to light yellow zones between brown palagonite and fresh glass. Cryptocrystalline precipitates can occur in layers on the palagonite surface (Thorseth et al., 1991). The olivine tholeiite glass is analogous to Helgafell's basaltic composition in this study.

Thorseth et al. (1991) proposed that to dissolve and keep Fe, Ti and Al in solution, an acidic $\text{pH} < 3$ is required, whereas an oxidizing environment with a $\text{pH} > 3$ facilitates the precipitation of these elements. They further suggest that brown palagonite develops with a $\text{pH} > 3$ (when precipitation of Fe, Ti and Al is encouraged) and white palagonite develops when $\text{pH} < 3$ (when Fe, Ti and Al dissolve, and Ca, Mg and Fe are leached from the glass). The glass-palagonite boundary reflects the rate of alteration with a sharp boundary associated with rapid alteration and dendritic patterns for slow alteration (Thorseth et al., 1991). The boundary area is often thick (5-10 μm) with closely spaced microfractures perpendicular to the alteration front, which may serve as water penetration pathways (Thorseth et al., 1991).

2.3.3.2 Pauly et al. (2011)

Pauly et al. (2011) compared subalkaline and alkaline basalt glasses from five different environments to see if depositional environment is related to the texture and composition of palagonite. Palagonitized samples were examined for water content in palagonite, palagonitization extent, and overall mass transfer. Based on observations of significant variability in rim thickness, they concluded that only when sideromelane compositions are identical can palagonite rim thickness indicate the duration of palagonitization.

They found that the original composition of sideromelane controlled palagonitization. For example, alkaline sideromelane dissolved slower than subalkaline sideromelane, based on mass balance calculations from isocon diagrams using scaled Zr, Nb, Sc, La and Nd as immobile elements (Pauly et al., 2011). The original sample porosity, termed ‘minus-cement’ porosity, (calculated by: % pore space + % zeolites - % lithic and crystal clasts) was found to have an inverse and linear relationship with palagonitization extent, thus having a control on palagonitization. Palagonitization extent (calculated by: % zeolites + % palagonite and smectite) was highest in submarine volcanoclastic samples, but a correlation of low minus-cement porosity with higher palagonitization extent was observed. Reflected light infrared spectroscopy (RL-FTIR) water content measurements in palagonite correspond to water contents calculated from microprobe totals, confirming that H₂O can be estimated from microprobe totals (Pauly et al., 2011).

Pauly et al. (2011) predicts that palagonitization is non-isovolumetric (the term ‘isovolumetric’ refers to no volume change occurring during the process) based on the observations of large mass changes in major elements that indicate significant dissolution and the formation of microporosity. Isocon diagrams based on immobile REE, Zr, Nb and Sc concentrations were used to calculate mass transfer, which revealed that mass change in SiO₂, Al₂O₃ and especially FeO and TiO₂ depend on whether the composition of sideromelane is subalkaline or alkaline. MgO concentration gradients (increasing towards the outer palagonite rim) are suggested to reflect high mobility and the conversion of a gel-palagonite layer to a phyllosilicate such as smectite as the sideromelane alteration layers progress towards equilibrium with the surrounding solution (Pauly et al., 2011).

2.3.3.3 Isovolumetric Assumption and Density

Some workers have proposed that palagonitization is isovolumetric (Furnes, 1978; Hay & Iijima, 1968; Jakobsson & Moore, 1986; Jercinovic et al., 1990), but other workers have suggested that it is not (Crovisier et al., 1987; Hekinian & Hoffert, 1975; Pauly et al., 2011; Schiffman et al., 2000; Thorseth et al., 1990; Zhou & Fyfe, 1989). The suggestion that palagonitization is isovolumetric is based on using known densities for palagonite and sideromelane (commonly from Hay & Iijima, 1968; Table 2), allowing the percent changes of each oxide relative to the parent glass to be calculated.

Table 2 Density values for sideromelane, palagonite and associated tuff material change due to differences in porosity and composition (Hay & Iijima, 1968; Staudigel & Hart, 1983).

Density of sideromelane (g/cm ³)	Density of palagonite (g/cm ³)
Fresh sideromelane: 2.75	Palagonite: 1.90 – 2.10
Fresh sideromelane tuff: 1.67	Dense palagonite tuff: 2.05

At Koko Crater, Oahu, Hawaii, Hay and Iijima (1968) studied the progressive conversion of unconsolidated ash deposits to opal-cemented tuff and dense palagonite tuff that had interacted with cold, percolating ground water. Dense palagonitized tuff (~6.1-11.5% porosity) is less porous than fresh deposits (~36% porosity), and deposits become more dense and palagonitized with depth (Hay & Iijima, 1968). The density of sideromelane, palagonite, and associated tuff was determined from porosity, grain density and bulk density calculations from 14 chemically analyzed samples (Hay & Iijima, 1968). Based on the isovolumetric assumption, chemical change between sideromelane and palagonite per unit volume was calculated using density values (Table 2, Hay & Iijima, 1968), which found small gains in Ti and variable loss/gain of Mg and Fe. Significant loss of Si, Al, Na, K and Ca was interpreted to mean that palagonite is not hydrated glass (Peacock, 1926) or devitrified glass (Bonatti, 1965) but a reaction product of glass (Hay & Iijima, 1968).

The isovolumetric argument is based on the observation that the volume relationship between palagonite, glass grains and precipitated material result in no change in volume of these materials within fractures in glass (palagonite equally replaces sideromelane; Jercinovic et al., 1990). The sideromelane's primary texture is preserved and undistorted, further suggesting that palagonitization is isovolumetric (Hay & Iijima, 1968; Jakobsson & Moore, 1986; Stroncik & Schmincke, 2001). It has been acknowledged, though, that palagonitization is not isovolumetric once authigenic, secondary minerals precipitate (Stroncik & Schmincke, 2001). Further differences between dissolution rates (glass) and growth rates (palagonite) support the argument that palagonitization is non-isovolumetric (Crovisier et al., 1987; Hekinian & Hoffert, 1975; Pauly et al., 2011; Zhou and Fyfe, 1989).

2.3.3.4 Determining Element Mobility and Calculating Mass Balance

In order to fully understand the processes by which sideromelane is converted to palagonite, it is important to know which elements are released into the fluid phase and are mobile, as well as those that always remain in the solid phase and are immobile (conserved).

Numerous authors have used mass balance calculations based on different assumptions in order to understand element mobility and mass transfer during palagonitization (Furnes, 1978; Furnes, 1984; Jercinovic et al., 1990; Pauly et al., 2011; Stroncik & Schmincke, 2001, 2002; Thorseth et al., 1990). Elements such as Ti, Fe and/or Al, have been assumed to be immobile for calculations based on their known chemical behaviour. Iron and Ti were both assumed immobile by Eggleton and Keller (1982), Staudigel and Hart (1983) and Crovisier et al. (1992). In an alteration experiment, Hoppe (1941) assumed Fe to be conserved in order to calculate relative leaching of components during palagonitization. Jakobsson (1972) also assumed Fe immobility for mass transfer calculations. Honnorez et al. (1972) assumed glass and palagonite to be anhydrous (water-free) for mass calculations but problems with these assumptions are apparent. For example, densities of palagonite vary over small distances due to porosity changes and major elements are generally mobile due to environmental effects (Honnorez et al., 1972). Thorseth et al. (1991) utilized element ratios with SiO₂ in an attempt to clarify if, and to what extent, cations were extracted selectively relative to the network-forming Si.

Furnes' (1978) equation uses the specific gravity of sideromelane and palagonite to calculate percent change in element oxides: $\% \Delta = \frac{(SG * C)_{palagonite} - (SG * C)_{glass}}{(SG * C)_{glass}} * 100$, where $\% \Delta$ = percent change in element oxides, SG = specific gravity, and C = wt.% oxide. Mass transfer during palagonitization ranges from -11% to -75% SiO₂, -24% to -84% Al₂O₃, 0% to -49% TiO₂, -31% Fe₂O₃ to +42% FeO, -63% to +12% MgO, -89% to +2% CaO, -99% to -47% Na₂O, -98% to -79% K₂O in studies by Hay and Iijima (1968), Hoppe (1941), Jakobsson (1972), Honnorez (1972), and Furnes (1978).

Jercinovic et al. (1990) proposed that the Ti-content in palagonite and glass are nearly, but not completely, identical and so assumed Ti to be immobile in mass balance calculations. They found that palagonite is depleted in Si relative to fresh basaltic glass, whereas elements with low hydroxide solubility products, such as Ti, Hf and Th, are insoluble and retained in palagonite rinds. More soluble elements are variably enriched or depleted in the palagonite relative to the parent glass (Jercinovic et al., 1990).

Stroncik and Schmincke (2001) conjectured that palagonitization is an evolutionary two-stage process from palagonite to smectite. Therefore, mass balance calculations assumed two aging steps with different palagonite densities. Generally, density for the palagonite material

progressively increased over time from 1.76 to 2.10 g/cm³. Gresens' (1967) mass balance calculations showed that mass loss is much lower during aging step II of palagonite's evolution than in step I (Stroncik & Schmincke, 2001). Gresens' (1967) mass transfer equation is:

$$\Delta m = (\rho_a / \rho_i) * (fv) * (C_a - C_i)$$

where C_i = concentration of some element in the original rock, C_a = concentration in the altered rock, ρ_i = density of initial rock, ρ_a = density of altered rock, fv = ratio of final and initial volumes, and Δm = change in mass.

Stroncik and Schmincke (2001) also recognized smectite's enrichment in MgO relative to sideromelane or palagonite, therefore, mass balance was additionally calculated as a function of percent MgO accumulation:

$$\% MgO = \frac{MgO_{palagonite} - MgO_{glass}}{MgO_{glass}} * 100.$$

As MgO concentrations in palagonite increase towards those of a smectite structure, a decrease in loss of SiO₂ was found, whereas TiO₂ and FeO show progressive loss (Stroncik & Schmincke, 2001). Al₂O₃, Na₂O and K₂O also show progressive loss but only in seawater-altered samples, and no consistent mass transfer was found for meteoric water-altered samples (Stroncik & Schmincke, 2001).

2.3.3.5 Assessment of Element Gains and Losses

Using Gresens' methods and assuming constant volume, with known density values for palagonite and sideromelane, will produce different results than assuming immobile elements. Most recently, isocon diagrams (Grant, 1986) consistently plotted immobile elements (Zr, Nb, Sc, La, Nd and REE's) on an isocon line (constant mass; no loss or gain during palagonitization) (Pauly et al., 2011). Elements that did not plot on the isocon line, such as Rb, V and Cr, were considered mobile and either added or removed. They calculated mass change of all major and trace elements using isocon diagrams (with above-mentioned immobile elements) for each sample, and found that palagonitization in subalkaline samples had more mass loss (-35.9 to -63.7%) than alkaline samples (-13.0 to -43.2%) (Pauly et al., 2011).

Studies of trace elements in the submarine palagonitization of basaltic glass showed enrichment in B, Li, Rb, Cs, Pb, Cu and LREE, and less significant change in V, Cr, Co, Ni, Zn, Sr, Y, Zr, Nb, Ba, Hf and HREE occurred (see review in Furnes, 1978). Furnes (1978)

documented consistent enrichment in Cr, Co, Cu, depletion in V, Nb, Ce, Nd and variable trends for Ni, Zn, Rb, Sr, Y, Zr, Ba, La in palagonitized subglacial hyaloclastites of olivine tholeiite composition in Iceland. Furnes (1978) also found that all major elements, except H₂O and Fe₂O₃, are depleted in palagonite relative to sideromelane, and that LREE's are considerably more affected during palagonitization than other REE's. Moreover, Furnes (1978) noted an important relationship between the H₂O-content of palagonite and the degree of element mobility during palagonitization, specifically, that increased H₂O in palagonite leads to increased mobility. Pauly et al. (2011) observed that LREE's were slightly less enriched than HREE's as a result of palagonitization, but compositional traverses show that other immobile elements increase in concentration progressively from the fresh glass towards the outer rim of palagonite.

Even though Furnes (1978) studied one composition of palagonitized basaltic glass (olivine tholeiite), he predicted that if chemically different basaltic glasses under identical physio-chemical conditions were compared, different compositions of palagonite would result. This thesis project using Wells Gray (alkaline) and Helgafell (tholeiite) samples tests the above-mentioned hypothesis set out by Furnes (1978).

2.3.3.6 High-Aluminum vs. Low-Aluminum Palagonite

Retention or loss of Al to the aqueous solution during palagonitization is discussed extensively by Jercinovic et al. (1990) in their study of three Canadian Cordilleran subglacial volcanoes in the Cassiar mountains, northern British Columbia. They suggested that low-Al palagonite results from closed-system alteration conducive to precipitation of Al-silicate authigenic cements.

Volcanic gases (CO₂, SO₄, etc.) forced into glacial meltwater create a low-pH environment that supports the precipitation of Al-silicate authigenic cement (Jercinovic et al., 1990). Conversely, rapid glacial melting produces fresh water to then increase the pH towards alkaline conditions. Jercinovic et al. (1990) suggested that the microenvironment of alteration is critical to palagonite formation and that compositionally different palagonite can form on the scale of metres or even millimetres.

The minimum solubility for Al is reached at a pH of 6.7, the point at which Al is retained (Jercinovic et al., 1990). Therefore, a low pH yields a low-Al palagonite because the Al is

soluble at lower pH, which was supported by the observation that Ni, Co, and Cr (more soluble at low-pH) were maintained in high-Al and released in low-Al palagonite (Jercinovic et al., 1990). In alkaline environments (high pH), Al is entirely in the form of $\text{Al}(\text{OH})_4^-$ in the solution and clay formation (e.g. nontronite; possibly a significant portion of palagonite) is difficult (Jercinovic et al., 1990). If a net Al-depletion is reached during palagonitization and elemental release rates from the glass are not exceeded by solution flow rates, then the solubility limits of Al-silicates will be reached, thus supporting zeolite and clay formation (Jercinovic et al., 1990).

2.3.4 Water in Palagonitization

Water in the volcano-ice/meltwater system is especially important since it is well-known that water diffuses into the non-crystalline structure of glass over time (Oehler & Tomozwa, 2014; Seligman et al., 2016). In fact, diffusivities of water and hydration rates in compositionally different glass types (basalt, dacite, and rhyolite) have been estimated based on experiments (Friedman & Smith, 1960; Okumara & Nakashima, 2006; Seligman et al., 2016).

Although there is minimal magmatic water (0.1 to 0.6 wt.%) in fresh volcanic glasses, over time they absorb water with similar deuterium content as meteoric water of local origin. Water absorption has been used for geochronometry (Friedman & Smith, 1960). Therefore, secondary hydration of glass is inevitable whether from post-eruptive meteoric water over time (Friedman & Smith, 1960; Seligman et al., 2016) or, in the case of glaciovolcanism, from contact with the voluminous amounts of glacial meltwater (syn-eruptive). On a micro-scale, each glass grain reacts with water along its edge or within fractures accessible to water (Thorseth et al., 1991).

2.3.5 Controls on Palagonitization from Atomic Structure

The evaluation of palagonite's structural formula suggests a smectite-like character and it can be optically anisotropic to isotropic, and is amorphous (Drief & Schiffman, 2004; Jakobsson & Moore, 1986; Jercinovic et al., 1990; Pauly et al., 2011; Stroncik & Schmincke, 2001; Walton and Schiffman, 2003). The colloidal, gel-like nature of palagonite allows for the effective adsorption of REE's, Rb, Cs, Sr and Ba (Jercinovic et al., 1990). This could be due to the special properties of colloidal materials, such as an increase in surface area (from a fibrous texture) and surface energy, and having a two-phase system: internal (material of

colloids) and external (material in which the colloids are dispersed; Calvert, 2015). Also, when supersaturation is reached at the glass interface, insoluble material precipitates (Jercinovic et al., 1990). Special conditions induce supersaturation, such as a sudden decrease in temperature (affects solubility), pH, or volume of solution, or an increase in pressure (Williams & Crerar, 1985).

Palagonite has been found to be abundant in low ionic-potential (low charge/radius ratio) elements (Jercinovic et al., 1990). For example, Rb^+ and Cs^+ (since Rb^+ and Cs^+ have larger radii) relative to K^+ , or Ba^{2+} (since Ba^{2+} has a larger radius) relative to Sr^{2+} (and possibly Ca^{2+}) (Railsbacks, 2007). This preferential concentration of low ionic-potential elements may be due to the fact that the physical adsorption offered by amorphous gels (palagonite) is a more effective process than in crystalline materials (Jercinovic et al., 1990). Adsorption depends on surface area and amorphous gels offer increased surface area that is irregular (amorphous) and heterogeneous for adsorption than stable crystals (Bakaev & Steele, 1996).

2.3.6 Temperature

Temperature has a significant role in controlling reaction rates, development of textures and element mobility during palagonitization (Pauly et al., 2011; Schiffman et al., 2000; Stroncick & Schmincke, 2001). While eruption temperatures of basaltic magmas are as high as 1200 °C, ash-size grains can cool to ambient temperatures quickly (Guðmundsson, 2003). Following the stages of fragmentation, eruption and deposition, the tephra pile cools and undergoes burial-diagenetic palagonitization; this is common in submarine volcanoclastic deposits (Pauly et al., 2011) and probably at glaciovolcanic edifices (Guðmundsson et al., 1997). Schiffman et al., (2000) and Pauly et al. (2011) have proposed two fundamentally different temperature regimes for palagonite formation (Appendix C.1): high-temperature and low-temperature.

High-temperature, hydrothermal palagonitization (Appendix C.1) occurs during and directly following an eruption, resulting in thin rinds and few zeolites due to the short duration of alteration (Pauly et al., 2011). In contrast, porosity and water content decrease over time during low-temperature, diagenetic palagonitization (Pauly et al., 2011). Over hundreds or thousands of years, thick, highly palagonitized rinds enriched in REE and depleted in water are observed (Pauly et al., 2011). Environmental controls on low-temperature tephra alteration

were found to be annual rainfall, temperature and soil pH, although the importance of the controls or their relationship to mechanisms such as dissolution are unknown (Schiffman et al., 2000).

At Surtsey, Jakobsson and Moore (1986) observed temperature-dependent changes to the consolidation and formation of palagonite tuff only two years after the cessation of volcanic activity. Twelve years following Surtsey's 1963-67 eruption on the seafloor south of Iceland, an international scientific exploration project successfully drilled the edifice to a depth of 181 metres to study hydrothermal mineralization, palagonitization and alteration rates (Jakobsson & Moore, 1986). Now 50 years old, Surtsey provides a mineralogical and petrographic framework to understand hydrothermal and palagonitization processes; a second drilling project is scheduled for the fall of 2017 (M. T. Guðmundsson, personal communication, February 2017; DOSECC Exploration Services, 2016). A cooling rate of ~ 9 °C per year was found in the hottest segment of the hole, which was 150 °C (Jakobsson & Moore, 1986). The palagonitization process (conversion of sideromelane to palagonite and secondary minerals) dominated the tephra deposit, which was determined to have the rate of palagonitization doubled for every 12 °C increase in temperature (Jakobsson & Moore, 1986). The rate of palagonitization was measured by the thickness of palagonite rims on sideromelane for different sections of the drill core and estimating the effective 12-year average temperatures. At 60 °C, < 40% of the glass was palagonitized (Appendix C.1), and above 100 °C, > 90% was palagonitized (Jakobsson & Moore, 1986). In areas above 120 °C, olivine rims were replaced by nontronite, a smectite clay dominating the ten hydrothermal minerals found between 25 - 150 °C (Appendix C.1), in addition to analcite, phillipsite and tobermorite (Jakobsson & Moore, 1986).

Palagonitization and consolidation of vitric tephra deposits can also occur in geothermal environments with condensed steam (> 50 °C), such as caldera-bounding faults (Schiffman et al., 2000). At Kilauea's summit in Hawaii, palagonite was only apparent near fault systems that define the caldera's walls. There active steam vents at the > 100-year old Steaming Bluff region (north side) and halfway between Crater Rim Drive and the caldera floor (south side) measured 72°-79° C, and 55°-60° C, respectively (Schiffman et al., 2000).

Models for palagonitization in these geothermal environments include: 1) a syn-depositional model with water/steam controlling palagonitization during phreatomagmatic

eruptions, and 2) a post-depositional model where downward-percolating meteoric water chemically reacts with glassy tephra (Schiffman et al., 2000). The incipient palagonitization of tephra at Surtsey and Kilauea differs from weathering of basaltic tephra, which produces pedogenic clays and soils (Appendix C.1).

Schiffman et al. (2000) proposed that submarine basalt alters by low-temperature, steady-state diffusion with a time-thickness relationship, $T=(kt)^{1/2}$, where T = rim thickness (μm), k = rate constant ($\mu\text{m}^2/\text{ka}$), and t = time (10^3 years). Rates vary from as low as $1 \mu\text{m}^2/10^3$ years in Iceland subglacial basalts (Le Gal et al., 1999) to $2000 \mu\text{m}^2/10^3$ years in Hawaii for submarine basalts (Moore, 1966) as outlined in Schiffman et al. (2000).

2.3.7 Porosity

Porosity is critical to the formation of palagonite because pores significantly increase the surface area of the tephra that can react with water. Stroncik and Schmincke (2002) found that porosity decreased from 36% to 9% due to formation of secondary phases, and Hay and Iijima (1968) reported that density (Table 2) increased from 1.67 g cm^{-3} in a sideromelane tuff to 2.05 g cm^{-3} in the palagonite tuff. Secondary phases tend to fill pore spaces, causing cementation that results in mass increase and an increase in bulk rock density (Stroncik & Schmincke, 2002). Palagonite has a lower density than fresh, non-vesicular sideromelane, although palagonite's density increases with age as it transforms into crystalline material (Stroncik & Schmincke, 2002). Since original sample porosity was found to vary linearly and inversely with palagonitization extent (as measured by the sum of percentage zeolites, palagonite and smectite), Pauly et al. (2011) suggested that porosity is a controlling factor in palagonitization.

2.3.8 Stages of Palagonitization

Four previous studies have identified distinct stages of palagonitization.

Bonatti (1965) describes two stages associated with the formation of palagonite: 1) hydration, and 2) devitrification of glass. First, the catalyzing action of water disrupts the glass by entering its random structure, and second, the Si and Al tetrahedra in the glass re-arrange into a new, ordered structure that is dependent on the available cations (Bonatti, 1965). Most volcanic glasses have < 1% magmatic water but can have 4-5% non-magmatic water largely introduced by diffusion (Ross & Smith, 1955).

Honnorez (1981) proposed three stages of reaction. Initially, unaltered glass forms palagonite (altered, residual glass), and authigenic minerals (e.g., clays, zeolites, K-Mg-rich smectite, Na>K phillipsite) form in voids and vesicles. This is accompanied by an increase in alkalis, especially K, and Mg, but loss of Ca, with many other elements unchanged. A second stage results in fully altered glass and the replacement of palagonite by smectite, phillipsite and zeolites (e.g., K>Na smectite and gyrolite layers coat vesicle surfaces). Finally, all remaining glass and palagonite are replaced by authigenic minerals including Fe-Mn oxides (Honnorez, 1981).

Jercinovic et al. (1990) suggested five stages of palagonite formation with paragenesis of: 1) silicates and carbonates; 2) oxide minerals; 3) sulfides and arsenides of Fe, Ni, Co, Mo; 4) Pb and Zn sulfides; and 5) native metals and tellurides. The volcanic glass controls what elements are available to growing minerals while pore water pH increases due to glass hydrolysis (Jercinovic et al., 1990). They also propose that palagonite must be high in Ca in order to be replaced by clay, and that when Ca stays in the rind, palagonite first alters to smectite (Fe-saponite), and then zeolites in the order of phillipsite, chabazite and finally nontronite.

Stroncik and Schmincke (2001) found that the chemical composition of palagonite was at least partly controlled by the aging process because element loss was higher during early stages (the initial formation of palagonite) than over the entire process. For example, early-stage palagonitization can show 65 wt% element loss in comparison to only 28 wt% element loss during the entire palagonitization process (Stroncik & Schmincke, 2001). The rate of element loss decreases as palagonite ages and secondary phases form.

Stroncik and Schmincke (2001) proposed a two-step process, with Figure 4 illustrating element behaviour in sideromelane (left) and palagonite (right) during Aging Steps I and II. Chemically heterogeneous palagonite and crystalline material are produced during Aging Step I, whereas, with the exception of TiO₂, FeO and H₂O, higher concentrations of elements are found in the crystalline material than in palagonite during Aging Step II. Based on these findings, chemical variation is greatest in Aging Step I. As palagonite ages, its water content decreases and Si, Al, Mg, Na and K increase relative to the initial palagonite composition (Stroncik & Schmincke, 2001).

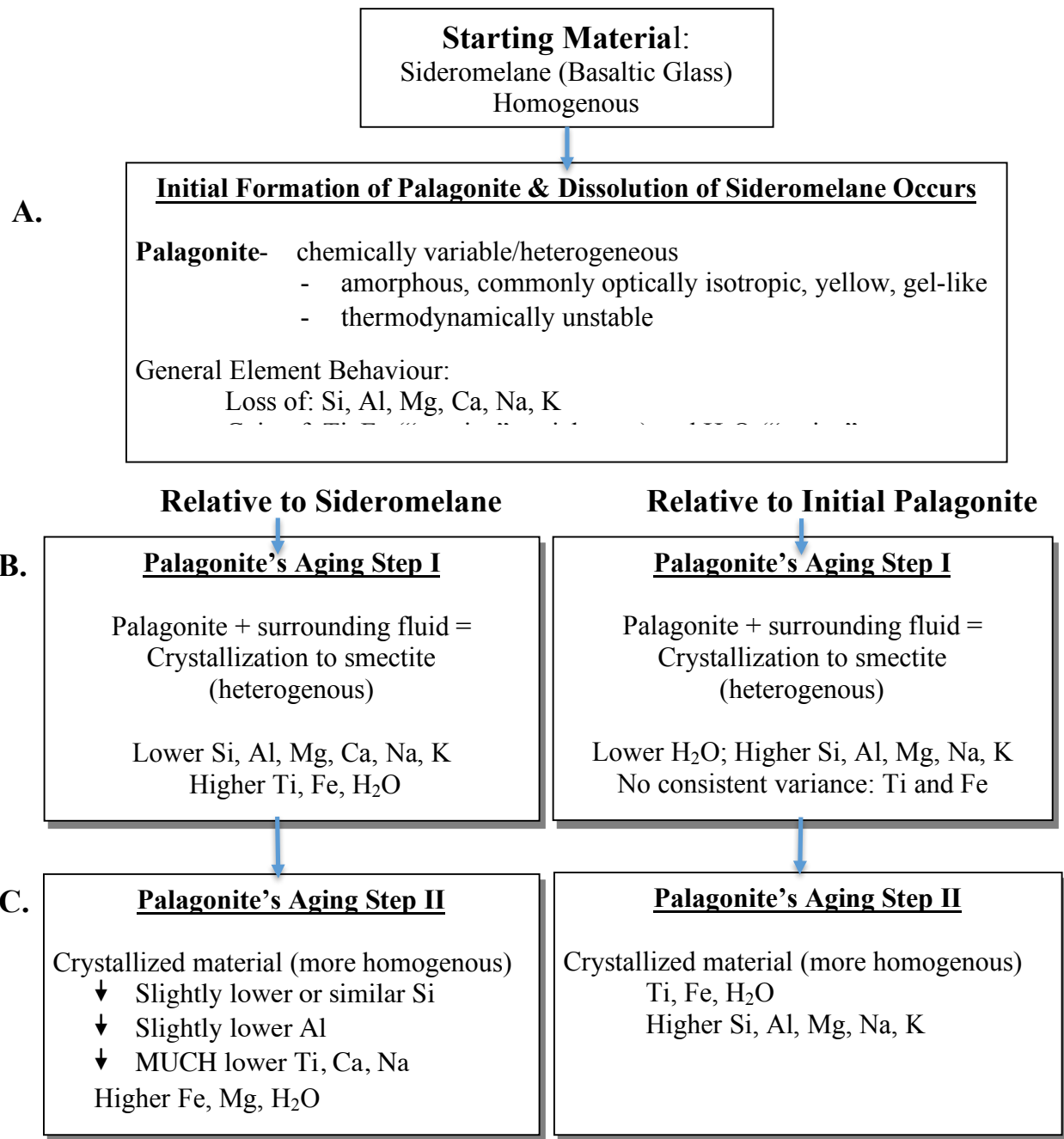


Figure 4 Aging steps of palagonitization, from A) initial formation of heterogeneous palagonite and dissolution of sideromelane, B) palagonite's aging step 1, and C) palagonite's aging step 2. Geochemical variation relative to either the original sideromelane (left column) or relative to the initial palagonite (right column) (summarized from Stroncik & Schmincke, 2001).

2.3.9 Thermodynamics and Kinetic Considerations

The formation of palagonite follows the Ostwald step sequence of irreversible reaction, with movement away from unstable and higher free energy phases (i.e. volcanic glass) to thermodynamically stable crystalline phases (Jercinovic et al., 1990). These steps are

kinetically controlled, resulting in the fast nucleation and supersaturation of Al-silicate gels, with little to no crystal growth, and in the formation of smectite at the glass interface (Jercinovic et al., 1990). During hydrolysis, the breakdown of sideromelane by water is exothermic and occurs simultaneously with the reprecipitation of insoluble materials at the glass-palagonite interface (Jercinovic et al., 1990).

2.4 Summary

Although it has been studied for more than 100 years, palagonite and the processes that create it are not well understood. It is an amorphous material that forms from basaltic glass and has a range of associated minerals. It appears to be most common in places where eruptions happen in or around a source of water. Most workers agree that it is a multi-stage process with little agreement on the nature of the stages.

2.5 Outstanding Issues

Several debates are ongoing about palagonitization. Jercinovic et al.'s (1990) proposal that palagonitization is isovolumetric disagrees with work by Crovisier et al. (1987), Thorseth et al. (1990) and Pauly et al. (2011). Estimated extents of overall mass change for the major elements vary widely, especially for FeO and TiO₂ (Pauly et al., 2011).

This study will test the hypothesis that the original composition of the sideromelane is the most important factor for controlling the mineralogy and composition of the resulting palagonite. Palagonite formation is compared in glaciovolcanic environments of similar age (Pleistocene) but with different sideromelane compositions. Furthermore, this research will explore: a) whether there are textural-geochemical relationships that help us to understand the palagonitization process, and b) which components are enriched or depleted during palagonitization, and whether they are the same independent of the sideromelane composition. Site descriptions of Helgafell and Wells Gray are outlined in Chapter 3, followed by analytical and statistical methods in Chapter 4. Results are reported in two sub-sections in Chapter 5: 1) descriptions of modal proportions and textures of glass-palagonite materials, and 2) geochemical data and analysis. Chapter 6 discusses the project's textural-geochemical results and a detailed comparison with data from a previous study (Pauly et al., 2011). In conclusion, the study's key findings are summarized with suggestions for future work related to the subject.

Chapter 3: Site Description

The purpose of this project is to compare the process of palagonitization at two glaciovolcanic ridges that differ in location and magma chemistry. The two chosen sites are Helgafell, in southwest Iceland and Wells Gray (Second Canyon) in southeast British Columbia. Helgafell is located on the Reykjanes Peninsula, which is a continuation of the Mid-Atlantic ridge divergent boundary between the North American and the Eurasian plates. The Wells Gray-Clearwater Volcanic Field is the result of continental rifting or ‘relaxing’ of the lithosphere within the Cordilleran of Western Canada (Hickson, 1986). The eruptions at both localities occurred in extensional plate tectonic settings (Bowman et al., 2011; Hickson et al., 1995; Schopka et al., 2006) and during the Pleistocene when large parts of the northern and southern hemispheres were repeatedly covered with thick glacial ice, including Iceland and BC.

3.1 Helgafell, Reykjanes Peninsula, SW Iceland

The onland extension of the ~ 20,000 km long Mid-Atlantic ridge (Figure 5) enters SW Iceland at latitude 63°48'N as the highly oblique Reykjanes Ridge, where the Reykjanes Peninsula plate boundary has a trend of ~ N76° E (Hreinsdóttir et al., 2001). The constructive ridge formed by the separation of the Eurasian and North American tectonic plates with a relative plate velocity of 18.9 mm ± 0.5 mm/year (Hreinsdóttir et al., 2001). The Reykjanes Peninsula has been active since 20-25 Ma ago, with the last volcanic event estimated to have occurred around 1240 A.D. (Jóhannesson & Einarsson, 1998). Between longitudes 24°30'W and 23°30' W, the ridge gradually bends eastward to orient itself ~ 30° oblique to the direction of plate motion (DeMets et al., 1994). The ridge exits Iceland to the north and continues on as the Kolbeinsey Ridge (Figure 5).

Active spreading on the Reykjanes Peninsula was initiated by a significant ridge jump about 6.5 million years ago (Jóhannesson, 1980; Sæmundsson, 1979), which produced arrays of eruptive fissures about 5 km apart with a mean strike of 40°. These fissures comprise five fissure systems, each with their own magma supply, and geothermal and fault systems (Figure 6) (Jakobsson et al., 1978; Sæmundsson, 1979). Extensional fractures (no shear displacement),

shear fractures (normal faults), and fractures that exhibit both shear and extension are found within these fissure swarms (Jakobsson et al., 1978; Sæmundsson, 1979).



Figure 5 Helgafell, Reykjanes Peninsula, SW Iceland is the glaciovolcanic ridge sampled for this project (Image: Smithsonian Institution, courtesy of US Geological Survey).

Although the last known eruption on the Reykjanes Peninsula was in the 13th century, eruptive fissures and lava shields were active throughout the Holocene (Sæmundsson, 1995). Subglacial and post-glacial fissure eruptions formed prominent NE-trending ridges, tuyas, tephra cones, rows of craters and lava fields that define the topography of the Reykjanes Peninsula (Figure 6) (Sæmundsson, 1995).

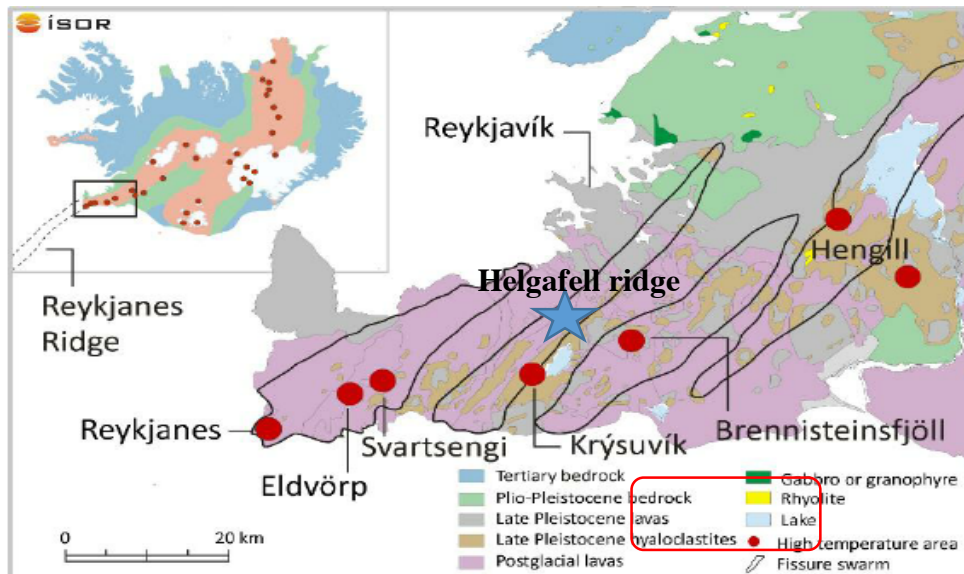


Figure 6 NE-SW trending fissures swarms in the Reykjanes Peninsula, SW Iceland. (Based on a geological map of Iceland by Jóhannesson and Sæmundsson, 1999, modified in Harðardóttir et al., 2009). Permission granted by the Geological Society of America.

Helgafell, the Icelandic site for this study, sits 340 metres above sea level on the Reykjanes Peninsula and is near the village of Hafnarfjörður, just southwest of Iceland's capital, Reykjavík (Schopka et al., 2006). Helgafell is thought to have formed during the Pleistocene in a single subglacial fissure eruption under at least 500 m of glacial ice, with the thickness of ice estimated from pressure (~ 1 MPa) calculated from volatile concentrations (0.26-0.37 wt.% H_2O) in volcanic glass from its southeast side (Schopka et al., 2006). Holocene basaltic lavas (40-80 m thick) later surrounded the ridge, which was originally ~ 2 km long, 0.8 km wide and 300 m high (Schopka et al., 2006).

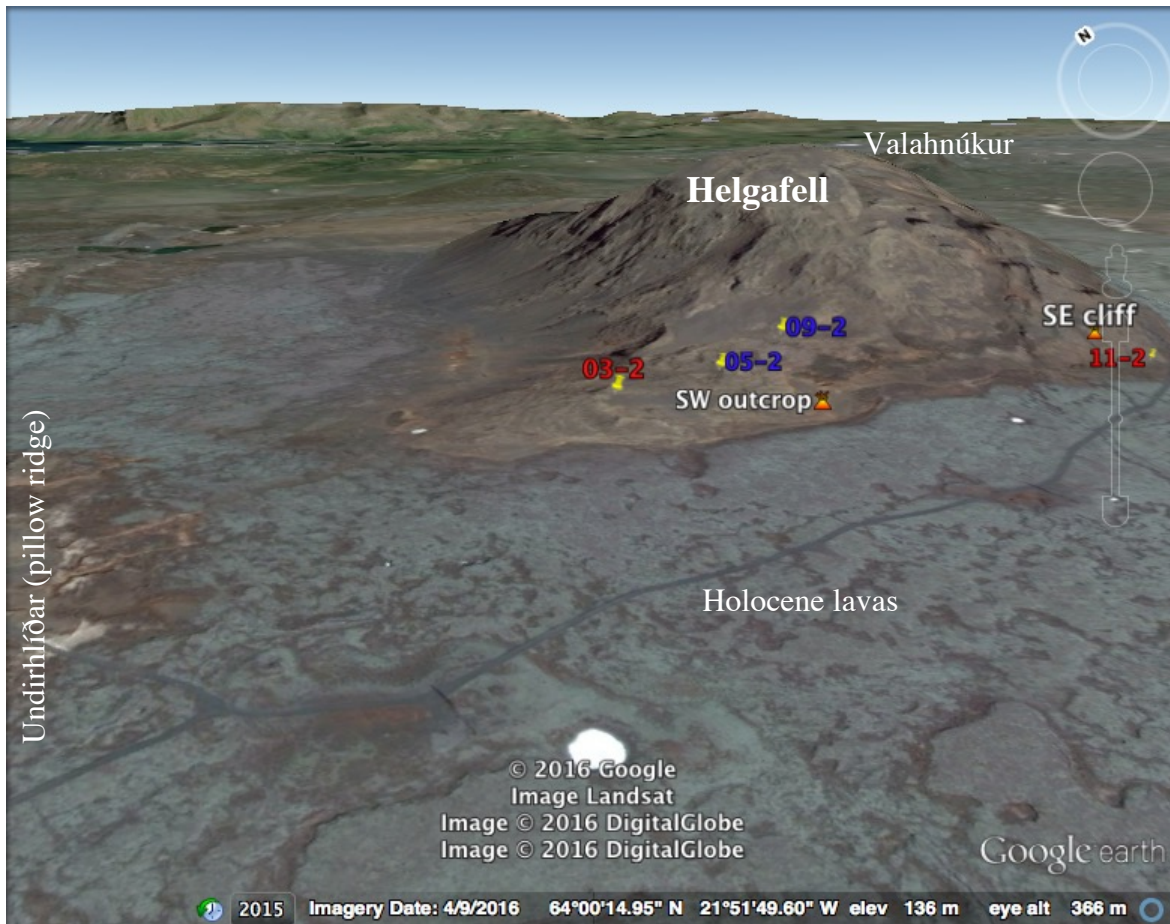


Figure 7 Helgafell ridge (2 km x 0.8 km x 300 m) located on the Reykjanes Peninsula, SW Iceland, is the result of a subglacial fissure eruption under a ≥ 500 m thick Pleistocene ice sheet (Schopka et al., 2006). Samples were collected incrementally upwards along the SW outcrop and the SE cliff. (Map data © 2016 Google).

Undirhlíðar ridge, which is parallel to, but west of Helgafell (Figure 7), is primarily made of pillow lavas whereas Helgafell mostly comprises palagonitized tephra, dikes and minimal pillow lavas (Schopka et al., 2006; Pollock et al., 2014; this study). Schopka et al. (2006) suggested that a former ice wall on Helgafell's southeast side can account for the unsorted, eruption-fed lapilli tuff, tuff breccia and high cliffs (Schopka et al., 2006), whereas on Helgafell's southwest side, lapilli tuff is moderately to well-sorted, indicating water-transported fluvial material that produced bedded stratigraphy (Figures 8 and 9). No tillite has been observed intercalated with or covering the deposits, which indicates that no glacial advances have covered Helgafell since its formation, and that it formed during the very late stages of Pleistocene glaciation.

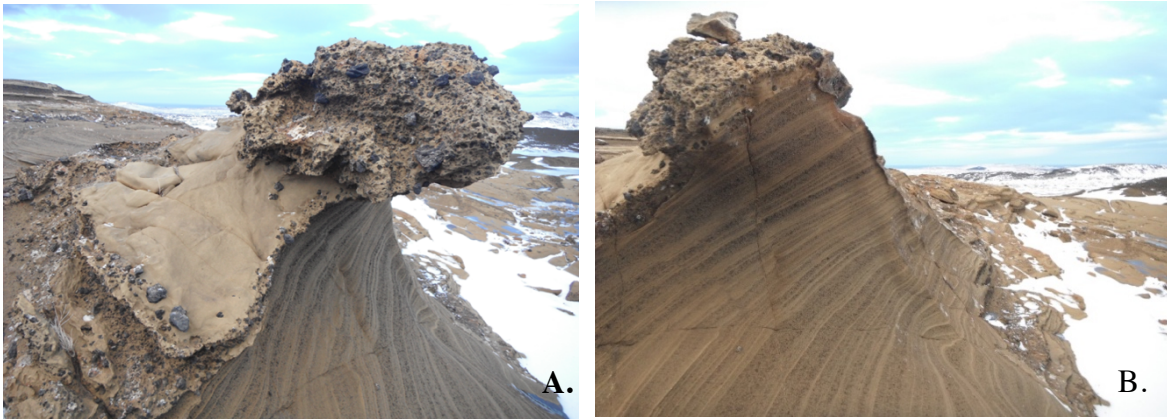


Figure 8 Helgafell, Iceland: location of sample #09-2 near the top of the SW outcrop, which is fine- to moderately bedded, cemented and palagonitized lapilli tuff.

On January 2, 2014, hand samples (approximate width: 10-20 cm) for this project were collected by rock hammer from both the southeast cliff (unsorted, massive hyaloclastites) and southwest (bedded, moderately to well-sorted) outcrops (Figure 7). Samples ranged in texture, grain-size and elevation. Along the southwest outcrop, samples of palagonitized, diagenetically-cemented lapilli tuff from almost vertically-oriented beds (Figure 8) and horizontally-laid beds (Figure 9) were collected from lower to higher elevations to inspect for stratigraphic variability of palagonitization.

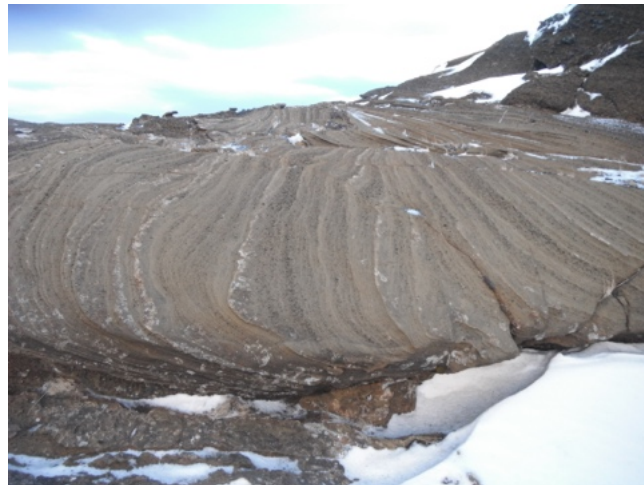


Figure 9 Subhorizontal, cemented palagonitized lapilli tuff with fine to coarse bedding at Helgafell.

There is little to no plant life on Helgafell's glaciovolcanic ridge. One of the most prominent and stark features at Helgafell is cemented lapilli tuff that has been sculpted as wind-

formed erosional features (Figure 10). Pillow lava or remnants of pillows (Figure 11) are rare and only observed on the north side of Helgafell.



Figure 10 Top of Helgafell ridge showing little to no plant life. Palagonitization has cemented the lapilli tuff, which has subsequently been sculpted as wave-formed erosional features.



Figure 11 Pillow lava is relatively rare at Helgafell but remnant outcrops of pillows are embedded in cemented, palagonitized lapilli tuff.

3.2 Wells Gray-Clearwater Volcanic Field, Clearwater, BC, Canada

The Wells Gray-Clearwater Volcanic Field (WGCVF) is located within Wells Gray Park (nicknamed “Canada’s Waterfall Park” and “Valley of Fire and Ice”) near Clearwater, BC and about 130 km north of Kamloops, BC in east-central British Columbia, Canada. It is in the Quesnel-Shuswap Highland region (Hickson, 1995). To the west lies the Kootenay terrane,

and to the east and north-east are the allochthonous Slide Mountain, Quesnellia terranes and ancestral North America (Hickson & Vigouroux, 2014). Small ($< 1 \text{ km}^3$) volume (Metcalf, 1987) basaltic eruptions in WGCVF have formerly been attributed to a 600-km-long east-north-easterly trending mantle hot spot that is associated with movement of the northern edge of the Juan de Fuca subduction plate (Bevier et al., 1979; Souther et al., 1987). But further studies of absolute plate motion (Hickson, 1986) suggest that WGCVF is too far south of the Anahim hot spot, and, instead resulted from crustal extension and subsequent partial melting (Figure 12) that yielded transitional to alkali olivine basalt (Hickson & Vigouroux, 2014). The basaltic cinder cones, shield volcanoes, dike swarms and subvolcanic plutons comprising the 14.5 Ma - 0.007 Ma Anahim Hotspot/Volcanic Belt (Bevier et al., 1979) lie directly to the west of WGCVF (Figure 12) (Hickson, 1986).

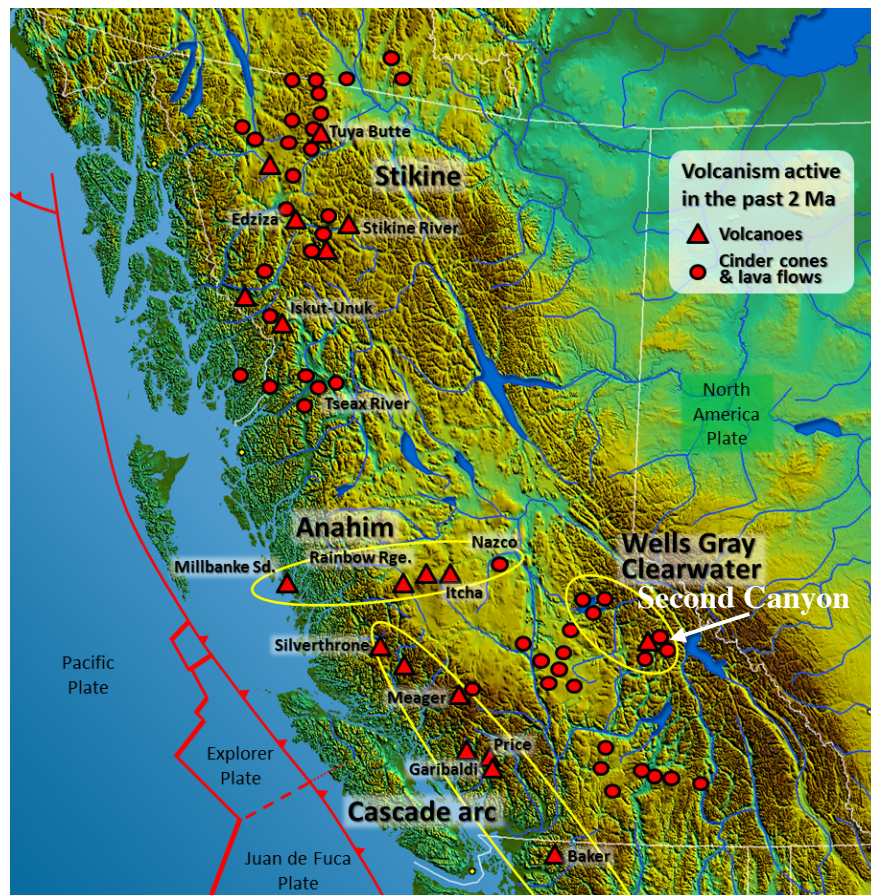


Figure 12 Location of the Wells Gray-Clearwater Volcanic Field, BC, Western Canada. Map used with permission from Earle, S. (2015) including volcanic locations by Hickson, C.

The glaciovolcanic activity in WGCVF produced three types of features: 1) tuyas, 2) subglacial mounds, and 3) ponded, valley-edge deposits where glacial ice confined debris to

one side of the valley (Figure 13). Volcanism in WGCVF is relatively young, with the youngest eruption $\sim 7560 \pm 110$ radiocarbon years and the oldest known eruption estimated (K-Ar dating) at ~ 3.2 Ma. The most extensive basalts are likely ~ 2 Ma (Hickson, 1986). The site sampled for this study, Second Canyon, is situated in Sheep Track Bench (K-Ar dates: ~ 0.27 Ma) and resulted from the third type of feature when volcanism on the east side of Clearwater Valley was confined and ponded by a glacier-filled valley (Hickson & Vigouroux, 2014).

While several suitable sampling locations were explored in WGCVF (e.g. Hyalo Ridge and White Horse Bluff), for the purposes of sample quality similar to Helgafell, Iceland, and accessibility, samples were collected at Second Canyon (Figures 13 and 14). Wells Gray is densely forested but Second Canyon provided excellent exposures of palagonitized tephra for sampling.

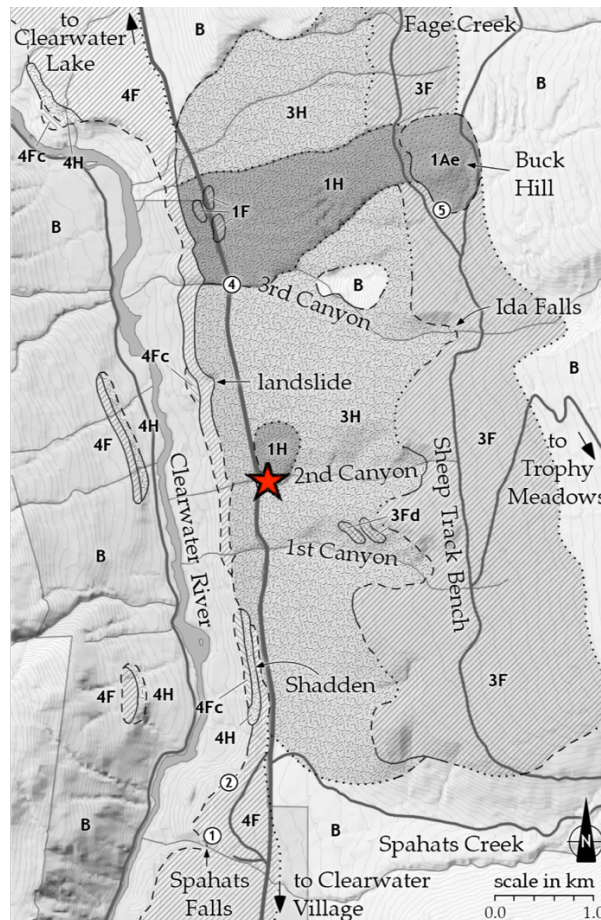


Figure 13 Second Canyon (label: red star) is situated at the south-east end of ~ 23 volcanic eruptive sites in Wells Gray-Clearwater Volcanic Field in BC, Canada. 1-waning Fraser Glaciation volcanism; 3-Sheep Track Bench sub-unit (ice contact); 4-Clearwater Unit; B-basement (Kootenay terrane/Slide Mountain terrane/Raft batholith; F-flows; H-hyaloclastite; A-agglomerate; d-dikes; c-fluvial/colluvial/glacial; (Map from Hickson & Vigouroux, 2014; used with permission from Geological Society of America).

During the Pleistocene, repeated advances of the Cordilleran Ice Sheet (CIS) covered British Columbia, reaching its last maximum size of 1.5 million km² with ice depths estimated to have been 2000-3000 m thick ~ 18,000 years ago (Ryder & Clague, 1989). Volcanism occurred during at least four glacial-interglacial periods in BC and Wells Gray (Edwards & Russell, 2002; Hickson, 2000; Hickson & Vigouroux, 2014), with glaciovolcanic evidence indicating that ice sheets exceeded a thickness of 2100 m during the Fraser glaciation (11–20 ka; Hickson et al., 1995).

Second Canyon is one of three canyons with creeks that cut through glaciovolcanic deposits that comprise the ~ 350 m thick Sheep Track Bench on the east wall of Clearwater Valley (Figure 14). Sheep Track Bench unconformably overlies the older valley-filling Clearwater unit and basement rock (Hickson, 1995). Dykes ranging from 0.2 to 1 m wide are common in Sheep Track Bench, and have quenched margins with embedded hyaloclastite (Hickson, 1986). Beginning ~2 Ma, volcanism resulted from extension along pre-existing Mesozoic crustal faults on the eastern side of Clearwater Valley where Second Canyon, the sampling site, is situated (Hickson & Vigouroux, 2014). Subsequent erosion has culminated in steep canyons where creeks continue to cut deep gorges into the subglacial volcanic pile.

Second Canyon provides a ~ 40 m high cliff exposure of palagonitized lapilli tuff, tuff breccia, and rare pillow fragments that rises parallel to and above the east-west trending Second Canyon Creek. It runs perpendicular to and under the Clearwater Valley Road and cuts into Sheep Track Bench. The rocks that line the creekside wall, and where sample #20-2 was collected, along the south side of Second Canyon Creek are primarily a poorly sorted and massive lapilli tuff cemented by palagonite (Figure 15A). Locally, broken pieces of pillow lava are mixed with the lapilli tuff. The formation of the ‘cement’ will be discussed further as part of this study.

The outcrops on Second Canyon’s south side become tuff-breccia parallel to the east side of Clearwater Valley Road, with several dykes of variable widths (~0.5 to 1.2 m) cross-cutting the deposit at an angle (Figure 16). The dykes have quenched margins in contact with palagonitized lapilli tuff.



Figure 14 Second Canyon sample site area on Sheep Track Bench in Wells Gray-Clearwater Volcanic Field (Map data © 2016 Google).



Figure 15 Second Canyon, Wells Gray, BC. A) Creekside wall of palagonitized lapilli tuff with occasional pillow lava pieces (WG #20-2). Scale bar: ~ 30 cm. B) Cliff samples (WG #21a and 21b).

The clast size at Second Canyon varies from lapilli tuff (< 64 mm) to tuff-breccia (2 – 60 mm). At ~ 765 m elevation, two hand samples #21a and 21b (Figure 15A) were collected about half-way up the Second Canyon cliff that parallels the creek (Figure 17). The cliff measures 39.5 m high to an elevation of ~ 787 metres above sea level (m.a.s.l.) next to Clearwater Road. The lower portion (0 to 10 m) is well-bedded and alternates from fine-grained to coarse-grained lapilli tuff from the bottom until an opening in the cliff at 7.8 m coincides with a change in clast size and bedding features. A thick palagonitized tuff-breccia layer begins at this point and it is cross-cut by a creek-parallel dyke (#1) with a strike and dip of 110°/80° S.



Figure 16 Dykes with quenched margins cross-cutting tuff-breccia along Clearwater Valley Road at Second Canyon, Wells Gray. A) almost vertical 1.5 m wide dyke #2. B) steeply dipping sinuous dykes.

A separate ~ 1.5 m wide dyke (#2) with a strike-dip of 135°/84° S is perpendicular to Clearwater Road and disappears above at an unconformity (20.7 m) where a ~ 19 m thick layer of a glacial till (unsorted glacial sediment) overlies the glaciovolcanic edifice and dykes that run parallel to the road (Figure 17). At least two smaller, more sinuous dykes, ranging in width from 60-70 cm with orientations of 150°/80 °S and 110°/85° S, rise vertically through the palagonitized breccia pile about 65.9 m and 98.3 m further south from dyke #2 alongside Clearwater Road (Figure 16). Unlike Helgafell, glacial till at Second Canyon indicates that glaciovolcanism preceded at least one period of glacial advance. Second Canyon's stratigraphic column illustrates the mid-cliff sampling location (21a, 21b), with alternating coarse- to fine-grained fragmental (lapilli tuff) material, tuff breccia and dykes cross-cutting the volcanic pile.

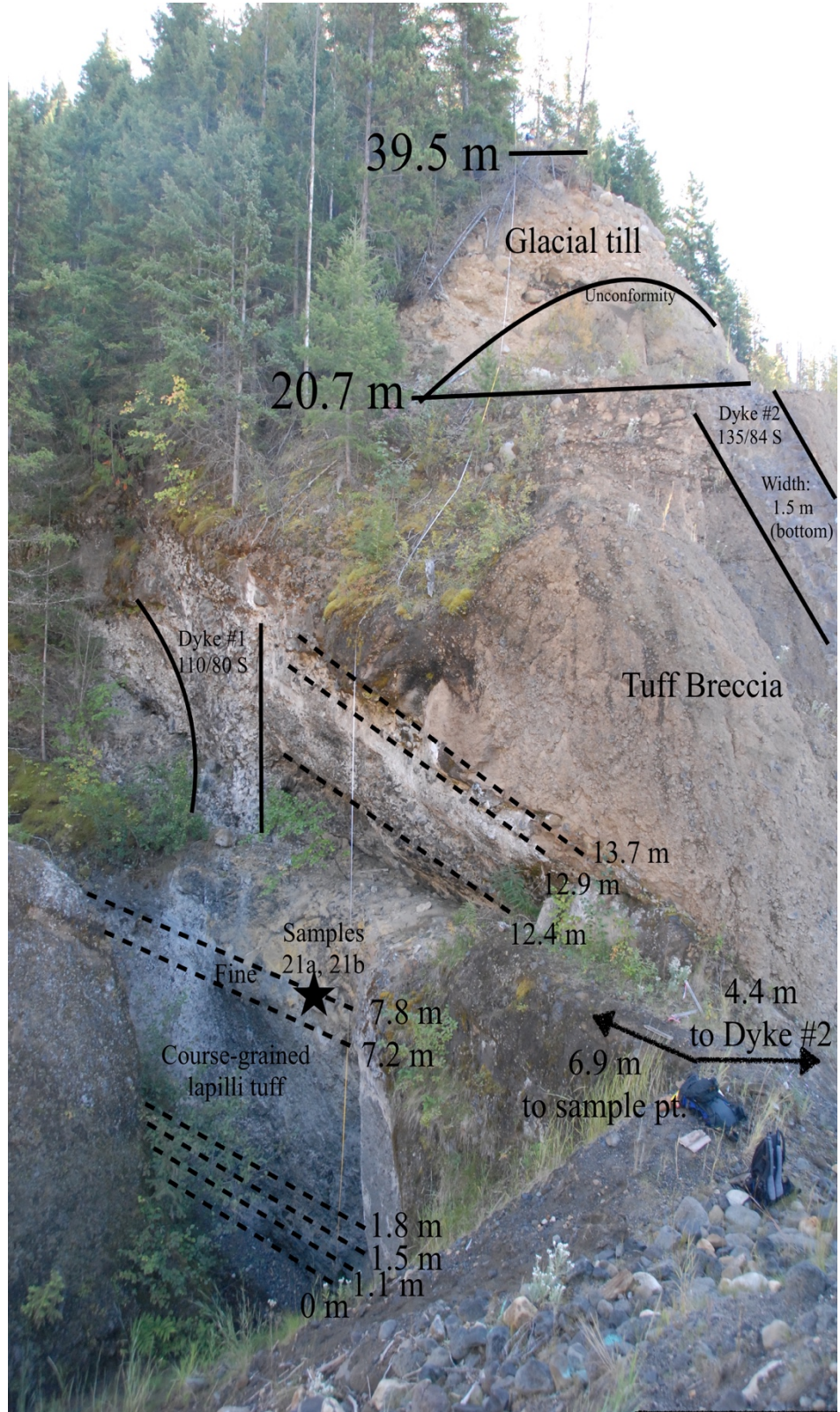
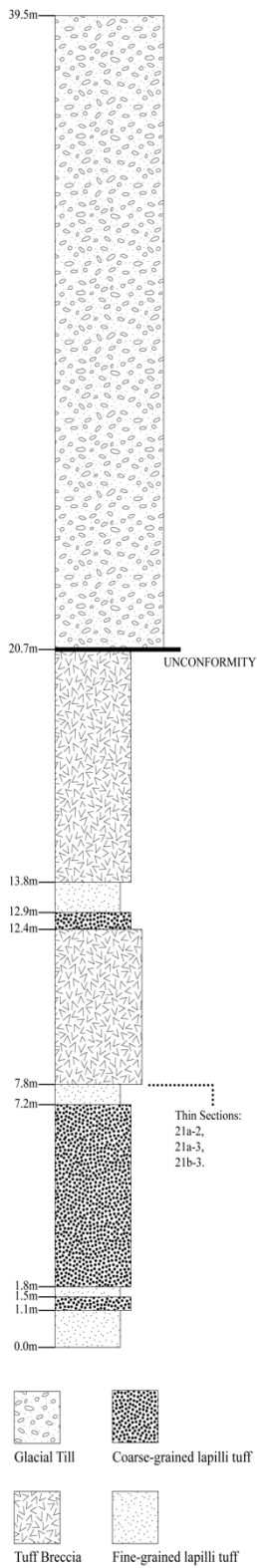


Figure 17 Second Canyon's stratigraphic column, illustrating mid-cliff sampling location with alternating course- to fine-grained fragmental material and dykes cross-cutting the volcanic pile.

Chapter 4: Methodology

4.1 Sample Preparation

Hand specimens were cut into blocks ~ 3.5 cm x 1.5 cm x 2 cm in size, and shipped to Steve Wood at the University of Western Ontario, ON, Canada for the preparation of twenty-one thin sections.

Each thin section was petrographically examined and photographed to document the sideromelane, tachylite, palagonite, mineral grains, microlites, void materials and grain textures. Photographs were taken with plane polarized light (PPL), cross polarized light (XPL) and reflected light (RL), and ten representative sections selected for the Scanning Electron Microscope - Energy Dispersive Spectrometry (SEM-EDS), Electron Microprobe - Wavelength Dispersive Spectrometry (EMP-WDS) and Laser Ablation Inductively Coupled Plasma Mass Spectrometry (LA-ICP-MS).

C.F. Mineral Research Ltd. in Kelowna, BC, carbon coated (~225 Å) the sections and eight were chemically analyzed (Table 3). Optical microscopy, SEM-EDS and EMP examination and analyses were carried out at UBC Okanagan's FiLTER lab in the Charles E. Fipke Centre for Innovative Research. LA-ICP-MS analyses were carried out at the University of Toronto.

Table 3 Summary of samples and matching glass-palagonite pairs analyzed by EMP (48 glass-palagonite pairs; 96 spots) and LA-ICP-MS (32 glass-palagonite pairs; 64 spots).

Sample	Location	Sideromelane (Glass)		Palagonite Rim	
		EMP	LA-ICP-MS	EMP	LA-ICP-MS
03-2	Helgafell, Iceland, SW outcrop	6	4	6	4
05-2	Helgafell, Iceland, SW outcrop	6	4	6	4
09-2	Helgafell, Iceland, SW outcrop	6	4	6	4
11-2	Helgafell, Iceland, SE cliff	6	4	6	4
20-2	Wells Gray, BC, creekside wall	6	4	6	4
21a-2	Wells Gray, BC, cliff	6	4	6	4
21a-3	Wells Gray, BC, cliff	6	4	6	4
21b-3	Wells Gray, BC, cliff	6	4	6	4
8	TOTAL	48	32	48	32

4.2 Photomicrographs and Images

Three types of images are presented from different instruments: 1) optical microscopy, 2) SEM and 3) EMP.

Photomicrographs captured from the optical microscope range from 5x to 50x magnification and can be in three types of light (Figure 20; see List of Figures): 1) plane polarized light (PPL), cross-polarized light (XPL) and 3) reflected light (RL).

High magnification SEM-EDS images result from: 1) secondary electrons (SE) (useful for topographic information), 2) backscattered electrons (BSE), or 3) x-rays (elemental line scans and maps). BSEs are beam electrons that have ricocheted out of the specimen and the resulting images represent the density of electrons (Figure 18). The dependency on atomic number in BSEs shows relative compositional contrast with high-density (high mean atomic number) materials appearing bright white (e.g. Fe- or Cu-rich secondary minerals, pyrite or chalcopyrite), medium-density materials are medium gray (e.g. sideromelane or olivine), low-density materials are dark gray (e.g. palagonite or plagioclase) and voids are black.

Element distributions have been mapped across glass-palagonite pairs using 1) quantitative EMP-WDS traverses (Figure 60; see List of Figures) to yield an image constructed from a grid of x-ray measurements, and 2) qualitative SEM-EDS line scans (Figure 63). The colours in SEM-EDS element maps (Figure 64) reflect the number of counts for particular energy levels (elements).

High magnification EMP images of glass-palagonite pairs result from backscattered electrons (BSE). The image provides details of the palagonite rim's texture, such as a spherical pattern at the inner portion of the rim along the glass-palagonite interface (Figure 18). The sideromelane was typically microlite-rich in Wells Gray (Figure 18), so microprobe analyses were made far from microlites in the glass.

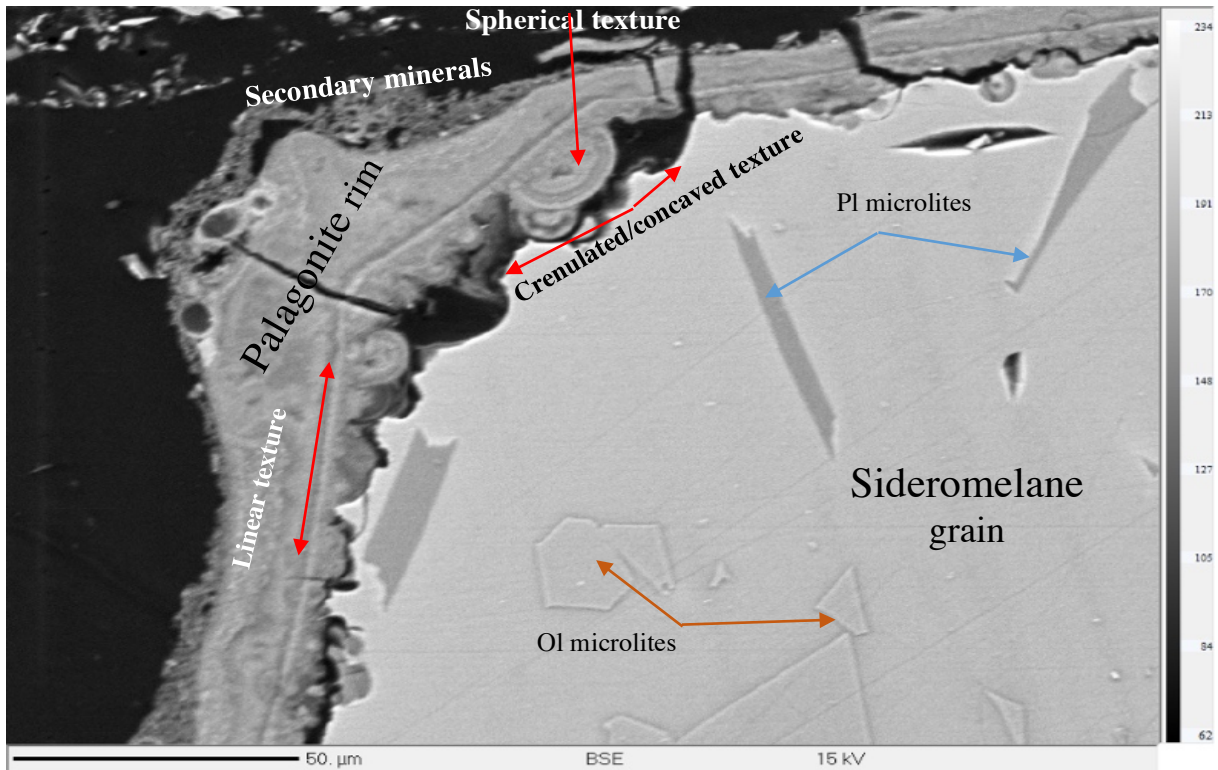


Figure 18 BSE image of a Wells Gray glass–palagonite pair analysis area with thick palagonite rims. Texturally, palagonite appears to be heterogeneous. The sideromelane grain has a concaved and crenulated edge. Secondary minerals occur near the outer edge of palagonite rims. Black area = void; Ol = olivine; Pl = plagioclase.

4.3 Analytical Methods

4.3.1 Polarizing Light Microscopy

Nikon Eclipse 50iPOL and Olympus BH2-UMA petrographic microscopes in the FiLTER lab, UBCO, were used for optical microscopy and photomicrographs.

Samples were point-counted with a Leica DM4500 P LED petrographic microscope (21,800 points) to quantify the modal proportions of constituents such as sideromelane, tachylite, phenocrysts, microlites, palagonite, gel-material, vesicles, voids, porosity, secondary minerals, e.g. sulfides (pyrite, chalcopyrite), zeolite-like, and clay-like materials.

4.3.2 Scanning Electron Microscope – Energy Dispersive Spectroscopy

A Tescan Mira 3 XMU Field Emission Scanning Electron Microscope with an Energy Dispersive Spectrometer (SEM-EDS) was used to analyze glass, palagonite and mineral phases. The SEM instrument employed a field emission gun for high image resolution and elemental composition was determined for major elements on an Oxford Instruments X-Max

80 mm² silicon drift detector (EDS). Pure copper was used to calibrate the SEM-EDS and operating conditions were set to a 20 keV accelerating voltage and an electron beam intensity of 97 nA.

The SEM-EDS analyzed major elemental concentrations of sideromelane (honey-coloured glass), tachylite (opaque glass), palagonite, microlites and phenocrysts (i.e., olivine and plagioclase). Secondary minerals in voids or vesicles such as Fe-oxides, pyrite, chalcopyrite, spinels (e.g. chromite), and zeolite-like materials were also analyzed to confirm identification.

4.3.3 Electron Microprobe Analysis

A Cameca SX5-FE (field emission) Electron Microprobe equipped with wavelength dispersive spectrometers (EMPA-WDS) was used to collect major element data on glass-palagonite pairs.

Four slides each from Helgafell and Wells Gray (Table 3) with six glass-palagonite pairs per slide were analyzed for major elements, totaling 48 glass-palagonite pairs. Analytes included ten major oxides (SiO₂, TiO₂, MgO, FeO, CaO, K₂O, Na₂O, MnO, FeO, P₂O₅), Cl and F. Two microprobe traverses were completed across two glass-palagonite pairs.

Smithsonian (SMS) and Micro-Analysis Consultants Ltd. (MAC) standards were used to calibrate the EMP (Table 4). A total of 37 analyses were completed on SMS Hornblende (Kakanui, New Zealand) NMNH 143965 (Jarosewich, 1980), and used to calculate precision and assess accuracy (Appendix A.1).

Table 4 Standards used for calibration of the EMP.

External Standard for Calibration	Element
Smithsonian Hornblende-1 (Kakanui) NMNH 143965	Si, Na, Mg, Al, Ca, Ti, Fe
Smithsonian Hornblende-2 (Arenal) NMNH 111356	Fe
Smithsonian Microcline NMNH 143966	Si, K
Smithsonian Omphacite NMNH 110607	Na
MAC Orthoclase	K
MAC Apatite 2	P, Ca
MAC Garnet Spessartine	Mn
MAC Fluorite	F
MAC KCl	Cl

The EMP beam spot size for glass and palagonite analyses was 10 μm for Wells Gray and 5 μm for Helgafell (due to thinner palagonite rims on Helgafell samples), with operating conditions of 15 keV accelerating voltage. Special consideration was taken for possible volatilization of alkalis and water in the palagonite rim by setting the beam strength at 20 nA and minimizing counting times (generally 2s).

Fractures occur across palagonite rims about every 5 - 30 μm , therefore, long and wide microprobe spots were chosen to correspond with spots selected for laser ablation work. In the case of glass analyses, spots were chosen at least $\sim 100^+$ μm from microlites and phenocrysts to ensure no overlap.

All EMP totals for glass analyses were consistently between 98.0 and 101.5%, supporting high-quality individual glass analyses (Table 8). This is especially important because H_2O in palagonite is assumed as the missing component in low palagonite totals (Table 9).

4.3.4 Laser Ablation Inductively Coupled Plasma Mass Spectrometry

Trace elements were analyzed by LA-ICP-MS at the University of Toronto by Dr. John Greenough and Dr. Colin Bray, with a Thermo Elemental (VG) PlasmaQuad PQ ExCell ICP-MS coupled to a Nu-Wave UP-213 Laser.

Palagonite rims were difficult to see using the laser optics; therefore, reflected light was used to view the boundaries of the palagonite rims, and compared to SEM back-scatter images that showed the precise spots where glass and palagonite were determined by EMP. Helgafell's palagonite rims are generally thinner than at Wells Gray, therefore, the laser ablation beam width was different depending on location. For Helgafell's glass-palagonite pairs, the laser line width was generally 12 μm for glass (two were 10 μm) and 8 μm for palagonite. Wells Gray glass-palagonite laser line width settings were 18 μm for glass and 8 μm for palagonite (10 μm for two thicker palagonite rims).

The line widths ablated on the standards, NIST 610 and BCR-2G, were 55 μm and 25 μm , respectively. NIST 610 was used as an external standard and within-run replicates of BCR-2G, treated as an unknown, furnished checks on precision and accuracy. Each slide sample was a different "run". A total of 14 analyses per run were conducted in the following order: two NIST 610, four glass-palagonite pairs, two BCR-2G followed by two NIST 610.

Rastering along a line in glass or palagonite used a power of 45% at 10Hz and 20 $\mu\text{m}/\text{sec}$ for the entire laser ablation analysis. Each analysis started with 20 s of background and then 60 s with the laser on. The ICP-MS was tuned to produce maximum sensitivity and oxide production < 2% by monitoring ThO^+/Th (248/232) and U/Th (238/232). The laser ablation data were reduced at UBCO using Glitter software to convert raw counts per second to ppm. SiO_2 was used as an internal standard.

Four glass-palagonite pairs on each of eight slides (32 glass-palagonite pairs total) analyzed by EMP were chosen for LA-ICP-MS analysis (Table 3). This study analyzed for 35 trace elements, but three (As, Sb and Cs) were deleted from the data set because they were not detected in most samples. Rb was generally below detection limit (BDL) in Helgafell samples but detectable in Wells Gray samples. All reported (32) trace elements were detected in at least 50 percent of analyses using the isotopes: ^{45}Sc , ^{51}V , ^{52}Cr , ^{59}Co , ^{60}Ni , ^{65}Cu , ^{66}Zn , ^{85}Rb , ^{88}Sr , ^{89}Y , ^{90}Zr , ^{93}Nb , ^{137}Ba , ^{139}La , ^{140}Ce , ^{141}Pr , ^{146}Nd , ^{147}Sm , ^{153}Eu , ^{157}Gd , ^{159}Tb , ^{163}Dy , ^{165}Ho , ^{166}Er , ^{169}Tm , ^{172}Yb , ^{175}Lu , ^{178}Hf , ^{181}Ta , ^{208}Pb , ^{232}Th , ^{238}U , in addition to ^{29}Si , the internal standard.

4.3.5 Precision and Accuracy from Reference Materials

EMP precision and accuracy (Appendix A.1) for major element data are based on replicate analyses of Smithsonian Hornblende (Kakanui) NMNH 143965 (Jarosewich, 1980). LA-ICP-MS precision and accuracy (Appendix A.2) for trace element data are based on BCR-2G (Jochum et al., 2005; Jochum & Nohl, 2008). Precision and accuracy were calculated as follows:

$$\text{Precision:} \quad \% = \frac{\text{Std Dev}}{\text{Mean}} * 100$$

$$\text{Accuracy:} \quad \% = \left| \frac{(\text{Mean} - \text{Standard Reference Value})}{\text{Standard Reference Value}} * 100 \right|$$

where *Std Dev* = standard deviation and *Mean* = mean detected value.

4.4 Statistical Methods

Two primary statistical methods are used: multi-dimensional scaling and Gresens' isocon diagrams.

4.4.1 Multi-Dimensional Scaling

Multi-dimensional scaling (MDS) is a powerful exploratory multivariate statistical method used to find similarities and dissimilarities between either samples or the chemical data in two or more dimensions (Greenough & MacKenzie, 2015; Greenough & Ya'acoby, 2013). As a spatial model, MDS operates directly on dissimilarities and scales distances, not axes. Calculations used Systat™ software. Data were standardized (z-scored):

$$z = \frac{(x-\mu)}{\sigma}$$

where x = concentration of an element in an analysis, μ = mean, and σ = standard deviation. A matrix of Pearson-correlation coefficients, which measures the strength of linear relationships between two variables ($r=1$ indicates a perfect positive linear relationship), was calculated. In Systat™, MDS scaled similarity and dissimilarity matrices using a Kruskal loss function, an iterative process utilizing mathematical algorithms that optimize the relationship between measured (Pearson-correlation coefficients) and plotted distances between points on the MDS diagrams. Multi-dimensional scaling plots were used to compare locations, materials and elements in the data.

4.4.2 Gresens' Isocon Diagrams and Mass Balance

Gresens (1967) investigated composition-volume relationships and introduced the Gresens' equation to calculate mass transfer during hydrothermal alteration, metasomatism and migmatization. Grant (1986) proposed an alternative means to solve Gresens' (1967) equation by graphing concentrations of components in altered rock against those in the original rock. An isocon (regression line) through immobile components (assumed mass change is zero) is plotted by forcing the regression line through the origin. The slope of the isocon defines mass change during alteration (Grant, 1986). Elements sitting above the isocon line increased in mass and those below were lost during alteration.

Elements thought to generally be immobile during hydrothermal alteration include: Ti, Al, Fe, Zr, Hf, Th, Nb, Y, Sc, and the REE's (La, Ce, Pr, Nd, Pm, Sm, Eu, Gd, Tb, Dy, Ho, Er, Tm, Yb, Lu; and Y, Sc) (Greenough et al., 1990; MacLean & Barrett, 1993; Pauly et al., 2011; Winchester & Floyd, 1977). Conversely, Si, Mg, Ca, Na, P, K, Sr, Ba, and Rb, are generally considered mobile during hydrothermal alteration (Greenough et al., 1990; MacLean & Barrett, 1993; Pauly et al., 2011; Winchester & Floyd, 1977).

Eight immobile elements were selected for isocon diagrams in this study: Sc, Y, Zr, Nb, La, Nd, Ta, Th based on reasonable precision (Appendix A.2), the tendency to show little scatter about the regression line (Figure 19) and previous studies (Nesbitt & Young, 1984; Pauly et al., 2011; Shikazono et al., 2005; Stroncik & Schmincke, 2002).

4.4.2.1 Mathematical Assumptions for Water in Data Sets for Mass Balance

Since the glaciovolcanic environment is aqueous and palagonite is known to be hydrous, water content in glass and, especially, palagonite is an important factor. Water cannot be measured by the analytical methods used (SEM, EMP and LA-ICP-MS). Two data sets prepared for mass balance calculations contain end-member assumptions about water (outlined in Table 5) in sideromelane and palagonite. Data set 1 (Appendix B.2, B.3) is the conventional assumption for water that most previous studies have made (Pauly et al., 2011; Stroncik & Schmincke, 2001); glass is anhydrous (normalized to 100) and palagonite is hydrous (100 - EMP total = wt.% water). The other assumes that there is equal water in sideromelane and palagonite, therefore mathematically normalizing the water in palagonite to equal the water in sideromelane (data set 2). The results for multi-dimensional scaling (MDS) and Gresens' mass balance calculations shown in Chapter 5 are based on data set 1 and become the focus of the discussion in Chapter 6. The results for mass balance from data set 2 are in Appendix B.8 to 0 for reference.

As outlined in Chapter 2, pioneering workers, such as Peacock (1926), thought that palagonite was hydrated glass until other work by Moore (1966) and Hay and Iijima (1968) suggested otherwise (Stroncik & Schmincke, 2002). Since palagonitization is open to mass transfer, it is critical to identify which chemical constituents are actually leaving or being added to the system. A concern of approaching mass transfer by only looking at the difference between glass and palagonite is that the addition of water to either material automatically forces other components to decrease in concentration whether or not they have actually been removed.

Table 5 Two data sets prepared with different mathematical assumptions for water in sideromelane and palagonite. The conventional data set 1* is used for MDS and Gresens' mass balance calculations in this study. Mass balance results from data set 2 are available for reference (Appendix B.8 and B.9).

Data Set	Mathematical Assumption for Water
1*	Sideromelane: anhydrous, normalized to 100 without water Palagonite: hydrous, water is the missing component in low microprobe totals (100 – EMPA = water)
2	Sideromelane: hydrated, normalized to the water in palagonite (in each pair) Palagonite: hydrous, water is the missing component in low microprobe totals (100 – EMPA total = water)

The two data sets were assessed using the Gresens' mass balance method to produce an isocon diagram with a regression line (isocon) and slope using eight immobile elements (Sc, Y, Zr, Nb, La, Nd, Ta, Th) for each glass-palagonite pair. The slope was used in the following Gresens' formula to calculate % mass change for each major and trace element/oxide:

$$\% = \frac{C^A - (C^O * slope)}{C^O * slope} * 100$$

where C^A = concentration in the alteration material (palagonite), and C^O = concentration in the parent/original material (sideromelane/glass). Each glass-palagonite pair has an isocon diagram. Helgafell glass-palagonite pair #05-2 4P is shown as an example (Figure 19) of an isocon (regression line) forced through the origin to produce a slope (0.8903) for the mass balance calculation:

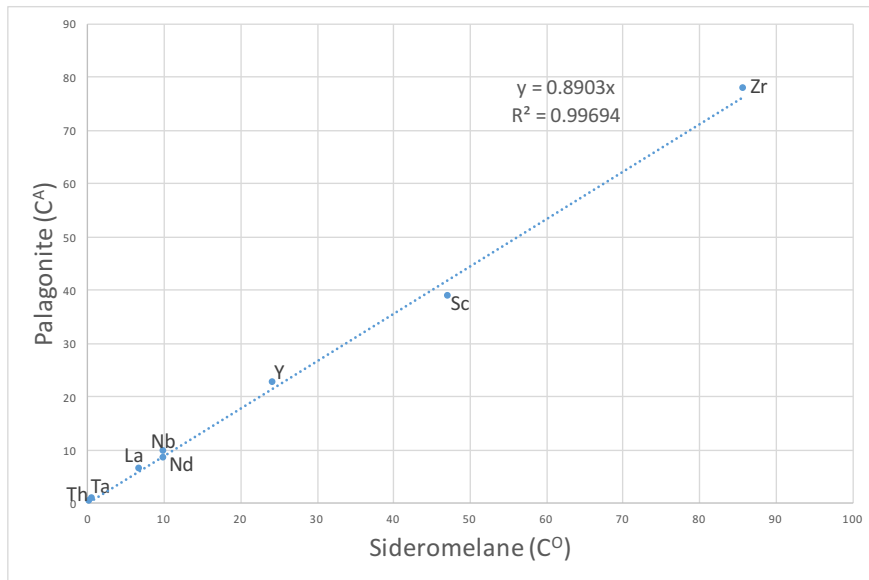


Figure 19 Isocon diagram for one glass-palagonite pair, using eight immobile elements (Sc, Y, Zr, Nb, La, Nd, Ta, Th) forced through the origin (y-intercept = 0) to produce a regression line (isocon) and slope (0.8903) for Gresens' mass balance calculations (Helgafell #05-2 4P).

Chapter 5: Results

This chapter is organized into two sections: petrography and geochemistry. Descriptions of samples and modal proportions of sideromelane, palagonite, minerals and vesicles provide a reference framework for presentation of the geochemical results.

5.1 Petrography: Modal Proportions, Textures, and Secondary Minerals

All samples contain a similar set of materials, including primary (e.g. sideromelane, tachylite, microlites and phenocrysts) and secondary materials (e.g. palagonite rims, gel-material, pyrite/chalcopyrite), vesicles and voids (Table 6; see Appendix B.1). In this study, the term ‘phenocryst’ refers to large crystals (> 300 μm) with microphenocrysts (100-300 μm) and microlites (< 100 μm) progressively decreasing in size, following Murphy et al. (2000). At higher magnifications (SEM and EMP), palagonite rims usually have a linear feature running down the central area of the rim and/or a spherical texture at the inner rim near the glass-palagonite interface (Figure 18). Palagonite rims have regular fractures perpendicular to the sideromelane interface, about every 5-30 μm (Figure 18). A gel-material lacks form or shape and appears translucent, light to dark yellow-brown and is anisotropic (Figure 21). Sideromelane is texturally homogeneous (except for microphenocrysts), featureless, and often has a crenulated edge (Figure 18).

Table 6 Modal proportions (average) summarize materials and features in Helgafell and Wells Gray samples. Thin section point counting (21,000⁺) details appear in Appendix B.1.

Modal Group	Modal Type	Helgafell (Avg. %)	Wells Gray (Avg. %)
Basaltic Glass	Sideromelane	29.2	38.0
	Tachylite	2.1	5.2
Palagonite	Dark rim	8.9	14.4
	Gel-material	19.1	6.2
Crystals/Minerals in Glass	Microlites (Plag/Olivine)	0.1	12.3
	(Primary) Phenocryst (Olivine)	0.4	2.0
Crystals/Minerals in Voids	Pyrite/Chalcopyrite	1.2	0.4
	(Secondary) (Sulfides)		
Brown, unknown material	Unknown	1.5	3.5
Vesicles and Amygdules	Vesicle/Amygdule Total	30.7	4.9
	(portion of total vesicles) Zeolite-like (Si, Na) mineral	5.6	1.4
Voids	Void Total	7.1	13.1
Porosity	Vesicles + Voids	37.8	18.0

Vesicles in samples from Helgafell and Wells Gray can appear empty, fractured (thin section preparation cut through the edge of the vesicle rim) or filled with either concentric zones or a variety of secondary minerals.

5.1.1 Wells Gray, British Columbia, Canada

A typical sample from Wells Gray, BC, includes both types of basaltic glass: 1) isotropic, microlite-rich, honey-coloured sideromelane (38.0%) with well-defined, generally fibrous, dark-brown palagonite rims, and 2) cryptocrystalline, opaque, virtually palagonite-free tachylite (5.2%) (Figure 20A, B). Sideromelane grains can range from 0.25 to 3 mm in size. Under crossed polars (XPL), sideromelane is isotropic. Palagonite rims appear dark brown to black and almost isotropic but can vary from isotropic to minimally anisotropic (Figure 20). A gel-material differs from the palagonite rim by appearing translucent, light yellow-brown to dark brown, anisotropic, and lacks form or shape especially under high intensity illumination (Figure 21). Microlites (12.3%) are typically plagioclase and olivine that range in size (0.01 to 0.03 mm), and olivine grains are euhedral and contain chromite inclusions. Larger phenocrysts (0.5 to 1.5 mm) of olivine are rare (average ~0.4% in Helgafell and ~2.0% in Wells Gray) in comparison to microlites.

Sulfides (0.4%), a brown unknown material (3.5%) and a zeolite-like (1.4%) mineral occur in voids (13.1%), vesicles (4.9%) and in interstitial areas. Sulfides are typically pyrite and chalcopyrite (Figure 20C). Sample porosity, including vesicles and voids, is ~ 18.0%.

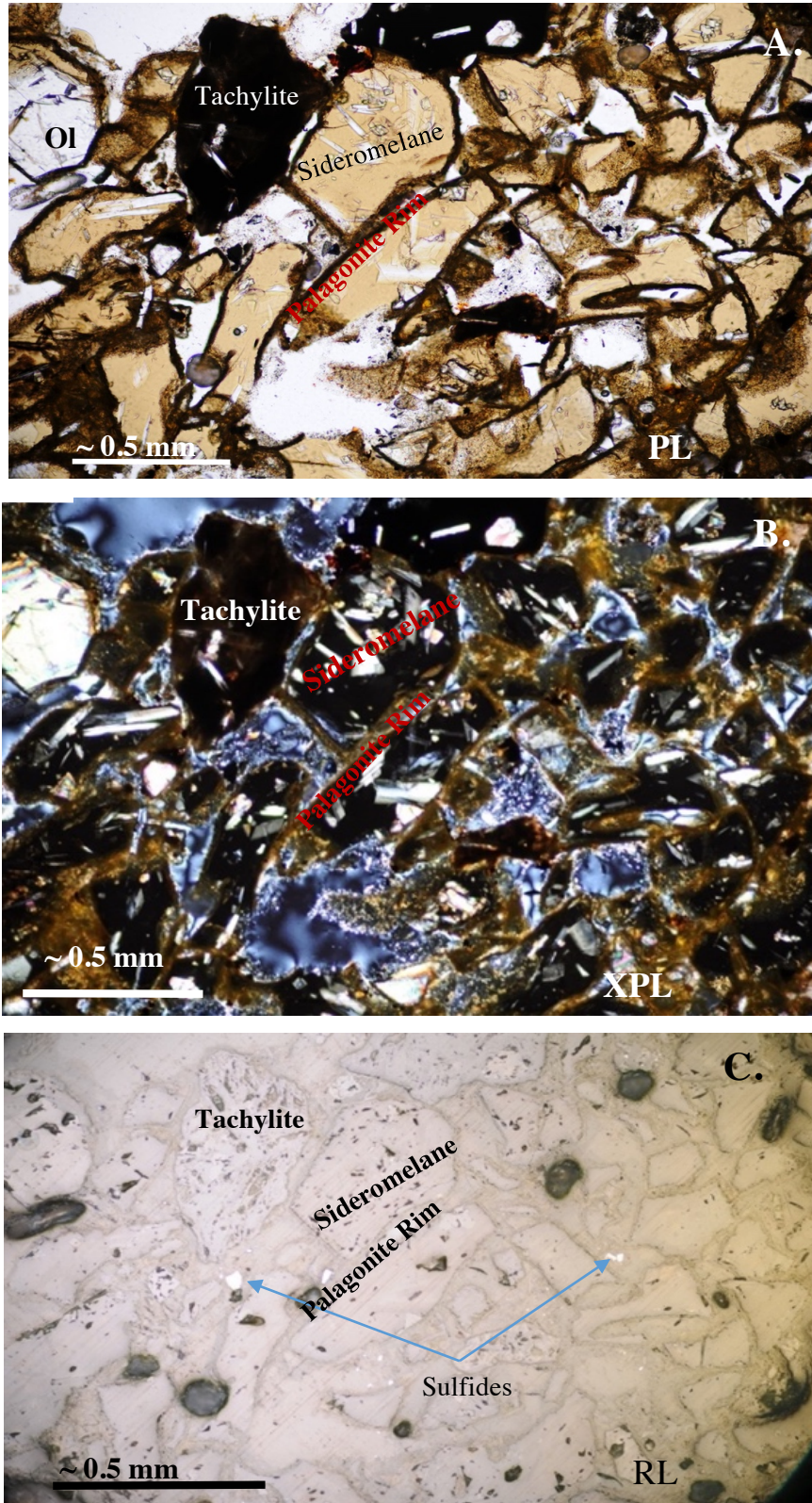


Figure 20 Photomicrographs of sideromelane and tachylite glass, palagonite, sulfides and olivine (Ol). The same spot illustrated in A) PPL; B) XPL and C) Reflected light. Wells Gray #21a-3.

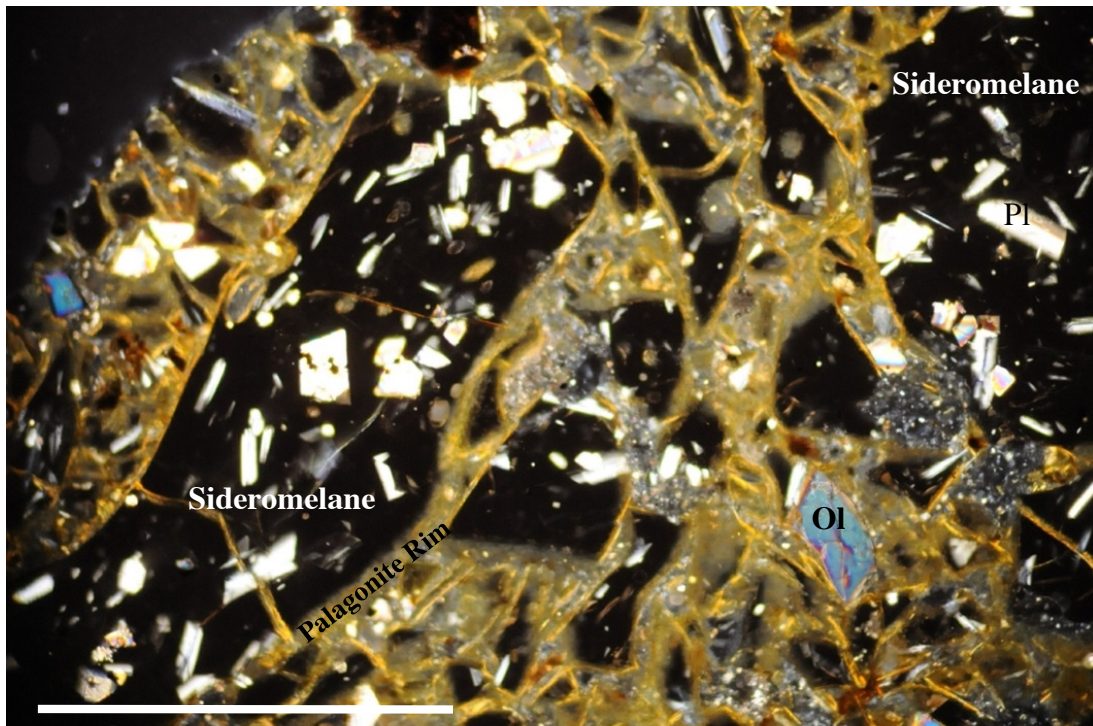


Figure 21 Photomicrograph (XPL reostat control adjusted to high intensity of illumination) showing the isotropic, microlite-rich (olivine (Ol) and plagioclase (Pl)) alkali olivine basaltic sideromelane at Wells Gray and its isotropic to anisotropic palagonite rims and translucent formless gel-material. Scale bar = 0.5 mm.

5.1.2 Helgafell, Iceland

Sideromelane and tachylite varieties of glass are present at both localities but sideromelane (~29.2%) is much more abundant than tachylite (~2.1%). Palagonite rims can range in appearance from amorphous gel-material (translucent, anisotropic) to fibrous, almost isotropic and thinner (~ 6–12 μm) than in Wells Gray (~10-25 μm) samples. Sulfides (opaque in PPL and gold-coloured in RL), Fe-oxides, an unidentified green-brown material (PPL) and zeolite-like (low-relief) materials occur between tuff fragments and in vesicles. Helgafell sideromelane does not have abundant microlites of plagioclase and olivine (~0.1%). Rare and large phenocrysts of olivine (~0.4%) sit within some sideromelane grains.

Modes (Table 6) show a lower percentage of palagonite rims at Helgafell (average ~8.9%) than Wells Gray (average ~14.4%) and more sideromelane (average ~38.0%) at Wells Gray than at Helgafell (average ~29.2%). Sideromelane grains from Helgafell are, on average, 0.5 to 2.5 mm in size and ~30.7% vesicular (Table 6). Palagonite rims occur within vesicles and

on the edges of glass grains. The glass grains can be so riddled with vesicles that it is a challenge to locate distinguishable boundaries between separate glass grains (Figure 22).

5.1.3 Comparison Between Sites

Optical microscopy shows two main differences between Helgafell and Wells Gray samples. First, a translucent, anisotropic gel-material is more abundant at Helgafell (average ~19.1%) than Wells Gray (average ~6.2%; Table 6), and is distinctly different from isotropic sideromelane and virtually isotropic palagonite rims (Figure 23). Palagonite rims are easily distinguishable in PPL, but indiscernible in cross-polarized light (XPL), whereas sideromelane grains and the gel-material appear to be honey-coloured (but texturally different) in PPL and are easily differentiated in XPL (isotropic sideromelane vs. anisotropic, translucent gel-material; Figure 23). Second, Helgafell's sideromelane is highly vesicular (~30.7%) with few microlites (average ~0.1%), whereas Wells Gray glass is almost free of vesicles (average ~4.9%) and microlite-rich (average ~12.3%) (Figure 24; Table 6). Palagonite rims at Helgafell are thinner (~6-10 μm) than at Wells Gray (~10-20 μm).

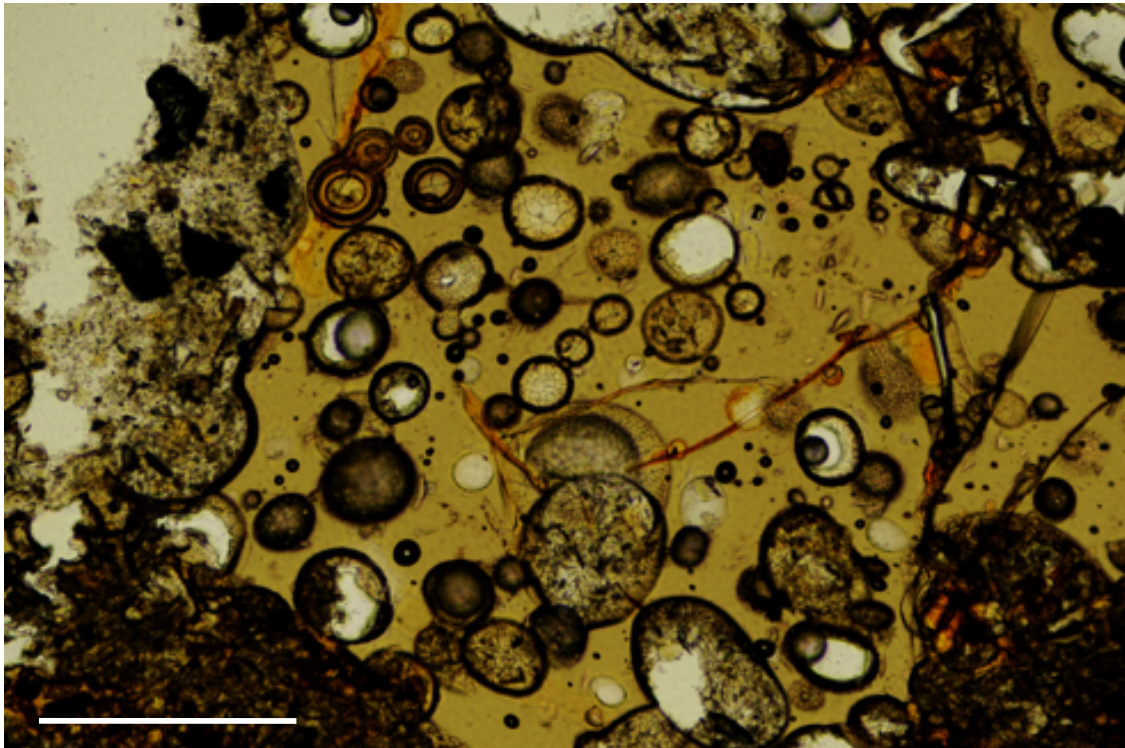


Figure 22 Typical sideromelane grain at Helgafell (PPL) is highly vesicular with dark-brown, virtually isotropic palagonite rims on vesicles and grain edges. Numerous materials/minerals are abundant in vesicles. Scale bar = 0.25 mm (sideromelane grain is about 0.75 mm wide).

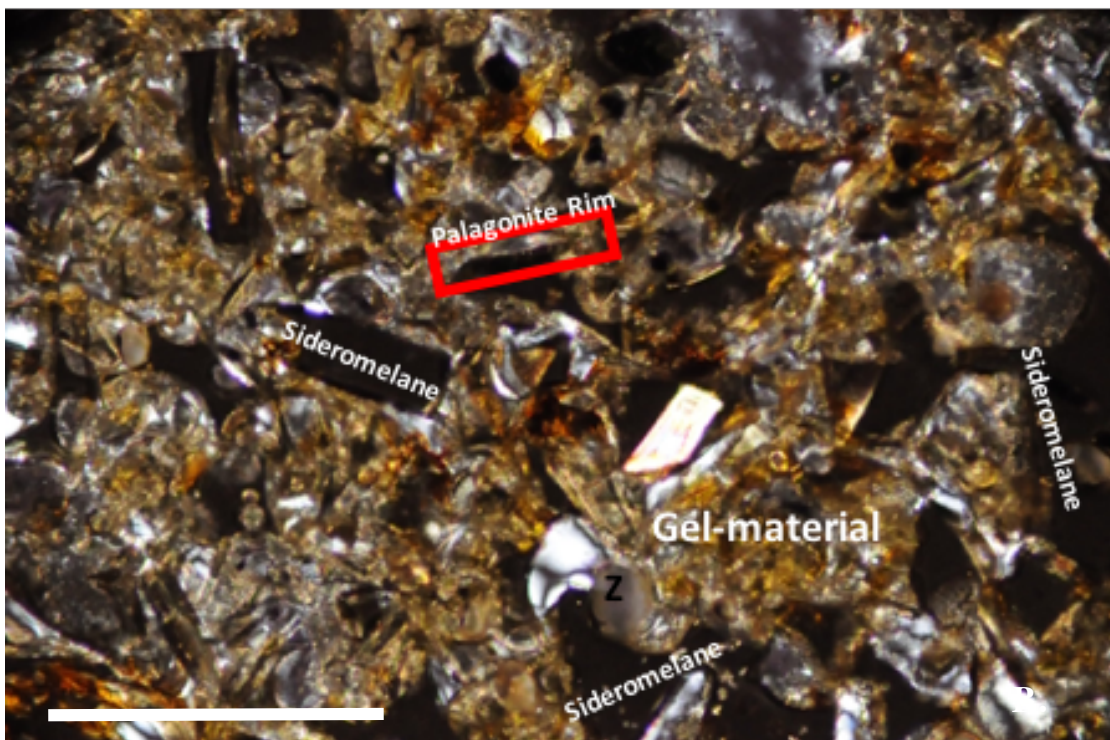


Figure 23 Photomicrographs of sideromelane (isotropic) grains, an amorphous gel-material (translucent, anisotropic) and palagonite rim (virtually isotropic and indiscernible) and zeolite-like material (Z) in A) PPL, and B) XPL (#09-2 Helgafell). Image scale ~ 0.5 mm.

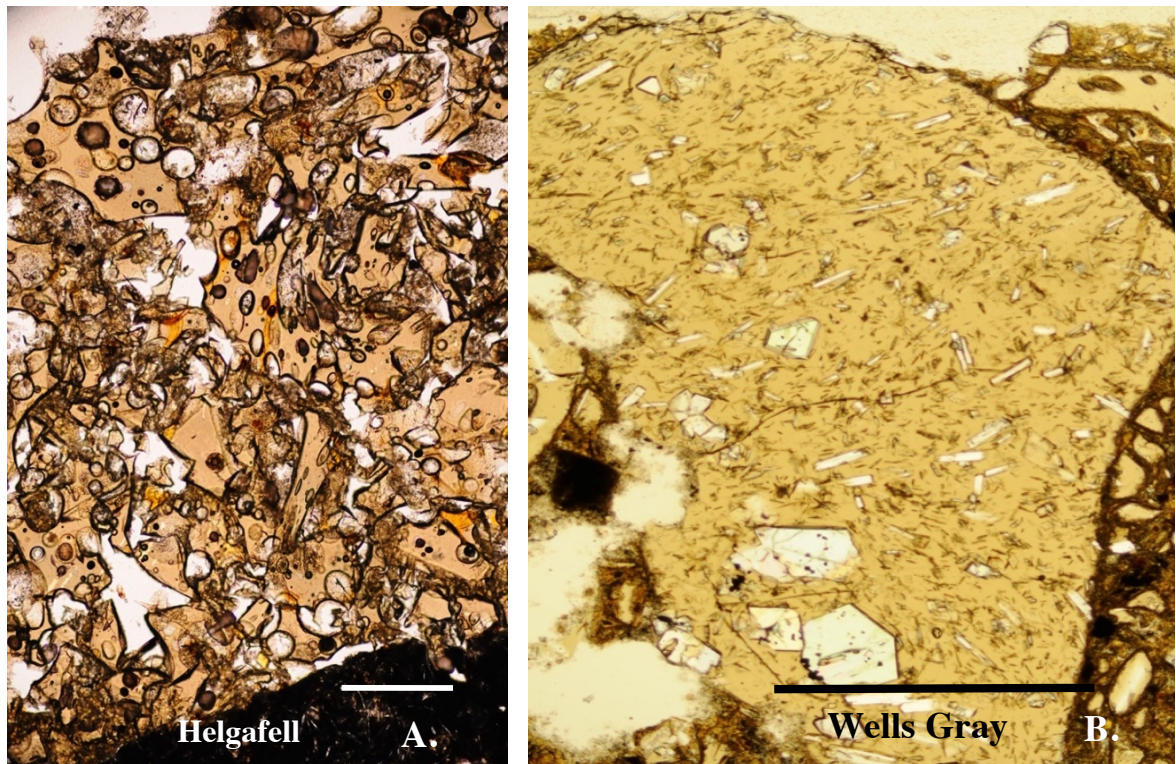


Figure 24 Textural differences illustrated in PPL photomicrographs: A) Helgafell (#05-2) has highly vesicular sideromelane with minimal microlites. B) Wells Gray (#21b-3) has virtually non-vesicular and microlite-rich sideromelane (scale bar = 1 mm).

Completely altered sideromelane, with remnant palagonite rims and unaltered plagioclase lathes, can be situated next to fresh sideromelane grains (Figure 25). Although the thickness of palagonite rims is dependent on locality (thicker rims in Wells Gray) and not on degree of alteration, the phenomenon of completely altered grains situated next to fresh grains was more obvious in the smaller, more numerous, and, more distinctly separate from each other, glass grains in Wells Gray and not prevalent in the larger, highly vesiculated glass grains in Helgafell.

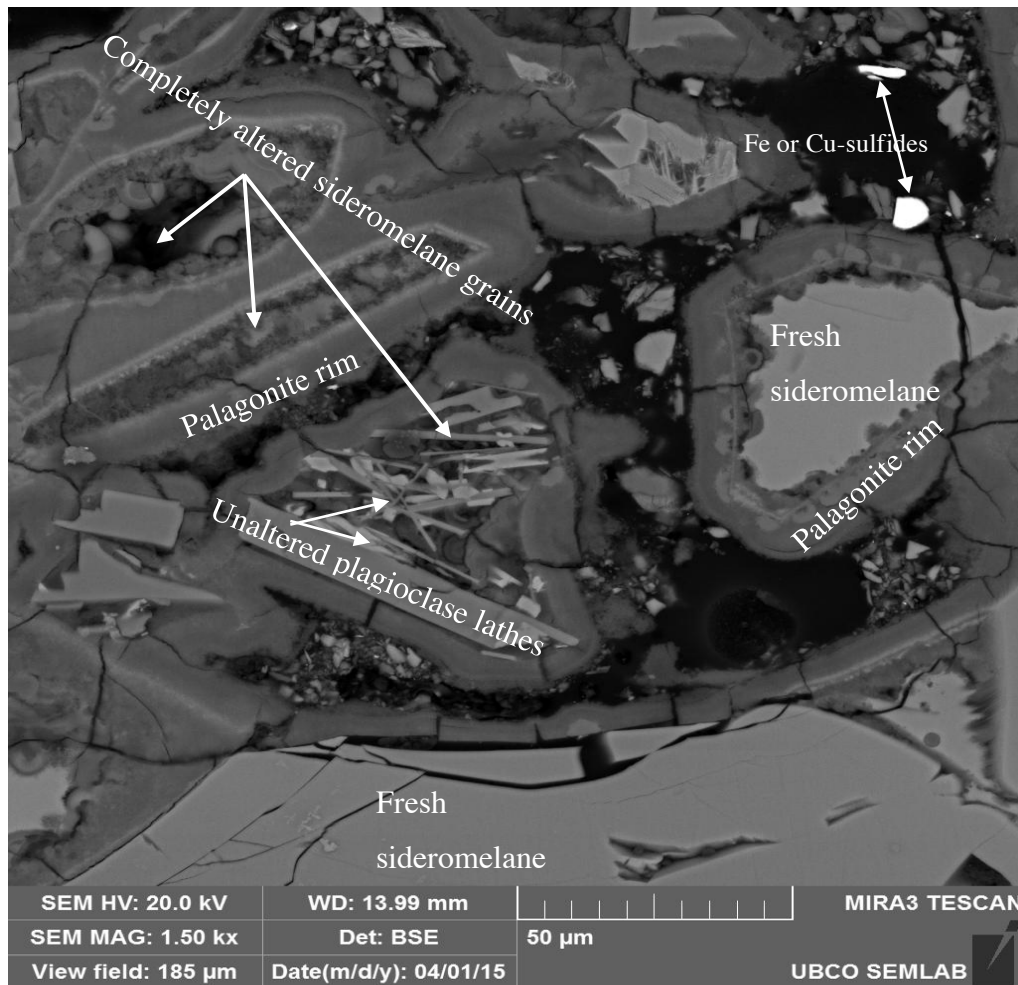


Figure 25 Completely altered sideromelane with remnant palagonite rims and plagioclase lathes situated next to fresh sideromelane grains (SEM backscatter image). Scale: 50 μm = 0.05 mm. WG #21b-3.

5.1.4 Unique Textures

Some unique textures and features in sideromelane and palagonite include fluidal glass, concentrically zoned vesicles in glass, zoning in palagonite rims, concave and crenulated edges on glass grains, dissolution textures linking vesicles, spherical textures near the glass-palagonite interface, and tubules or tunnelling textures in sideromelane.

Fluidal glass is mainly identified by the presence of in situ vesicles that appear to be stretched. It is more abundant in Helgafell sideromelane (Figure 26).

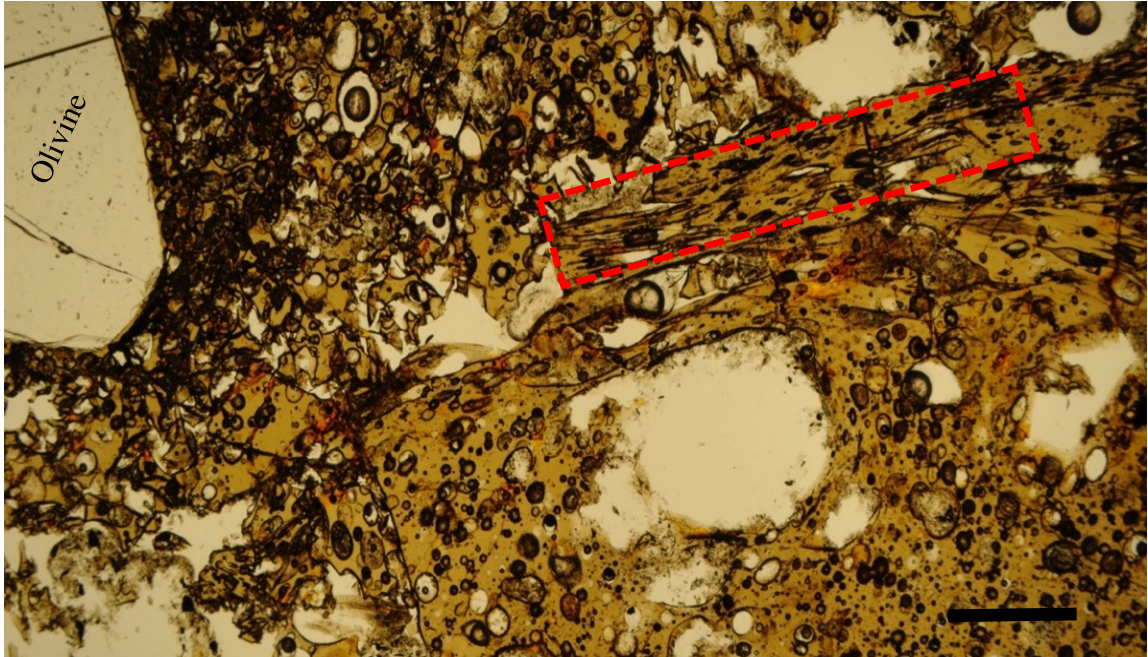


Figure 26 Fluidal or stretched glass, outlined in red. Helgafell #03-2 (PPL). Scale ~ 1 mm.

Concentrically zoned spheres in sideromelane grains are presumably a unique type of infilled vesicle or devitrification feature (Figure 27) especially abundant at Helgafell.

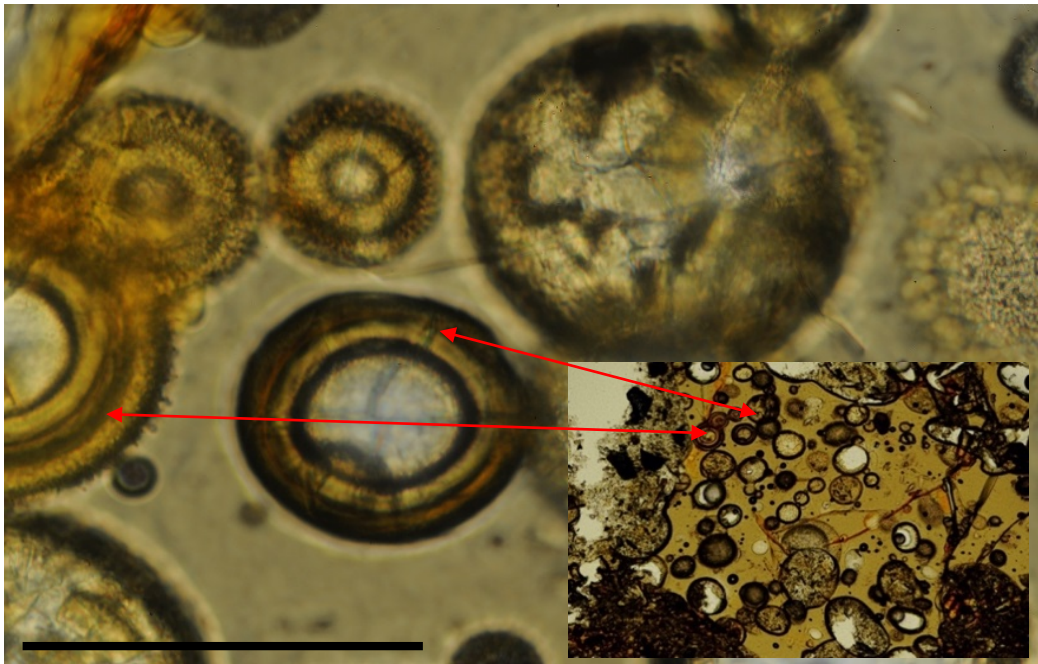


Figure 27 Concentrically zoned vesicles in a sideromelane grain from Helgafell #03-2 (PPL). Inset shows zoned vesicles at lower magnification. Scale ~ 0.5 mm.

Typically, palagonite rims are texturally zoned. A white linear zone (visible only with the SEM or EMP) separates the inner spherical texture from the rest of the palagonite rim. Two types of spherical textures have been identified:

1) hemispheres and spheres within the inner portion of the palagonite rim and adjacent to glass (Figure 28). In PPL, these spheres appear similar to the concentric rings shown in Figure 1.

2) zoned hemispheres or pie-shaped partial-spheres that exist as separate features from the palagonite rim. They appear to emanate away from the palagonite rim and into the sideromelane (Figure 29).

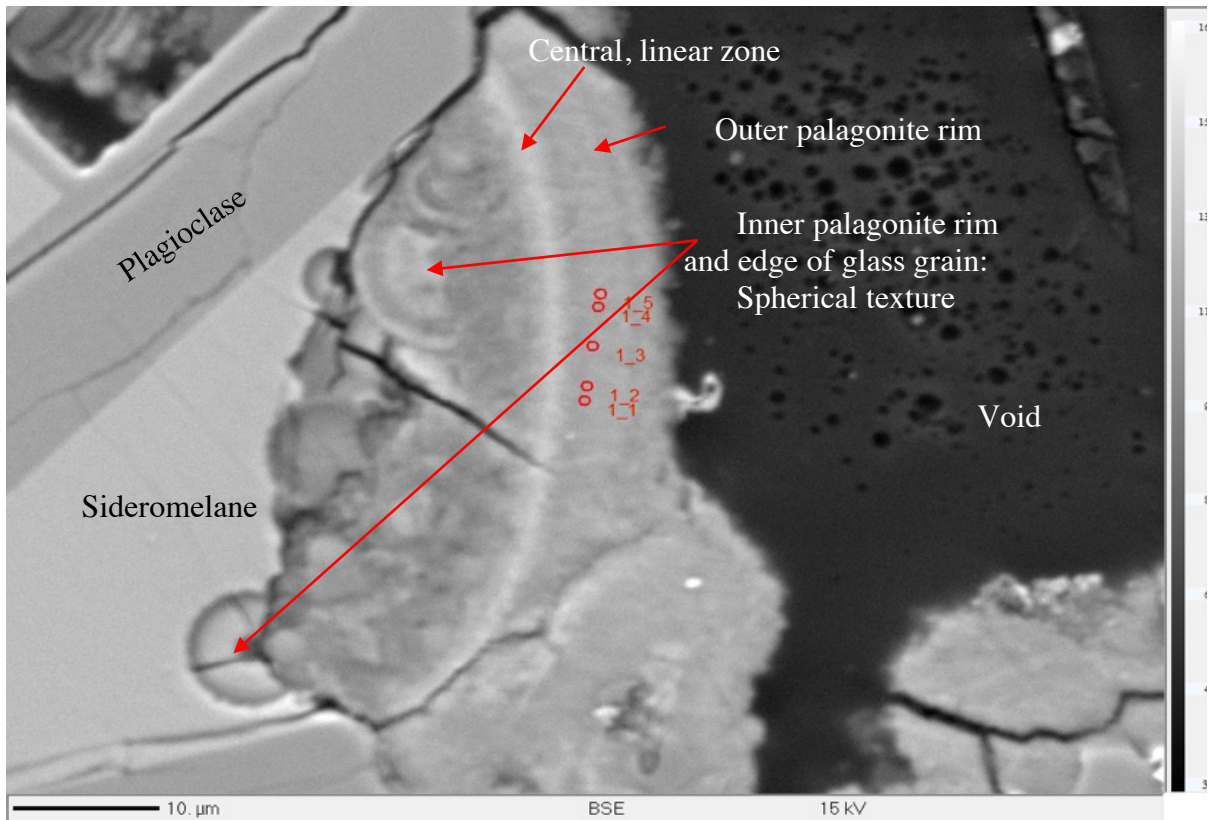


Figure 28 EMP backscatter image showing zoned palagonite rim with a central white linear zone and a spherical texture in the inner portion of the palagonite rim that propagates into the glass (Wells Gray #21a-2). Scale bar: 10 μm = 0.01 mm.

The glass-palagonite interface varies in width, hosts unique textures and is usually, but not always, empty (Figure 29). A concentric-zoned, spherical texture is common in the glass and inner portion of the palagonite rim near the interface (Figure 28). The outer portion of the

palagonite rim is uniform and lacks obvious structure in comparison to the inner area near the interface.

Locally, banded circles appear to radiate into sideromelane from palagonite rims (Figure 29; shown by red arrows). The edges of sideromelane grains commonly have a crenulated, concave texture that opens towards the glass-palagonite interface (Figure 29).

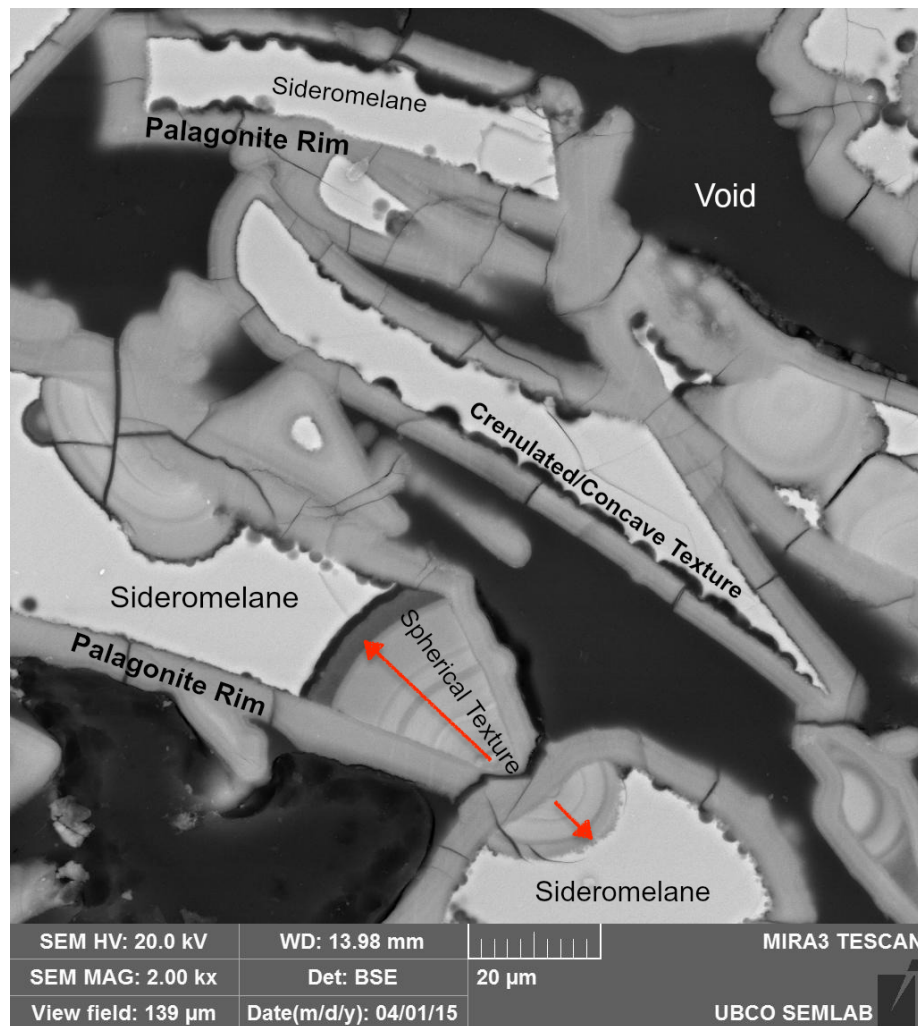


Figure 29 SEM backscatter image showing microzoned semicircular texture that propagates from the glass-palagonite interface into sideromelane grains (shown by red arrows), and is distinct from palagonite rims. Glass grain edges commonly have a crenulated, concave texture at the interface (Helgafell #09-2). Black area = empty void. Scale bar: 20 µm = 0.02 mm.

Microlites and phenocrysts of plagioclase or olivine, and Fe-sulfides (e.g. pyrite) appear to be unaltered even though they are surrounded by altered glass (Figure 30).

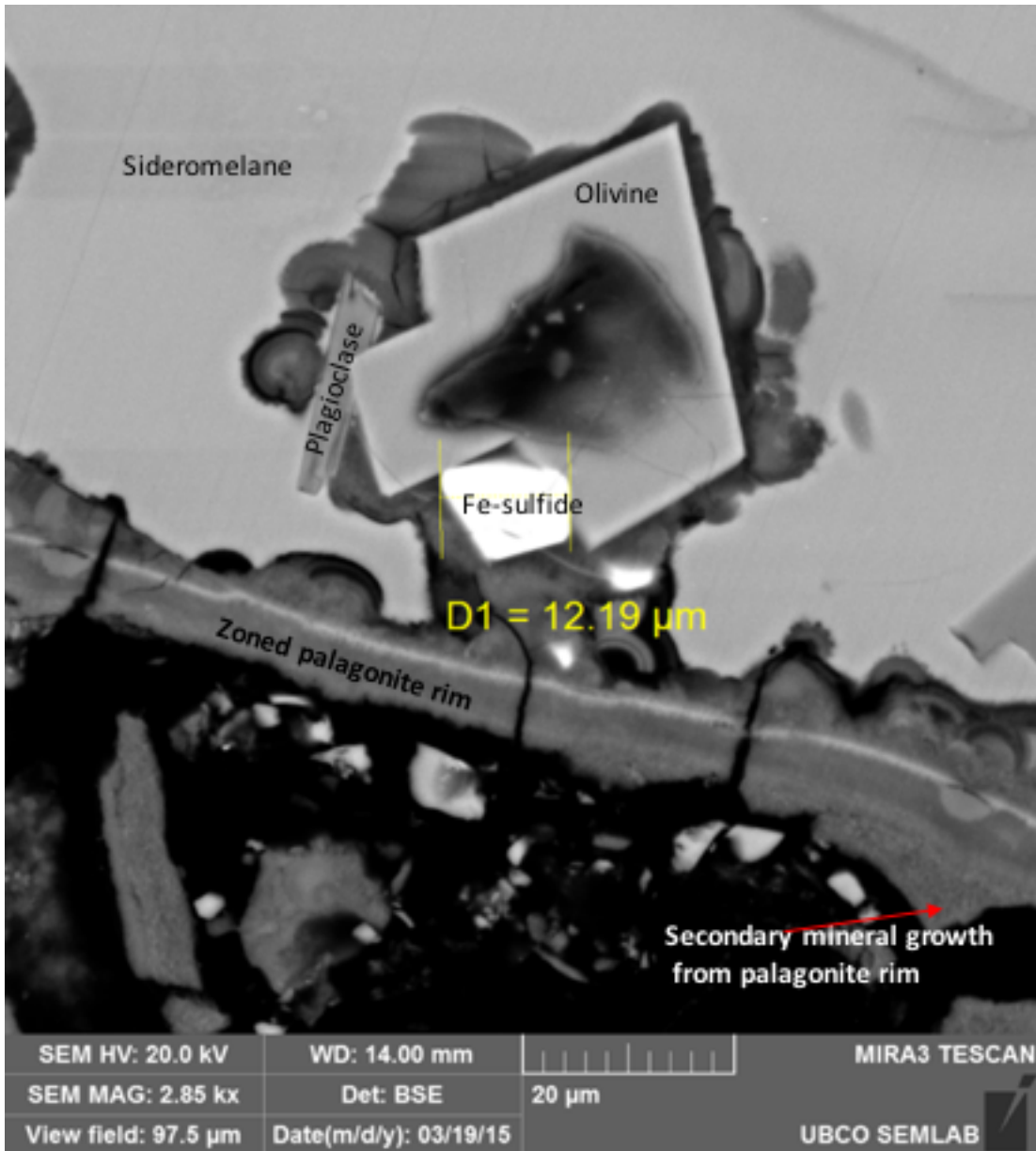


Figure 30 SEM backscatter image showing zoned palagonite rim with a spherical texture at the glass-palagonite boundary and secondary minerals on the outer edge of the palagonite rim (bottom right rim). An olivine phenocryst, plagioclase microlite and pyrite grain in the glass remain unaltered (Wells Gray #21a-3). Scale bar: $20 \mu\text{m} = 0.02 \text{ mm}$.

At both Helgafell and Wells Gray, multiple, sub-parallel and linear microveins link vesicles in sideromelane (Figures 31 and 32). The microveins appear to cut through the glass symmetrically from a central microfracture, which usually connects fractures in the vesicles'

palagonite rims. The microvein texture does not penetrate the palagonite rim, except usually at one central fracture in the rim (Figure 32).

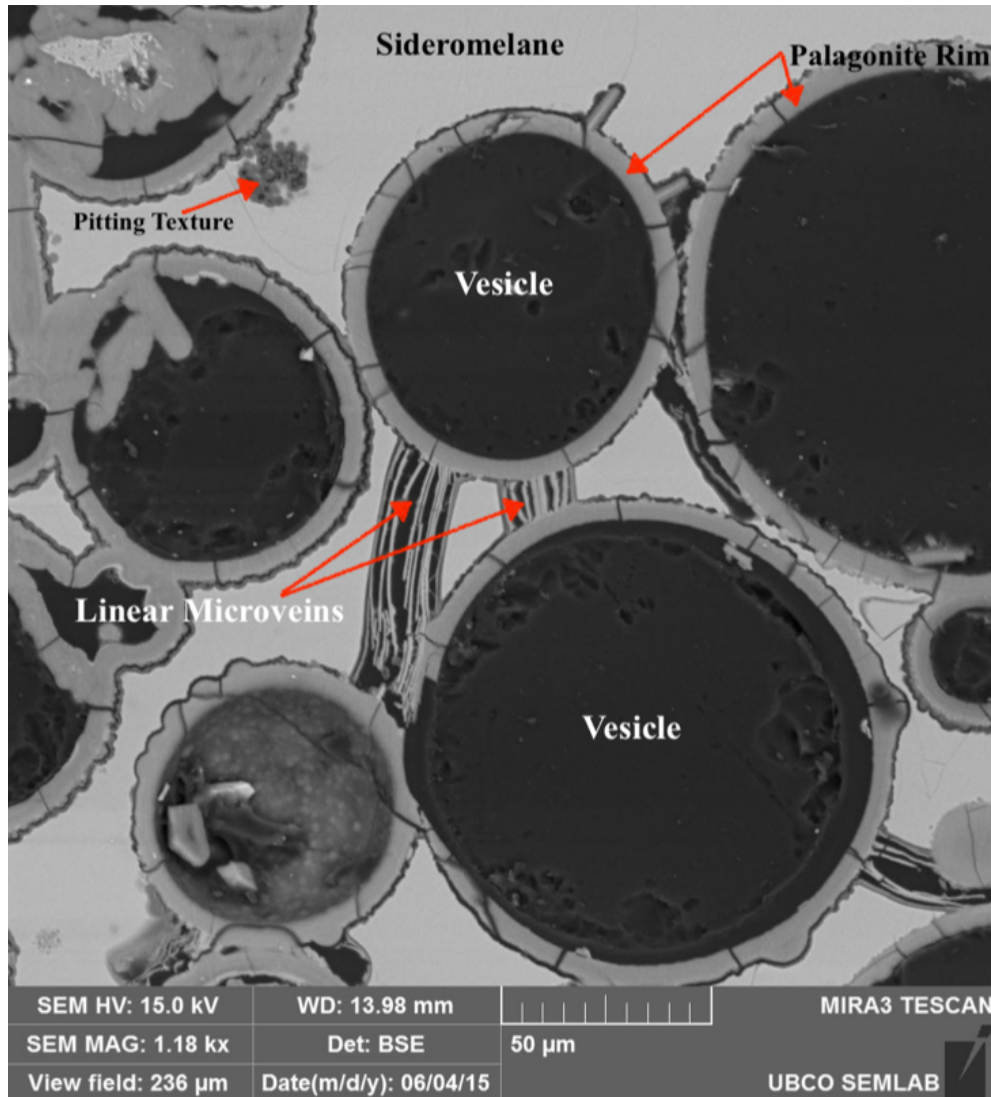


Figure 31 SEM backscatter image showing multiple, sub-parallel, linear microveins linking vesicles in sideromelane (Helgafell #11-2). Scale bar: 50 µm = 0.05 mm.

Although fractures in glass that palagonitize have been reported previously (Furnes et al., 2008; Jercinovic et al., 1990; Stroncik & Schmincke, 2001), the multiple, sub-parallel, linear microvein texture in sideromelane has apparently not been previously documented. Optically (PPL) the texture appears as orange-coloured lines in the sideromelane. The SEM-EDS profile across a microvein shows element concentration fluctuations across the texture (Figure 32).

Electron Image 21

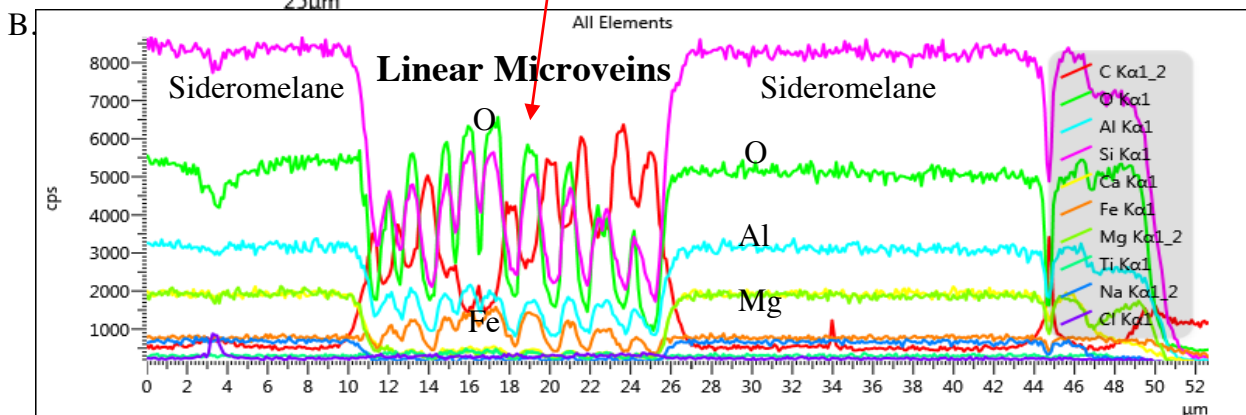
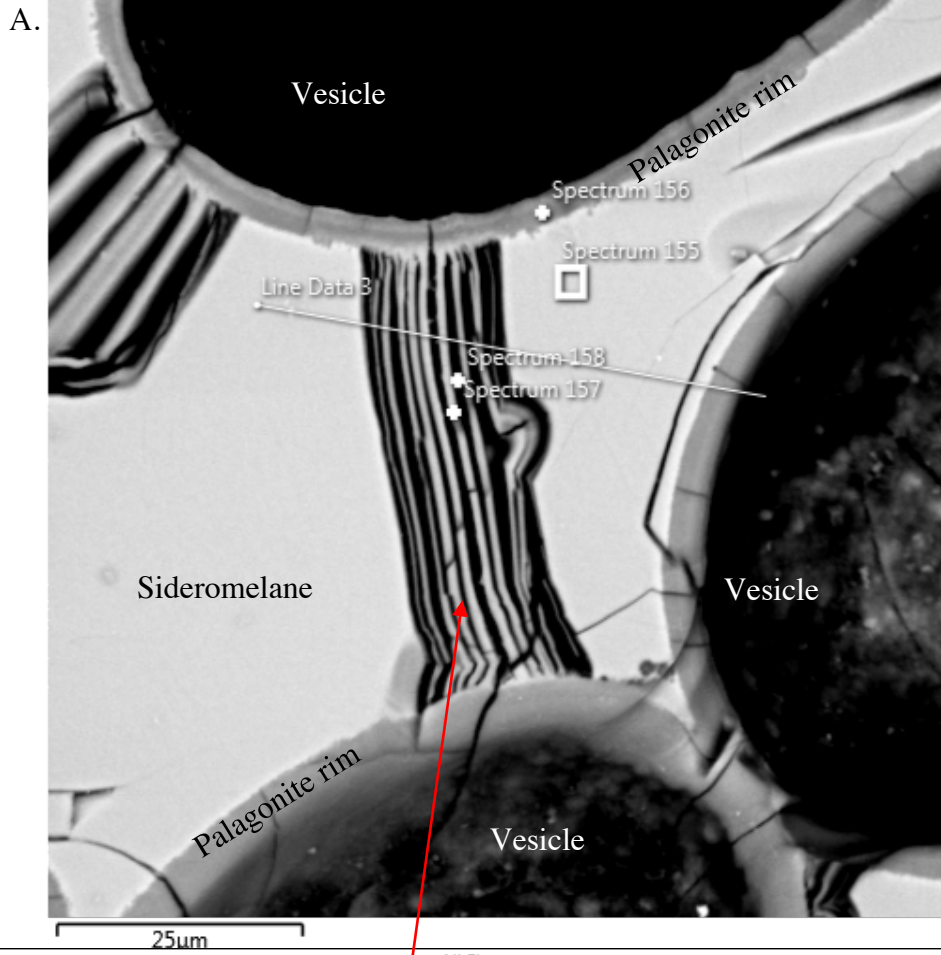


Figure 32 Multiple, sub-parallel, linear microveins in sideromelane join vesicles. A) backscatter SEM image and B) element map. Carbon coating (red) is disregarded (Helgafell #14-2). Scale bar: 25 µm = 0.25 mm.

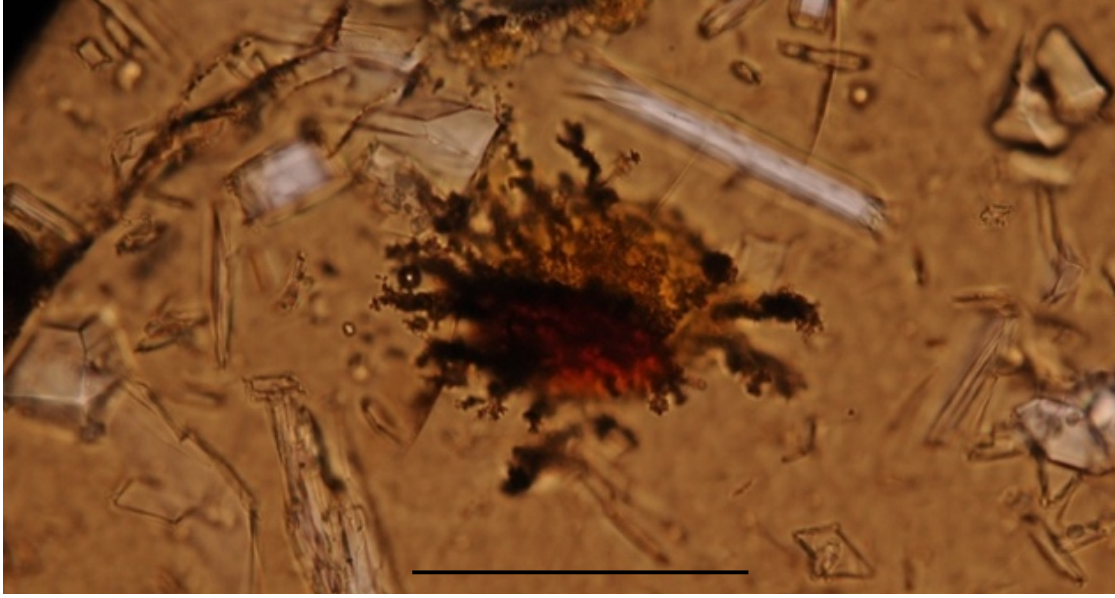


Figure 33 Photomicrograph of a dendritic texture (scale: ~0.1 mm) in sideromelane (PPL) (WG #20-2).

Helgafell and Wells Gray sideromelane contains very irregular dendritic (Figure 33) and tunnelling textures. Fisk and McLaughlin's (2013) description of tunnelling in basaltic glass (Figure 1) matches the texture emanating from the palagonite-rimmed vesicle in Figure 34.

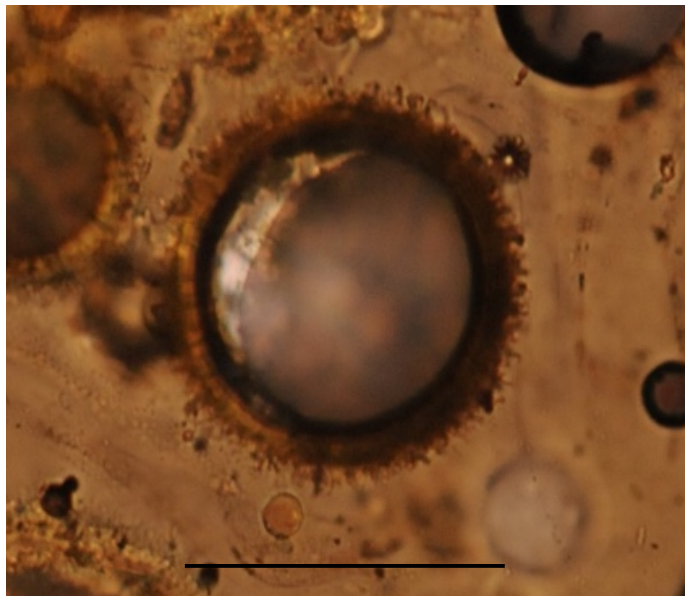


Figure 34 Photomicrograph of a dendritic texture emanating away from a vesicle in sideromelane (PPL) (HG #09-2). The vesicle is filled with a low-relief secondary mineral. Scale bar: ~0.1 mm.

5.1.5 Secondary Minerals

SEM-EDS analyses were used to identify secondary minerals associated with palagonite, and in vesicles. The most common secondary minerals are the Fe-sulfides pyrite (FeS_2) and chalcopyrite (CuFeS_2) (Figures 35 and 36A). Ilmenite (FeTiO_3) and what appear to be clay minerals (Figure 36B) and zeolites (Figure 37) were found in voids and vesicles.

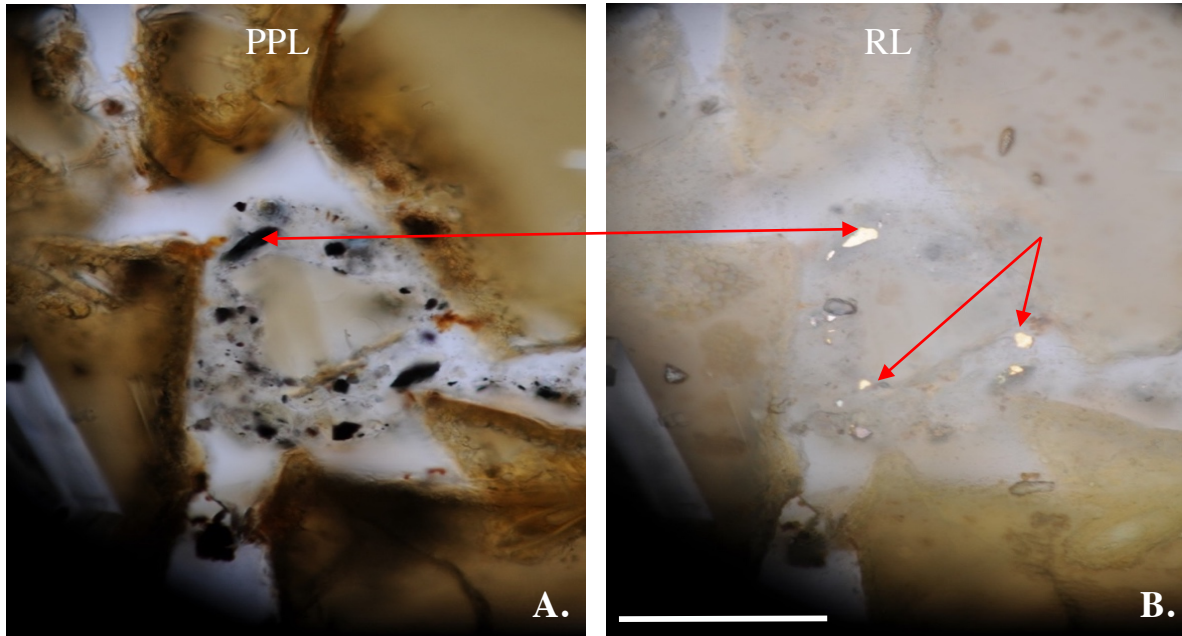


Figure 35 Photomicrographs showing sulfides (e.g. pyrite, chalcopyrite) in voids and vesicles appearing A) dark blue to black in PPL; and B) brassy yellow in RL (WG #21a-3). Scale bar = 0.25 mm.

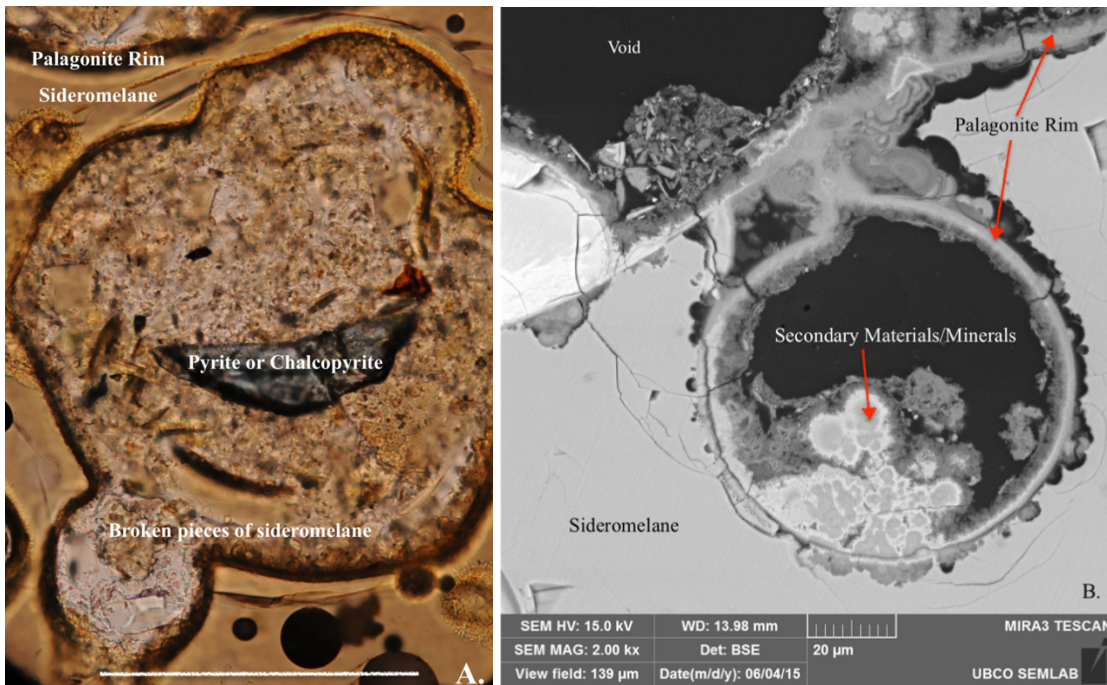


Figure 36 Photomicrographs showing material in vesicles: broken glass, palagonite rims, and minerals such as this A) sulfide, chalcopyrite or pyrite (PPL) scale bar = 0.1 mm. Helgafell #11-2. B) SEM backscatter image of secondary minerals/materials that may be clay minerals within vesicles in sample WG #20-2. Scale bar: 50 μm = 0.5 mm.

A secondary mineral of similar appearance in all samples is most commonly found inside vesicles (Figure 37). Optical microscopy shows that it has low relief and is light pink in PPL. Preliminary SEM-EDS data reveal very low Al_2O_3 (1.49 wt.%) and high SiO_2 (66.83 wt.%) and Na_2O (11.75 wt.%). The missing 9.37 wt.% from the low total of 90.63 wt.%, was assumed to be water since clay and zeolite minerals have water in their structure. Further electron microprobe analyses at these same locations (Helgafell #09-2) showed more variable compositions (Table 7) and more detailed images of the material within vesicles (Figures 37 to 40). Clearly visible only in electron photomicrographs, the mineral appears to vary in texture, but is generally spherical and light-coloured in the central area of a vesicle, fibrous and dark-coloured along the sides. It is tentatively identified as a zeolite, a clay or a Na-metasilicate known as water glass.

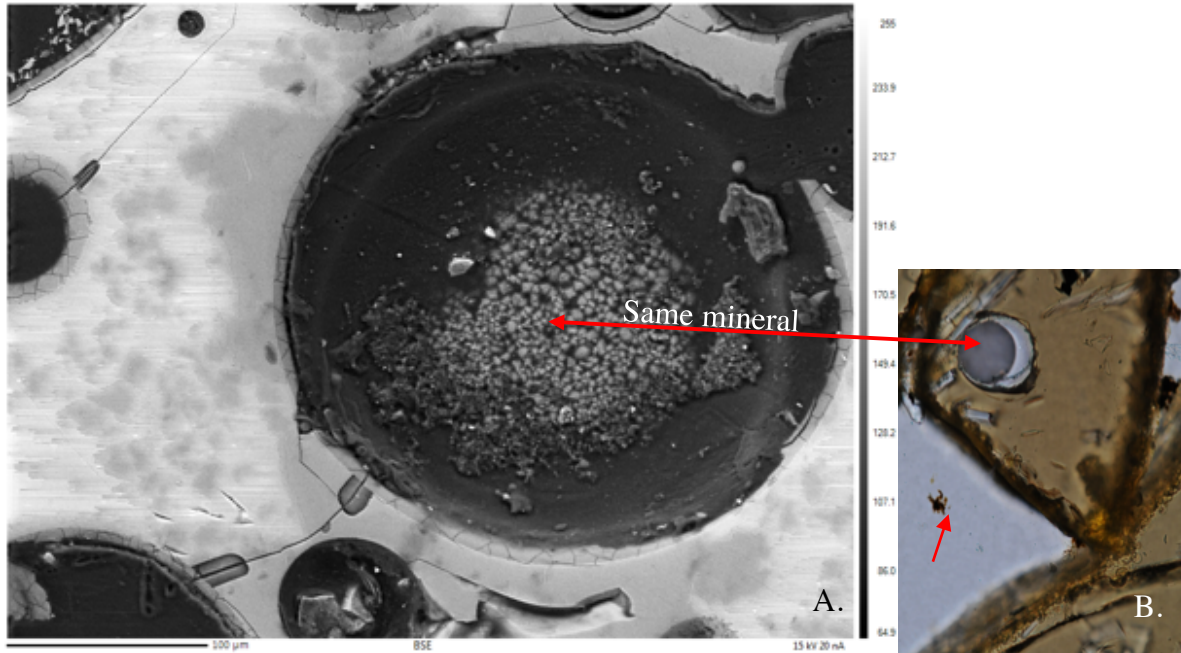


Figure 37 Images of a Na-rich, Al-poor zeolite-like mineral in vesicles (Vesicle #1, Table 7). A) EMP backscatter image (HG #09-2). Scale bar: 100 μm = 0.1 mm; and B) photomicrograph (PPL) shows high negative relief. Arrow points to a common unidentified dark-red globular material in voids. Image width \sim 0.5 mm.

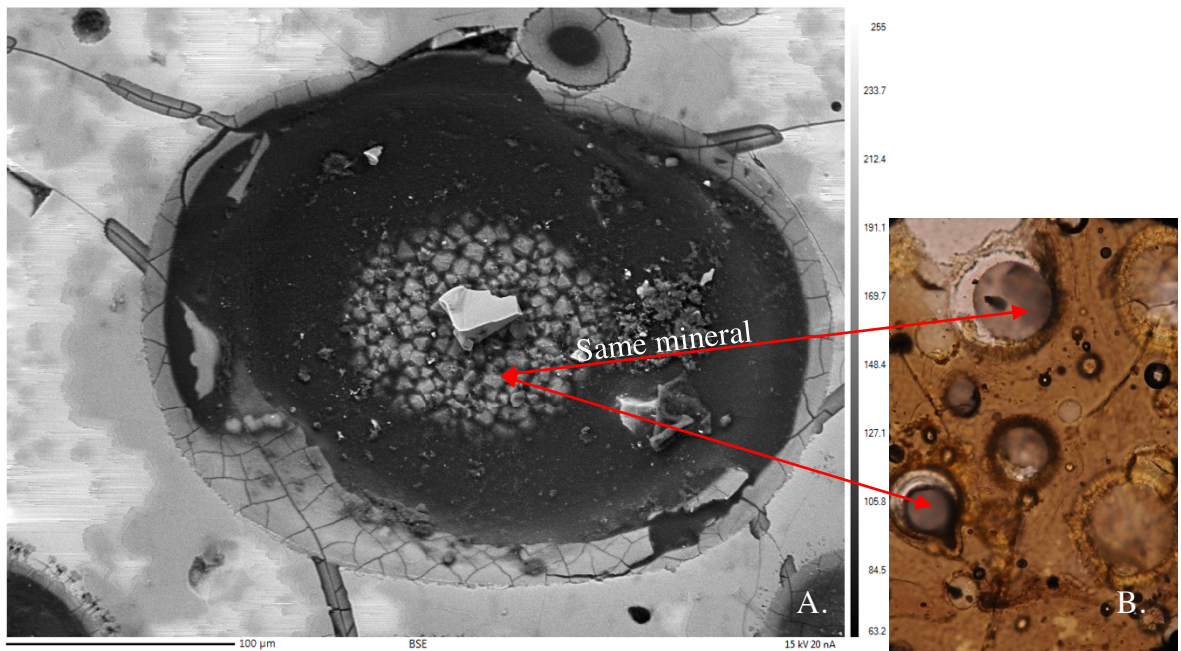


Figure 38 Similar Na-rich, Al-poor zeolite-like mineral as Figure 37, collecting in a vesicle (Vesicle #5, Table 7). A) EMP backscatter image. Scale bar: 0.1 mm. Fractures are becoming palagonitized. A foreign object, likely glass, occurs at the centre of a circular collection of secondary mineral grains. A palagonite rim in the vesicle appears to be cracked possibly due to dehydration. b) same mineral in a photomicrograph (PPL). HG #09-2. Image width \sim 0.5 mm.

Table 7 EMP data for the secondary mineral in vesicles measured in oxide wt.%. Based on low EMP totals, the missing component was assumed to be H₂O (100-EMP total = H₂O). All Fe as FeO. Ratios of (Na+K)/Ca and Si/Al provided below, and the average composition for the mineral shown in column 1. Images of vesicles (labelled Ves.) numbered 1, 4, 5 and 6 correspond to vesicle numbers in Figures 37 to 40.

Vesicle No.	Average	Ves. 1	Ves. 1	Ves. 1	Ves. 1	Ves. 2	Ves. 4	Ves. 4	Ves. 5	Ves. 5	Ves. 5	Ves. 5	Ves. 6b
SiO ₂	54.59	55.05	53.50	57.25	55.21	56.25	55.05	50.23	49.07	57.70	48.87	60.21	56.72
TiO ₂	0.03	0.03	0.03	0.01	0.03	0.03	0.00	0.03	0.05	0.04	0.07	0.02	0.04
Al ₂ O ₃	1.13	1.15	1.03	1.14	1.09	1.11	1.72	1.84	1.02	1.08	1.05	1.15	0.12
Cr ₂ O ₃	0.01	0.01	0.00	0.01	0.01	0.00	0.00	0.00	0.02	0.01	0.02	0.00	0.01
FeO	0.16	0.14	0.08	0.15	0.17	0.14	0.19	0.16	0.17	0.15	0.27	0.13	0.15
MnO	0.01	0.00	0.01	0.00	0.00	0.00	0.00	0.04	0.00	0.00	0.00	0.03	0.01
NiO	0.01	0.00	0.00	0.00	0.02	0.03	0.01	0.02	0.00	0.00	0.00	0.00	0.02
MgO	2.81	2.90	2.63	3.06	2.78	2.97	2.77	2.56	2.56	2.90	2.58	3.16	2.84
CaO	4.69	4.71	4.49	4.92	4.61	4.86	4.60	4.63	4.22	4.92	4.29	5.15	4.84
Na ₂ O	8.71	9.00	9.60	10.07	9.94	5.59	10.34	9.60	8.40	11.49	8.21	11.51	0.76
K ₂ O	0.70	0.71	0.69	0.75	0.72	0.77	0.68	0.62	0.65	0.72	0.66	0.76	0.71
H ₂ O	27.16	26.30	27.94	22.64	25.42	28.25	24.64	30.27	33.84	20.99	33.98	17.88	33.78
Total	100.00	100.00	100.00	100.00	100.00	100.00	100.00	100.00	100.00	100.00	100.00	100.00	100.00
(Na+K)/Ca	2.01	2.06	2.29	2.20	2.31	1.31	2.40	2.21	2.14	2.48	2.07	2.38	0.30
Si/Al	48.53	47.87	51.94	50.22	50.65	50.68	32.01	27.30	48.11	53.43	46.54	52.36	472.67

Based on 22 oxygens, the chemical formula for this unknown mineral is estimated to be Na_{3,0}Ca_{0,9}K_{0,2}(Mg,Fe)Al_{0,2}Si_{9,3}O₆(OH)₂.14(H₂O), highlighting the low Al- and high Na-content.

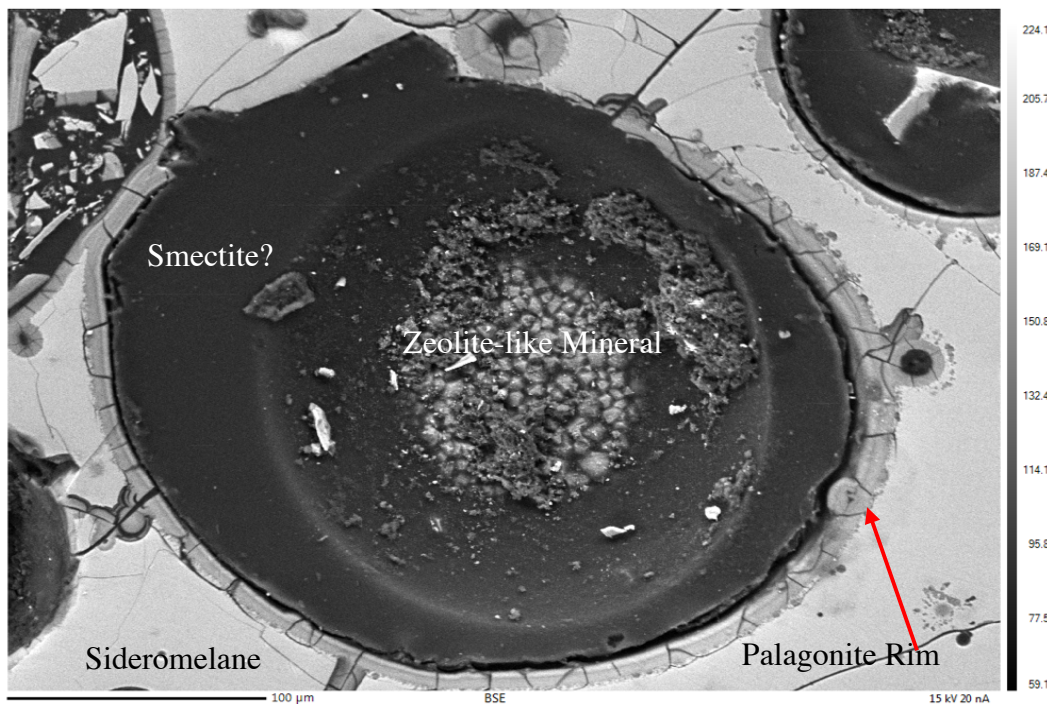


Figure 39 Similar zeolite-like mineral to that shown in Figures 37 to 40 is forming in a vesicle lined with an exceptionally thick, uniform material (likely smectite) separate from the palagonite rim. Scale bar: 100 μm = 0.1 mm. EMP backscatter image. HG #09-2. Vesicle #4, Table 7.

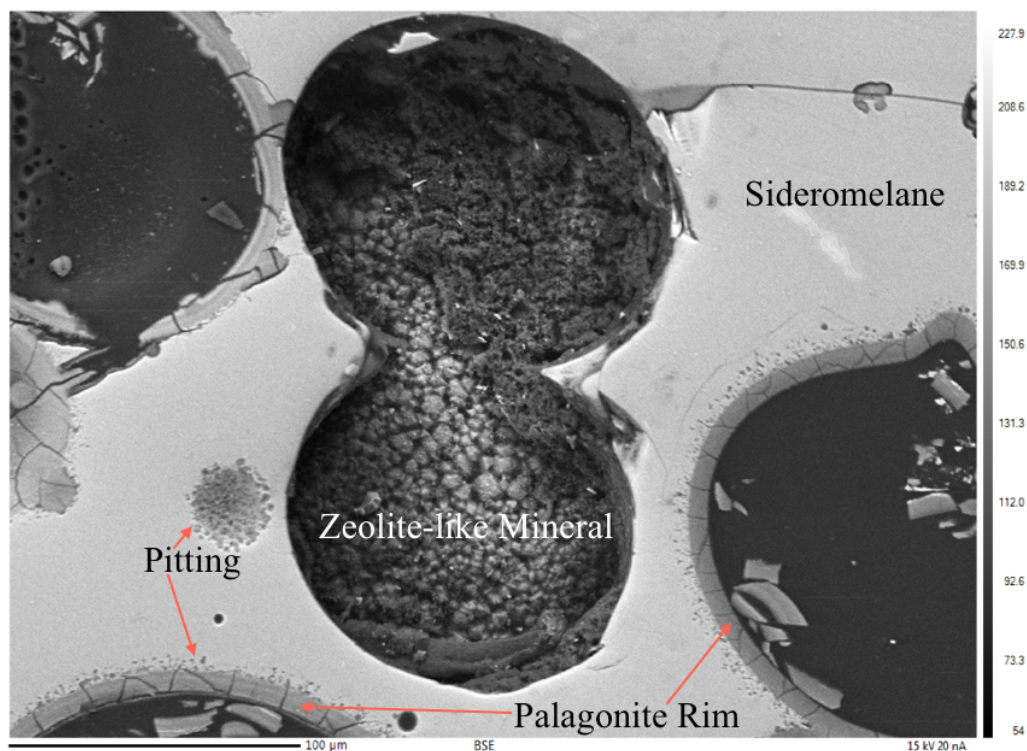


Figure 40 Abundant zeolite-like mineral with low Na and Al, and high H₂O relative to other analyses (Figures 37 to 39). Pitting in glass (bottom left) is common. Scale bar: 100 μm = 0.1 mm. EMP backscatter image. HG #09-2. Vesicle #6 (bottom vesicle in image analyzed, 6b/2) in Table 7.

5.2 Major and Trace Element Geochemistry of Sideromelane and Palagonite

The major and trace element compositions of sideromelane and palagonite are critical for constraining the process of palagonitization. The chemical information is the basis for mass balance calculations, and for analyzing the products of reactions that occur during the process. The composition of sideromelane reflects that of the basaltic magma when it was quenched by glacial meltwater and ice. Helgafell and Wells Gray were chosen as study sites specifically because their magma compositions are geochemically different. As an extension of the mid-Atlantic ridge, the magmas erupted at Helgafell are typically subalkaline, tholeiitic basalt whereas those at Wells Gray are alkali olivine basalt.

Major element data for sideromelane (Table 8) and palagonite (Table 9) are separated into three groups because Helgafell has two distinct geochemical populations. Within the three groups, sideromelane is geochemically homogeneous, whereas palagonite is heterogeneous. Major and trace element compositions (Tables 8 to 11) are from the same glass-palagonite

pairs, and normalized major element compositions for both are reported in Appendix B.2 and B.3. Major and trace element geochemistry data sets include the mean, standard deviation (std dev) and variance for each basalt type (Tables 8 to 11), with precision and accuracy for reference (List of Equations, pg. xvii). The low standard deviation for glass compositions from one locality shows all glasses are very similar. The chemical variation of glass approaches analytical error (precision). In contrast, palagonite compositions are highly variable at both localities (Table 9).

Two basalt types were found at Helgafell. Basalt 1 has higher SiO_2 (~49.47%) and lower FeO (~12.05%), MgO (~8.01%) and Na_2O (~1.70%) than basalt 2 (SiO_2 ~47.77%, FeO ~12.31%, MgO ~8.15% and Na_2O ~2.17%). Wells Gray's sideromelane has higher alkalis (~3.52% Na_2O and ~1.0% K_2O) compared to Helgafell's basalt 1 (~1.70% Na_2O and ~0.22% K_2O) or basalt 2 (~2.17% Na_2O and ~0.23% K_2O).

An estimate of variation due to precision errors (Appendix A.1) shows that sideromelane from Helgafell is homogenous, since standard deviation < precision error in almost all cases (Table 12). Homogeneity of sideromelane from Wells Gray is less clear since standard deviation > precision error for Al and Na (could be plagioclase), and Fe and Mg (could be olivine). Palagonite is heterogeneous: the standard deviation > precision error in virtually all cases. This verifies the homogeneity of sideromelane, heterogeneity of palagonite, and that the process for the formation of palagonite is not uniform.

Table 12 Estimate of variation due to precision errors for sideromelane glass (G) and palagonite (P).

Analysis No.	G/P	SiO ₂	TiO ₂	Al ₂ O ₃	FeO	MnO	MgO	CaO	Na ₂ O	K ₂ O	P ₂ O ₅	F	Cl	H ₂ O	Total
Precision %: [(Std Dev/Mean)*100]		1.227	1.815	0.837	1.632	32.381	1.116	1.456	2.994	3.205	58.934	32.055	37.049	n/a	n/a
Group 1 Basalt: Helgafell (Higher SiO₂)		0.01													
Mean	G	49.26	1.82	14.72	12.00	0.19	7.98	11.82	1.69	0.22	0.23	0.06	0.01	0.00	100.00
Std Dev	G	0.17	0.03	0.11	0.14	0.02	0.08	0.09	0.07	0.02	0.03	0.04	0.01	0.00	0.00
Est. of Variation due to precision errors	G	60.46	3.31	12.32	19.59	6.02	8.91	17.21	5.06	0.70	13.40	1.89	0.46	0.00	0.00
Group 2 Basalt: Helgafell (Lower SiO₂)															
Mean	G	47.87	1.82	14.95	12.33	0.18	8.17	11.95	2.17	0.23	0.23	0.07	0.02	0.00	100.00
Std Dev	G	0.20	0.04	0.15	0.12	0.03	0.09	0.12	0.06	0.02	0.02	0.07	0.01	0.00	0.00
Est. of Variation due to precision errors	G	58.75	3.31	12.51	20.13	5.81	9.12	17.40	6.51	0.73	13.78	2.19	0.74	0.00	0.00
Group 3 Basalt: Wells Gray															
Mean	G	49.35	2.21	15.00	11.81	0.16	5.93	10.44	3.53	1.00	0.44	0.09	0.05	0.00	100.00
Std Dev	G	0.40	0.06	0.30	0.23	0.04	0.15	0.12	0.24	0.05	0.04	0.08	0.01	0.00	0.00
Est. of Variation due to precision errors	G	60.57	4.01	12.55	19.27	5.22	6.62	15.20	10.56	3.22	25.68	2.97	1.67	0.00	0.00
Group 1 Basalt: Helgafell (Higher SiO₂)															
Mean	P	27.47	1.49	6.91	12.69	0.08	4.65	3.57	0.05	0.19	0.08	0.06	0.09	42.67	100.00
Std Dev	P	5.91	1.02	2.30	1.16	0.04	1.43	2.06	0.06	0.10	0.03	0.05	0.05	9.83	0.00
Est. of Variation due to precision errors	P	33.72	2.71	5.78	20.72	2.64	5.19	5.19	0.14	0.60	4.62	1.84	3.33	96.70	0.00
Group 2 Basalt: Helgafell (Lower SiO₂)															
Mean	P	42.07	2.04	12.64	11.53	0.11	5.68	5.13	0.16	0.18	0.08	0.04	0.08	20.27	100.00
Std Dev	P	5.57	0.59	2.13	0.89	0.04	1.40	1.74	0.12	0.06	0.05	0.05	0.05	6.44	0.00
Est. of Variation due to precision errors	P	51.63	3.71	10.58	18.81	3.50	6.34	7.46	0.47	0.57	4.55	1.43	2.83	41.44	0.00
Group 3 Basalt: Wells Gray															
Mean	P	45.42	2.11	14.35	13.52	0.05	2.73	1.50	0.56	1.31	0.12	0.04	0.15	18.14	100.00
Std Dev	P	4.46	1.16	2.48	2.86	0.05	1.29	0.60	0.48	0.43	0.03	0.05	0.16	7.63	0.00
Est. of Variation due to precision errors	P	55.75	3.83	12.01	22.06	1.69	3.05	2.19	1.67	4.18	7.27	1.43	5.54	58.29	0.00

5.2.1 Water in Palagonite

A preliminary look at the water content in palagonite, as estimated from low microprobe totals, shows that the average water for each sample ranges from ~ 15 to 44 weight percent (Figure 41). Helgafell palagonite has higher apparent water concentrations (especially basalt 1 samples: 03-2 and 11-2) than Wells Gray palagonite.

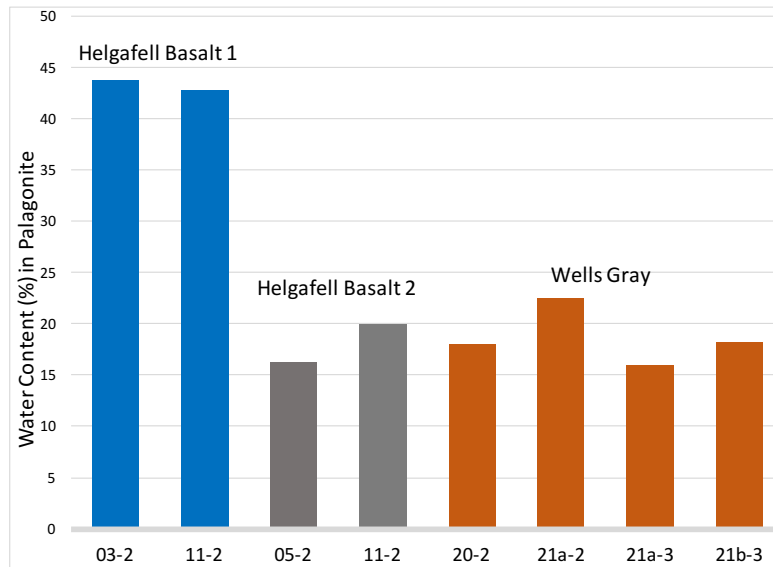


Figure 41 Average estimated water content of palagonite from Helgafell (HG) and from Wells Gray (WG).

5.2.2 Geochemical Variation

Based on differences in major elements, sideromelane can be divided into two tholeiitic types at Helgafell and alkali olivine basaltic magma composition at Wells Gray, but total chemical variation (eg. range in SiO_2) is similar for both localities (Figure 42). Lower alkalis ($\text{Na}_2\text{O} + \text{K}_2\text{O}$) and higher Mg and Fe are found at Helgafell than at Wells Gray. Helgafell's two basalt compositions are similar in TiO_2 , Al_2O_3 , CaO and K_2O but differ slightly in SiO_2 , FeO, MgO and Na_2O . Therefore, even though this study is a comparison of two locations, it more accurately is a comparison of palagonitization of three different sideromelane compositions.

Phenocrysts in sideromelane grains were analyzed by SEM-EDS to compare the An-content of plagioclase and Fo-content of olivine. Plagioclase averages $\text{An}_{63.6}$ in Wells Gray and $\text{An}_{69.9}$ in Helgafell, whereas olivine averages $\text{Fo}_{81.4}$ in Wells Gray and $\text{Fo}_{83.0}$ in Helgafell.

The mean values of trace elements in sideromelane do not vary substantially between the two basalts at Helgafell (Table 10). Sideromelane at Helgafell has higher concentrations of lighter trace elements (Sc to Cu), and Wells Gray's sideromelane is higher in some heavier elements (Zn to U, except Tm and Yb). Palagonite is trace element-rich in Wells Gray compared to Helgafell, with only Sc higher in Helgafell (Table 11). Rb was generally only

detected in Wells Gray samples. Most trace elements (Cu to U) are higher in Wells Gray, except V, Ni, Y, Gd and Er, which are variable. Chromium and Co are the same at Helgafell.

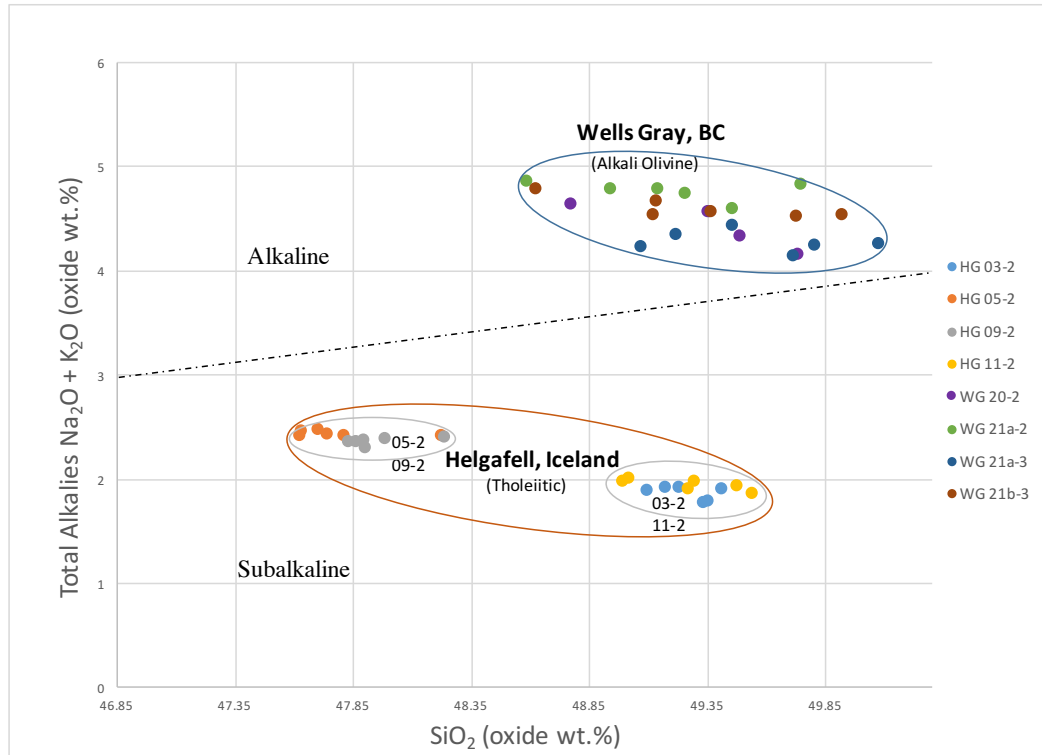


Figure 42 Total alkalis-silica diagram showing sideromelane from Helgafell and Wells Gray. (Alkaline-subalkaline dividing line from Kuno, 1966).

Nb/Y and Zr/TiO₂ ratios are higher in Wells Gray relative to Helgafell, and the two basaltic compositions at Helgafell are chemically distinct (Figure 43).

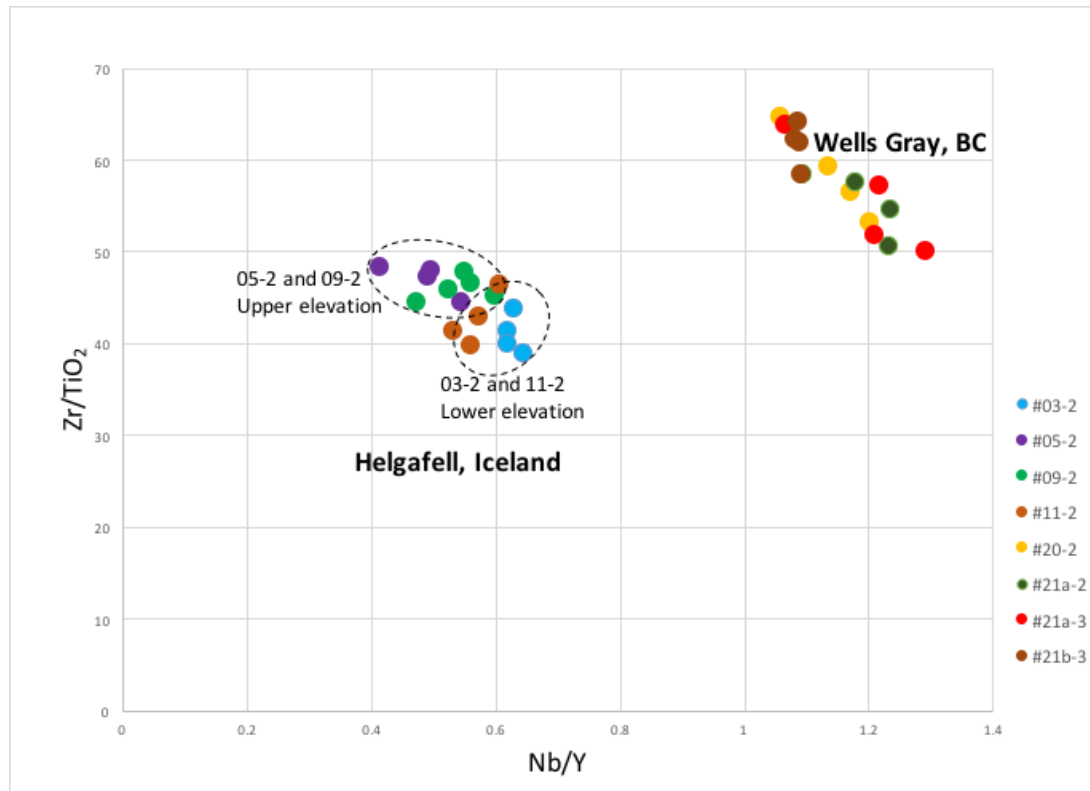


Figure 43 Nb/Y vs. Zr/TiO₂ diagram of sideromelane at Helgafell and Wells Gray.

The SiO₂ and FeO concentrations of palagonite (Figure 44) are highly variable at both locations, but Helgafell palagonite tends to vary more in SiO₂ and Wells Gray palagonite tends to vary more in FeO (Figure 44). Wells Gray glass is slightly lower in FeO and higher in SiO₂ than Helgafell's glass.

Concentrations of TiO₂ in palagonite are variable at both locations (Figure 45). Two low SiO₂ Wells Gray palagonite analyses plot with Helgafell palagonite.

At both locations, SiO₂/TiO₂ and FeO/TiO₂ ratios in palagonite form linear arrays (Figure 46). Hand-drawn dashed lines emphasize that there may be two populations of palagonite at Helgafell (Figure 46).

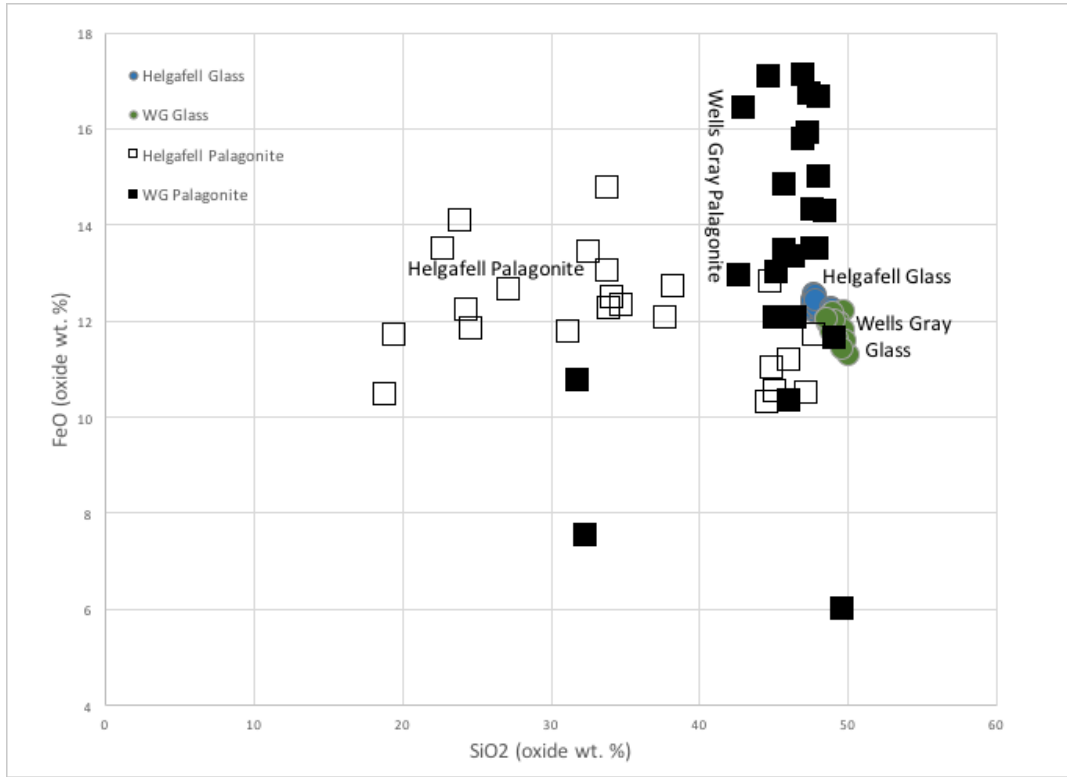


Figure 44 Helgafell vs. Wells Gray SiO_2 vs. FeO chemical variation diagram for glass and palagonite.

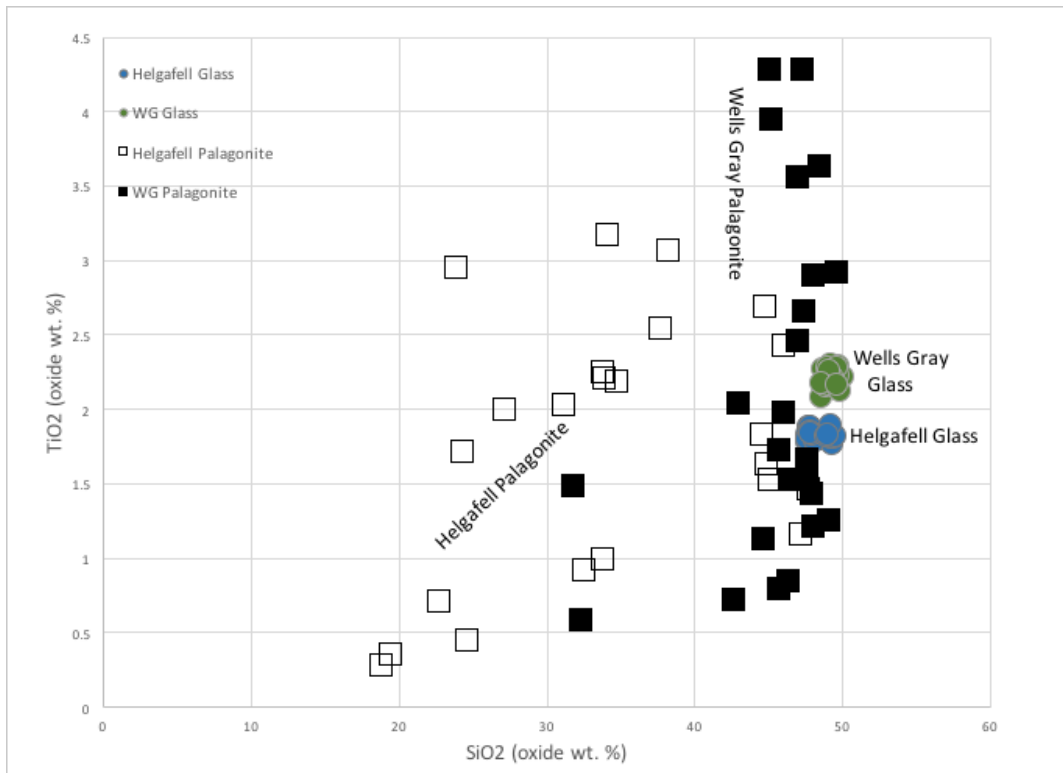


Figure 45 Helgafell vs. Wells Gray SiO_2 vs. TiO_2 chemical variation diagram for glass and palagonite.

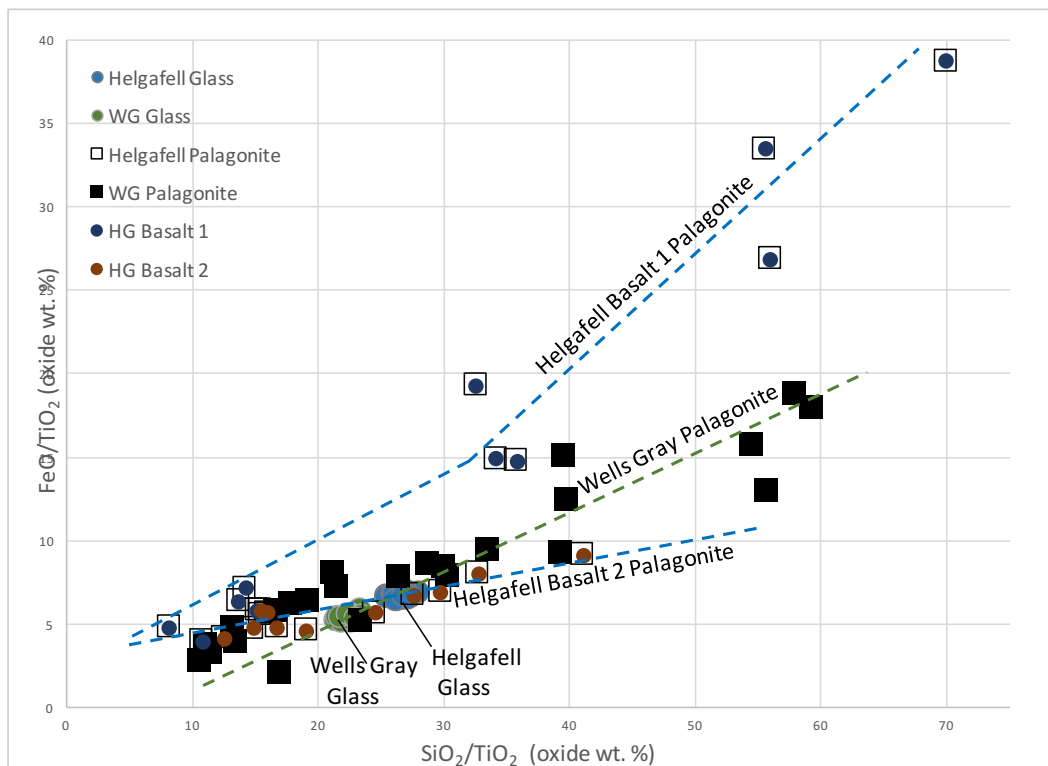


Figure 46 Helgafell vs. Wells Gray $\text{SiO}_2/\text{TiO}_2$ vs. FeO/TiO_2 diagram for glass and palagonite.

Helgafell sideromelane and palagonite tend to have lower Al_2O_3 than Wells Gray (Figure 47). At each location one sample has distinctly high-Al palagonite relative to the other samples; #05-2 in Helgafell and #20-2 in Wells Gray.

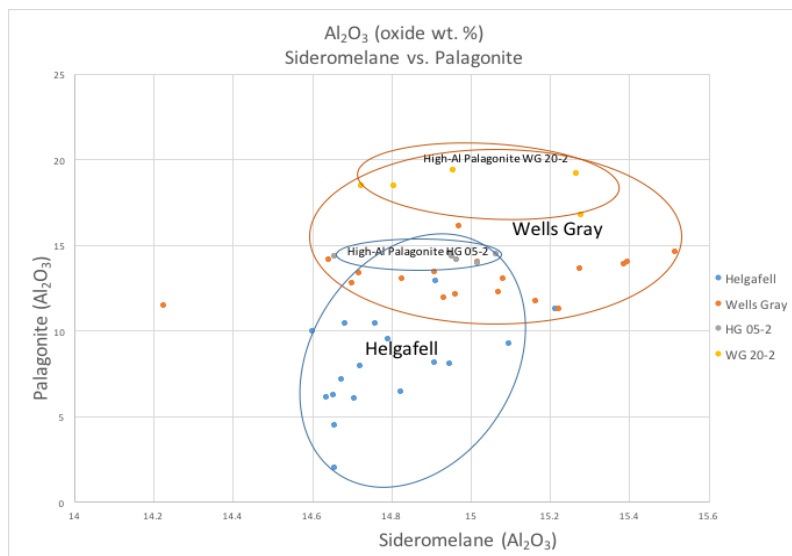


Figure 47 Al_2O_3 diagram for sideromelane vs. palagonite at Helgafell and Wells Gray.

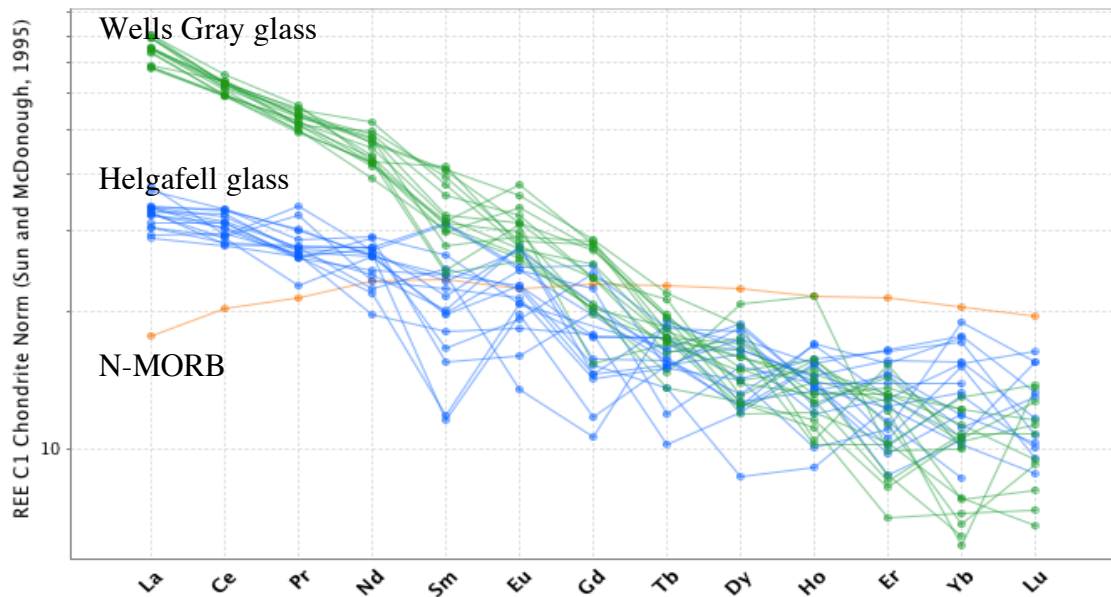


Figure 48 Chondrite-normalized Helgafell (blue) and Wells Gray (green) sideromelane. N-MORB (orange) line from Gale et al. (2013). Chondrite normalizing values from Sun and McDonough, (1995).

Helgafell glass shows depletion in LREEs and higher HREEs relative to Wells Gray. For reference, average N-MORB shows lower LREE than for Helgafell even though Helgafell is considered part of the mid-Atlantic ocean ridge (Figure 48).

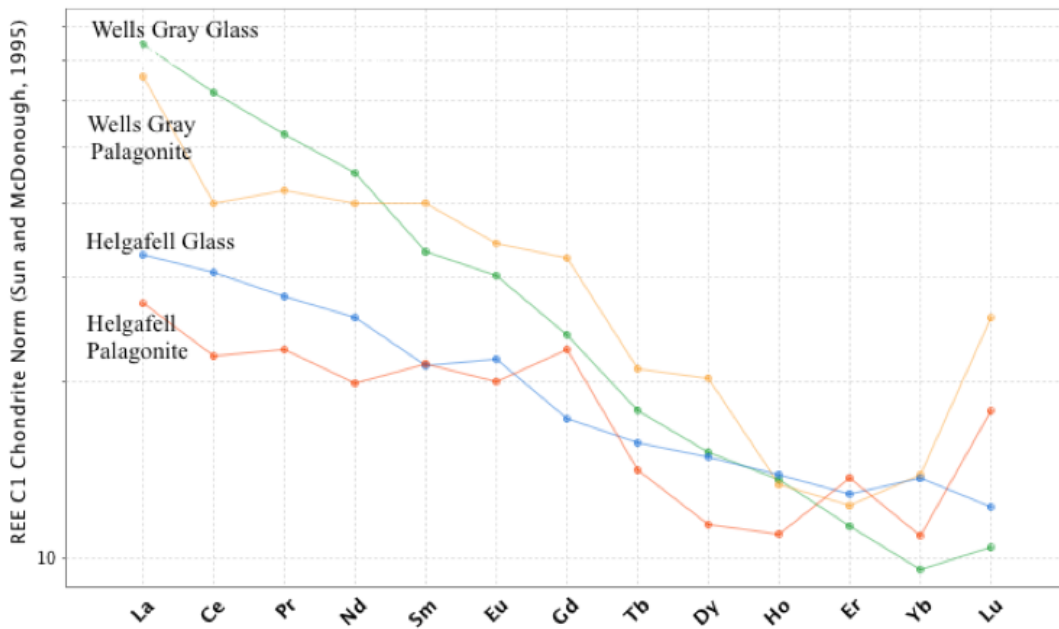


Figure 49 Chondrite-normalized REE's in glass and palagonite from Helgafell and Wells Gray. (Rock/C1 Chondrite from Sun and McDonough, 1995).

REEs in glass and palagonite from each location show overall similar slopes on chondrite normalized diagrams (Figures 48 and 49). But at Wells Gray, palagonite is enriched in the middle REE's (Sm to Dy) and depleted in the lighter REE's (La to Nd) relative to glass (Figure 49). At Helgafell, palagonite is more variable and enriched only in four HREE's (Gd, Er, Yb and Lu) and depleted in most lighter REE's (La to Nd), relative to glass. Generally, LREE's (La to Nd) are lower in palagonite at both localities, but HREE behaviour differs between the locations (Figure 49).

Wells Gray has a higher Nb/Y (Figure 50) ratio than that found at Helgafell. Proxies for % melting (Nb/Y; Figure 50), depth of melting (SiO_2 ; Figure 50) (Greenough & Ya'acoby, 2013), and extent of differentiation (Mg number; Figure 51) (Best, 2003, their pp. 300; Finney et al., 2008) are used in the discussion to assess the petrogenetic implications of two basalt types at Helgafell.

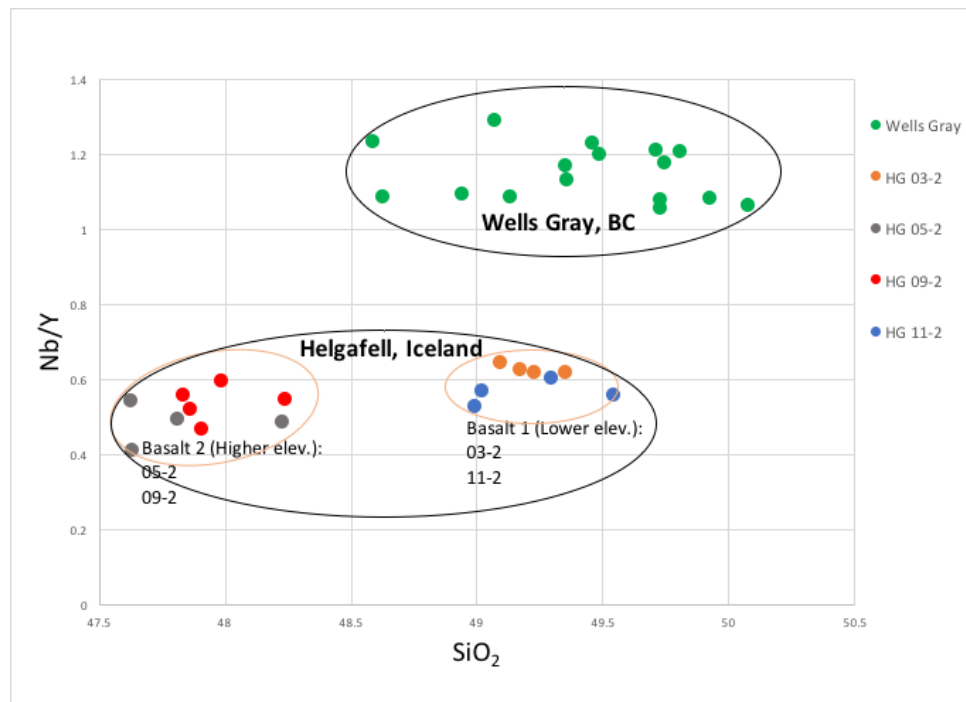


Figure 50 Concentration of SiO_2 plotted against Nb/Y in sideromelane.

At Helgafell, the Mg# ($\text{Mg}/(\text{Mg} + 0.9\text{Fe})$; in mole percent) remains constant while SiO_2 changes (Figure 51).

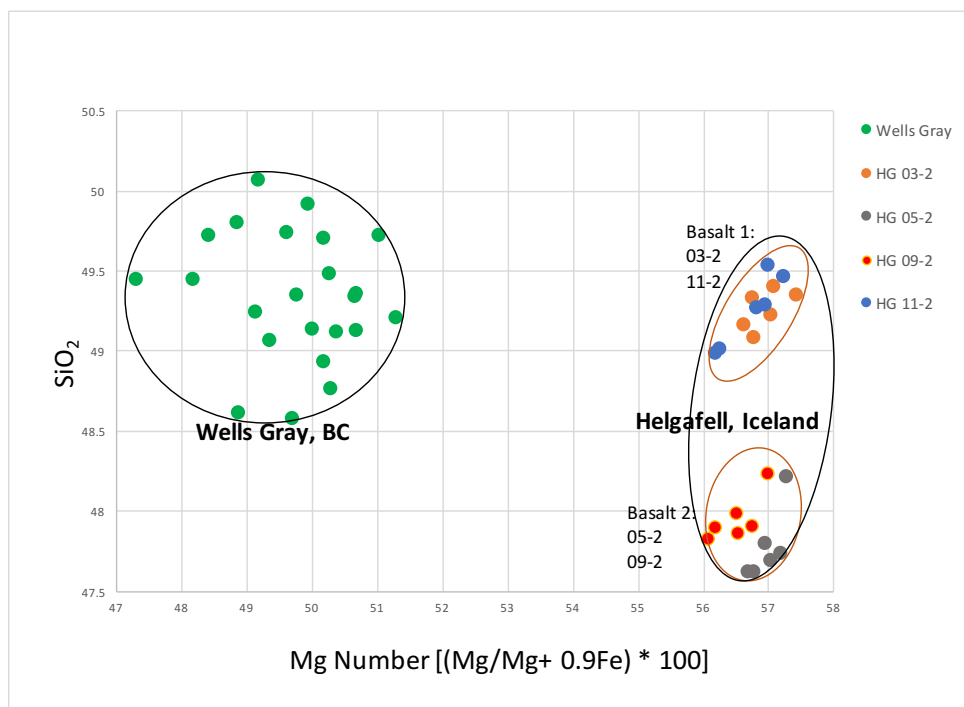


Figure 51 Concentration of SiO₂ versus Mg# in sideromelane.

5.2.3 Multi-Dimensional Scaling (MDS) Statistics

Although multi-dimensional scaling (MDS) does not provide direct information on processes or causes for observed patterns, it is an effective tool to show important relationships (similarities and differences) within geochemical data (Greenough & MacKenzie, 2015; Greenough & Ya-acoby, 2013). A two dimensional MDS plot shows the unique geochemical relationship between sideromelane and palagonite. Helgafell's glass and palagonite separate geochemically in a different dimension from Wells Gray's glass and palagonite, illustrating three important points (Figure 52):

1. All Helgafell glass and palagonite analyses separate from Wells Gray analyses along dimension 1.
2. All palagonite analyses are separated from all glass analyses along dimension 2 indicating similarities in the palagonitization process between the two localities.
3. All glass analyses from one location are similar but palagonite shows far greater variability.

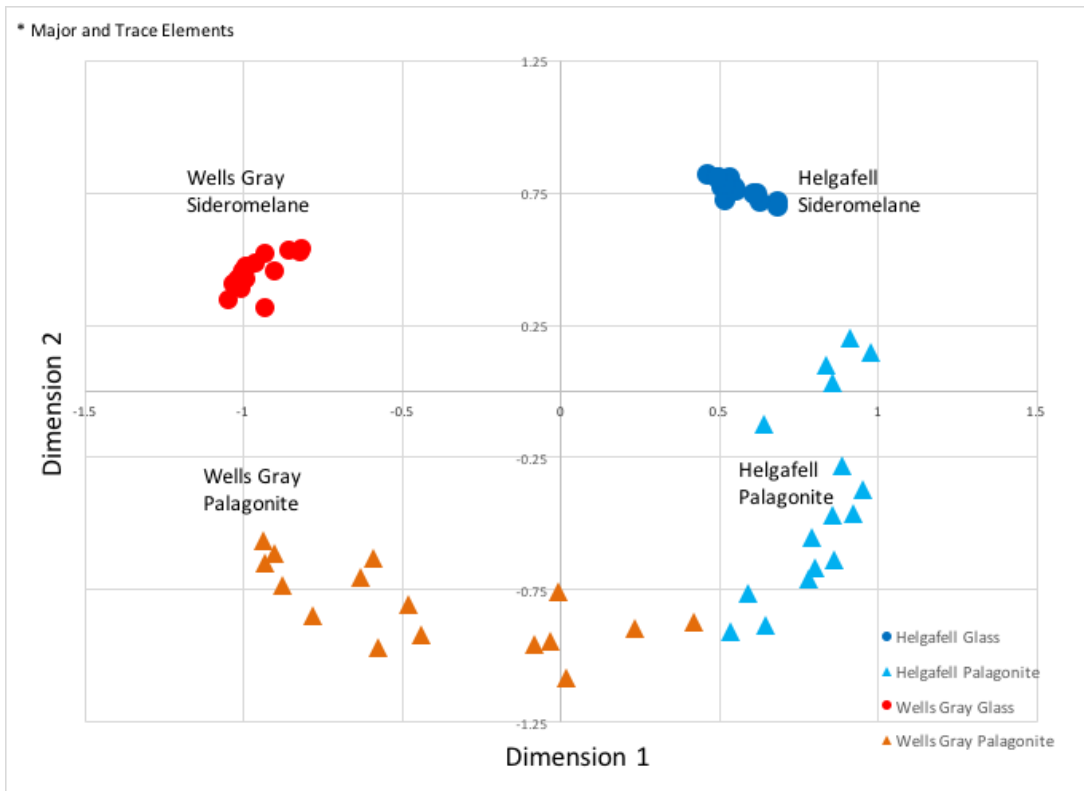


Figure 52 MDS plot of Helgafell (HG) and Wells Gray (WG) glass and palagonite illustrates the compositional relationship between palagonite and sideromelane, based on major (normalized; Appendices B.2, B.3) and trace element (Table 10 and 11) data.

A two dimensional MDS plot of major elements in sideromelane shows that dimension 1 separates sideromelane by locality (Helgafell vs. Wells Gray) and dimension 2 separates Helgafell's two basalts and shows the range of variability within glass from one locality (Figure 53), confirming what has previously been shown in several diagrams: Wells Gray is distinct from Helgafell's basalt 1 and 2.

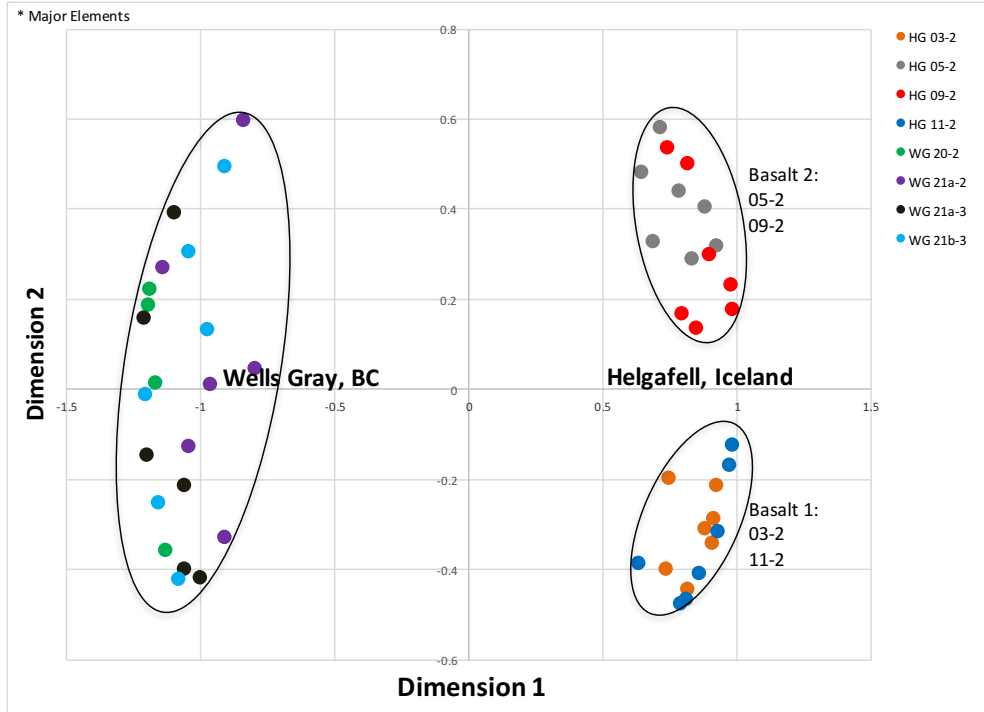


Figure 53 MDS plot of Helgafell (HG) and Wells Gray (WG) sideromelane based on major element data (normalized; Appendices B.2, B.3).

An MDS plot for Helgafell palagonite shows dimension 1 to generally separate basalt 1 and 2, and palagonite compositions relate to the sample from which they came (Figure 54).

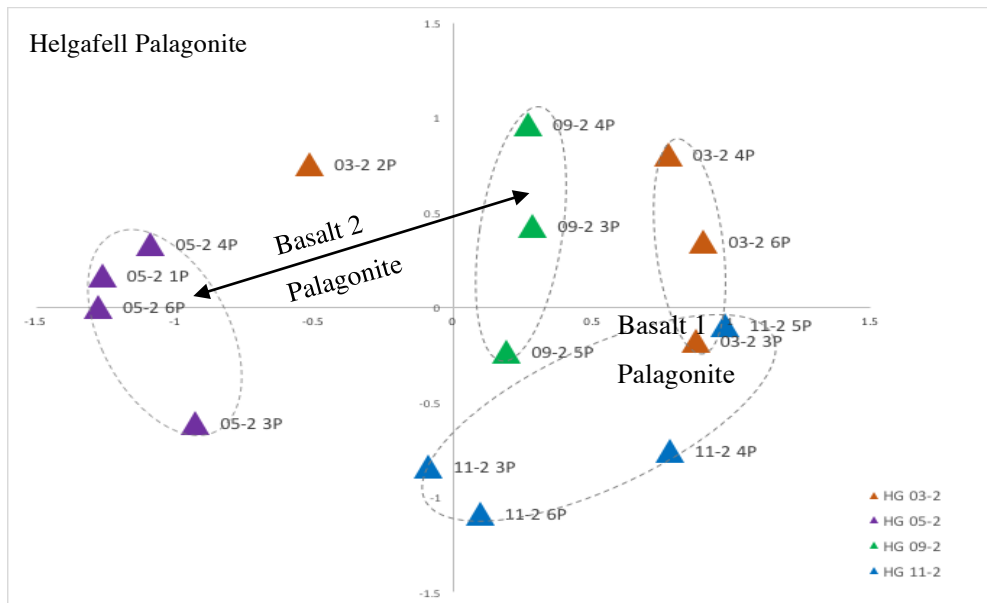


Figure 54 MDS plot of Helgafell palagonite based on major (normalized; Appendix B.3) and trace element (Table 11) data. Triangles: Basalt 1 (orange and blue); basalt 2 (purple and green).

The MDS plot for Wells Gray palagonite, based on major and trace element concentrations, shows strong clustering by sample, especially 20-2 (Figure 55).

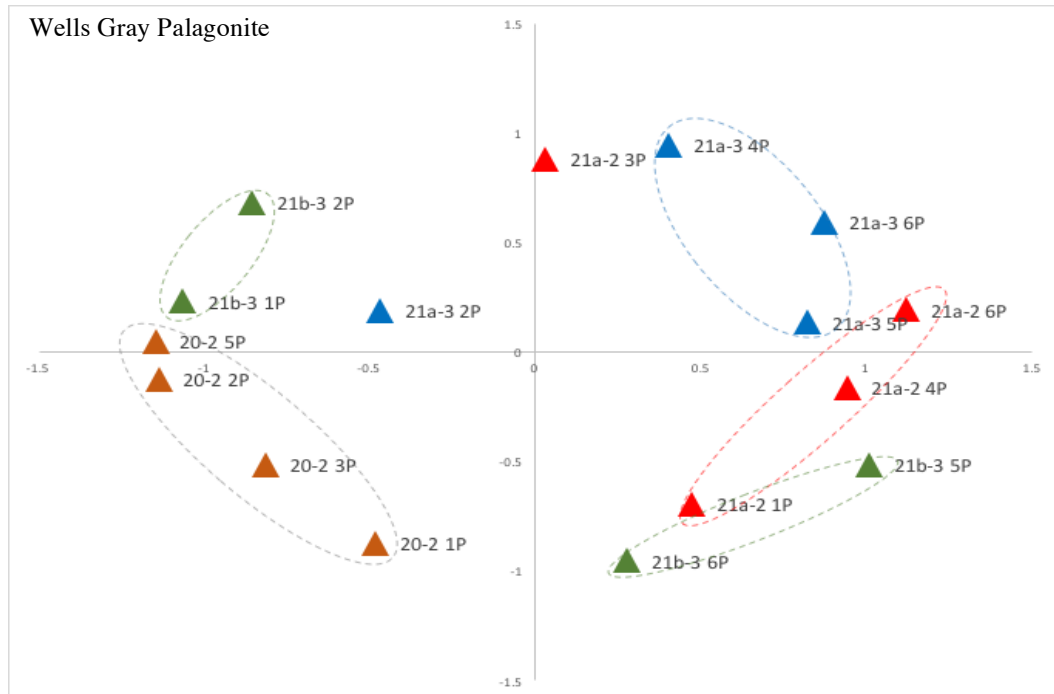


Figure 55 MDS plot of Wells Gray palagonite based on major (normalized; Appendix B.3) and trace element (Table 11) data.

MDS plots can also be used to develop an understanding of chemical controls on palagonite formation (Greenough et al., 2010; Greenough & MacKenzie, 2015; Greenough & Ya'acoby, 2013). All MDS diagrams comparing element behaviour (Figures 56 to 58) show that, when detected, water-soluble elements (e.g. Na, Mn, K, Cl, Cu, P and Rb) associate with water on the negative quadrants of dimension 1, and are separate from insoluble elements that tend to be immobile (i.e. rare earth elements and high field strength elements) on the right side of dimension 1. Note that Rb is not detected in Helgafell sideromelane or palagonite.

In Wells Gray palagonite, REE's are mostly in the positive quadrant of dimension 1 and 2, and all major elements except Ca and Al are negative in dimension 1 (Figure 56). Note the association of Ca and Al, and grouping of Ca, Ba and Sr. Additionally, major elements

comprise a diagonal trend through the centre of the plot and some transition metals cluster together, such as Ni and Co, and Sc and Ti.

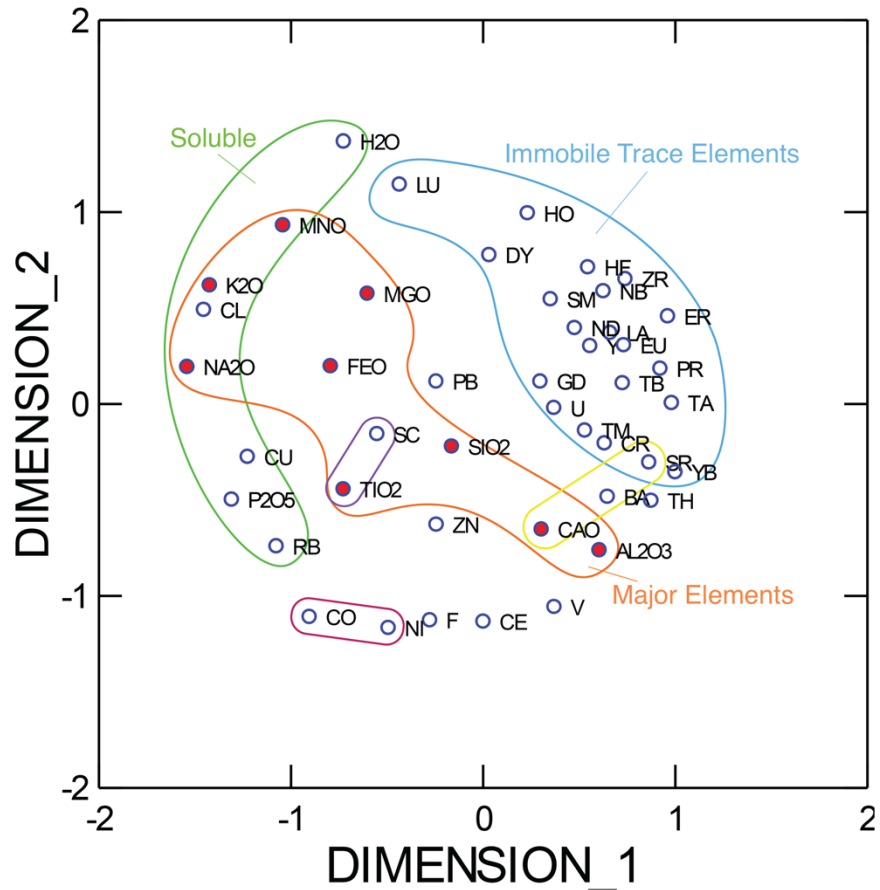


Figure 56 MDS plot comparing element behaviour in Wells Gray palagonite. Lines: Green = H₂O with soluble elements. Blue = immobile trace elements. Orange = array of major elements. Purple, yellow and pink lines = chemical associations. Based on major (Appendix B.3) and trace (Table 11) element data.

Element behaviour in Helgafell basalt 1 and 2 palagonite (Figures 57 and 58) shows on both plots that SiO₂, Al₂O₃, MgO and Ba consistently cluster together with immobile elements, but are separate from water-soluble elements. Similarly, both plots show associations between a) V and TiO₂, b) Nb and Ta, and c) Cr (Figure 57 and 58).

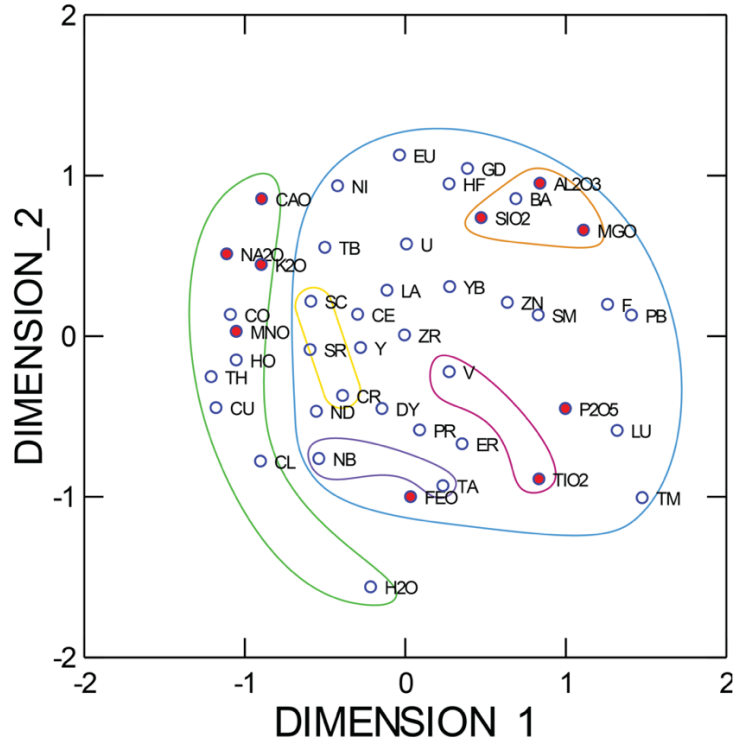


Figure 57 MDS plot comparing element behaviour in Helgafell's basalt 1 palagonite. Lines: Green = H₂O with soluble elements. Blue = immobile trace elements. Orange = SiO₂, MgO, Al₂O₃. Purple, pink and yellow = chemical associations. Based on major (Appendix B.3) and trace (Table 11) element data.

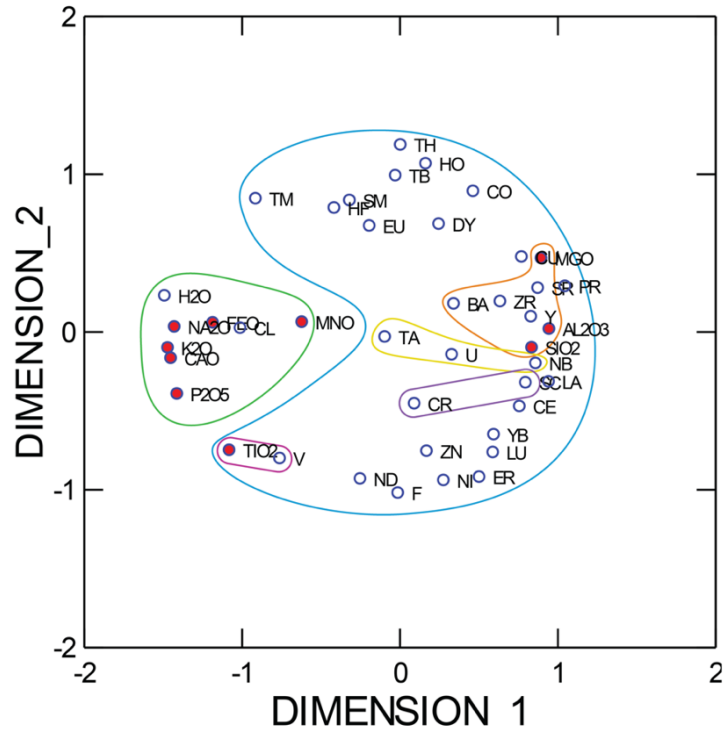


Figure 58 MDS plot comparing element behaviour in Helgafell's basalt 2 palagonite. Lines: Green = H₂O with soluble elements. Blue = immobile trace elements. Orange = SiO₂, MgO, Al₂O₃. Purple, pink and yellow = chemical associations. Based on major (Appendix B.3) and trace (Table 11) element data.

When palagonites from Helgafell and Wells Gray are compared using major element data alone (Figure 59), dimension 1 clearly segregates palagonite by locality (basalt composition). Dimension 2, on the other hand, generally organizes palagonite by water content (low water-content, $y \sim -1$ to 0 , to high water-content, $y \sim 0$ to 1). A microprobe analysis of pore-lining smectite from a tholeiitic basalt/glass HSDP drill core from Mauna Loa, Hawaii (Walton & Schriffman, 2003) plots with low- H_2O palagonite derived from Helgafell tholeiitic glass (Figure 59).

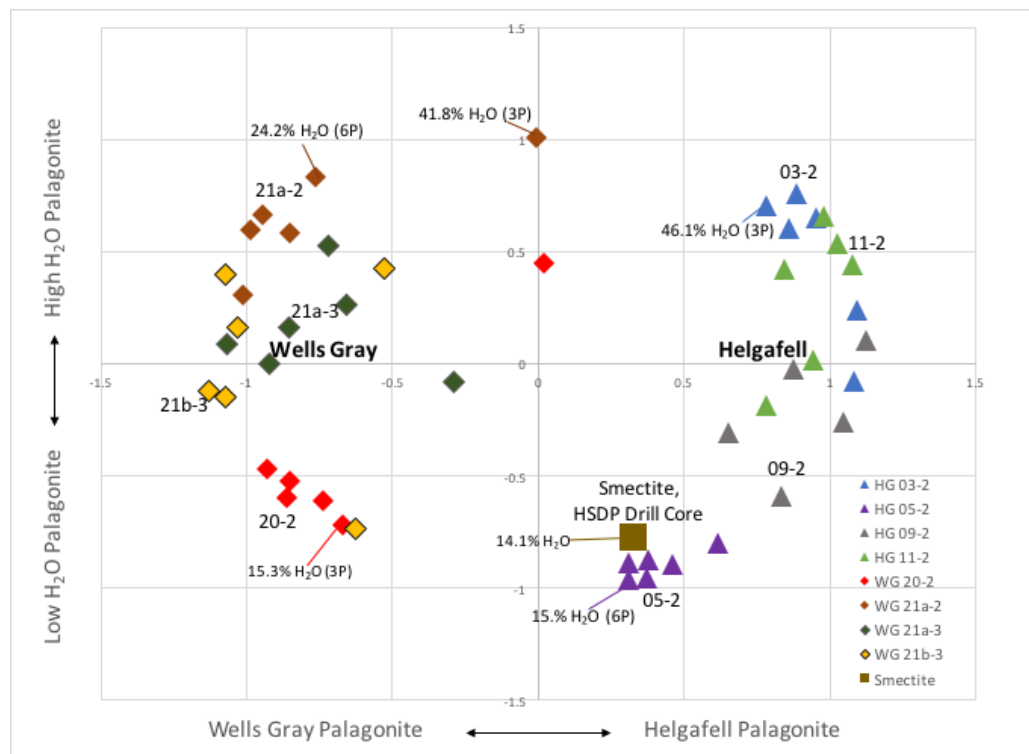


Figure 59 MDS plot of palagonite from Helgafell (tholeiitic) and Wells Gray (alkali olivine basalt), based on major (Appendix B.3) element data. A pore-lining smectite (microprobe) analysis from a tholeiitic Hawaiian basalt (HSDP Phase 1; Walton & Schiffman, 2003, Table 2, 1238 mbsl) included for comparison.

5.2.4 Microprobe Traverses and Element Maps

Microprobe traverses across sideromelane-palagonite boundaries illustrate similarities and differences in element behavior at Helgafell (Figure 60) and Wells Gray (Figure 61). In both traverses, FeO increases and Al₂O₃, CaO and MgO decrease in the palagonite rim relative to

sideromelane. Also, next to the pronounced glass-palagonite interfaces in both traverses, the innermost rim shows a spike in TiO_2 followed by a similar spike in MgO . The innermost rim has a noticeably different spherical texture in the Wells Gray traverse (Figure 61), with a material high in CaO attached to the outer edge of the rim.

The Helgafell traverse includes two palagonite rims (Figure 60), one beside a vesicle and the other on the glass grain's edge. Similarities include a decrease in SiO_2 , and presence of TiO_2 and MgO zones. However, the vesicle's palagonite rim shows matching oscillations in SiO_2 and Al_2O_3 , and MgO gradually increases towards the outer rim. Oscillations are absent in the palagonite rim at the edge of the glass grain.

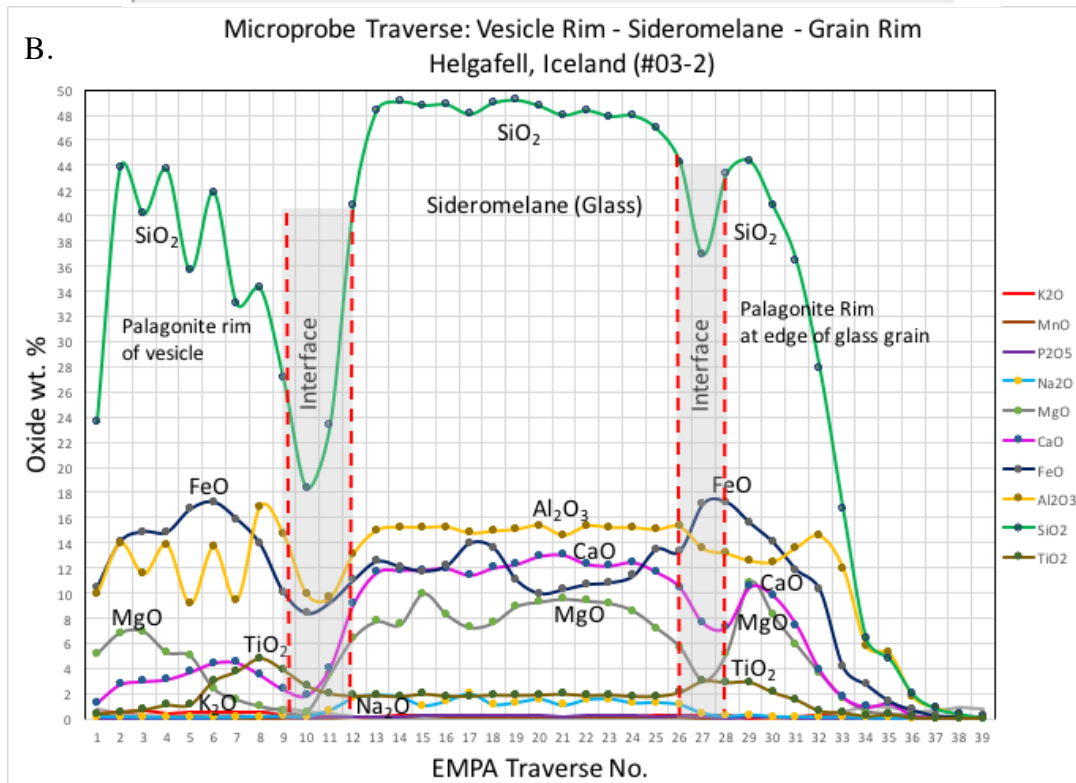
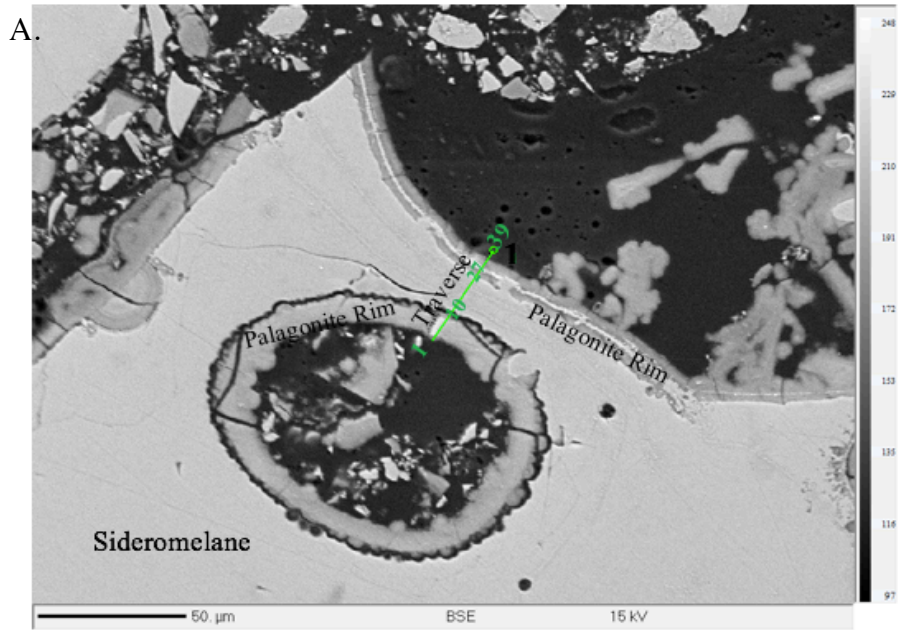


Figure 60 Helgafell microprobe traverse in sample #03-2. A) EMP backscatter image; B) Glass-palagonite traverse includes two palagonite rims, one in a vesicle and a second at the glass grain's edge. Distance between spot analyses $\sim 0.99 \mu\text{m}$. Total distance of traverse = $37.58 \mu\text{m}$. Data: Appendix B.4.

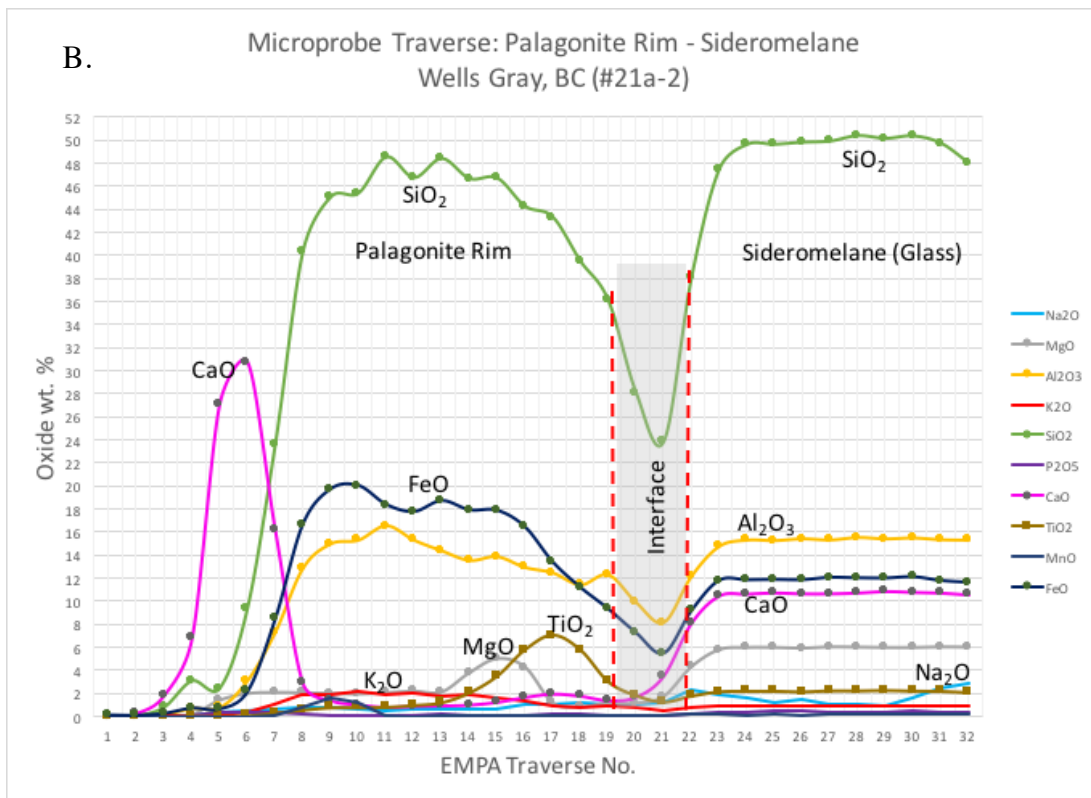
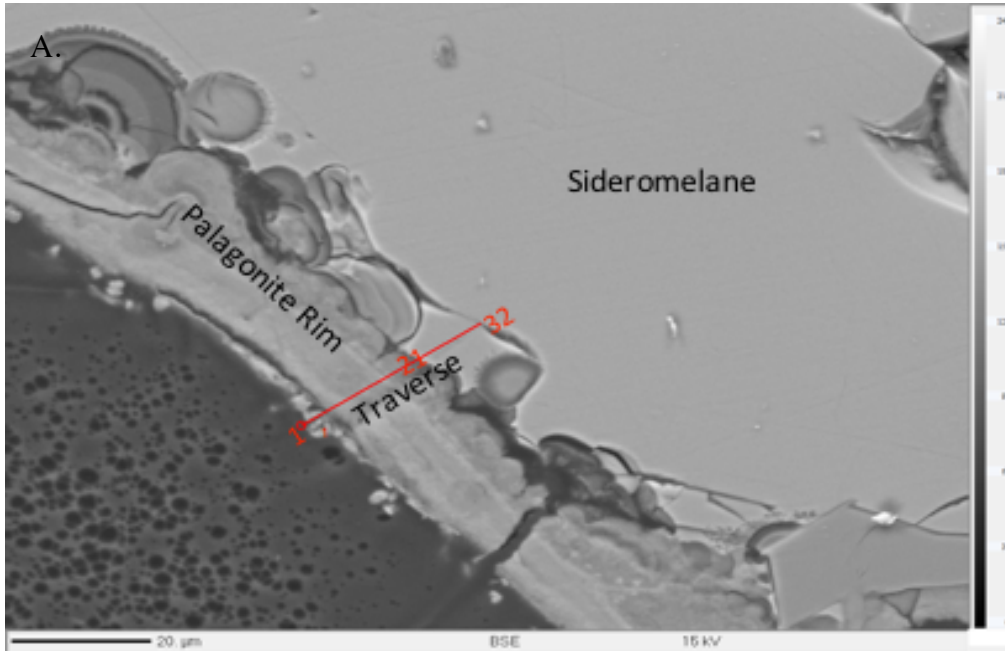


Figure 61 Wells Gray microprobe traverse across a glass-palagonite interface in sample #21a-2. A) EMP backscatter image; B) Glass-palagonite traverse reveals trends in element behaviour. A CaO-rich mineral occurs at the palagonite rim's outer edge. Distance between spot analyses $\sim 0.99 \mu\text{m}$. Total distance of traverse = $30.53 \mu\text{m}$. Data table: Appendix B.5.

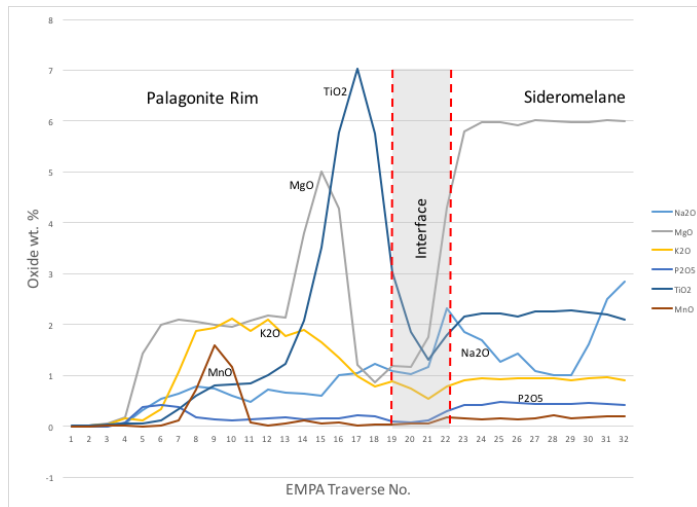


Figure 62 Same microprobe traverse as Figure 61 (Wells Gray sample #21a-2) except only showing minor element trends. Data table: Appendix B.5.

TiO₂, MgO, and MnO show prominent spikes that represent enrichment zones (Figure 62). K₂O increases whereas Na₂O and P₂O₅ decrease in the outer half of the palagonite rim. Sodium concentrations are variable at the sideromelane's outer edge and decrease across the interface and palagonite rim.

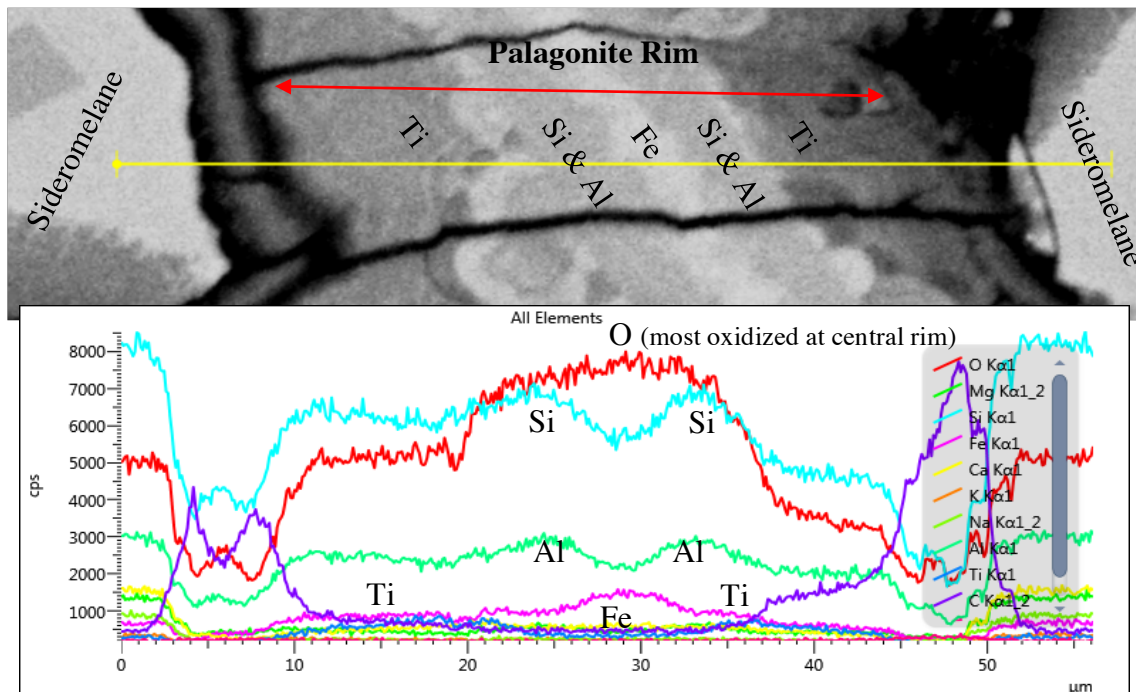


Figure 63 A SEM line scan across a palagonite rim between two glass grains reveals geochemical and textural zones symmetrical from the centre. The central zone is O- (red) and Fe-rich (pink), followed by a Si- and Al-rich (blue and green) zone on either side, and a Ti-rich zone at the glass-palagonite interface. The accompanied backscatter image (A.) is labelled to reflect this zoning. Thin section carbon-coating (C; purple line) can be disregarded. Wells Gray #28-2.

A SEM line scan across a palagonite rim between two glass grains in Wells Gray sample #28-2, shows symmetry with a central Fe-rich zone between Si- and Al-rich zones and Ti-rich zones (Figure 63). Similar to the microprobe traverses (Figures 60 and 61), the Ti-rich zone lies next to the glass-palagonite interface (Figure 63). SiO₂ and Al₂O₃ behave in unison on either side of the O- and Fe-rich central zone farthest from the glass-palagonite interface.

A SEM element map (Figure 64) from a Helgafell sample shows element behaviour in palagonite rims. Mg (yellow) is concentrated at the outer edge of the palagonite rim, which matches its behaviour in a microprobe traverse (Figure 60). No striking change occurs in Al and Ti (green), Si (blue) or Fe (orange). Ca (pink) almost completely disappears in the palagonite rims but it is very oxygen-rich (bright green) (Figure 64).

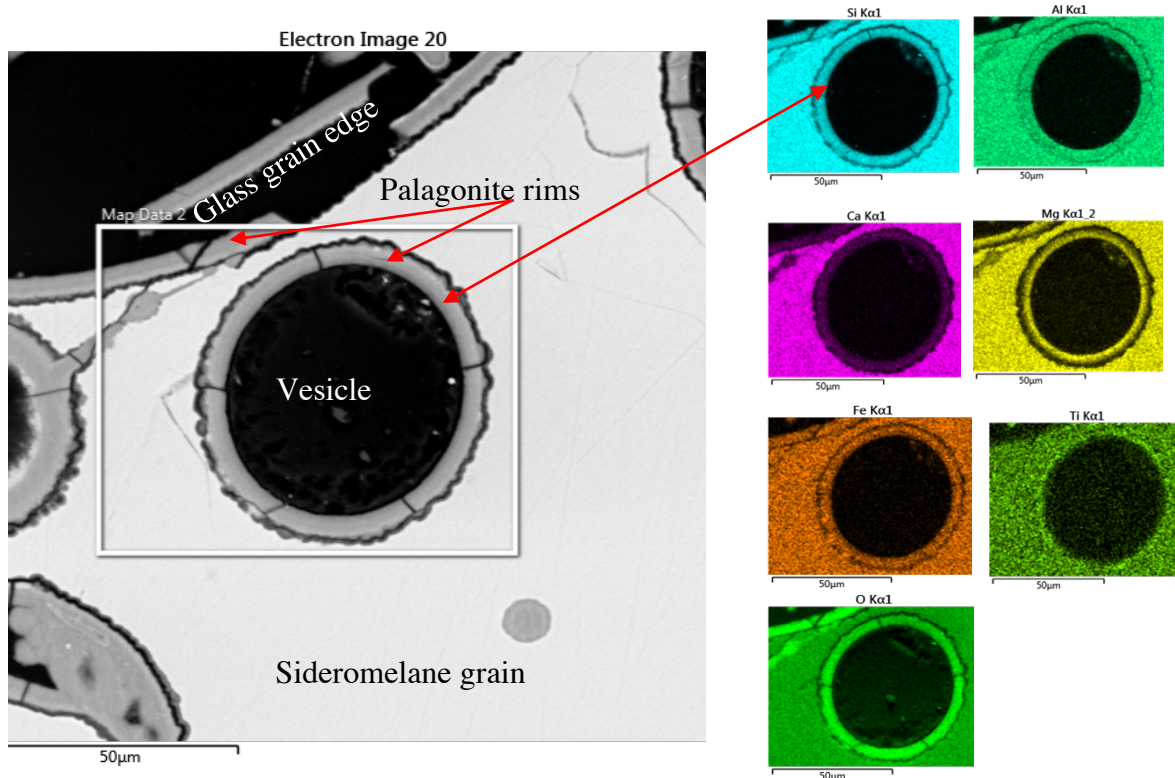


Figure 64 Element maps (images on right) of a sideromelane grain with palagonite rims on the grain's edge and in a vesicle. Helgafell #11-2 (SEM backscatter image).

5.2.5 Mass Balance Calculations

Mass balance calculations were completed in order to understand similarities and differences between palagonite formation in the three different glasses. Grant (1986) used the Gresens' isocon method for mass balance calculations. Here, eight elements (Sc, Y, Zr, Nb,

La, Nd, Ta, Th) thought to be immobile in glass were used to calculate an isocon regression line. These elements were tested to insure that they were relatively immobile (Figure 65). Error bars on the ratio plots (Appendix B.6) were calculated using the formula from Ragland (1989):

$$q = Q * \sqrt{\left(\frac{a}{A}\right)^2 + \left(\frac{b}{B}\right)^2}$$

where q = ratio error; Q = ratio value; a = numerator error; A = numerator value, b = denominator error, and B = denominator value.

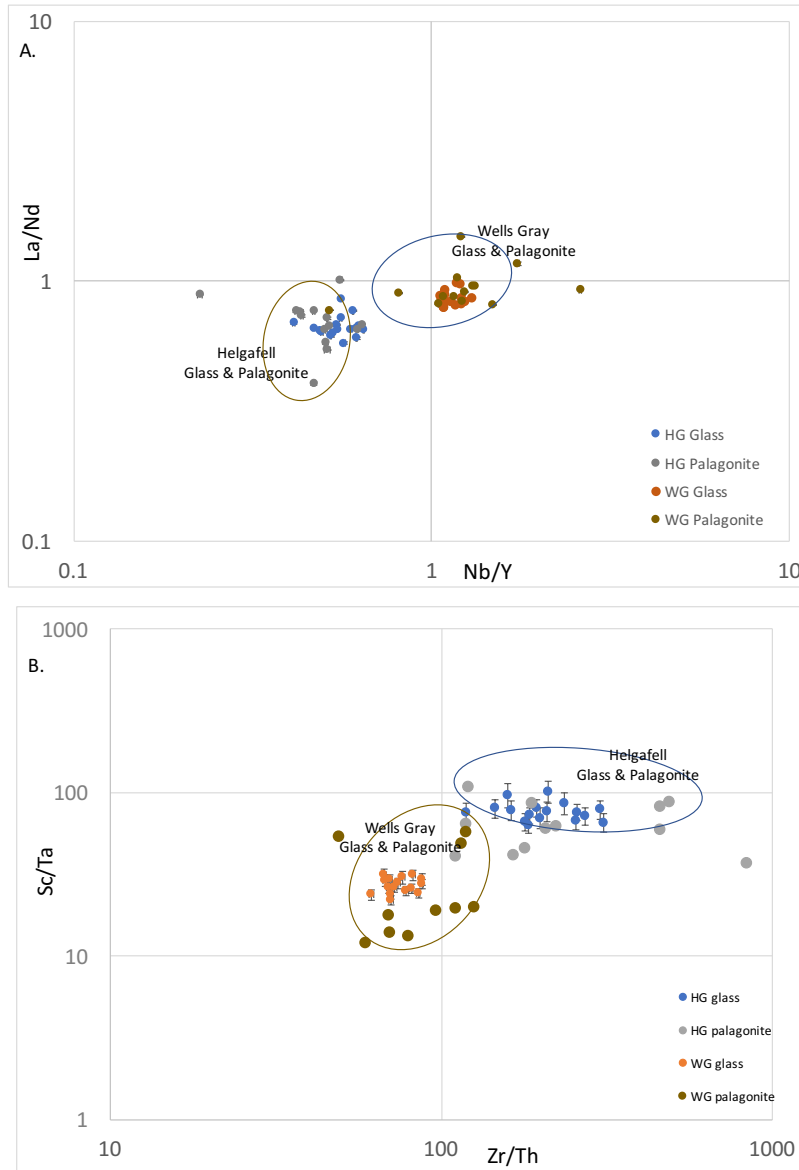


Figure 65 Log-ratio plots of A) Nb/Y vs. La/Nd and B) Zr/Th vs. Sc/Ta show Helgafell (HG) and Wells Gray (WG) glass and palagonite to generally overlap one another indicating the tendency to be immobile elements for isocon diagrams: Sc, Y, Zr, Nb, La, Nd, Ta, Th. Error bars based on precision in ratio calculations (Appendix B.6) from Ragland (1989).

Two different data sets were prepared (Table 5). Mass balance results on each glass-palagonite pair presented herein are calculated using the conventional data set 1 in Appendix B.2 (sideromelane normalized as anhydrous) and Appendix B.3 (hydrous palagonite, water assumed to be the missing component in low EMP totals). Mass balance results comparing both data set assumptions (Table 5) on each glass-palagonite pair are shown in Appendix B.8 and B.9.

Mass balance calculations for palagonitization are summarized for major (Table 13) and trace (Table 14) elements at Helgafell and Wells Gray and give:

1. the slope on the regression line (isocon) through the eight elements (Sc, Y, Zr, Nb, La, Nd, Ta, Th) shown to be immobile for each glass-palagonite pair; and
2. percent mass gain or loss calculated from Gresens' equation 5 (4.4.2; pg. 48).

Helgafell's basalt 1 (especially #03-2) shows greater mass loss for most elements than basalt 2 (#05-2 and #09-2) (Tables 13 and 14). Wells Gray shows highly variable SiO_2 and Al_2O_3 behaviour (large standard deviation on average percentage loss/gain) and CaO rather consistently had large losses (Table 13). Consistently, there is a mass loss in Na_2O , P_2O_5 and CaO throughout all samples.

Table 13 Mass balance calculations for Helgafell and Wells Gray major elements include average percent mass transfer during palagonitization. Gresens' isocon diagrams provided slopes (isocons) from regression of 8 immobile elements (Sc, Y, Zr, Nb, La, Nd, Ta, Th) for each glass-palagonite pair (analysis pair).

Analysis Pair	Slope (Isocon)	SiO ₂	TiO ₂	Al ₂ O ₃	FeO	MnO	MgO	CaO	Na ₂ O	K ₂ O	P ₂ O ₅	F	Cl
Helgafell Basalt 1:													
03-2 2P	1.0932	-37.2	-51.5	-60.4	13.4	-44.0	-45.0	-80.0	-98.4	-1.0	-69.5		724.7
03-2 3P	0.8429	-42.2	91.8	-49.7	38.8	-40.6	-67.4	-59.9	-97.9	-32.9	-47.7	-52.5	671.9
03-2 4P	0.8795	-36.9	23.1	-38.8	20.2	1.7	-61.2	-34.7	-87.2	107.0	-58.4		1158.6
03-2 6P	0.9708	-29.2	28.8	-44.4	5.0	-42.7	-55.1	-30.2	-89.5	45.2	-62.9		466.9
	Average	-36.4	23.1	-48.3	19.3	-31.4	-57.2	-51.2	-93.2	29.6	-59.6	-52.5	755.5
	Std Dev	5.4	58.7	9.2	14.4	22.1	9.6	23.2	5.7	60.8	9.1	n/a	290.8
11-2 3P	0.7874	-13.2	56.5	-38.0	40.0	-68.0	-23.9	-56.7		-59.3	-42.5	123.7	27.8
11-2 4P	0.6377	3.7	-24.2	7.2	76.3	-33.7	19.8	-61.9	-99.1	21.6	-11.9	57.3	372.0
11-2 5P	0.5280	-5.9	78.2	-22.0	89.0	-63.7	0.6	-32.6	-93.6	-0.1	-28.5	19.2	
11-2 6P	0.8109	-14.1	113.3	-12.4	25.9	-70.8	-31.8	-64.1	-98.6	-24.4	-62.2	148.4	645.2
	Average	-7.4	55.9	-16.3	57.8	-59.1	-8.8	-53.8	-97.1	-15.6	-36.3	87.2	348.4
	Std Dev	8.2	58.4	18.9	29.7	17.1	23.5	14.5	3.0	34.7	21.3	59.4	309.4
Helgafell Basalt 2:													
05-2 1P	1.1724	-15.5	-30.3	-16.7	-18.6	-29.6	-18.8	-76.1	-99.2	-74.0		-87.8	71.0
05-2 3P	0.8999	7.2	52.1	3.0	1.7	-51.1	-24.8	-56.3	-95.5	-17.5	-70.4	17.3	
05-2 4P	0.8903	5.2	15.2	8.0	-6.8	63.7	-15.7	-63.7	-94.5	-23.6	-74.5		236.0
05-2 6P	0.9486	4.5	-32.5	-0.3	-10.9	-65.2	-1.2	-69.8		-34.0			
	Average	0.4	1.1	-1.5	-8.6	-20.6	-15.1	-66.5	-96.4	-37.3	-72.5	-35.2	153.5
	Std Dev	10.6	40.5	10.7	8.4	58.0	10.0	8.5	2.5	25.4	2.9	74.3	116.7
09-2 3P	0.7339	-11.0	46.4	-16.9	30.4	-25.8	-22.0	-24.8	-86.6	8.5	-34.2		448.1
09-2 4P	0.8570	-15.5	39.5	-13.5	17.0	8.1	-24.3	-32.4	-83.1	-2.2	-36.0		482.1
09-2 5P	0.8365	-5.8	64.2	-23.3	15.1	-57.9	-52.7	-31.7	-83.3	14.8	-28.9	20.3	1944.5
	Average	-10.8	50.0	-17.9	20.8	-25.2	-33.0	-29.6	-84.3	7.0	-33.0	20.3	958.2
	Std Dev	4.8	12.8	5.0	8.3	33.0	17.1	4.2	2.0	8.6	3.7	n/a	854.3
	Overall Average:	-13.7	31.4	-21.2	22.4	-34.6	-28.2	-51.7	-92.8	-4.8	-48.3	30.7	604.1
	Overall Std Dev:	16.3	48.7	21.3	29.9	36.0	24.5	18.6	6.1	43.6	19.6	79.8	521.2
Wells Gray:													
20-2 1P	0.9965	-3.4	-25.4	25.0	20.2	-106.2	-65.1	-82.4	-99.7	-43.9	-66.4		-26.1
20-2 2P	1.7410	-44.2	-62.5	-27.9	-33.9	-86.8	-78.7	-88.9	-98.2	-41.7	-87.8	52.5	-31.4
20-2 3P	1.0221	-8.0	-33.8	26.5	-0.1	-73.8	-67.9	-81.9	-98.6	-5.8	-76.6	124.2	73.0
20-2 5P	1.6740	-42.7	-57.3	-25.2	-31.0	-96.7	-78.9	-89.1	-99.3	-43.6	-86.6		-69.9
	Average	-24.6	-44.7	-0.4	-11.2	-90.9	-72.6	-85.6	-98.9	-33.7	-79.3	88.4	-13.6
	Std Dev	21.9	18.0	30.2	25.9	13.8	7.2	4.0	0.7	18.7	10.0	50.7	60.9
21a-2 4P	0.9263	-2.5	-43.6	4.2	55.9	-74.3	-68.4	-88.8	-48.2	86.2	-43.4	-58.9	187.5
21a-2 6P	0.9386	-6.4	-63.0	-3.8	14.8	-28.5	-71.0	-90.1	-78.7	78.1	-63.3		758.6
21a-2 1P	1.0525	-10.5	-12.4	-11.4	-16.2	-106.0	-68.9	-81.0	-64.5	40.2	-79.0		521.0
21a-2 3P	1.1325	-42.6	-77.6	-29.0	-45.3	-2.6	-66.7	-93.3	-75.5	18.1	-80.5		1317.0
	Average	-15.5	-49.2	-10.0	2.3	-52.8	-68.7	-88.3	-66.7	55.6	-66.6	-58.9	696.0
	Std Dev	18.4	28.2	14.2	43.4	46.2	1.8	5.2	13.8	32.1	17.3	n/a	475.7
21a-3 2P	1.0835	-8.5	21.6	-25.2	-50.9	-84.7	-89.8	-90.4	-92.1	-32.4	-79.9		633.0
21a-3 4P	1.2204	-21.1	54.0	-36.7	7.2	-11.9	-22.9	-91.5	-89.1	27.3	-73.4		164.3
21a-3 5P	1.1760	-23.1	64.0	-32.1	-13.1	-88.7	-78.2	-90.4	-80.0	12.4	-78.7		219.0
21a-3 6P	0.9488	-0.4	65.2	-14.7	57.0	-33.3	-2.7	-90.7	-76.7	103.6	-73.2	4.9	46.8
	Average	-13.3	51.2	-27.2	0.1	-54.6	-48.4	-90.8	-84.5	27.7	-76.3	4.9	265.8
	Std Dev	10.7	20.4	9.6	44.9	38.1	42.2	0.5	7.3	56.6	3.5	n/a	255.1
21b-3 1P	1.2871	-26.7	-69.4	-29.3	-11.8	-94.4	-68.4	-87.3	-94.3	-3.3	-82.4	-100.0	238.5
21b-3 2P	1.2213	-21.2	-53.3	-29.1	6.3	-70.7	-58.6	-88.1	-93.5	10.3	-83.4	-87.2	3.7
21b-3 5P	0.7849	12.7	20.0	19.7	74.0	-85.8	-27.0	-78.8	-64.5	139.7	-43.6	-59.2	48.9
21b-3 6P	0.7442	32.8	-22.3	44.7	37.2	-81.9	-44.2	-64.3	-87.1	34.1	-69.9	1796.1	441.7
	Average	-0.6	-31.3	1.5	26.4	-83.2	-49.6	-79.6	-84.8	45.2	-69.8	387.4	183.2
	Std Dev	28.3	39.3	36.9	37.6	9.8	18.0	11.1	13.9	64.9	18.5	939.3	200.1
	Overall Average:	-13.5	-18.5	-9.0	4.4	-70.4	-59.8	-86.1	-83.7	23.7	-73.0	209.0	282.8
	Overall Std Dev:	20.6	48.88	25.51	37.39	32.84	23.66	7.18	15.06	55.12	13.36	645.8	372.4

The MDS analysis indicated the importance of water content in palagonite for controlling element concentrations in palagonite (Figure 59). Moreover, the average water content in palagonite can range from ~ 15.0 to 44.0 wt.% H₂O, resulting in high-H₂O palagonite and low-H₂O palagonite (Figure 41). To test for this apparent relationship, averaged results for the Gresens mass balance calculations were examined based on the four highest and four lowest water content palagonites at each locality. Elements were ordered from highest gain to greatest loss (Figures 66 to 69) based on the same order for Wells Gray low-H₂O palagonite.

Several patterns are evident in the mass balance bar graphs (Figures 66 to 69). In all cases, more elements show losses than gains. Elements significantly enriched (> 25%), most consistently, in all palagonite are Cu, Cl, Co, Ni, Yb, Rb and U, whereas significant losses (> 25%) typically occur for Na, Ca, Mg, P, V, Ce and Mn. Elements in palagonite that most consistently tend to show the lowest to moderate mass change are Zr, Pb, Er, Hf, Sc, Th, Si, Ti, Y, Al, Ho, Nb, Nd, Sm, La, and Cr. Similar to Wells Gray high-H₂O palagonite, from Er to Pr, thirteen elements show low to moderate losses and eight show low to modest gains in low-H₂O Wells Gray palagonite (Figure 66). Keeping in mind that major elements are most important as they will form secondary minerals, in each bar graph, Al₂O₃ and SiO₂ show similar low to moderate losses, and significant loss occurs in Na₂O, CaO, MgO and MnO. TiO₂ and FeO have variable low to moderate losses or gains with no preference for loss or gain between locality or water content. Low to moderate gains in K occur in all palagonite except Helgafell low-H₂O palagonite.

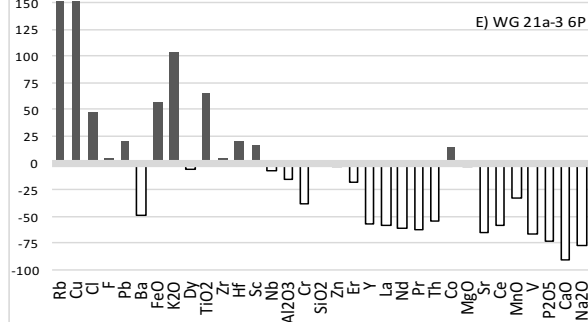
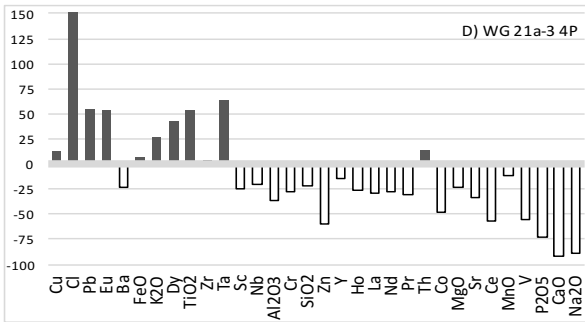
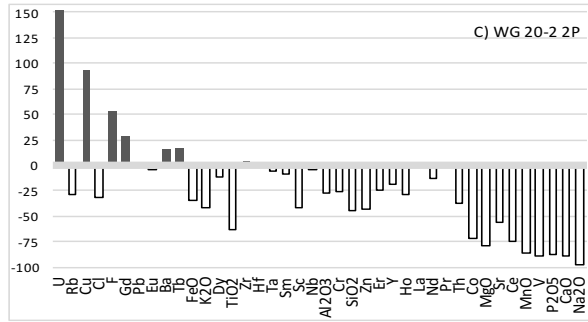
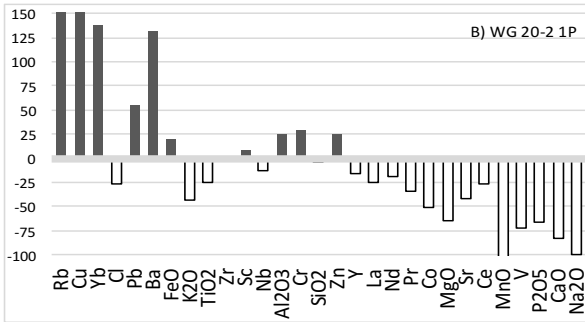
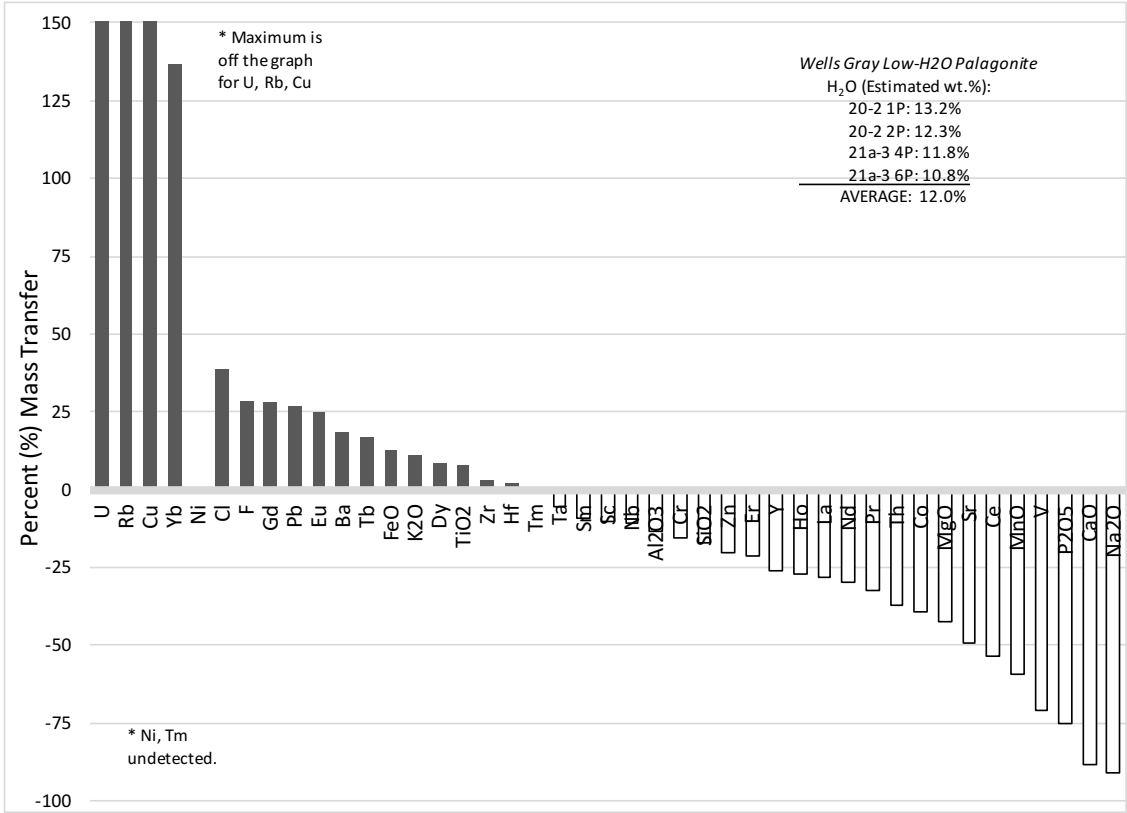


Figure 66 Wells Gray low-H₂O palagonite mass change A) sorted from highest gain to greatest loss by the average of the four lowest water palagonites at Wells Gray, and each representative glass-palagonite pair shown in the same order (undetected components not included in the following graphs): B) 20-2 1P, C) 20-2 2P, D) 21a-3 4P, and E) 21a-3 6P.

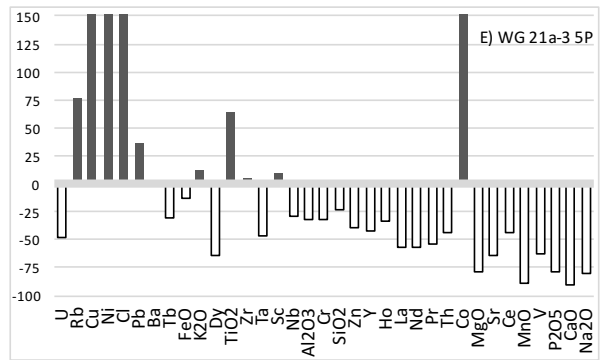
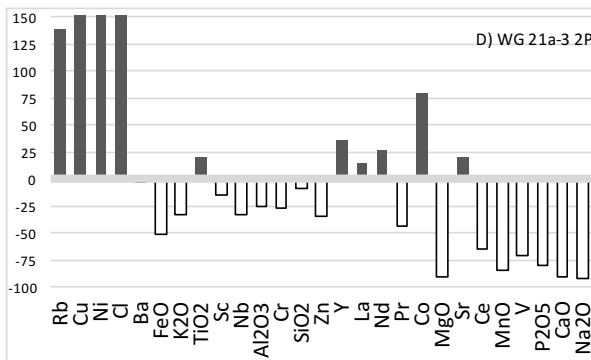
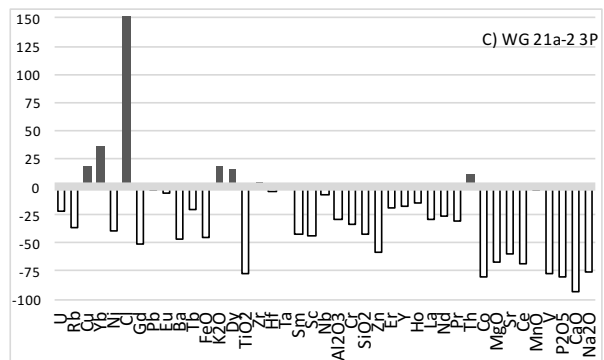
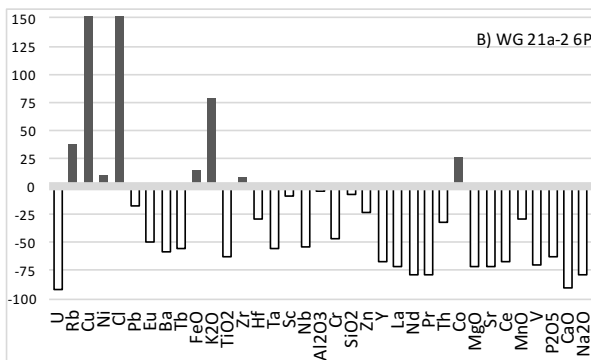
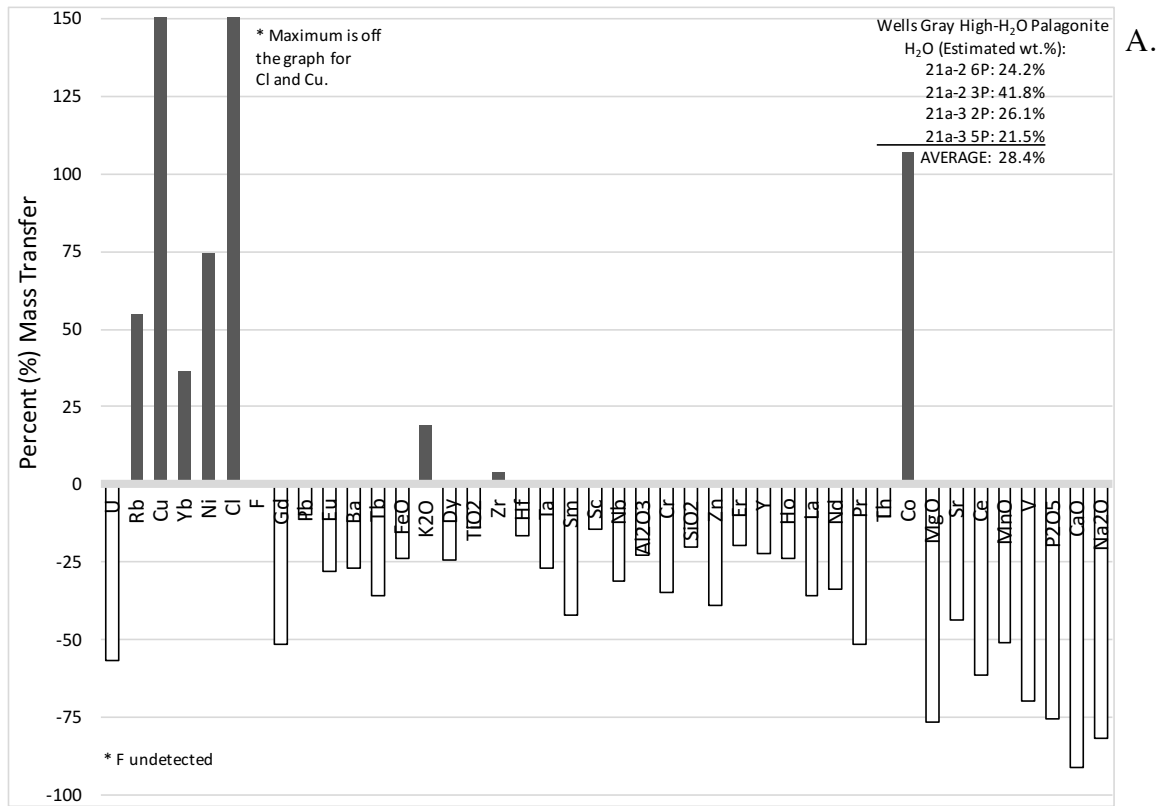
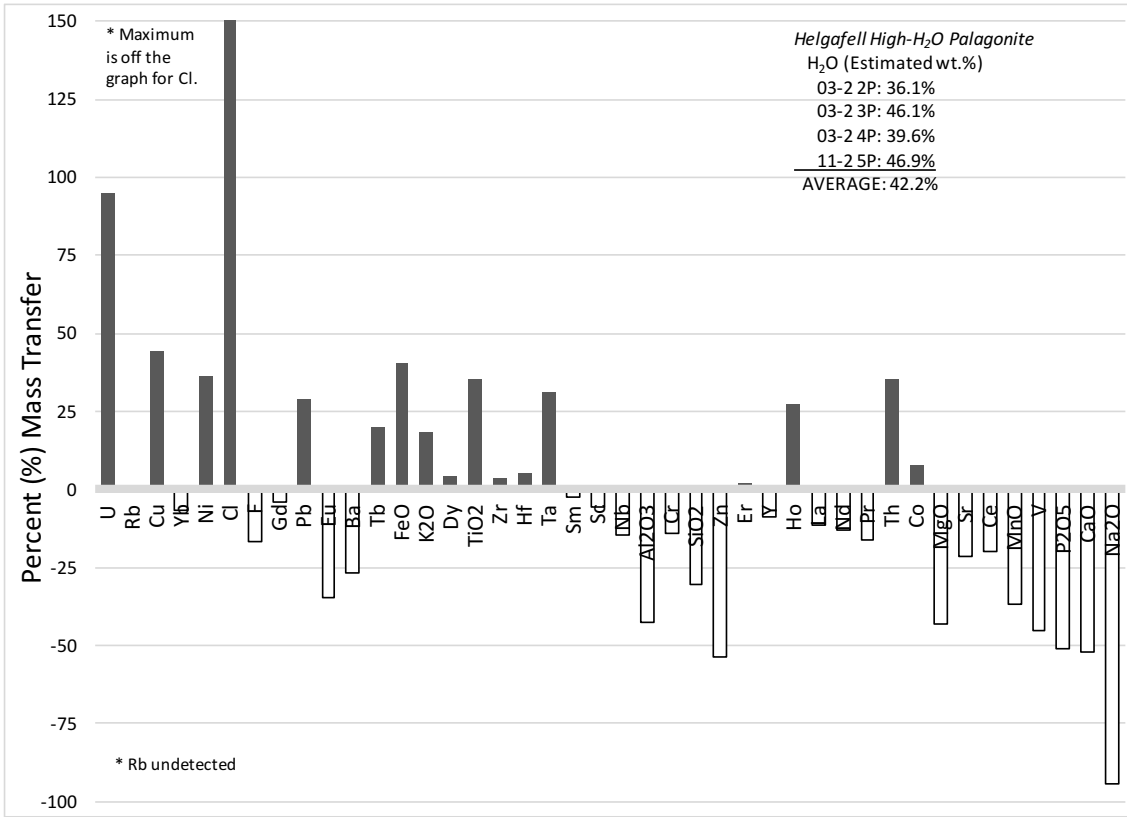


Figure 67 Wells Gray high-H₂O palagonite mass change shown by A) average of four highest water palagonite at Wells Gray sorted to the same element order as Wells Gray low-H₂O palagonite. Each representative glass-palagonite pair shown in the same order (undetected components not included in the following graphs): B) 21a-2 3P, C) 21a-2 6P, D) 21a-3 2P, and E) 21a-3 5P.



A.

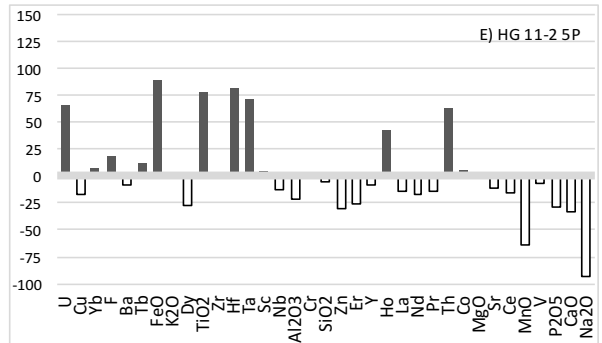
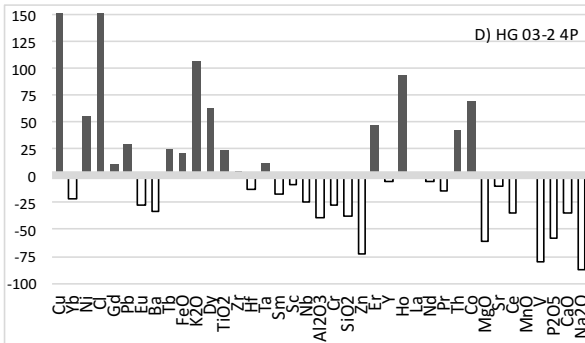
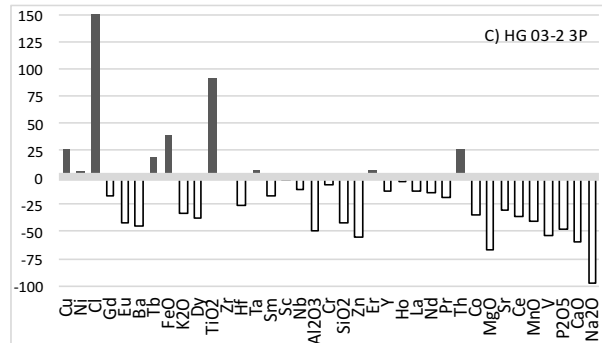
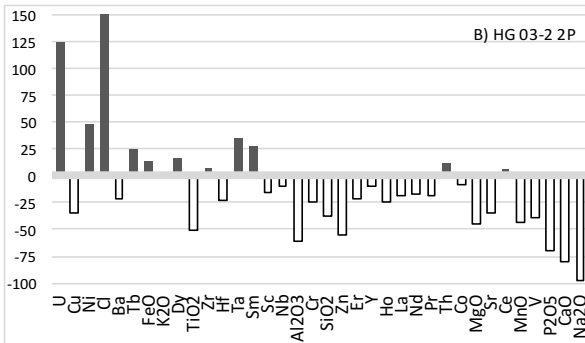


Figure 68 Helgafell high-H₂O palagonite mass change shown by the A) average of the four highest Helgafell water content palagonite sorted to the same element order as Wells Gray low-H₂O palagonite. Each representative glass-palagonite pair shown in the same order (undetected components not included in the following graphs): B) 03-2 2P, C) 03-2 3P, D) 03-2 4P, and E) 11-2 5P.

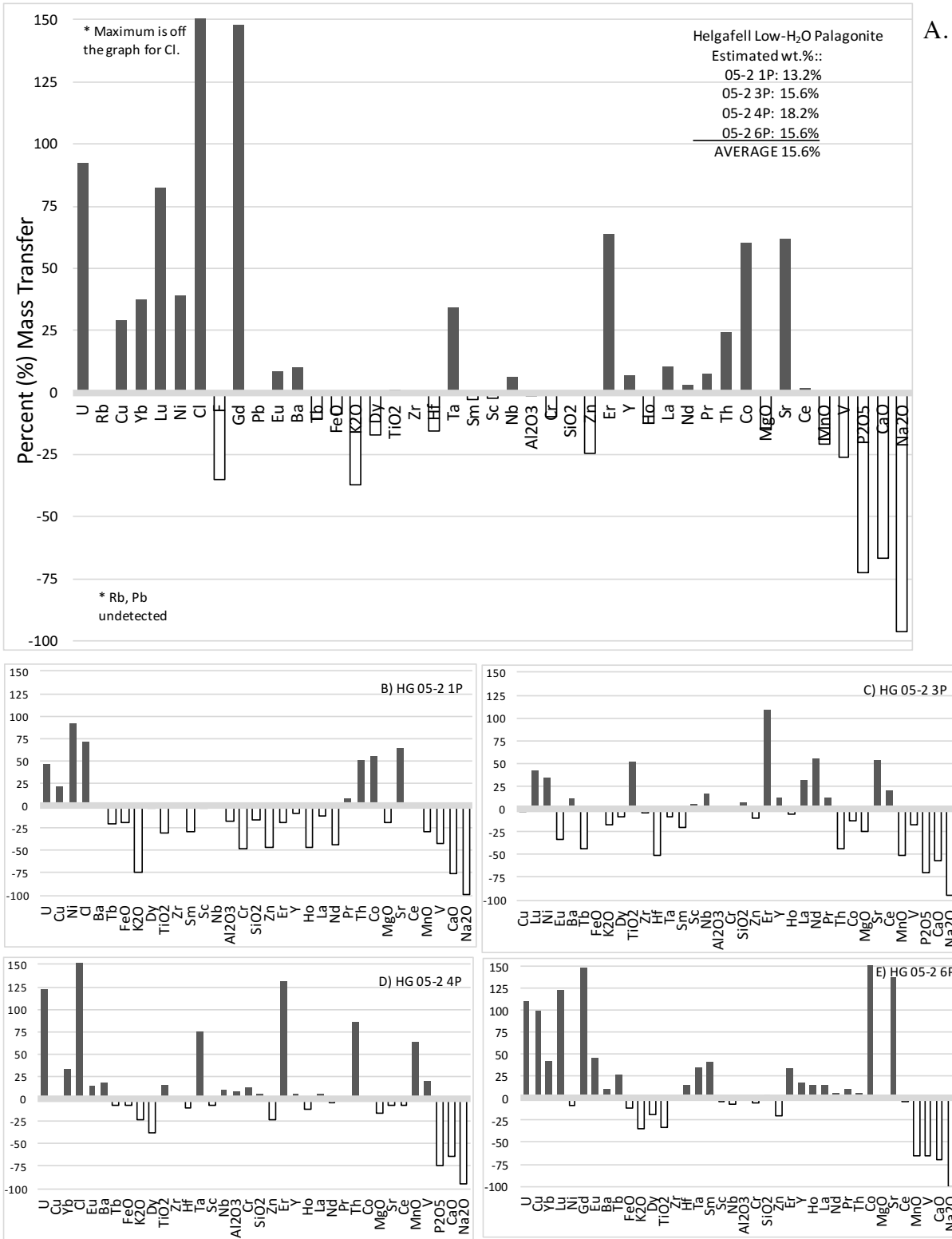


Figure 69 Helgafell low-H₂O palagonite mass change shown by the A) average of the four lowest Helgafell water content palagonite sorted to the same element order as Wells Gray low-H₂O palagonite. Each representative glass-palagonite pair shown in the same order (undetected components not included in the following graphs): B) 05-2 1P, C) 05-2 3P, D) 05-2 4P, and E) 05-2 6P.

Chapter 6: Discussion

A primary goal of this thesis is to test the hypothesis that the major and trace element compositions of palagonite reflect the compositions of parental basaltic glass (sideromelane). A secondary goal is to explore links between textural development of palagonite and mass balance during the process. The study compares tholeiitic rocks from Helgafell, Iceland with alkali basalts from Wells Gray, British Columbia, Canada. Palagonitization at both localities presumably occurred under similar subglacial conditions, involved relatively “pure” meltwater, and occurred relatively recently during the Pleistocene. Thus, there are controls for the potential impact of environmental conditions and age on palagonite formation. Using a variety of data analysis techniques, from exploratory statistics to Gresens’ mass transfer calculations, the study also assesses geochemical similarities in the palagonitization process at the two localities. Results are compared to previous studies from different environments (e.g. Pauly et al., 2011) and a five-stage model is proposed for palagonitization. Discussion proceeds from a comparison of the composition of the Helgafell and Wells Gray sideromelane, to an assessment of elements in palagonite that reflect glass composition, and then focusses on the behavior of elements during palagonitization revealing similarities in the palagonitization process between the two localities.

6.1 Sideromelane Compositions

The total alkalis versus silica diagram (Figure 42; see List of Figures), higher Nb/Y ratios (Figure 43), and steeper slopes of Wells Gray sideromelane on chondrite-normalized rare earth element (REE) diagrams (Figures 48 and 49) confirm that, for samples analyzed in this study, those from Wells Gray are more alkaline than those from Helgafell. Sideromelane analyses from the two Helgafell outcrops appear to have distinguishable characteristics with those low in the stratigraphic section showing subtly higher Nb/Y ratios (Figure 43) consistent with higher percentages of melting (Condie, 2003; Floyd & Winchester, 1975; Greenough & MacKenzie, 2015; Greenough & Ya’acoby, 2013) as well as subtly lower Zr/TiO₂ (Figure 43) indicative of slightly less differentiation (Hastie et al., 2007; Motoki et al., 2015; Murphy, 2007). The eruption that produced the unit may have been precipitated by the arrival of a new batch of magma to the magma chamber. Quantitative modelling of these mantle-melting and magma-chamber differentiation processes is beyond the scope of this study, but the data

indicate subtly distinct magma compositions associated with a single eruptive event at each locality. Chemical variability of sideromelane in a single Wells Gray sample (e.g. 21a-2), in terms of Nb/Y and Zr/TiO₂ (Figure 43) and other chemical characteristics (Figures 44 and 53), can be as large as that observed between the two sampled outcrops at Helgafell. If the chemical variation is real, it implies that sideromelane in Wells Gray samples is heterogeneous. The variation could indicate that the sideromelane grains may have been hydrologically transported, and represent mixtures of material extruded during a prolonged eruption, or from multiple eruptions (fluctuations in the volume of glacial ice and meltwater occurred during the steep valley-sided eruption; Hickson & Vigouroux, 2014). Locally at Second Canyon, where the samples were collected at Wells Gray, broken pieces of pillow lava are mixed with the lapilli tuff, suggesting explosive activity breaking pillows and allowing the fragments to roll downslope and mix with lapilli tuff. Again, petrogenetic modelling of this subtle chemical variability in sideromelane is beyond the scope of the thesis, but it apparently exists, and must be considered in evaluations of the controls on palagonitization. However, in general, it is obvious from various diagrams that sideromelane chemical variability at both localities is very small (Figures 44 and 52; Table 12) even though palagonite compositions are extremely variable (Figures 46 and 52; Table 12).

6.2 Relict Sideromelane Signatures in Palagonite

Many elements show immense concentration variation in palagonite at both localities (Tables 9 and 11; Figures 46 and 52). For the major elements, some of this is ascribable to variable dilution of element concentrations by the addition of water. Water was not directly measured but low totals in electron microprobe analyses indicate concentrations between 10.76 and 41.75 wt. % in Wells Gray analyses, between 31.27 and 61.73 wt. % in Helgafell basalt 1, and between 13.2 and 33.9 wt. % in Helgafell basalt 2 (Figure 41; Tables 9 and 11). However, water dilution cannot explain concentrations for elements that are higher in palagonite than in associated sideromelane.

Any two samples plotting close together on a MDS diagram have highly correlated element concentrations. The spread of geochemical analyses along the X and Y axes of MDS diagrams are thought to reflect the dominant processes that affected the samples; variation along dimension 1 should reflect the more dominant process (Greenough et al., 2010; Greenough &

MacKenzie, 2015; Greenough & Ya'acoby, 2013). Thus, the observation that palagonite and sideromelane from each locality plot at a common dimension 1 value (Figures 52 and 53; see List of Figures) indicates that palagonite retains a significant sideromelane signature that reflects the composition of its parental sideromelane.

Similarly, all palagonite and all sideromelane analyses, regardless of whether they came from Helgafell or Wells Gray, are separated along Dimension 2 (Figure 52). This indicates that the other dominant, but secondary “process” controlling the concentration of elements in analyses reflects the impact of palagonitization. The symmetry of the plot is consistent with the process of palagonitization affecting elements in a similar manner at both localities. Thus, the data organization on the MDS diagrams is consistent with the hypothesis that the signature of parent sideromelane composition remains in palagonite, but also that the process of palagonitization produces some common geochemical changes.

The MDS diagrams comparing samples (Figures 52 to 55) used Pearson correlation coefficients calculated using all chemical data (Appendix B.2 and B.3; Tables 10 and 11) as a measure of similarity between individual analyses. If there is a relict sideromelane signature in palagonite, its identification requires the use of element ratios that are immune to dilution effects, and that are calculated from elements that tend to be immobile during alteration. Palagonite at both localities generally retains sideromelane-like values based on element ratios for immobile elements (Figure 65). Thus, the immobile element composition of palagonite reflects original sideromelane compositions, even if actual element concentrations have been modified by water dilution. The fact that these elements tend to be insoluble (Greenough et al., 1990; MacLean and Barrett, 1993; Pauly et al., 2011; Winchester & Floyd, 1977) demonstrates that palagonite must be derived from sideromelane to retain the immobile element ratio signature. Elements will vary from immobile to highly mobile, but the MDS diagram comparing sideromelane and palagonite analyses (Figure 52) indicate that, based on all elements (most are trace elements, many of which are relatively immobile), original sideromelane composition determines palagonite composition. Based on only major elements the MDS results separate samples along dimension 1 based on whether they are palagonite or sideromelane analyses, but all Helgafell and Wells Gray analyses are separated along dimension 2 (Figure 52). If dimension 1 represents dominant variation in the data set, then the

major elements may be more important for separating sideromelane from palagonite than the large number of “immobile” trace elements.

6.3 Geochemistry of Palagonite Formation

MDS diagrams provide testable clues to chemical processes operating during palagonitization. Whereas analyses of both palagonite and sideromelane for each locality plot at equivalent dimension 1 values, analyses are separated along dimension 2 based on whether they are sideromelane or palagonite analyses (Figure 52). Thus, it is possible that chemical changes associated with palagonitization were similar at both localities. A MDS diagram comparing only palagonite analyses (Figure 59) shows that, as discussed in the previous section (Figures 52 and 53), analyses plot by locality along dimension 1. However, on dimension 2, labelling analyses with water content shows that both Helgafell and Wells Gray palagonites with high water content tend to have high Dimension 2 values. This diagram indicates that the overall composition of Wells Gray and Helgafell palagonite is substantially related to palagonite water content. These MDS diagrams comparing analyses involved the calculation of Pearson correlation coefficients for all analysis pairs and used all geochemical data describing each analysis.

Palagonite compositions at both Helgafell and Wells Gray vary considerably. One means of investigating the processes that may have generated geochemical variability is to use MDS to compare element behavior in palagonite (Figures 56 to 58; see List of Figures). The MDS analyses always show four elements (H_2O , Cl, Mn, K), and at times also Na, Cu, P, Rb, Th, Ho, Co and/or Fe, to plot, like water, on the same side of each diagram. They may have been added with water during palagonitization. Most elements plot in a large field on the opposite side of the diagram and many of these tend to be considered “immobile” during alteration (Greenough et al., 1990; MacLean & Barrett, 1993; Pauly et al., 2011; Winchester & Floyd, 1977). The implication is that the palagonitization process apparently affected most elements the same way at both localities.

For Wells Gray and Helgafell basalt 1, major elements are “controlled” by at least two processes given the spread in dimension 1 and 2. For Helgafell basalt 1, dimension 1 controls most of the spread in major elements and is likely the dominant process.

Within the large fields surrounding “mostly” immobile elements in Helgafell’s palagonite (Figures 57 and 58), there is a tendency for Al_2O_3 , SiO_2 , MgO and Ba to consistently plot quite close together. It has been proposed that smectite is an important component of palagonite. The clustering of Al_2O_3 , SiO_2 and MgO with mostly immobile elements in only Helgafell’s basalt 1 and 2 palagonite, and not in Wells Gray palagonite, indicates that palagonite at Helgafell may be more smectite-like and therefore possibly in a later stage of palagonitization. Smectite associated with altered Hawaiian tholeiites has a major element composition that plots with Helgafell palagonites, also derived from tholeiitic basalt (Figure 55). The Hawaiian smectite is enriched, relative to palagonite, in SiO_2 , MgO , FeO , MnO , K_2O and sometimes Al_2O_3 depending on depth of the HSDP drill core (Walton & Schiffman, 2003, their Tables 2, 3). Thus, the apparent “immobility” of these elements may reflect their utilization in forming smectite. For element associations such as Co and Ni , it is not clear whether these two elements are plotting together because of primary (igneous), sideromelane variability inherited by palagonite, or whether they simply behaved the same during palagonitization (Figure 56).

6.4 Element Addition and Removal Based on Gresens Calculations

The MDS diagrams discussed in the previous two sections highlight the dominant patterns in the data set. They indicate relationships between samples/analyses based on locality (Helgafell versus Wells Gray; Figures 52 and 53), type of material (sideromelane or palagonite; Figure 52), and the water content of palagonite (Figure 59). Similarly, MDS diagrams assessing element behavior at the two localities are consistent with element concentrations in palagonite being tied to water addition during palagonitization, with similar elemental effects at both locations (Figures 56 to 58). Bar graphs summarizing the results of the Gresens calculations (Figure 67) were set up to test the hypotheses that came from inspection of the MDS diagrams.

In general, U , Rb (when detected), Cu , Yb , Ni , Cl and commonly K_2O and Co had relative mass gains during palagonitization, and some of these elements (e.g. Rb , Cu , Ni , Cl , K_2O) tended to, like water, have low dimension 1 values on the MDS diagrams comparing element behavior (Figures 56 to 58). The majority of elements/major element oxides from Ba to Co (Figures 66 and 67) tend to show minor losses or in rarer cases small gains during palagonite formation. Elements/oxides from MgO to Na_2O were generally lost during palagonite

formation (Figures 66 and 67). However, the overall patterns for element behavior are similar for both Wells Gray and Helgafell.

Key major elements tending to show minor loss or gain during palagonitization are SiO_2 , Al_2O_3 , TiO_2 , K_2O and FeO from Gresens bar graphs (Figures 66 and 67) whereas Na_2O , CaO , MgO , MnO and P_2O_5 show significant losses. Low water-content palagonite is somewhat consistent with smectite formation since they show similarities in MDS (Figure 59), but Gresens' results are not consistent with smectite formation since MgO is much higher in smectite (Walton & Schiffman, 2003) yet is significantly lost in palagonite (bar graphs; Figures 66 and 67). Palagonite must be able to incorporate Ba, major element oxides (e.g. SiO_2 , Al_2O_3), and accommodate some (FeO - Fe_2O_3 , K_2O , TiO_2) into its structure. Uranium behavior in bar graphs indicates that oxidizing conditions yielded a highly-mobile element that tends to be concentrated in palagonite. Uranium is mobile under oxidizing conditions but fixed (reduced) under reducing conditions (Bonotto, 2017; Bots & Behrends, 2008).

Copper is known to be mobile in low-temperature environments (Godlevskiy, 1967) and shows mass gain in palagonite, and perhaps may be dissolved in smectite or form sub-micron oxide/carbonate phases (malachite/azurite) with Cu. Copper sulfides, e.g. chalcopyrite, occur locally in voids between glass shards although it is unknown whether they formed before or during palagonitization.

Ubiquitous loss of phosphorous (P_2O_5) during palagonite formation remarkably indicates that this high-field-strength-element (HFSE) is soluble (most are not), and elements with the highest charge/radius ratios are mobile. In the case of phosphorous, it is an essential nutrient for plants and animals, and life on Earth is made possible by the solubility of phosphorous (Egli et al., 2012).

The Gresens summary bar graphs also test the hypothesis from MDS diagrams (Figure 59) that some element concentrations reflect the water content of palagonite. For both Wells Gray low and high water palagonite (Figures 66 and 67, respectively) and Helgafell, (Figures 68 and 69, respectively) no clear relationships between water content and the addition of water soluble elements are evident.

Furnes (1978) noted an important relationship between the H_2O -content of palagonite and the degree of element mobility during palagonitization: increased H_2O in palagonite leads to increased mobility. Although this is logical, the bar graphs show similar trends in element

mobility independent of water content and locality (Figures 66 to 69). Perhaps the high-H₂O palagonite represents an earlier stage of palagonitization (non-crystalline phases) than low-H₂O palagonite (crystalline phases), as hypothesized by Stroncik and Schmincke (2001) (Figure 4).

Other than a mass gain in Rb⁺ in Wells Gray palagonite (Rb not detected in Helgafell samples) and Ba²⁺ in low water palagonite at both localities, no consistency in mass gain of low ionic-potential (low charge/radius ratio) elements was apparent. This differs from Jercinovic et al.'s (1990) suggestion that the gel properties and increased surface area of palagonite (compared to glass) would facilitate the adsorption of low ionic potential elements (e.g. Rb⁺, Cs⁺, Ba²⁺ and possibly Ca²⁺).

Major and trace element transfer due to palagonitization shown in mass balance calculations and microprobe traverses appear to be independent of the composition of sideromelane since similar trends occur. This finds disagreement with the conclusion of Pauly et al. (2011), that mass change for SiO₂, Al₂O₃, and especially TiO₂ and FeO are dependent on whether sideromelane is subalkaline or alkaline.

6.5 The Aqueous Environment of Sideromelane and Palagonite

The aqueous environment of glaciovolcanism initially facilitates high water-rock ratios and rates of chemical reactions. Rapid quenching of the melt forms basaltic glass, and the streaming of magmatic gases through water should acidify the water. Palagonite may form on glass grains during and/or immediately following the eruption but it can also form later, over long periods of time and under different conditions (e.g. water volume and chemistry, temperature and pH). The rate of palagonitization is probably related to water temperature, which can vary depending on the position of deposits within the larger volcano-ice setting. On the scale of metres, millimetres or even microns, palagonite is heterogeneous because the microenvironment of alteration is variable (this study; Jercinovic et al., 1990).

In this study, hydrating sideromelane mathematically by normalizing its composition to the water measured in palagonite was important for assessing the effects of water on mass transfer. In the physical process of water diffusion in glass (Tomozawa, 1985), H⁺ and OH⁻ ions, and H₂O molecules enter into the glass without the loss of other dissolved or leached ions/molecules (Honnorez, 1981). Hydration of rhyolitic obsidian produces bulbous or

rounded textures, e.g. spherulites, that form from the diffusion of water (Gardner et al., 2012). The zoned hemispherical to spherical textures (Figure 29) that propagate inwards from the edges of glass grains (next to the glass-palagonite interface) may texturally represent the chemical diffusion of water in sideromelane.

Pauly et al. (2011) suggests that water content in palagonite, and palagonitization extent (estimated from % zeolites + % palagonite and smectite), are correlated linearly and inversely, such that palagonite's water content decreases as palagonitization extent increases. In addition, original porosity of samples (estimated from % pore space + % zeolites - % lithic and crystal clasts), linearly and inversely correlate with water content in palagonite (Pauly et al., 2011). Helgafell's group 1 basalt has on average over twice the water content (~42.7% H₂O) in palagonite rims as Helgafell's group 2 basalt (~20.3% H₂O) or Wells Gray (~18.14% H₂O). Thus, according to the Pauly et al. (2011) hypothesis, Wells Gray and Helgafell's basalt 2 samples represent more extensive palagonitization. The difference in palagonitization extent (based on different water content in palagonite) at close proximity of Helgafell's two basaltic compositions indicates localized anomalies, such as thermal or pH anomalies.

Similar to Pauly et al. (2011), Stroncik and Schmincke's (2001) review claims that as alteration progresses from Aging Step I (sideromelane + water = gel palagonite) to Aging Step II (gel palagonite converts to secondary minerals), water content in palagonite decreases as secondary minerals crystalize. Based on this hypothesis, the lower water-content palagonite in Wells Gray represents a later Aging Step than the higher water-content palagonite in Helgafell (especially Helgafell's basalt 1). Palagonite rims in Wells Gray are also thicker than at Helgafell, further identifying Wells Gray samples as being more palagonitized (if rim thickness is indeed an appropriate measurement). Alternatively, a reasonable hypothesis is the gel-palagonite referenced in previous studies (Stroncik and Schmincke, 2001) may be an effective indicator for palagonitization extent since glass is known to convert to gel in the dissolution process (Bunker & Casey, 2016; Pauly et al., 2011; Peacock, 1926; Stroncik & Schmincke, 2001). The highly vesicular sideromelane at Helgafell provides more surface area for palagonitization and has more gel-material (19.1%) than at Wells Gray (Figure 23). Therefore, these two indices for extent of palagonitization give conflicting results.

Rock density increases as sideromelane tuff is converted to palagonite tuff since pore space decreases during palagonitization (Hay & Iijimi, 1968). Porosity has been found to decrease

from 36% (early stages) to 9% (later stages) during palagonitization (Stroncik & Schmincke, 2002). Based on these observations, the high porosity in Helgafell's samples (37.8%) indicates that the deposit is at an early stage of palagonitization. It is important to remember that 1) the porosity of Helgafell samples includes an initially highly vesicular (~30.8%) sideromelane with voids (~7.1%), and 2) samples collected for this study are surficial (not from drill holes), thus not compacted, which would cause density to increase. At Wells Gray, sample porosity (~18.0%) is about half that at Helgafell. This is likely due to its low vesicularity (~4.9%) resulting from either increased pressure from thicker glacial ice during volcanism at Wells Gray or a lower primary water content.

6.6 Microprobe Traverses

Microprobe traverses provide insights into geochemical zoning in palagonite rims, which can then be correlated with textures. Compositional zoning in palagonite rims has been previously observed (Jercinovic et al., 1990), and is thought to be caused by changes in solution pH over time, with the innermost area of the palagonite rim, next to glass, forming last. This inner area at the glass-palagonite interface is important because abrupt chemical shifts occur at this point in the microprobe traverses.

This section discusses element behaviour in palagonitization by interpreting the two glass-palagonite microprobe traverses from Helgafell and Wells Gray. Additionally, major element data sets published from five traverses (subalkaline samples) by Pauly et al. (2011) across palagonite are plotted for comparison. Figure 70 summarizes the basalt composition and environments of formation for all traverses discussed below.

6.6.1 Helgafell and Wells Gray

Helgafell (Figure 60) and Wells Gray (Figure 61) glass-palagonite traverses reveal generally similar geochemical zones indicating that while sideromelane composition seems to control the overall composition of palagonite, it has less influence on zoning in palagonite rims. Moving from the inner contact of the sideromelane with palagonite, a number of geochemical and texture zones are observed.

The innermost zone is mainly characterized by high TiO_2 at both Helgafell and Wells Gray, indicating the tendency for TiO_2 to be insoluble and immobile. TiO_2 prefers to not be included

in the metastable structure that is forming in the palagonite rim, thus collects at the inner rim near the interface. The TiO_2 -rich zone may correlate with the observed formation of titaniferous spherules (40-50 wt. % TiO_2) in palagonitized glass (Walton & Schiffman, 2003). The presence of the TiO_2 -rich zone may be a useful proxy for measuring palagonitization extent as it accumulates within the inner rim over time. Jercinovic et al. (1990) also observed that insoluble elements reprecipitate immediately at the glass-palagonite interface. Unlike TiO_2 , FeO (total Fe) increases towards the outer zone farthest from the glass interface. Thorseth et al. (1991) proposed that a $\text{pH} > 3$ and an oxidizing environment result in precipitation of Fe, Ti and Al to form brown palagonite like Helgafell and Wells Gray palagonite. Although the increase in Fe and Ti in palagonite supports this hypothesis, Al decreases in palagonite. White palagonite observed by Thorseth et al. (1991) was thought to result from an acidic $\text{pH} < 3$ environment (Fe, Ti and Al to remain in solution) but white palagonite was not observed in Helgafell and Wells Gray samples therefore indicating a less acidic environment.

Moving towards the centre of the palagonite rim and away from the glass-palagonite interface, Helgafell and Wells Gray traverses show a Mg-rich zone. The traverse across a vesicle's palagonite rim (Figure 60) shows that MgO sharply decreases at the glass-palagonite interface, then increases progressively towards the outer edge of the rim. This is a common trend seen in the element map (Figure 64) and five traverses (Figures 71 to 75) from Pauly et al. (2011). Although purely speculative, a gradual increase in MgO across and towards the outer edge of the palagonite rim or a MgO-rich zone may indicate the progression towards a metastable structure, such as clay minerals that are concentrated in MgO. Pauly et al. (2011) recognized the same trend in MgO, indicating that MgO does not record the dissolution of sideromelane, but shows the conversion of gel-palagonite to phyllosilicate. An alternate explanation is that the MgO-rich zone is related to formation of brucite ($\text{Mg}(\text{OH})_2$), a mineral known to precipitate at a high $\text{pH} > 10.0$ when Mg becomes insoluble with increased hydroxide (Faure, 1998). In this case, MgO activity in the palagonite rim would indicate a progression from lower pH at the glass-interface (where dissolution of glass produces silicic acid) towards a higher pH at the edge of palagonite rims where more alkaline solutions can circulate causing Mg to become more insoluble and precipitate.

Moving towards the centre of the palagonite rim and following the TiO₂ and MgO zones, there is a smaller brief spike in MnO (Figure 62). MnO behaves unpredictably across the palagonite rim and does not follow FeO.

The sharp decrease in CaO at the glass-palagonite interface and across the entire palagonite rim, is not consistent with Jercinovic et al.'s (1990) claim that palagonite must be high-Ca in order to be replaced by clay. It was hypothesized that when Ca stays in the palagonite rim, smectite (Fe-saponite) is the first alteration product followed by zeolites and late-stage nontronite (Jercinovic et al., 1990). In this study, microprobe traverses, element maps, line scans, and mass balance all show palagonite rims to be significantly depleted in CaO (high % mass loss). The high % mass loss of CaO in the palagonite rim may indicate that 1) Ca has been removed in solution, 2) Ca has been incorporated into other secondary minerals (e.g. calcite), or 3) palagonite can be replaced by low-Ca clay (e.g. kaolinite, vermiculite) and zeolite. The sharp spike in CaO on the outside of Wells Gray's palagonite rim (Figure 61) is likely due to the presence of calcite, a common secondary mineral associated with palagonitization (Appendix C.1).

Across all zones, an increase in FeO and decrease in Al₂O₃ is found in palagonite. Iron tends to increase towards the outer palagonite rim possibly due to oxidation of Fe²⁺ to insoluble Fe³⁺ at the outer palagonite rim. Aluminum tends to favour the glass but in palagonite Al₂O₃ generally remains constant or can oscillate in unison with SiO₂ (Figure 60). The matching behaviour of SiO₂ and Al₂O₃ across the vesicle palagonite rim indicates that palagonite is a metastable structure, since they can replace one another in crystal lattices that have more atomic ordering than amorphous glass. Although K₂O concentrations are low in glass and palagonite, the microprobe traverses indicate an increase in K₂O in all palagonite zones relative to glass (Figure 62). This does not support Furnes' (1978) hypothesis that environment controls K₂O. The study found that non-marine (subglacial) palagonite is depleted in K₂O (Furnes, 1978), whereas palagonite in marine environments shows enrichment in K₂O (Moore, 1966). Compared to glass, Na₂O concentrations are significantly low in all palagonite zones likely due to its removal in solution.

The Wells Gray traverse shows some correlation between geochemical and textural zoning. The inner TiO₂-rich zone of palagonite rims has spherical textures that project across

the glass-palagonite interface into the glass (Figure 61). The MgO-rich zone and outer FeO-rich zone appear to have linear features separating them.

Geochemical-textural trends in Wells Gray and Helgafell microprobe traverses (Figures 60 and 61) appear to match patterns in a SEM line scan across a palagonite rim between two glass grains (Figure 63). For example, a TiO₂-rich zone occurs next to both glass interfaces and FeO increases in the rim towards its centre, forming a symmetric pattern. A zone enriched in SiO₂ and Al₂O₃ lies between the TiO₂ and FeO zones (Figure 63), confirming that Si and Al behave similarly (as in the Helgafell's vesicle traverse; Figure 60). A similar spherical texture occurs in the TiO₂-rich inner zones, but in the line scan the SiO₂ and Al₂O₃-rich zone also appears to have a spherical texture. Another geochemical-textural relationship is the white band that runs linearly down the centre of the palagonite rim and that appears to be associated with a high mass element like FeO (Figure 63).

6.6.2 Reanalysis of Subalkaline Glass-Palagonite Microprobe Traverses

In order to determine if our results differ from those of previous workers, we have reanalyzed sideromelane-palagonite EMP traverses from Pauly et al. (2011), who studied palagonite formation in different environments (glaciovolcanic and marine), sample types (surface or subsurface) and for different magma compositions (alkaline to subalkaline) (Figure 70).

Steps in palagonitization involve the: 1) formation of gel-palagonite as a result of the addition of water to sideromelane, followed by 2) the addition of water and addition/subtraction of other cations to gel-palagonite to form palagonite, zeolites, smectite and other secondary minerals. Basaltic glass has been experimentally measured to become saturated at ~3-5% H₂O (Bonatti, 1965; Ross & Smith, 1955; Seligman et al., 2016) at low temperature but for glass-gel (otherwise known as gel-palagonite), there are no constraints since the solubility of H₂O in sideromelane and gel are poorly known.

Most previous workers have assumed 0% solubility of H₂O in sideromelane and 'gel-palagonite' (e.g. Pauly et al., 2011). We want to investigate the apparent changes in concentrations of all elements that result from simple hydration of sideromelane, and then of gel-palagonite. To show this (Figure 71), we first add 5 wt.% H₂O to the measured sideromelane composition and renormalize (dotted lines, labelled B). Then we add an amount

of H₂O to sideromelane that is equivalent to what the assumed H₂O is in palagonite (dashed lines, labelled C), which is a similar model to the assumption for water in data set 2 (Table 5; Appendix B.8 and B.9). This highlights the apparent concentration changes that would be expected from simple hydration, assuming isochemical behaviour of all other elements.

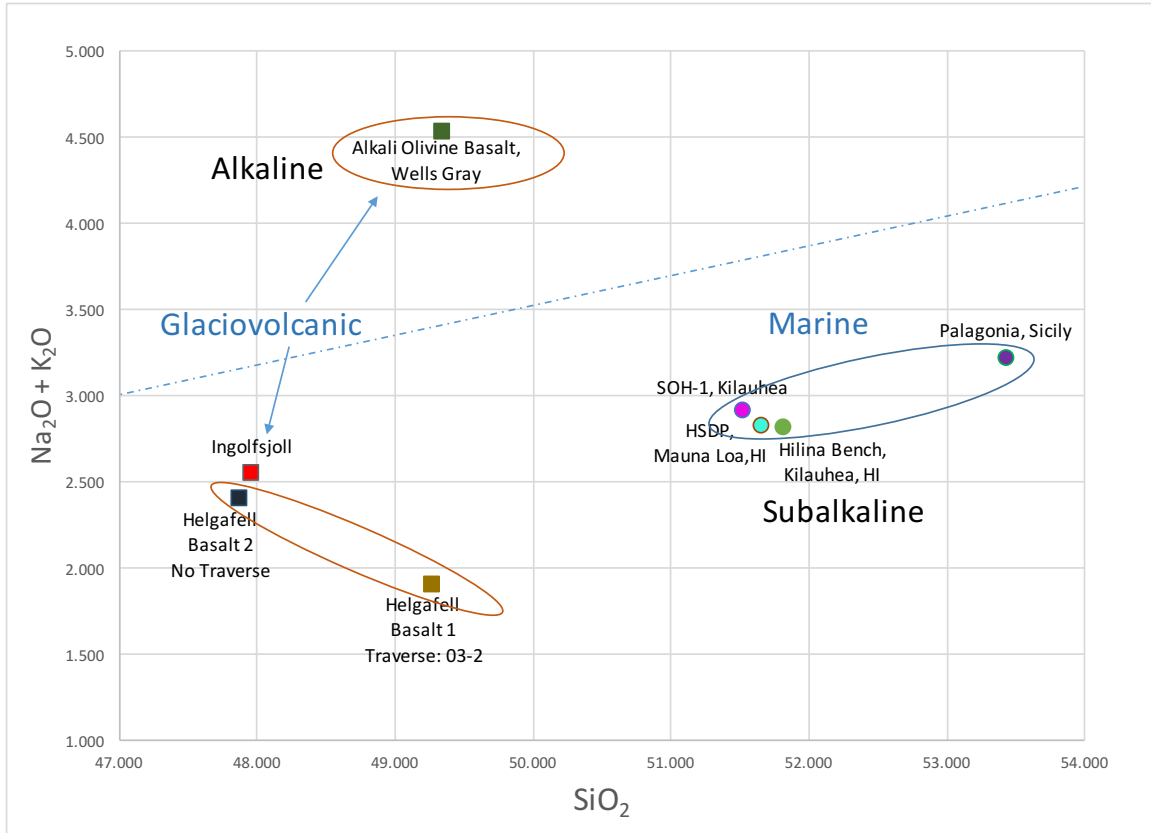


Figure 70 Total alkali silica diagram showing glass compositions (subalkaline or alkaline), environments (glaciovolcanic or marine), or sample type (surficial or drillcore) associated with glass-palagonite traverses. Wells Gray and Helgafell data from this study. All other data from Pauly et al. (2011). Alkaline-subalkaline boundary from McDonald (1968).

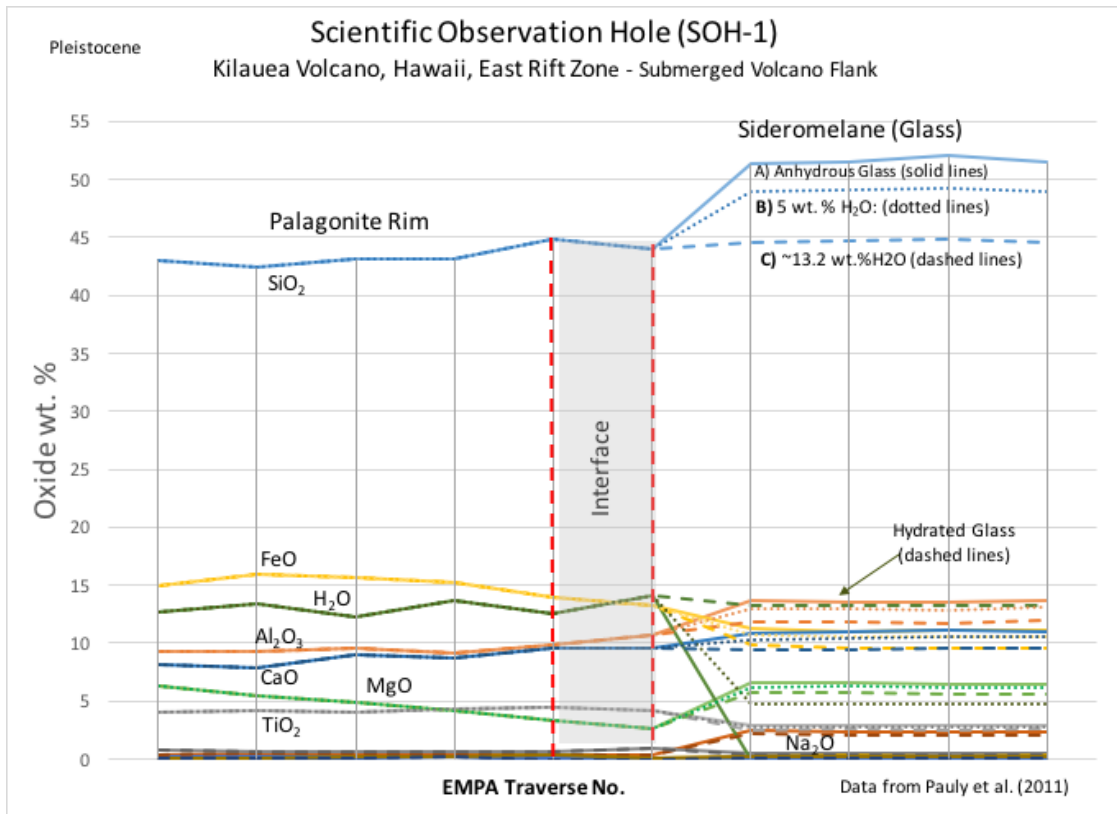


Figure 71 Kilauea, HI SOH-1 microprobe glass-palagonite traverse of subalkaline sideromelane/glass as A) anhydrous (solid lines), B) hydrated with 5 wt.% H₂O (dotted lines), and hydrated to the average water in palagonite ~ 13.2% H₂O (dashed lines). Data are from Pauly et al. (2011).

In the SOH-1 (submarine, drill core, subalkaline) glass-palagonite traverse, Fe and Ti increase, whereas Al, Ca and Na decrease (Figure 71). If glass is hydrated to palagonite's H₂O, the concentration of Si appears to be isochemical. Whether glass is hydrated or anhydrous, Mg sharply decreases, then gradually increases towards the outer rim. This resembles Helgafell's element map of two palagonite rims in one glass grain (Figure 60). Similar to Helgafell and Wells Gray, and, whether glass is anhydrous or hydrated: 1) Ti increases in palagonite, but in this case remains constant across the entirety of the palagonite rim, 2) Fe increases in palagonite, while 3) Al decreases in palagonite.

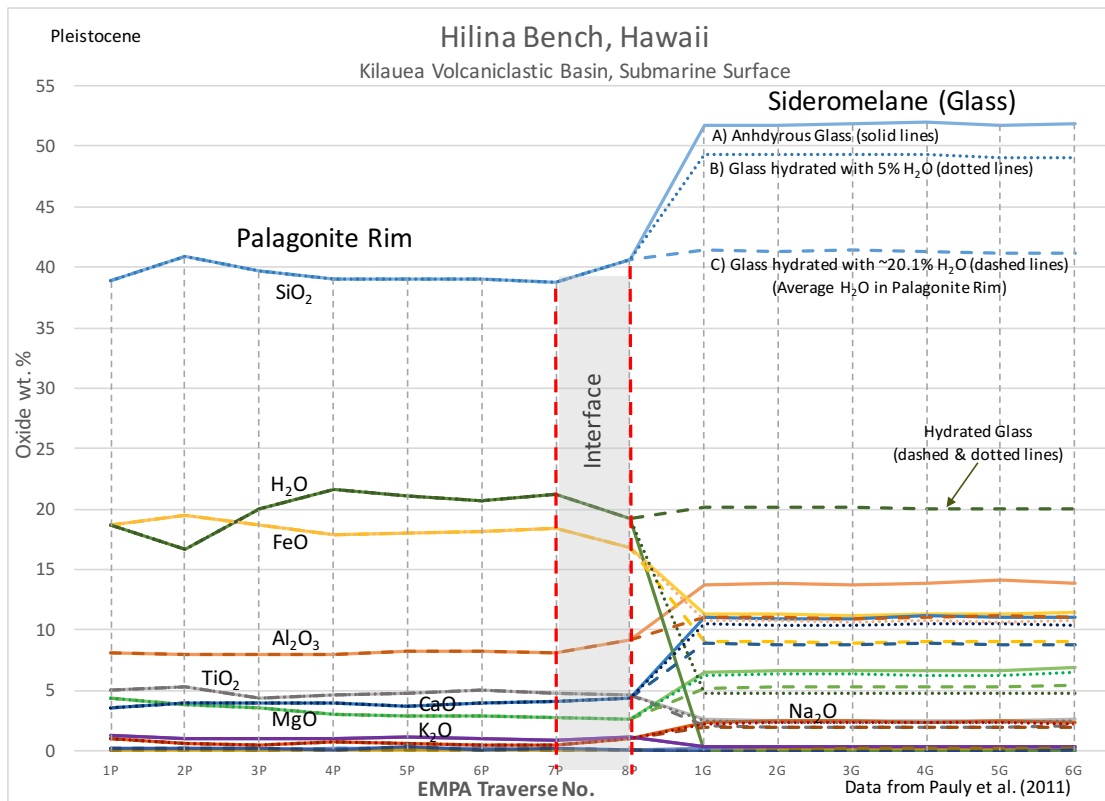


Figure 72 Hilina Bench, HI microprobe glass-palagonite traverse of subalkaline composition (Kilauea volcano's submarine offshore basin) showing sideromelane/glass as A) anhydrous (solid lines), B) hydrated with 5 wt.% H₂O (dotted lines), and C) hydrated to the average water (~20.1%) in the palagonite rim (dashed lines). Data is from Pauly et al. (2011).

In the Hilina Bench, HI (submarine, drill core, subalkaline) glass-palagonite traverse, whether glass is anhydrous or hydrous, and similar to that observed in Helgafell and Wells Gray: 1) Fe and Ti increase, 2) Al, Ca and Na decrease, and 3) Mg sharply decreases at the interface but gradually increases across and towards the rim's outer edge (Figure 72). Although Ti increases in palagonite (similar to Helgafell and Wells Gray, whether glass is anhydrous or hydrated), its behaviour differs from other traverses because it shows a small TiO₂-rich zone at the outer edge of the rim (Figure 72). Similar to the glass-palagonite traverse from the SOH-1 drill hole (Figure 71), when glass is hydrated Si appears to be isochemical. The samples from SOH-1 and Hilina Bench, Hawaii represent palagonitization from the same environment (marine), composition (subalkaline) and sample type (drill core). But, importantly, they show element behaviour resembling that for Helgafell and Wells Gray samples formed in a

glaciovolcanic environment, were surface samples, and represent both subalkaline and alkaline magma compositions.

The HDSP program drilled a 3.06 km-deep core on Mauna Loa volcano's southeast flank to examine low-temperature alteration of basalts in suboceanic-island environments (Walton & Schiffman, 2003). The HDSP glass-palagonite traverse (Figure 73) is from a sample from the lower 2 km of the drill core (Walton & Schiffman, 2003).

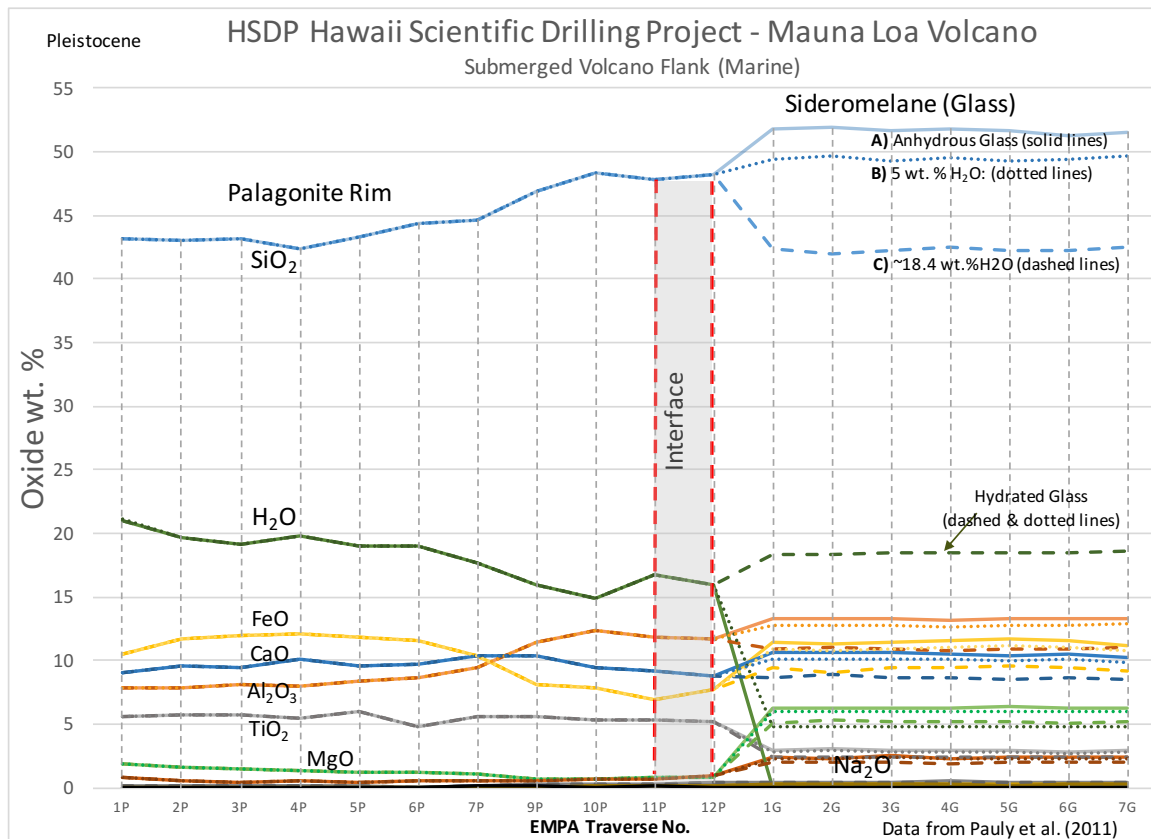


Figure 73 Hawaii Scientific Drilling Project (HSDP) glass-palagonite microprobe traverse showing sideromelane/glass as A) anhydrous (solid lines), B) hydrated with 5 wt.% H₂O (dotted lines), and hydrated to the average water in palagonite ~ 18.4% H₂O (dashed lines). Data is from Pauly et al. (2011).

The HSDP (submarine, drill core, subalkaline) glass-palagonite traverse shows several chemical trends similar to those from Helgafell and Wells Gray, whether glass is anhydrous or hydrated (Figure 73): 1) Ti increases, 2) Mg sharply decreases, then slightly increases gradually towards the outer edge of the palagonite rim, 3) Na sharply decreases, and 4) Ca generally remains constant across the glass and palagonite (isochemical). Unique to the HDSP

traverse, the Fe and Al concentrations change drastically at the palagonite rim's centre (not at the glass-palagonite interface), and Si either decreases (compared to anhydrous glass) or increases (compared to hydrated glass). In the hydrated glass, Si appears isochemical in the outer half of the palagonite rim, and Fe and Al appear to be isochemical overall but their concentrations change similar to other traverses at the centre of the rim (Fe increases and Al decreases).

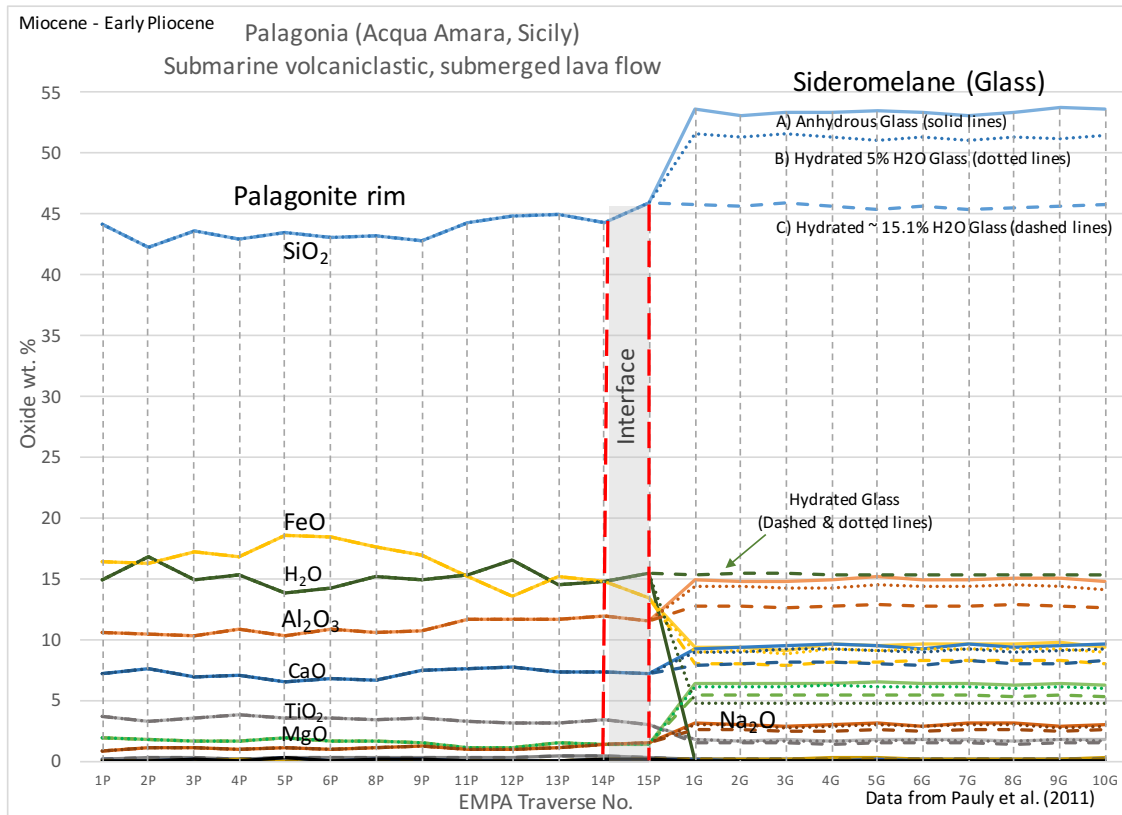


Figure 74 Palagonia, Sicily submarine volcanoclastic glass-palagonite microprobe traverse showing sideromelane/glass as A) anhydrous (solid lines), B) hydrated with 5 wt.% H₂O (dotted lines), and hydrated to the average water (~15.1%) in palagonite (dashed lines). Data is from Pauly et al. (2011).

In Palagonia's (submarine, surficial, subalkaline) glass-palagonite traverse, whether glass is anhydrous or hydrated (Figure 74), and similar to Helgafell and Wells Gray: 1) Ti and Fe increase in the palagonite rim relative to glass (Ti remains constant and Fe peaks near the rim's centre), 2) Fe increases in palagonite, 3) Al, Ca and Na decrease in palagonite, and 4) Mg sharply decreases at the interface then gradually increases towards the palagonite rim's outer edge (Figure 74). Si appears to be isochemical or slightly decreases (~ 1.0%) when glass is

hydrated. Aluminum, Ca, Mg and Na decrease to a lesser degree with hydrated glass. Fe and H₂O appear to behave antithetically, for example, at the rim's centre, Fe peaks and H₂O falls, and closer to the glass interface H₂O peaks at the point that Fe falls (Figure 74).

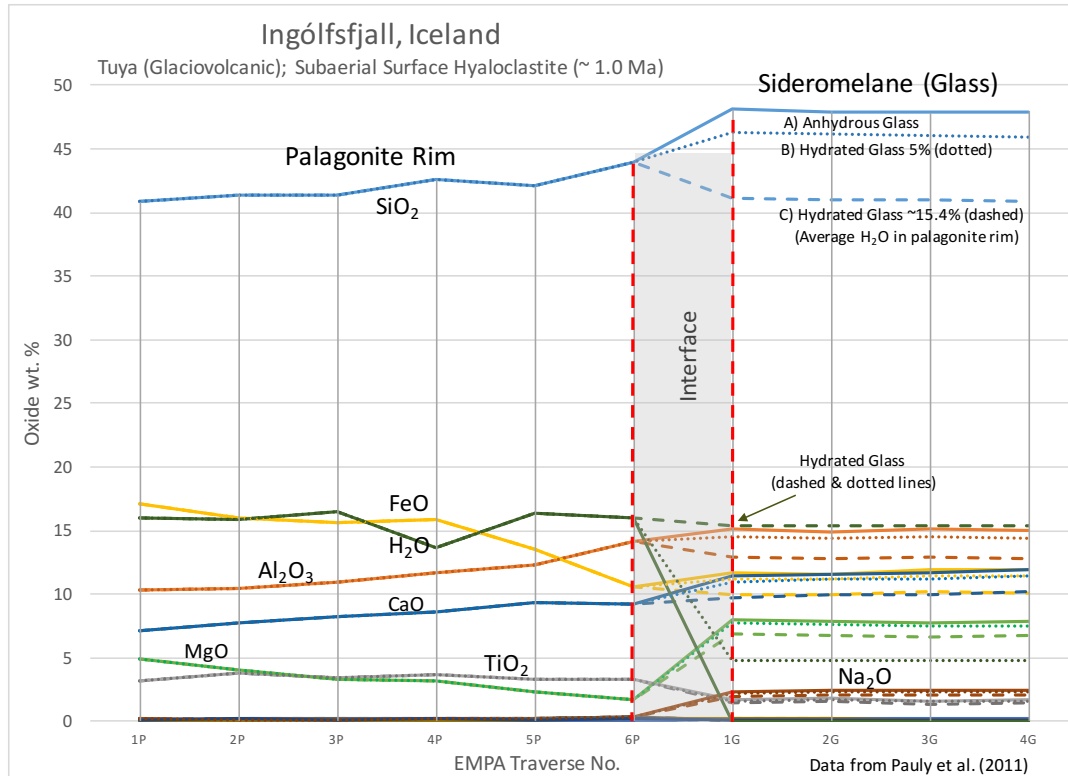


Figure 75 Ingólfssjall, Iceland glaciovolcanic glass-palagonite microprobe traverse showing sideromelane/glass as A) anhydrous (solid lines), B) hydrated with 5 wt.% H₂O (dotted lines), and hydrated to the average water (~15.4%) in palagonite (dashed lines). Data is from Pauly et al. (2011).

In the Ingólfssjall Icelandic (glaciovolcanic, surficial and subalkaline) glass-palagonite traverse, whether or not glass is anhydrous or hydrated (Figure 75), and similar to Helgafell and Wells Gray, 1) Ti and Fe increase in the palagonite rim relative to glass, with Ti staying constant across the palagonite rim and Fe peaking across the outer half of the palagonite rim, 2) Mg sharply decreases (relative to the glass) at the interface then gradually increases towards the rim's outer edge, and 3) Al, Ca and Na decrease (to a lesser extent when glass is hydrated) in the rim relative to the glass. Si appears to be isochemical or slightly increases (~1.0%) when glass is hydrated. Fe and H₂O appear to behave antithetically across the palagonite rim and have similar concentrations in the outer half of the palagonite rim.

Wells Gray and Helgafell traverses tend to match the most prominent trends in Hawaiian, Palagonia and Iceland traverses derived from Pauly et al. (2011) data. Trends do not correlate with glass composition, environment, or sample type (surface/subsurface). The prominent trends include (Table 15):

- 1) Al has higher concentrations in glass than in palagonite except in Wells Gray palagonite, which reaches the same Al-content as glass in the outer half of the rim;
- 2) Ti-content either spikes at the inner palagonite rim (Helgafell and Wells Gray) or remains constant at a higher level in the palagonite than the glass (all five traverses in Pauly et al., 2011);
- 3) Fe has increased concentrations in palagonite relative to glass except in the Hawaiian HSDP marine drillhole;
- 4) Mg sharply decreases at the inner palagonite rim, relative to glass, then progressively increases across and towards the outer palagonite rim;
- 5) Si decreases ~ 3–10 % in palagonite, relative to anhydrous glass. When glass is hydrated, Si appears isochemical.
- 6) Ca and Na decrease in palagonite relative to glass, in all cases; and
- 7) Si and H₂O show antithetic behaviour across palagonite rims in all cases, whereas Fe and H₂O behave antithetically only in subalkaline, surficial samples irrespective of environment.

The seven glass-palagonite microprobe traverses examined here show consistent element behaviour across differing magma compositions (alkaline and subalkaline), sample types (surficial and subsurface), and environments (glaciovolcanic/non-marine and submarine). This key observation agrees with Shikazono et al.'s (2005) study at Mt. Fuji. Apparently, during the natural conversion of volcanic ash to soil, patterns of element mobility do not depend on the composition of the ash, even though rates of glass weathering do (e.g. basaltic ash weathers more rapidly than rhyolitic ash) (Shikazono et al., 2005).

Abrupt geochemical change occurs at the glass-palagonite interface (this study, Hay & Iijima, 1968, Thorseth et al., 1991), indicating that this is a key location in the palagonitization process. Although Thorseth et al. (1991) suggested that rapid alteration forms a sharp textural boundary and slow alteration forms dendritic patterns, this distinction was not clearly apparent in this study. Although geochemical trends at the boundary are consistently sharp, textures

vary in location and consistency. Within one sample, spherical textures can proliferate at the glass-palagonite interface but dendritic textures can emanate outwards from vesicle palagonite rims within glass grains, therefore making it difficult to correlate texture to speed of alteration. Nowhere were gradational concentrations obvious, indicating that diffusion alone is not controlling palagonitization on the scale of measurement spacings.

Table 15 Element trends across the glass-palagonite interface and in palagonite rims in seven subalkaline/tholeiitic (6) and alkaline (1) microprobe traverses from Helgafell and Wells Gray (this study), and Pauly et al. (2011). Eight prominent trends (red, bolded) occur in at least 5/6 cases, and two trends (black, bolded) occur in at least 4-6 cases.

Location	Helgafell	Wells Gray, BC	SOH-1 Kilauea	Hilina Bench Kilauea	HSDP Mauna Loa	Palagonia	Ingólfssjall
Composition	Subalkaline	Alkali Olivine	Subalkaline	Subalkaline	Subalkaline	Subalkaline	Subalkaline
Environment	Glaciovolcanic	Glaciovolcanic	Marine	Marine	Marine	Marine	Glaciovolcanic
Sample Type	Surficial	Surficial	Drill core	Surficial	Drill core	Surficial	Surficial
Element Flux in Palagonite Rim	Massey	Massey	Pauly et al.	Pauly et al.	Pauly et al.	Pauly et al.	Pauly et al.
Ti-rich inner zone in palagonite	✓	✓	✓				
Ti higher in palagonite than glass			✓	✓	✓	✓	✓
Fe increases & Al decreases at interface	✓	✓	✓	✓		✓	
Fe increases & Al decreases near interface							✓
Fe higher in palagonite than glass	✓	✓	✓	✓		✓	✓
Fe decrease then increase (towards outer rim)					✓		
Fe-rich central zone	✓ vesicle only					✓	
Fe & H ₂ O are antithetic				✓		✓	✓
Al lower in palagonite than glass	✓		✓	✓	✓	✓	✓
Mg decreases, inner rim	✓ vesicle	✓	✓	✓		✓	✓
Mg increases progressively across rim	✓		✓	✓	✓	✓	✓
Mg-zone next to Ti-zone	✓	✓					
Si decrease ~3-10% (anhydrous glass)	✓	✓	✓	✓	✓	✓	✓
Si isochemical (hydrated glass)	✓		✓	✓		✓	✓
Si increases (hydrated glass)		✓			✓		
Si & H ₂ O are antithetic	✓		✓	✓	✓	✓	✓
Ca lower in palagonite than glass	✓	✓	✓	✓	✓	✓	✓
Na lower in palagonite than glass	✓	✓	✓	✓	✓	✓	✓

6.7 Major and Trace Element Mass Transfer

Mass transfer calculations for major and trace elements during palagonitization in Helgafell and Wells Gray show significant ranges of percent mass gains and losses in each of 31 glass-palagonite pairs (Table 13; Table 14). For example, concentrations of SiO_2 at Helgafell range from -42.2 to +7.2% (average: -13.7%), and at Wells Gray from -44.2 to +32.8% (average: -13.5%). A range of mass transfer is reasonable since palagonite is zoned geochemically and texturally. Previous studies generally presented an averaged value for mass transfer (not a range). For example, Pauly et al. (2011) found from isocon diagrams that SiO_2 decreases by an average of -58.0% in subalkaline and -48.5% in alkaline sideromelane. Conversely, microprobe traverses indicate more variation in mass change from sideromelane across to the palagonite rim. For example, traverse results from this study and Pauly et al. (2011) show the following decreases in concentrations during palagonitization: SiO_2 (-7.3 to -16.2 wt.%), MgO (-3.9 to -9.9 wt.%), MnO (-0.1 to -1.58 wt.%), CaO (-1.8 to -10.3 wt.%), and Na_2O (-1.9 to -2.4 wt.%). FeO increases in palagonite (5.0 to 9.4 wt.%) relative to glass in almost all cases except where FeO remains constant (Hawaiian HSDP drill core/marine sample). Al_2O_3 decreases in palagonite by -4.6 to -8.0 wt.% relative to glass in all cases but remains generally constant in Wells Gray and Helgafell glass and palagonite. TiO_2 increases by 1.5 to 3.1 wt.%, relative to glass, and remains constant across the palagonite rim, although in two cases (Helgafell and Wells Gray), there is an inner TiO_2 -rich zone in the palagonite rim. At Helgafell, the TiO_2 -rich zone contains ~ 5 wt.% TiO_2 (vesicle) and 3 wt.% (glass grain edge) relative to 2.0 wt.% in the glass. At Wells Gray, the TiO_2 -rich zone spikes to ~ 7 wt.% compared to ~2.3 wt.% in the glass. K_2O increases (0.2 to 1.3 wt.%) in palagonite in all cases, except for a loss (-0.4 wt.%) in one HSDP drill core/marine sample. P_2O_5 decreases (-0.3 to -0.4 wt.%) in all cases except where it remains constant in the Ingólfssjall glaciovolcanic sample. SO_3 increases (0.1 to 0.3 wt.%) in all cases (traverses from Pauly et al., 2011). Water content always increases in palagonite (14.1 to 30.8 wt.%), relative to anhydrous glass.

The changes in elemental concentrations indicate that the process cannot be entirely isochemical (Pauly et al., 2011; Stroncik & Schmincke, 2001). However, the observed changes can be explained in several ways. Addition of any elements to the sideromelane will force the relative concentrations of all other elements to decrease (see hydrated concentrations on

microprobe traverses (Figures 71 to 75). Similarly, loss of any element from the sideromelane will produce relative increases to the concentrations of other elements. The observation that some concentrations consistently decrease (Si, Mg, Ca, Mn, Na) and others consistently increase (H₂O, Fe, Ti) indicates similar reaction mechanisms during the conversion of sideromelane (alkaline and tholeiitic) to palagonite regardless of formation environment. Variations in the behaviour of Al may be more subject to environmental controls (e.g. pH). The ranges in concentrations are interpreted as indicating that any given sample may have preserved variable amounts of reaction progress between parental sideromelane (0% reaction) and palagonite (100% reaction).

6.8 Secondary Minerals: Compositional Control and Importance

Vesicles in Helgafell and Wells Gray sideromelane can, but not always, have three domains: 1) a palagonite rim (Figures 22, 36 and 39) 2) a uniform material that fills and lines the vesicle (Figure 39), and 3) a zeolite-like mineral primarily in the centre (Figures 37 to 40). Palagonite has been stoichiometrically associated with the clay mineral smectite, which is thought to partially replace palagonite prior to zeolitization (Drief & Schiffman, 2004; Jakobsson, 1972; Jercinovic, 1990; Pauly et al., 2011; Stroncik & Schmincke, 2001, 2002). The uniform material that lines and fills a vesicle at Helgafell (Figure 39) matches the smooth and uniform texture common for smectite (S. Jakobsson, personal communication, July 2015; Walton & Schiffman, 2003).

This succession of vesicle-lining materials (palagonite rim to smectite-lining and zeolite-filling minerals inwards from glass to the vesicle centre) was also observed by Drief and Schiffman (2004; Figure 4c). It is apparent that, first, hydrated palagonite forms at the edge of the vesicle when the sideromelane begins to react. A second layer forms on the palagonite in variable thicknesses as a uniform pore-lining smectite. Thirdly, in later stages of palagonitization, zeolite(s) accumulate on top of the smectite-like layer. Metastable phases during palagonitization reduce the total free energy of sideromelane/glass, as does the later precipitation of stable crystalline materials (Stroncik & Schmincke, 2001). In other words, the evolution of palagonitization reflects processes that continue to reduce the total free energy in the system.

The general formula for a common clay material associated with palagonitization is a variety of smectite (montmorillinite; $\text{Na}_{0.2}\text{Ca}_{0.1}\text{Al}_2\text{Si}_4\text{O}_{10}(\text{OH})_2 \cdot 10(\text{H}_2\text{O})$), which has too little Na and Ca, and too much Al to match the zeolite-like mineral in this study (Figure 37). A Na-rich zeolite, natrolite ($\text{Na}_2\text{Al}_2\text{Si}_3\text{O}_{10} \cdot 2\text{H}_2\text{O}$), also has too much Al in order to identify the secondary mineral. The sodium (Na_2SiO_3) or calcium (Ca_2SiO_4) metasilicate known as water glass is renowned for its high water absorption yet again is not a match. The identity of this study's zeolite-like mineral remains unconfirmed.

Smectites and zeolites that form from palagonitization in glaciovolcanic environments are important proxies for interpreting eruptive phases in glaciovolcanic and subaerial activity (Ackiss et al., 2016, 2017; Johnson & Smellie, 2007; Paque et al., 2016). Paque et al. (2016) found that ash erupted during the glaciovolcanic phase at Eyjafjallajökull has smectite but the subaerial phase does not. Zeolites in glaciovolcanic deposits at James Ross Island, Antarctica, were used to differentiate marine from freshwater deposits (Johnson & Smellie, 2007). A zeolite-rich palagonite measured by spectra on suspected glaciovolcanoes in the Sisyphi Montes region of Mars was used as a paleoclimate proxy for the location of prior ice sheets (Ackiss et al., 2016, 2017).

The conversion of ocean floor tholeiitic glasses to palagonite and authigenic minerals, such as smectite and phillipsite, was found to transition phillipsite from Na>K (early stages) to K>Na in later stages (Honnorez, 1981). It was hypothesized that early phillipsite (Na>K) selectively and irreversibly exchanged Na for K from solution to become K-rich. Perhaps, the unusually high-Na zeolite-like mineral analyzed at Helgafell (but it also appears in Wells Gray samples) represents an early-stage zeolite. It is important to note that the depletion of Na in palagonite apparent in microprobe traverses and mass transfer calculations may have been the source for the Na-rich zeolite-like mineral in vesicles.

6.9 Controlling Mechanisms

Extensive possibilities exist for compounds to form or dissolve as palagonitization progresses, especially in the incipient aqueous environment of glaciovolcanism, and although the controlling mechanisms for palagonitization are ambiguous, a discussion follows.

Dissolution initially leaches alkali cations from glass as a function of the sq. root of time ($t^{1/2}$), until solution saturation prevents further dissolution (Bunker & Casey, 2016, pg. 445).

Studies on silica-glass have found that its non-crystalline structure is made of silicate rings that can have openings equal to or larger than the size of a water molecule, therefore, glass (sideromelane) can be penetrated by water via molecular diffusion (Bunker & Casey, 2016, pg. 461). The microzoned hemispheres that propagate into glass grains may be a texture representing diffusion of water into the glass grain from the glass-palagonite interface (Figure 29). The palagonite rim may function as a diffusion barrier.

Dissolution of sideromelane occurs over time and has an effect on pH (Kawana, 1997). Hydrolysis involves the chemical breakdown of volcanic glass due to reactions with water, when H^+ and OH^- ions can easily enter glass. A hydroxide (OH^-) can function as a vehicle for water to get into loose structures such as glass (Bunker & Casey, 2016).

As described in Chapter 2, corrosion processes occur in the breakdown of glass and formation of alteration materials including palagonite. The concaved and crenulated texture at the edge of glass grains and at the glass-palagonite interface (Figure 29) has a similar appearance to glass associated with corrosion (Anaf, 2010, their Figure 5). Grambow (2011) suggested that alkaline Earth cations (e.g. Ca^{2+} , Mg^{2+}) increase resistance to corrosion. Based on this hypothesis, Helgafell's tholeiitic sideromelane (higher Mg and Ca) should be more resistant to corrosion than the alkali olivine basaltic sideromelane at Wells Gray.

The aqueous corrosion of glass is thought to proceed as follows: 1) hydration of glass Si-networks, 2) formation of a thin reaction zone, 3) congruent (complete) dissolution of all hydrated glass elements, and 4) the formation of glass-gel (Vernaz & Dussossoy, 1992).

In the early magma-ice/meltwater environment, each glass grain (including vesicles) forms a reaction zone along the edge and a palagonite rim (Step 2, Figure 76). Primarily at the glass-palagonite interface (and possibly at other areas in the glass grain), a gel-material (Figure 23) forms over time as the glass network breaks down (Step 3, Figure 76). Secondary crystalline minerals accumulate in vesicles and between grains increasing density and cement the tuff deposit (Step 4; Figure 76). When the glass completely dissolves, a chemically and texturally zoned palagonite rim remains with or without primary minerals (i.e. olivine, plagioclase) that remain unaltered (Figure 25) for a significant time (Step 5, Figure 76).

This 5-step evolutionary process (Figure 76) summarizes the stages of palagonitization based on previous studies of palagonitization (Pauly et al., 2011; Stroncik & Schmincke, 2001, Figure 3), more general studies of the breakdown of glass (Bunker & Casey, 2016; Vernaz &

Dussossoy, 1992) and the results of this comparative study of palagonitization at Helgafell and Wells Gray.

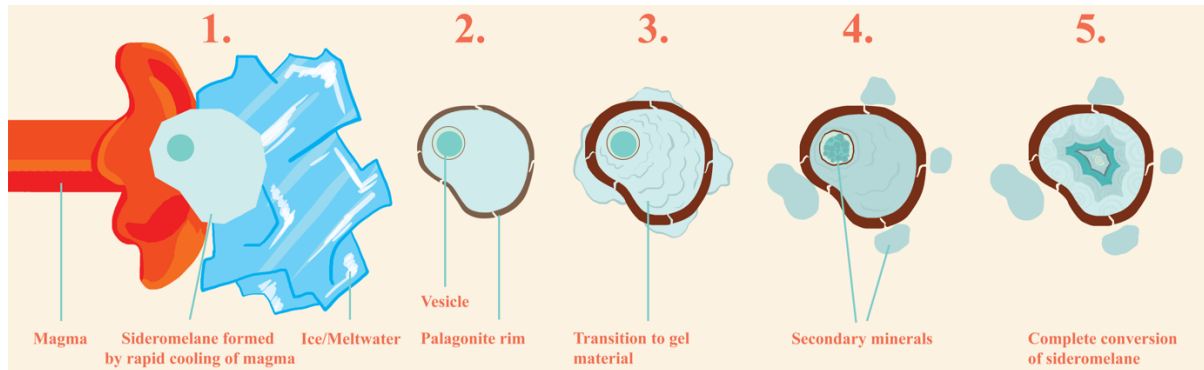


Figure 76 Palagonitization summarized as a five-step alteration process that progressively forms: 1) sideromelane grains by rapid cooling in the magma-ice/water environment, 2) a palagonite rim, 3) gel-material, and 4) secondary minerals, followed by 5) complete conversion of glass into palagonite and secondary minerals (no glass remaining). (Illustration: Alexis Shuffler, 2015).

6.10 Palagonite Rim Thickness and Gel-Material

The dark brown-coloured palagonite rims at Wells Gray and Helgafell are inconsistent with the hypothesis (Furnes, 1975; Jakobsson, 1978; Stroncik & Schmincke, 2001:) that dark-brown to red-brown palagonite is less common and forms at higher temperatures (e.g. fumaroles, tropical climates). Wells Gray and Helgafell are neither tropical or a place where features such as fumaroles have been observed and the palagonite rims are dark brown. Unless deep burial or high geothermal conditions (e.g. intrusion of dikes) occurred, high temperatures would not be expected following the glaciovolcanic eruptions at Wells Gray or Helgafell.

The terms gel-palagonite and fibro-palagonite, first introduced by Peacock (1926), have been used to describe differences in texture during palagonitization. Stroncik and Schmincke (2001) suggested that the term palagonite be used only for the gel-phase, because fibro-palagonite was hypothesized to be a mixture of gel-palagonite and smectite.

The lower modal proportions of palagonite rims at Helgafell (~8.7% vs. ~14.4%) than Wells Gray, and higher percentage of gel-material at Helgafell (~18.9% vs. 6.2%) indicate that more glass at Helgafell has converted to gel-material than at Wells Gray (palagonite rims and gel-material were described in section 5.1). Helgafell samples have a higher percent of the secondary zeolite-like mineral (~5.6% vs. ~1.4%), which also indicates increased palagonitization extent. The higher proportion of sideromelane in Helgafell samples compared

to Wells Gray (~28.5% vs. ~18.0%) reflects the abundance of microlites and thicker palagonite rims on Wells Gray sideromelane. It is plausible that palagonitization extent is measurable by the proportion of gel-material and secondary material rather than the thickness of palagonite rims, since rim thickness appears to remain constant whether the sideromelane is fresh or completely reacted (Figure 25).

Palagonite is defined in this study as the amorphous and hydrated material forming defined rims around glass grains, in vesicles, and in fractures. The gel-material is translucent and lacks form or shape, thus it is petrographically different from isotropic sideromelane grains and anisotropic palagonite rims. As previously discussed (Chapter 2 and this chapter), early phases in hydrolysis (chemical breakdown of glass dissolution by water) commonly produce hydrated gel-glass in synthetic glass studies (Anaf, 2010; Bunker & Casey, 2016; Grambow, 2011), whereas gel-palagonite or fibro-palagonite are terms for materials produced in natural basaltic glass studies (Jercinovic, 1990, Thorseth et al., 1991; Stroncik & Schmincke, 2001). The gel-material (Figure 23) is optically similar in colour (honey-coloured) to sideromelane in PPL, differs from palagonite rims (dark brown in PPL and delineates glass grains), and is translucent without form or shape. Due to its reference in previous natural and synthetic glass studies, gel-material is an important stage in palagonitization yet requires further study for defining and understanding its properties.

6.10.1 Palagonitization Extent and Rates

The similar thickness of palagonite rims in one locality, whether sideromelane grains are fresh or completely altered, indicate that, contrary to previous studies, palagonite rim thickness is not a reliable indication of palagonitization extent (Pauly et al., 2011). Jacobsson and Moore's (1986) observation of palagonitization of the seafloor volcano, Surtsey, found that increased temperatures induced thicker palagonite rims. Based on these observations and the thicker palagonite rims observed in Wells Gray samples, the glaciovolcanic material at Second Canyon, Wells Gray may have cooled more gradually, been exposed to a warmer overall climate or had a more active geothermal system over a longer duration than at Helgafell. But, the increased gel-material at Helgafell points to increased rates of reaction that are indicative of increased palagonitization extent, rather than the thickness of palagonite rims.

Abrajano (1988) found that silica leach rates are dependent on glass composition and argued that one of the primary controls on the extent of palagonitization is the composition of sideromelane, and not the age of deposition. Abrajano's (1988) experimental study of the effects of glass composition on silicate-detachment rates (destabilizing the Si-tetrahedra by hydration, corrosion or leaching) found a significant correlation between composition and hydration rate (the rate glass is hydrated). Therefore, in addition to other controls on palagonitization (i.e. temperature, pH, time, or depth of burial), compositionally different sideromelane formed in glaciovolcanic environments should have different silicate-detachment reaction rates. If this hypothesis is correct, then Helgafell's tholeiitic sideromelane is expected to have higher silicate-detachment reaction rates due to lower alkali-content than at Wells Gray. This is consistent with the higher palagonitization extent at Helgafell based on higher proportions of both gel-material and secondary mineral growth (zeolite-like).

Although the higher modal proportion of gel-material found at Helgafell supports the claim of Pauly et al. (2011) that alkaline sideromelane dissolves more slowly than subalkaline sideromelane, the thicker palagonite rims at Wells Gray do not. Helgafell's subalkaline sideromelane appears to be dissolving into gel-material (18.9%) at more than double the extent of Wells Gray's alkali sideromelane (6.2%) even though palagonite rims are thicker at Wells Gray (~10-20 μm) than Helgafell (~6-10 μm).

Completely altered sideromelane grains (100% palagonitization) have concentric zones progressing inwards from the palagonite rim with the innermost zone spherically textured at the empty cavity (geode- or agate-like). Palagonite rims on remnant or fresh sideromelane grains are of similar thickness (Figure 25). The banded appearance of completely palagonitized sideromelane grains does not appear to have been previously reported, although an illustration in Stroncik and Schmincke (2002: their Figure 12a) is remarkably similar to Figure 25.

6.10.2 Vesicularity and Microlites

Vesicularity (vesicle count) and microlite content in sideromelane provide important information about the magma at the time of fragmentation, and affect the palagonitization process. Not only are Helgafell and Wells Gray basalts compositionally different, Helgafell sideromelane is vesicular (~30.7%) and microlite-poor (0.1%), whereas Wells Gray sideromelane is microlite-rich (12.3%) and poorly vesicular (4.9%). Vesiculation allows sulfur

and other gases to be exsolved from the melt at water depths of < 200 m (Moore, 1973). Moore (1973) found that alkalic (K_2O -rich) basalt was more vesicular than tholeiitic (K_2O -poor) basalt possibly due to higher initial water-content in higher K_2O -content lavas. Primary controls on vesicularity are the volatile content of magma at the time of eruption and confining pressures from the overlying water column (Duffield, 1979). This study does not support Moore's (1973) hypothesis, since Helgafell's tholeiitic (lower K) sideromelane is significantly more vesicular than Wells Gray's alkali (high K) basalt, but higher confining pressure from a deep water/ice column may have existed at Wells Gray.

6.11 Unique Textures

Some of the unique textures described in Chapter 5 allude to microscopic processes that contribute to palagonitization but are not well understood. In Helgafell and Wells Gray sideromelane, multiple, subparallel and linear microveins between vesicles formed after palagonitization with one central microfracture connecting palagonite rims through the microveins (Figure 31). The microveins may form from stresses related to the formation of palagonite, or with associated hydration and expansion that yield stresses in glass that lead to more fracturing between vesicles and formation of microveins. Alternatively, the microveins may result from gas expansion in vesicles. The orange colour of the microveins in PPL indicates that they result from oxidative process but it is not obvious how or why the microveins form.

Some glass and palagonite have spherical textures at their interface (Figures 29 and 30), which have been reported by other studies (Eggerton & Keller, 1982; Trichet, 1970 as referenced in Zhou & Fyfe, 1989; Zhou & Fyfe, 1989; Thorseth et al., 1991). A $\sim 100\text{--}8000 \text{ \AA}$ spherical texture comprising 70% of the active leaching zone at the edge of glass grains was thought to result from the mechanical erosion of circulating water (Trichet, 1970 as referenced in Zhou & Fyfe, 1989). More recent hypotheses are that the spherical features represent phases formed during hydration (Eggerton & Keller, 1982), and have been described as 200 – 600 \AA in diameter within gel-palagonite (Zhou & Fyfe, 1989). The spherical texture reported by Thorseth et al. (1991; Figure 4a) is similar in appearance to those found in Helgafell and Wells Gray sideromelane and palagonite. The spherical textures represent key stages in the palagonitization process. Although the origin of the texture remains unclear, possible

mechanisms responsible for their formation may be: 1) spherical devitrication (spherulites), 2) Liesegang bands, or 3) spinodal decomposition.

Concentrically banded spherical textures may represent Liesegang bands, which result from diffusion of water in silica gels (Kumar & Steed, 2014). The German chemist and geologist, R. E. Liesegang, first studied their formation using silica-gel experiments. He proposed that colloidal particles of silica partially lose water to become a silica gel. Regular rhythmic precipitation forms concentric bands (Driscoll, 1938). Liesegang bands have been associated with the intriguing features in agates, which are composed of cryptocrystalline anhydrous silica with concentric, circular bands (Driscoll, 1938). Gel-phases (known to host Liesegang bands) are associated with supersaturation and non-equilibrium (Driscoll, 1938), which also may be present in the environment at the glass-palagonite interface.

Spinodal decomposition occurs spontaneously without nucleation in order to reduce free energy in unstable systems (Favvas, 2008). Since glass is thermodynamically unstable, it may undergo spinodal decomposition as well. Crovisier (1987) suggested that spheres in glass result from a metastable, non-spontaneous system (non-spinodal), and not an unstable system (spinodal). The zoned spherical textures in glass and palagonite could represent nucleation points where phase separations occur, or be related to hydration/dehydration processes occurring at the glass-palagonite interface.

The dendritic texture can resemble tubules or tunnels emanating away from vesicles (Figure 34) which numerous studies attribute to microbial activity in glass (Banerjee et al., 2006; Furnes et al., 2007; Ivarsson, 2012). The bioalteration texture in Figure 1 (Fisk & McLaughlin, 2013) closely resembles the tubular texture in sideromelane from Wells Gray (Figures 33 and 34). Pitting of sideromelane grains is common at Helgafell and Wells Gray (Figure 40), which is also a texture hypothesized to result from microbial activity (Banerjee et al., 2006; Fisk & McLaughlin, 2013; Furnes, 2008; Nikitzuk et al., 2013).

6.12 Future Work Recommended

The recent knowledge developing from experimental studies on the alteration of natural and synthetic glasses (Anaf, 2010; Bunker & Casey, 2016; Grambow, 2011;) should be integrated into future studies on palagonitization. Data analysis will measure molecular-bonded and non-bonded H₂O in sideromelane, the palagonite rim and gel-material (including

the spherical texture at the glass-palagonite interface) in order to prevent misguided assumptions for water and to improve data interpretation since water is the significant component involved in the palagonitization process. Specific observations for textural-geochemical relationships from microprobe traverses on compositionally different sideromelane (basaltic magma type) originating from similar and different environments will help to interpret key processes and the controls on chemical variability in palagonitization.

Chapter 7: Conclusions

The conversion of basaltic volcanic glass to palagonite is a complex process. The prediction of Furnes (1978) that chemically different basaltic glasses under similar physio-chemical conditions will have compositionally different palagonite is supported by the results of this study.

Tholeiitic sideromelane at Helgafell alters to a distinctly different composition of palagonite than that formed from alkali olivine basalt at Wells Gray. Although sideromelane composition strongly controls the composition of palagonite, the process of palagonitization appears to be independent of sideromelane composition. Additional controls on palagonite's chemistry, shown by multi-dimensional scaling, were the H₂O-content in palagonite, element solubility and igneous processes occurring in the melt when sideromelane formed.

The examination of seven microprobe traverses indicates that similar trends in element flux occur across the glass-palagonite interface and palagonite rim with no preference to original composition (alkaline or subalkaline), environment (marine or freshwater) or surface type (surfiical or drill core sample). Moreover, eight prominent trends in palagonite relative to sideromelane include: 1) either an increase in Ti or a Ti-rich inner zone, 2) Fe increasing and 3) Al decreasing in palagonite, 4) Ca and Na virtually disappearing in the palagonite rim, 5) Mg decreasing at the inner palagonite rim followed by a gradual increase in concentration towards the outer palagonite rim, 6) Si decreasing ~ 3-10% in palagonite when glass is assumed to be anhydrous, but appearing to be isochemical when the percent water in sideromelane is normalized to the percent water in palagonite (data set 2). 7) Si and/or Fe can behave antithetically with H₂O in palagonite. The behaviour of Mg indicates the progression from lower pH at the glass-palagonite interface to a higher pH (related to the solubility of Mg) towards the outer area of the palagonite rim.

Multi-dimensional scaling shows certain soluble elements group similarly with water, whereas immobile elements (e.g. REEs) cluster in opposing dimensions and, in some cases, with SiO₂, MgO and Al₂O₃ indicating retention through smectite formation (situated with immobile elements). Palagonite compositions may reflect igneous processes such as plagioclase and olivine formation in the melt when the basaltic glass and palagonite first formed in the active glaciovolcanic environment. The MDS analyses of all major element data

for sideromelane, palagonite and smectite shows that samples associate based on water content. Further, the largest gains and greatest losses in mass transfer occurring in high water and low water palagonite do not appear related to water content but water shows to be a controlling factor in one dimension when comparing all palagonite with a smectite analysis. Thus, the role of water content must be crucial to palagonitization due to its significant amount in palagonite and should be further tested in detail in future studies.

The evidence of a post-eruptive glacial advance at Wells Gray's lower latitude but not at Helgafell's more northern latitude indicates that glaciovolcanic activity occurred in a later part of the Pleistocene at Helgafell, and that the Wells Gray deposit may be older. Although palagonite rims are slightly thicker in Wells Gray samples, there is no other indicator of relative ages. The thickness of palagonite rims generally remain the same within one locality whether they are on fresh or completely altered sideromelane. The geode or agate-like appearance of fully altered sideromelane indicates that palagonite acts a barrier at the periphery of sideromelane grains during dissolution-precipitation processes primarily inside the rim.

The extent of gel-material may more clearly indicate palagonitization extent than the thickness of palagonite rims (appears to remain the same at one locality throughout palagonitization). Helgafell samples have more than twice the gel-material (~19.1%) than Wells Gray (~6.2%) samples. Even though Helgafell's palagonite rims are thinner, the palagonitization extent based on percent gel-material appears to be greater at Helgafell. The higher vesicularity at Helgafell (~30.7%) than at Wells Gray (~4.9%) indicates higher pressures from a greater thickness of glacial ice/meltwater during glaciovolcanism at Wells Gray. Since volcanic activity at Helgafell is estimated to have erupted into a >500 m thick glacier (Schopka et al., 2006), the extent of glacial thickness infilling Clearwater Valley at Wells Gray is estimated to have been greater than 500 m, and may have exceeded 1000 – 2000 m (from estimations of ice thickness in the Canadian cordillera during the Pleistocene) during glaciovolcanism.

Geochemical-textural relationships provide clues to processes occurring during palagonitization. The zoned spherical textures in glass and/or palagonite at the glass-palagonite interface may represent diffusion of water into sideromelane, hydration/dehydration processes occurring at the glass-palagonite interface and/or indicate phase changes in metastable materials (glass and palagonite) during non-spinodal decomposition. Unique textures, such as

multilinear parallel textures in sideromelane that link vesicles record diverse processes at work during palagonitization.

Five stages describe palagonitization as commencing when sideromelane forms from superecooled magma during glacial ice/meltwater interaction. A hydrated palagonite rim demarcates sideromelane grains acting as a barrier (e.g. solution) which is followed by the formation of gel-material and secondary minerals. Eventually, the complete conversion of sideromelane leaves a remnant palagonite rim with progressive layers of precipitated materials and secondary minerals in a geode or agate-like form that consolidate the glaciovolcanic environment.

References

- Abrajano, T. A., Jr., Bates, J. K., & Bohlke, J. K. (1988). Linear free energy relationships in glass corrosion. *Material Research Society Symposium Proceedings*, 125, 383-392. doi: 10.1557/PROC-123-253
- Abe-Ouchi, A., Salto, F., Kawamura, K., Raymo, M. E., Okuno, J., Takahashi, K., & Blatter, H. (2013). Insolation-driven 100,000-year glacial cycles and hysteresis of ice-sheet volume. *Nature*, 500, 190-193. doi: 10.1038/nature12374
- Ackiss, S. E., Horgan, B., Campbell, A., Seelos, F. P., Farrand, W. H., & Wray, J. J. (2016). Mineralogical Evidence for Subglacial Volcanoes in the Sisyphi Montes Region of Mars. LPI Contributions 1926, *47th Lunar and Planetary Science Conference*. Abstract #1305.
- Ackiss, S. E., Horgan, B., Gudnason, J., Haberle, C., Thorsteinsson, T., & Thordarson, T. (2017). The mineralogic variability of Icelandic palagonites: An analog study for Mars. LPI Contributions R617. *48th Lunar and Planetary Science Conference*. Abstract #2500.
- Allen, C. C., Gooding, J. L., Jercinovic, M., & Keil, K. (1981). Altered basaltic glass; a terrestrial analog to the soil of Mars. *Icarus*, 45, 347-369.
- Anaf, W. (2010). Study on the formation of heterogeneous structures in leached layers during the corrosion process of glass. *CeROArt: Hors series*, 1. Retrieved from <http://ceroart.revues.org/1561>
- Bakaev, V. & Steele, W. (1996). Computer simulation of adsorption on amorphous oxide surfaces. In A. Dabrowski and V. A. Tertykh (Ed.), *Studies in Surface Science and Catalysis: Vol. 99. Adsorption on new and modified inorganic solutions* (pp. 335-339).
- Banerjee, N. R., Furnes, H., Muehlenbachs, K., Staudigel, H., & de Wit, M. (2006). Preservation of ~3.4-3.5 Ga microbial biomarkers in pillow lavas and hyaloclastites from the Barberton Greenstone Belt, South Africa. *Earth and Planetary Science Letters*, 241, 707-722. doi:10.1016/j.epsl.2005.11.011
- Baumgartner, L. P. & Olsen, S. N. (1995). A least-squares approach to mass transport calculations using the isocon method. *Economic Geology*, 90(5), 1261-1270. doi:10.2113/gsecongeo.90.5.1261
- Best, M. G. (2003). *Igneous and metamorphic petrology* (2nd ed.). Malden, MA: Blackwell Publishers.
- Bevier, M. L., Armstrong, R. L., & Souther, J. G. (1979). Miocene peralkaline volcanism in west-central British Columbia – its temporal and plate-tectonics setting. *Geology*, 7(8), 389-392. doi: 10.1130/0091-7613

- Bonatti, E. (1965). Palagonites, hyaloclastites and alteration of volcanic glass in the ocean. *Bulletin of Volcanology*, 28(1), 257-269. doi: 10.1007/BF02596930
- Bonotto, D. M., Jimenez-Rueda, J. R., Fagundes, I. C., & Filho, C. R. (2017). Weathering processes and dating of soil profiles from São Paulo State, Brazil, by U-isotopes disequilibria. *Applied Radiation and Isotopes*, 119, 6-15. doi: 10.1016/j.apradiso.2016.10.011
- Bots, P. & Behrends, T. (2008). Uranium mobility in subsurface aqueous systems; the influence of redox conditions. *Geochemistry of the Earth's Surface*, 72, 381-384. doi: 10.1180/minmag.2008.072.1.381
- Bowman, L., Pollock, M., Edwards, B. R., & Alcorn, R. J. (2011). Geochemical and field relationships of pillow and dike units in a subglacial pillow ridge, Undirhlíðar quarry, southwest Iceland. *Geological Society of America 2011 annual meeting*, 43, 102.
- Brown, N. E. & Navrotsky, A. (1994). Hematite-ilmenite (Fe₂O₃-FeTiO₃) solid solutions; the effects of cation ordering on the thermodynamics of mixing. *American Mineralogist*, 79(5-6), 485-496.
- Buddington, A.F. & Lindsley, D.H. (1964). Iron-titanium oxide minerals and synthetic equivalents. *Journal of Petrology*, 5(2), 310-357. doi:10.1093/petrology/5.2.3.1
- Bunker, B. C. & Casey, W. H. (2016). *The Aqueous Chemistry of Oxides*. New York: Oxford University Press.
- Bunsen, R. (1847). Beitrag zur Kenntnis des islandischen Tuff – gebirges. *Ann. Chem. Pharm.*, 61, 265-279.
- Calvert, J. B. (2002). *Properties of colloids: An introduction*. Retrieved from <http://mysite.du.edu/~jcalvert/phys/colloid.htm>
- Cannata, C., Rosa, R., Donato, P., & Taddeucci, J. (2014). Ash features from ordinary activity at Stromboli Volcano. *International Journal of Geosciences*, 5, 1361-1382. doi: 10.4236/ijg.2014.511111
- Cloutis, E. A., Mann, P., Izawa, M. R. M., Applin, D. M., Samson, C., Kruzelecky, R., ... Fry, C. (2015). The Canadian space agency planetary analogue materials suite. *Planetary and Space Science*, 119, 155-172. doi: 10.1016/j.pss.2015.09.001
- Clifton, A. (2003). Reykjanes Field Trip: Magmatic interaction at an oblique rift zone. *Nordic Volcanological Institute*. Retrieved from <http://www.norvol.hi.is/~thora/summer2003/notes/ReykjanesFieldTrip.pdf>
- Cockell, C. C., Changela, H. G., Bryce, C., & Brearley, A. J. (2014). SEM-TEM study of Icelandic palagonite; application to hydrated silicate gel interfaces in the nakhlite meteorites

- and secondary processes on Mars. *45th Lunar and Planetary Science Conference*. Abstract #2890 retrieved from <http://www.hou.usra.edu/meetings/lpsc2014/pdf/2890.pdf>
- Condie, K. C. (2003). Incompatible element ratios in oceanic basalts and komatiites: Tracking deep mantle sources and continental growth rates with time. *Geochemistry Geophysics Geosystems*, *4*(1), 1-28. doi: 10.1029/2002GC000333
- Cousins, C. R., Crawford, I. A., Carrivick, J. L., Gunn, M., Harris, J., Kee, T. P., ... Joy, K. H. (2013). Glaciovolcanic hydrothermal environments in Iceland and implications for their detection on Mars. *Journal of Volcanology and Geothermal Research*, *256*, 61-77. doi: 10.1016/j.jvolgeores.2013.02.009
- Crovisier, J. L., Fritz, B., Grambow, B., & Eberhart, J. P. (1985). Dissolution of basaltic glass in seawater: experiments and thermodynamic modelling. *Material Research Society Symposium Proceedings*, *50*. doi: 10.1557/PROC-50-273
- Crovisier, J. L. (1987). Dissolution of basaltic glass in seawater: Mechanism and rate. *Geochimica et cosmochimica acta*. *51*(11), 2977-2990. doi: 10.1016/0016-7037(87)90371-1
- Crovisier, J. L., Honnorez, J., Fritz, B., & Petit, J. C. (1992). Dissolution of subglacial volcanic glasses from Iceland – laboratory study and modeling. *Applied Geochemistry Supplement*, *7*(1), 55-81. doi: 10.1016/S0883-2927(09)80064-4
- DeMets, C., Gordon, R. G., Argus, D. F. & Stein, S. (1994). Effect of recent revisions to the geomagnetic reversal time scale on estimates of current plate motions. *Geophysical Research Letters*, *21*, 2191-2194. doi: 10.1029/94GL02118
- DOSECC Exploration Services (2016). *Surtsey volcano drilling project*. Retrieved from <http://dosecc.com/surtsey-volcano-iceland>
- Drief, A. & Schiffman, P. (2004). Very low-temperature alteration of sideromelane in hyaloclastites and hyalotuffs from Kilauea and Mauna Kea volcanoes: Implications for the mechanism of palagonite formation. *Clays and Clay Minerals*, *52*(5), 622-634. doi: 10.1346/CCMN.2004.0520508
- Driscoll, J. (1938). *A study on the origin of banded agates* (B.Sc. thesis). Retrieved from http://digitalcommons.mtech.edu/cgi/viewcontent.cgi?article=1081&context=bach_theses
- Duffield, W. A. (1979). Significance of contrasting vesicularity in basalt from DSDP sites 407, 408, 409 on the west flank of the Reykjanes Ridge. *U. S. Geological Survey Initial Reports of the Deep Sea Drilling Project*, *49*, 715-719.
- Earle, S. (2015). Physical Geology, BC Open Textbook Project. Volcanic locations: Wood (1993); Hickson, Cathie. Retrieved from <https://opentextbc.ca/geology>

- Edwards, B. R. & Russell, J. K. (2002). Glacial influences on morphology and eruptive products of Hoodoo Mountain volcano, Canada. In: Smellie J. L. & Chapman M.G. (Eds.) Volcano-ice interaction on Earth and Mars. *Geological Society of London Special Publication* (pp. 179-194).
- Edwards, B. R., Russell, J. K., & Anderson, R. G. (2002). Subglacial phonolitic volcanism at Hoodoo Mountain volcano, northern Canada Cordillera. *Bulletin of Volcanology*, 64(3), 254-272. doi: 10.1007/s00445-002-0202-9
- Eggleton, R. A. & Keller, J. (1982). The palagonitization of limburgite glass – a TEM study. *Neues Jahrbuch Mineral Monatsh*, 7, 321-336.
- Egli, M., Filip, D., Mavris, C., Fischer, B., Gotze, J., & Raimondi, S. (2012). Rapid transformation of inorganic to organic and plant-available phosphorous in soils of a glacier forefield. *Geoderma*, 189-190, 215-226. doi:10.1016/j.geoderma.2012.06.033
- Einarsson, P. (1994). Geology of Iceland. Rocks and landscape. Mál og Menning, Reykjavík, 309.
- Faure, G. (1998). Principles and applications of geochemistry: a comprehensive textbook for geology students (2nd ed.). Upper Saddle River, NJ: *Prentice Hall, Inc.* (pp. 121-123).
- Favvas, E. P. & Mitropoulos, A. Ch. (2008). What is spinodal decomposition? *Journal of Engineering Science and Technology Review*, 1, 25-27. Retrieved from <http://www.jestr.org/downloads/volume1/fulltext5>
- Finney, B., Turner, S., Hawkesworth, C., Larsen, J., Nye, C., George, R., Bindeman, I., & Eichelberger, J. (2008). Magmatic differentiation at an island-arc caldera: Okmok volcano, Aleutian Islands, Alaska. *Journal of Petrology*, 49(5), 857-894.
- Fisher, A. T. & Wheat, C. G. (2010). Mountains in the Sea: Seamounts as conduits for massive fluid, heat, and solute fluxes on ridge flanks. *Oceanography*, 23(1), 74-87.
- Fisk, M. & McLaughlin, N. (2013). Atlas of alteration textures in volcanic glass from the ocean basins. *Geosphere*, 9(2), 317-341. doi: 10.1130/GES00827.1
- Floyd, P. A., & Winchester, J. A. (1975). Magma type and tectonic setting discrimination using immobile elements. *Earth and Planetary Science Letters*, 27(2), 211-218. doi: 10.1016/0012-821X(75)90031-X.
- Fowler, A. D., Berger, B., Shore, M., Jones, M. I., & Ropchan, J. (2002). Supercooled rocks: Development and significance of varioles, spherulites, dendrites and spinifex in Archean volcanic rocks, Abitibi Greenstone belt, Canada. *Precambrian Research*, 115(1-4), 311-328. doi: 10.1016/S0301-9268(02)00014-1

- Fowler, A. P. G. (2015). Evolution of fluid-rock interaction in the Reykjanes geothermal system, Iceland: Evidence from Iceland Deep Drilling Project core RN-17B. *Journal of Volcanology and Geothermal Research*, 302, 47-63. doi:10.1016/j.jvolgeores.2015.06.009
- Francis, P. & Oppenheimer, C. (2004). *Volcanoes* (2nd ed.). New York: *Oxford University Press*.
- Friedman, I. I. & Smith, R. L. (1960). A new dating method using obsidian – Part I, The development of the method. *American Antiquity*, 25(4), 476-522.
- Furnes, H. (1978). Element mobility during palagonitization of a subglacial hyaloclasite in Iceland. *Chemical Geology*, 22, 249-264. doi:10.1016/0009-2541(78)90034-7
- Furnes, H. (1984). Chemical changes during progressive subaerial palagonitization of a subglacial olivine tholeiite hyaloclastite: a microprobe study. *Chemical Geology*, 43(3-4), 271-285. doi:10.1016/0009-2541(84)90054-8
- Furnes, H., McLoughlin, N., Muehlenbachs, K., Banerjee, N., Staudigel, H., Dilek, Y.,.... & Schiffman, P. (2008). Links between geological processes, microbial activities and evolution of life. *Oceanic pillow lavas and hyaloclastites as habitats for microbial life through time – a review*. (Eds. Dilek, Y., Furnes, H. and Karlis, Muehlenbachs). *Springer*, 4, 1-68.
- Gale A., Dalton, C. A., Langmuir, C. H., Su, Y., & Schilling, J. (2013). The mean composition of ocean ridge basalts. *Geochemistry Geophysics Geosystems*, 14, 489–518, doi:10.1029/2012GC004334
- Gardner, J. E., Befus, K. S., Watkins, J., Hesse, M., & Miller, N. (2012). Compositional gradients surrounding spherulites in obsidian and their relationship to spherulite growth and lava cooling. *Bulletin of Volcanology*, 74(8), 1865-1879.
- Godlevskiy, M. N. (1967). The differential mobility of components during the formation of copper-nickel-sulfide ores. *Geologiya Rudnykh Mestorozhdeniy*, 9(2), 17-31.
- Grambow, B. (2011). Corrosion of glass. In R. Winston Rene (Ed.), *Uhlig's Corrosion Handbook (3rd ed.)*. *John Wiley & Sons, Inc.* (pp. 399-420).
- Grant, J. A. (1986). The isocon diagram – a simple solution to Gresens' equation for metasomatic alteration. *Economic Geology*, 81, 1976-1982. doi: 10.2113/gsecongeo.81.8.1976.
- Greenough, J. D., Fryer, B. J., & Robinson, P. T. (1990). Geochemical effects of alteration of mafic rocks from Indian Ocean Site 706. *Proceedings of the Ocean Drilling Program, Scientific Results*, 115, 85-92. Retrieved from http://www-odp.tamu.edu/Publications/115_SR/VOLUME/CHAPTERS/sr115_08.pdf.

- Greenough, J. D., Fryer, B. J., & Mallory-Greenough, L. (2010). Trace element geochemistry of Nova Scotia (Canada) maple syrup. *Canadian Journal of Earth Sciences*, 47(8), 1093-1110. doi: 10.1139/E10-055
- Greenough, J. D. & Ya'acoby, A. (2013). A comparative geochemical study of Mars and Earth basalt petrogenesis. *Canadian Journal of Earth Sciences*, 50(1), 78-93. doi: 10.1139/cjes-2012-0023
- Greenough, J. D. & MacKenzie, K. (2015). Igneous rock associations 18. Transition metals in oceanic island basalt: Relationships with the mantle components. *Geoscience Canada*, 42(3), 351-367. doi: 10.12789/geocanj.2015.42.071
- Guðmundsson, M. T., Sigmundsson, F., & Björnsson, H. (1997). Ice-volcano interaction of the 1996 Gjalp subglacial eruption, Vatnajokull, Iceland. *Nature*, 389, 954-957. doi:10.1038/40122
- Guðmundsson, M. T. (2003). Melting of ice by magma-ice-water interactions during subglacial eruptions as an indicator of heat transfer in subaqueous eruptions. In J. D. L. White, J. L. Smellie & D. A. Clague (Ed.), *Explosive Subaqueous Volcanism*. American Geophysical Union, Washington, D. C. (pp. 61-72).
- Guðmundsson, M. T., Jonsdottir, K., Hooper, A., Holohan, E., Halldorsson, S. A., Ofeigsson, B. G., ... Aiuppa, A. (2016). Gradual caldera collapse at Bárðarbunga volcano, Iceland, regulated by lateral magma outflow. *Science*, 353(6296), 262. doi: 10.1126/science.aaf8988
- Harder, M. & Russell, J. K (2007). Basanite glaciovolcanism at Llangorse mountain, northern British Columbia, Canada. *Bulletin of Volcanology*, 69, 329-340. doi: 10.1007/200445-006-0078-1
- Harðardóttir V., Brown, K. L., Fridriksson, T., Hedenquist, J. W., Hannington, M. D., & Thorhallson, S. (2009). Metals in deep liquid of the Reykjanes geothermal system, southwest Iceland: Implications for the composition of seafloor black smoker fluids. *Geology*, 37(12), 1103-1106.
- Hastie, A. R., Kerr, A. C., Pearce, J. A., & Mitchell, S. F. (2007). Classification of altered volcanic island rocks using immobile trace elements: Development of the Th-Co discrimination diagram. *Journal of Petrology*, 48(12), 2341-2357. doi:10.1093/petrology/egm062
- Hay, R. L. & Iijima, A. (1968). Petrology of palagonite tuffs of Koko Craters, Oahu, Hawaii. *Contributions to Mineralogical and Petrology*, 17(2), 141-154. doi:10.1007/BF00373206
- Hein, J. R., Yeh, H. W., & Alexander, E. (1979). Origin of iron-rich montmorillonite from the manganese nodule belt of the North Equatorial Pacific. *Clay and Clay Minerals*, 27, 185-194. Retrieved from <http://www.clays.org/journal/archive/volume%2027/27-3-185.pdf>

- Hekinian, R. & Hoffert, M. (1975). Rate of palagonitization and manganese coating on basaltic rocks from the Rift Valley in the Atlantic Ocean near 36°50'N. *Marine Geology*, 19(2), 91-109. doi: 10.1016/0025-3227(75)90056-0
- Hickson, C. J. (1986). *Quaternary volcanism in the Wells Gray-Clearwater area, east central British Columbia* (Doctoral dissertation). Retrieved from <https://circle.ubc.ca>
- Hickson, C. J., Moore, J. G., Calk, L. C., & Metcalfe, P. (1995). Intraglacial volcanism in the Wells Gray-Clearwater volcanic field, east-central British Columbia, Canada. *Canadian Journal of Earth Sciences*, 32(7), 838-851. doi: 10.1139/e95-070
- Hickson, C. J. (2000). Physical controls and resulting morphological forms of Quaternary ice-contact volcanoes in western Canada. *Geomorphology*, 32(3-4), 239-261. doi: 10.1016/S0169-555X(99)00099-9
- Hickson, C. J. & Vigouroux, N. (2014). Volcanism and glacial interaction in the Wells Gray-Clearwater volcanic field, east-central British Columbia. *Geological Society of America Field Guide*, 38, 169-191. doi: 10.1130/2014.0038(08)
- Hodges, C. A. & Moore, H. J. (1980). Ice on Mars; some evidence from volcanoes. *EOS, Transactions, American Geophysical Union*, 61, 69, 70.
- Hoffman, P. F., Kaufman, A. J., Halverson, G. P., & Schrag, D. P. (1998). A Neoproterozoic snowball Earth. *Science*, 281, 1342-1346.
- Honnorez, J. (1972). Palagonitization; the submarine alteration of basic volcanic glass in Palagonia, Sicily. *Vulkaninst itut Immanuel Friedlander*, 9, 131.
- Honnorez, J. (1981). The aging of the oceanic crust at low temperature. C. Emiliani (ed.) The seas; ideas and observations on progress in the study of the seas. *The Oceanic Lithosphere*, 7, 525-587.
- Hreinsdóttir, S., Einarsson, P., & Sigmundsson, F. (2001). Crustal deformation at the oblique spreading Reykjanes Peninsula, SW Iceland: GPS measurements from 1993 to 1998. *Journal of Geophysical Research*, 106(B7), 13803-13816. doi: 10.1029/2001JB000428
- Ingólfsson, Ó., Norðdahl, H., & Hafliðason, H. (1995). Rapid isostatic rebound in southwestern Iceland at the end of the last glaciation, *Boreas*, 24(3), 245-259. doi: 10.1111/j.1502-3883.1995.tb00777.x
- Ivarsson, M. (2012). Subseafloor basalts as fungal habitats. *Biogeosciences*, 9, 3625-3635. doi:10.5194/bg-9-3625-2012.
- Jaiswal, P. K., Puri, S., & Das, S. K. (2012). Surface-directed spinodal decomposition: a molecular dynamics study. *Physical Review of E-Statistical, Nonlinear, and Soft Matter Physics*, 85, 5. doi: 10.1103/PhysRevE.85.051137

- Jakobsson, S. P. (1972). On the consolidation and palagonitization of the tephra of the Surtsey volcanic island, Iceland. *Surtsey Program Report*, 61, 1-8.
- Jakobsson, S. P., Honsson, J., & Shido, F. (1978). Petrology of the western Reykjanes Peninsula, Iceland. *Journal of Petrology*, 19, 669-705.
- Jakobsson, S. P. & Moore, J. G. (1986). Hydrothermal minerals and alteration rates at Surtsey volcano, Iceland. *Geological Society of America bulletin*, 97, 648-659.
- Jakobsson, S. P. & Guðmundsson, M. T. (2008). Subglacial and intraglacial volcanic formations in Iceland. *Jokull*, No. 58, 179-196.
- Jarosewich, E., Nelen, J. A. & Norberg, J. A. (1980). Reference Samples for Electron Microprobe Analysis. *Geostandards Newsletter*, 4(1), 43-47.
- Jercinovic, M. J., Keil, K., Smith, M. R., & Schmitt, R. A. (1990). Alteration of basaltic glasses from north-central British Columbia, Canada. *Geochimica et Cosmochimica Acta*, 54, 2679-2696.
- Jochum, K. P., Willbold, M., Raczek, I., Stoll, B., & Herwig, K. (2005). Chemical characterisation of the USGS reference glasses GSA-1G, GSC-1G, GSD-1G, GSE-1G, BCR-2G, BHVO-2G and BIR-1G using EMPA, ID-TIMS, ID-ICP-MS and LA-ICP-MS. *Geostandards and Geoanalytical Research*, 29(3), 285-302.
- Jóhannesson, H. (1980). Jarðlagaskipan og thróun rekbelta á Versturandi (Evolution of rift zones in western Iceland, in Icelandic with English summary). *Náttúrufræðingurinn*, 50(1), 13-31.
- Jóhannesson, H. & Einarsson, S. (1998). Lava near the Straumsvik area (in Icelandic). *Náttúrufræðingurinn*, 67, 171-177.
- Johnson, J. S. & Smellie, J. L. (2007). Zeolite compositions as proxies for eruptive paleoenvironments. *Geochemistry Geophysics Geosystems*, 8, 3.
- Johnson, J. R., Bell, J. F., Bender, S., Cloutis, E. A., Lemmon, M., Le Moulic, S., ... Pinet, P. (2014). Reflectance spectroscopy from ChemCam passive observations at the Curiosity landing site, Mars. *Geological Society of America 49th annual meeting*, 46, 40.
- Jones, J. G. (1969). Pillow lavas as depth indicators. *American Journal of Science*, 267(2), 181-195. doi: 10.2475/ajs/267.2.181.
- Jones, J. G. (1969). Intraglacial volcanoes of the Laugarvatn region, southwest Iceland. *Geol. Soc. London, Journal of Quaternary Science*, 124, 197-211.
- Kaminski, E. & Jaupart, C. (1997). Expansion and quenching of vesicular magma fragments in plinian eruptions. *Journal of Geophysical Research*, 102(12), 187-203.

- Kawano, M. & Tomita, K. (1997). Experimental study on the formation of zeolites from obsidian by interaction with NaOH and KOH solutions at 150 and 200 °C. *Clays and Clay Minerals*, 45(3), 365-377. Retrieved from <http://www.clays.org/journal/archive/volume%2045/45-3-365.pdf>
- Kirschvink, J. L. (1992). Late Proterozoic low-latitude global glaciation: The Snowball Earth. In: J. W. Schopf, C. Klein and D. Des Maris (Ed.), *The Proterozoic Biosphere: A Multidisciplinary Study*. Cambridge University Press (pp. 51-52).
- Kjartansson, G. (1943). Geology of Árnessýsla. (In Icelandic). In: *Árnesingasaga I*, 1-250.
- Kjartansson, G. (1960). The Móberg Formation. In: S. Thorarinsson ed. *On the geology and geophysics of Iceland*. International Geological Congress, 21. Session Guide to Excursion No. A2, 21-28.
- Koornneef, J. M. (2012). Melting of a two-component source beneath Iceland. *Journal of Petrology*, 53(1), 127-157. doi:10.1093/petrology/egr059.
- Koski, R. A. (1988). Ferromanganese deposits from the Gulf of Alaska seamount province: mineralogy, chemistry and origin. *Canadian Journal of Earth Sciences*, 25(1), 116-133.
- Kumar, D. K. & Steed, J. W. (2014). Supramolecular gel phase crystallization: orthogonal self-assembly under non-equilibrium conditions. *Chemistry Society Review*, 43, 2080. doi: 10.1039/c3cs60224a.
- Kuno, H. (1966). Lateral variation of basalt magma type across continental margins and island arcs. *Bulletin of Volcanology*, 29, 195-222.
- Lautze, N., Taddeucci, J., Andronico, D., Houghton, B., Niemeijer, A., & Scarlato, P. (2009). Insights into explosion dynamics and the production of ash and Stromboli from samples collected in real-time. *Special paper of the Geological Society of America*, 498, 124-139.
- Le Gal, X., Crovisier, J. L., Gauthier-Lafaye, F., Honnorez, J., & Grambow, B. (1999). Meteoric alteration of Icelandic volcanic glass: Long term changes in the mechanism. *Proceedings of the Academy of Sciences, Series IIa, Geo- and Astrosciences*, 329, 175-181.
- MacKenzie, W. S., Donaldson, C. H., & Guilford, C. (2002). *Atlas of Igneous Rocks and Their Textures*. London, UK: Pearson Education Limited.
- MacLean, W. H. & Barrett, T. J. (1993). Lithochemical techniques using immobile elements. *Journal of Geochemical Exploration*, 48(2), 109-133.
- MacLennan, J., Jull, M., & McKenzie, E. (2002). The link between volcanism and deglaciation in Iceland. *Geochemistry Geophysics Geosystems*, 3(11), 1062. doi: 10.1029/2001GC00282.

- Madsen, J. K., Thorkelson, D. J., Friedman, R. M., and Marshall, D. D. (2006). Cenozoic to recent plate configurations in the Pacific Basin: Ridge subduction and slab window magmatism in western North America. *Geosphere*, 2(1), 11-34.
- Mathews, W. H. (1947). 'Tuyas', flat-topped volcanoes in northern British Columbia. *American Journal of Sciences*, 245, 560-570.
- McBirney, A. R. & Howel, W. (1969). Geology and petrology of the Galapagos Islands. *Memoir: Geological Society of America*, 118, 197.
- Metcalf, P. (1987). Petrogenesis of Quaternary alkaline lavas in Wells Gray Provincial Park, British Columbia and constraints on the petrology of the subcordilleran mantle (*Ph.D. thesis*). University of Alberta, Edmonton.
- Moore, J. G. (1966). Rate of palagonitization of submarine basalt adjacent to Hawaii. *U. S. Geological Survey Professional Paper*, D163-D171.
- Moore, J. G. (1970). Water content of basalt erupted on the ocean floor. *Contributions to Mineralogy, and Petrology*, 28, 272-279.
- Moore, J. G. & Schilling, J. G. (1973). Vesicles, water, and sulfur in Reykjanes Ridge basalts. *Contributions to Mineralogy and Petrology*, 41(2), 105-118. doi:10.1007/BF00375036
- Motoki, A., Sichel, S. E., Vargas, T., Melo, D. P., & Motoki, K. F. (2015). Geochemical behaviour of trace elements during fractional crystallization and crustal assimilation of the felsic alkaline magmas of the state of Rio de Janeiro, Brazil. *Anais da Academia Brasileira de Ciencias*, 87(4), 1959-1979. Retrieved from <https://dx.doi.org/10.1590/0001-3765201520130385>.
- Murphy, M. D., Sparks, R. S. J., Barclay, J., Carroll, M. R., & Brewer, T. S. (2000). Remobilization of andesite magma by intrusion of mafic magma at the Soufriere Hills volcano, Montserrat, West Indies. *Journal of Petrology*, 41(1), 21-42.
- Murphy, J. B. (2007). Igneous rock associations 8. Arc magmatism II: geochemical and isotopic characteristics. *Geoscience Canada*, 1911-4850. Retrieved from <https://journals.lib/unb.ca/index.php/GC/article/view/10230/10607>
- Nesbitt, H. W. & Young, G. M. (1984). Prediction of some weathering trends of plutonic and volcanic rocks based on thermodynamic and kinetic considerations. *Geochimica et Cosmochimica Acta*, 48, 1523-1534.
- Ngaruye, J. (2009). Geological and geothermal mapping of the Slaga-Arnarvatn area, Reykjanes Peninsula, SW-Iceland. *United Nations University, Geothermal Training Programme*, 21, 435-460.

- Nikitczuk, M. P. C., Schmidt, M. E. & Flemming, R. L. (2013). Altered vesicular basaltic tuffs as potential habitable environments: implications for Mars. *44th Lunar and Planetary Science Conference*.
- Nikitczuk, M. P. C., Schmidt, M. E., & Flemming, R. L. (2014). The habitability of basaltic hydrovolcanic tuffs; implications for Mars. *American Geophysical Union Fall Meeting*.
- Oddsson, B., Guðmundsson, M. T., Edwards, B. R., Thorvaldur, T., Magnusson, E., & Sigurdsson, G. (2016). Subglacial lava propagation, ice melting and heat transfer during emplacement of an intermediate lava flow in the 2010 Eyjafjallajökull eruption. *Bulletin of Volcanology*, 78, 48. doi:10.1007/s00445-016-1041-4
- Oehler, A. & Tomozawa, M. (2004). Water diffusion into silica glass at a low temperature under high water vapor pressure. *Journal of Non-Crystalline Solids*, 347(1-3), 211-219.
- Okumura, S. & Nakashima, S. (2006). Water diffusion in basaltic to dacitic glasses. *Chemical Geology*, 227(1-2), 70-82.
- Paque, M., Detienne, M., Maters, E. C., & Delmelle, P. (2016). Smectites and zeolites in ash from the 2010 summit eruption of Eyjafjallajökull volcano, Iceland. *Bulletin of Volcanology*, 78, 61. doi: 10.1007/s00445-016-1056-x
- Pauly, B. D., Schiffman, P., Zierenberg, R. A., & Clauge, D. A. (2011). Environmental and chemical controls on palagonitization. *Geochemistry Geophysics Geosystems*, 12 Q12017, doi:10.1029/2011GC003639
- Peacock, M. A. (1926). The vulcano-glacial palagonite formation of Iceland. *Geological Magazine*, 63(9), 385-399. doi: 10.1017/S0016756800085137
- Peacock, M. A. & Fuller, R. E. (1926). Chlorophaeite, sideromelane and palagonite from the Columbia River Plateau. *Journal of American Mineralogist*, 360-383.
- Pearce, J. A. (2008). Geochemical fingerprinting of oceanic basalts with applications to ophiolite classification and the search for Archean oceanic crust. *Lithos*, 100(1), 14-48.
- Pollock, M. (2014). Geochemical and lithostratigraphic constraints on the formation of pillow-dominated tindars from Undirhlíðar quarry, Reykjanes Peninsula, southwest Iceland. *Lithos*, 200-201, 317-333.
- Quinn, R., & Orenberg, J. (1993). Simulations of the Viking gas exchange experiment using palagonite and Fe-rich montmorillonite as terrestrial analogs: Implications for the surface composition of Mars. *Geochimica et Cosmochimica Acta*, 57(19), 4611-4618.
- Ragland, P. C. (1989). *Basic Analytical Petrology*. New York: Oxford University Press, (pp. 68-69).

- Railsbacks, L. B. (2007). Some Fundamentals of Mineralogy and Geochemistry. *University of Georgia*. Retrieved from <http://www.gly.uga.edu/railsback/Fundamentals/IonicPotential04P.pdf>
- Raw, F. & Matley, C. A. (1943). Some altered palagonite tuffs from Jamaica and the origin and history of their chlorites. *Journal of Geology*, *51*, 215-243.
- Rees, C., Riedell, K. B., Proffett, J. M., Macpherson, J., & Robertson, S. (2015). The Red Chris porphyry copper-gold deposit, northern British Columbia, Canada: Igneous phases, alteration, and controls of mineralization. *Economic Geology*, *110*(4), 857-888. doi: 10.2113/econgeo.110.4.857
- Rocholl, A. (1998). Major and trace element composition and homogeneity of microbeam reference material: basalt glass USGS BCR-2G. *Journal of Geostandards and Geoanalysis*, *22*(1), 33-45.
- Ross, C. S. & Smith, R. L (1955). Water and other volatiles in volcanic glasses. *American Mineralogist*, *40*, 1071-1089.
- Russell, J. K., Edwards, B. R., Porritt, L., & Ryane, C. (2014). Tuyas: a descriptive genetic classification. *Quaternary Science Reviews*, *87*, 70-81.
- Ryder, J. M. & Clague, J. J. (1989). British Columbia (Quaternary stratigraphy and history, Cordilleran Ice Sheet). In R. J. Fulton (Ed.) *Quaternary Geology of Canada and Greenland*. Geological Survey of Canada, Geology of Canada, *1*, 48-58.
- Saemundsson, K. (1979). Outline of the geology of Iceland. *Jökull*, *29*, 7-28.
- Saemundsson, K. (1995). *Svartsengi geological map (bedrock) 1:25000*. Orkustofnun, Hitaveita Sudurnesja and Landmaelingar Islands. Reykjavik.
- Saemundsson, K. & Gunnlaugsson, E. (2014). *Icelandic Rocks and Minerals*. Reykjavik, Iceland. UNESCO City of Literature.
- Schiffman, P., Spero, H. J., Southard, R. J., & Swanson, D. A. (2000). Controls on palagonitization versus pedogenic weathering of basaltic tephra: evidence from the consolidation and geochemistry of the Keanakakoʻi Ash Member, Kilauea Volcano. *Geochemistry Geophysics Geosystems. Journal of Earth Sciences*, *1*, 1-16.
- Schiffman, P. & Drief, A. (2004). Very low-temperature alteration of sideromelane in hyaloclastites and hyalotuffs from Kilauea and Mauna Kea volcanoes: implications for the mechanism of palagonite formation. *Clays & Clay Minerals*, *52*(5), 622-634.
- Seligman, A. N., Bindeman, I. N., Watkins, J. M., & Ross, A. M. (2016). Water in volcanic glass: From volcanic degassing to secondary hydration. *Geochimica et Cosmochimica Acta*, *191*, 216-238.

- Sen, G. (2013). *Petrology: principles and practice*. Springer Science and Business Media, 39.
- Schopka, H. H., Guðmundsson, M. T., and Tuffen, H. (2006). The formation of Helgafell, southwest Iceland, a monogenetic subglacial hyaloclastite ridge: Sedimentology, hydrology and volcano-ice interaction. *Journal of Volcanology and Geothermal Research*, 152, 359-377.
- Shafiei, B. (2014). Geochemical behavior of Mo and precious metals during supergene enrichment in the SarCheshmeh porphyry Cu deposit, Iran. *Iranian Journal of Science and Technology*, 38A2, 145-158.
- Shikazono, N., Takino, A., & Ohtani, H. (2005). An estimate of dissolution rate constant of volcanic glass in volcanic ash soil from the Mt. Fuji area, central Japan. *Geochemical Journal*, 39, 185-196.
- Smellie, J. L. & Edwards, B. E. (2016). *Glaciovolcanism on Earth and Mars. Products, processes and paleoenvironmental significance*. UK: Cambridge University Press.
- Souther, J. G., Clague, J. J., & Mathewes, R. W. (1987). Nazko cone: a Quaternary volcano in the eastern Anahim Belt. *Canadian Journal of Earth Sciences*, 24(12), 2477-2485. doi: 10.1139/e87-232
- Staudigel, H. & Hart, S. R. (1983). Alteration of basaltic glass; mechanisms and significance for the oceanic crust-seawater budget. *Geochimica et Cosmochimica Acta*, 47, 337-350.
- Staudigel, H., Furnes, H., McLoughlin, N., Banerjee, N. R., Connell, L. B., & Templeton, A. (2008). 3.5 billion years of glass bioalteration: Volcanic rocks as a basis for microbial life? *Earth-Science Review*, 89, 156-176.
- Stokes, K. R. (1971). Further investigation into the nature of the materials chlorophaeite and palagonite. *Mineralogical Magazine*, 38, 205-214. doi: 10.1180/minmag.1971.038.294.10
- Stroncik, N. A. & Schmincke, H. U. (2001). Evolution of palagonite: Crystallization, chemical changes, and element budget. *Geochemistry Geophysics Geosystems*, 2. doi: 10.1029/2000GC000102
- Stroncik, N. A. & Schmincke, H. U. (2002). Palagonite – a review. *International Journal of Earth Sciences (Geology Rundsch)*, 91, 680-697. doi: 10.1007/s00531-001-0238-7
- Taddeucci, J., Pompilio, M., & Scarlato, P. (2004). Conduit processes during the July–August 2001 explosive activity of Mt. Etna (Italy): inferences from glass chemistry and crystal size distribution of ash particles. *Journal of Volcanology and Geothermal Research*, 137(1), 33-54.

- Thorseth, I. H., Furnes, H., & Tumyr, O. (1991). A textural and chemical study of Icelandic palagonite of varied composition and its bearing on the mechanism of the glass-palagonite transformation. *Geochemica et Cosmochimica Acta*, 55, 731-749.
- Tomozawa, M. (1985). Water in glass. *Journal of Non-Crystalline Solids*, 73(1-3), 197-204. doi: 10.1016/0022-3093(85)90346
- Trichet, J. (1969). Study of the structure of volcanic glass and its relation to the alteration of volcanic rocks. In L. Heller (Ed.) *Proceedings of International Clay Conference*, Vol. 1, Jerusalem: Israel University Press (pp. 443-453).
- van Bemmelen, R. W. & Rutten, M. G. (1955). Tablemountains of northern Iceland (and related notes). *Netherlands Organisation for Pure Research*, (pp. 217).
- Vernaz, E. Y. & Dussossoy, J. L. (1992). Current state of knowledge of nuclear waste glass corrosion mechanisms: the case of R7T7 glass. *Applied Geochemistry*, 7(1), 13-22.
- Walton, A. W. & Schiffman, P. (2003). Alteration of hyaloclastites in the HSDP 2 Phase 1 Drill Core 1. Description and paragenesis. *Geochemistry Geophysics Geosystems*, 4(5), 1-31.
- Wessel, P., Sandwell, D. T., & Kim, S. (2010). Mountains in the Sea: The global seamount census. *Oceanography*, 23(1), 24-33.
- Wicander, R. & Monroe, J. S. (2013). Historical Geology: Evolution of Earth and Life Through Time (7th Ed.). *Brooks/Cole*, (pp. 350).
- Williams, L. A. & Crerar, D. A. (1985). Silica diagenesis, II. General mechanisms. *Journal of Sedimentary Petrology*, 55(3), 312-321.
- Winchester, J. A. & Floyd, P. A. (1977). Geochemical discrimination of different magma series and their differentiation products using immobile elements. *Chemical Geology*, 20, 325-343.
- Xeidakis, G. S. (1996). Stabilization of swelling clays by Mg(OH)₂. Changes in clay properties after addition of Mg-hydroxide. *Engineering Geology*, 44(1-4), 107-120. doi:10.1016/S0013-7952(96)00047-6.
- Zhou, Z. & Fyfe, W. S. (1989). Palagonitization of basaltic glass from DSDP Site 335, Leg 37; textures, chemical composition, and mechanism of formation. *American Mineralogist*, 74, 1045-1053.

Appendices

Appendix A Precision and Accuracy Tables

A.1 Major element precision (variation when measured repeatedly) and accuracy (difference between the measurement and published value) by EMPA, determined on 37 replicate analyses of Smithsonian Standard: Kakanui NMNH 143965 (Hornblende-1). A) All oxides in wt.%, and FeO = total Fe. B) Mean value detected. C) Standard deviation. D) Precision % (Std Dev/Mean)*100. E) Published Values (from Smithsonian Standard: Kakanui NMNH 143965 (Hornblende-1). n/a = published value not available. F) Accuracy % ([Absolute Value (Mean Value – Std Dev)/Std Dev])*100. Note: lower percent = higher precision and accuracy.

A) Oxide	SiO ₂	TiO ₂	Al ₂ O ₃	FeO	MnO	MgO	CaO	Na ₂ O	K ₂ O	P ₂ O ₅	F	Cl	Total
B) Mean	40.84	4.99	14.48	11.06	0.09	12.94	10.64	2.61	2.15	0.03	0.26	0.02	100.10
C) Std Dev	0.50	0.09	0.12	0.18	0.03	0.14	0.15	0.08	0.07	0.02	0.08	0.01	0.43
D) Precision %:	1.23	1.81	0.84	1.63	32.38	1.12	1.46	2.99	3.20	58.93	32.05	37.05	0.43
E) Published Value	41.33	5.03	14.40	11.04	n/a	12.85	10.49	2.62	2.23	n/a	n/a	n/a	99.99
F) Accuracy %	1.20	0.87	0.56	0.16	n/a	0.69	1.41	0.41	3.45	n/a	n/a	n/a	0.11

A.2 Trace element precision (variation when measured repeatedly) and accuracy (difference between the measurement and published value) by LA-ICP-MS, determined on 16 replicate analyses of BCR-2G. All elements in ppm. A) numbers before elements represent the isotope selected for detection. B) Mean value detected. C) Standard deviation. D) Precision % (Std Dev/Mean)*100. E) Published Values (from Jochum et al, 2008, Table 2; Jochum and Nohl, 2005, Table 6). F) Accuracy % ([Absolute Value (Mean Value – Std Dev)/Std Dev])*100. Note: lower percent = higher precision and accuracy.

A) Element	B) Mean	C) Std Dev	D) Precision %	E) Published Values	F) Accuracy %
⁴⁵ Sc	31.81	2.23	7.00	33.00	3.60
⁵¹ V	447.66	28.05	6.27	425.00	5.33
⁵² Cr	26.28	4.16	15.84	17.00	54.58
⁵⁹ Co	39.78	2.22	5.59	38.00	4.68
⁶⁰ Ni	43.47	11.01	25.33	10.90	298.80
⁶⁵ Cu	19.69	1.06	5.39	21.00	6.24
⁶⁶ Zn	148.06	9.17	6.19	125.00	18.44
⁸⁵ Rb	47.77	2.82	5.90	47.00	1.63
⁸⁸ Sr	330.40	17.81	5.39	342.00	3.39
⁸⁹ Y	28.80	1.60	5.54	35.00	17.72
⁹⁰ Zr	154.35	8.27	5.36	184.00	16.11
⁹³ Nb	11.92	0.72	6.03	12.50	4.60
¹³⁷ Ba	620.22	32.78	5.29	683.00	9.19
¹³⁹ La	23.33	0.98	4.18	24.70	5.54
¹⁴⁰ Ce	49.46	2.67	5.41	53.30	7.20
¹⁴¹ Pr	6.33	0.32	5.12	6.70	5.49
¹⁴⁶ Nd	25.38	1.06	4.18	28.90	12.19
¹⁴⁷ Sm	5.89	0.31	5.33	6.59	10.57
¹⁵³ Eu	1.90	0.09	4.95	1.97	3.69
¹⁵⁷ Gd	5.43	0.38	6.96	6.71	19.12
¹⁵⁹ Tb	0.84	0.05	6.53	1.02	17.72
¹⁶³ Dy	5.10	0.26	5.12	6.44	20.74
¹⁶⁵ Ho	1.02	0.06	6.15	1.27	19.72
¹⁶⁶ Er	2.87	0.21	7.35	3.70	22.35
¹⁶⁹ Tm	0.40	0.03	7.88	0.51	21.91
¹⁷² Yb	2.70	0.23	8.33	3.39	20.32
¹⁷⁵ Lu	0.40	0.05	13.48	0.50	19.52
¹⁷⁸ Hf	4.00	0.28	6.98	4.84	17.38
¹⁸¹ Ta	0.66	0.05	7.51	0.78	15.78
²⁰⁸ Pb	9.74	0.46	4.69	11.00	11.49
²³² Th	5.00	0.22	4.49	5.90	15.22
²³⁸ U	1.57	0.10	6.47	1.69	6.97

Appendix B Data Tables

B.1 Modal proportions (%) for Helgafell and Wells Gray (total points counted: 21,097). Crystals/Minerals in voids = sulfides (e.g. pyrite, chalcopyrite, ilmenite, chromite, magnetite, rutile). Crystals/Minerals in glass = plagioclase (Pl) and olivine (Ol) by size: microlites (< 100 µm) and phenocrysts (> 300 µm), following Murphy et al. (2000). Unidentified brown material = within glass grains. Vesicles can be empty, infilled with fractures or materials, concentrically zoned, or contain the low-relief, zeolite-like (Si, Na-rich) mineral. Voids can be empty or contain materials, minerals or the zeolite-like (Si, Na-rich) mineral.

Sample	Basaltic Glass		Palagonite	Crystal/Min in voids	Crystals/Minerals in glass			Unidentified	Vesicle in glass			Void	Total				
	Sideromelane	Tachylite	Dark rim	Gel-material	e.g. sulfides, oxides	Microlites (Pl/Ol)	Phenocryst (Ol)	Brown (PPL)	Empty	Fractured	Material	Zoned	Si,Na-rich mineral	Empty	Material	Si,Na-rich mineral	Counts
03-2 Iceland Traverse																	
Counts (2078) 20x mag	581	0	201	377	28	0	35	2	182	85	316	41	162	51	17	0	2078
% material	27.96	0.00	9.67	18.14	1.35	0.00	1.68	0.10	8.76	4.09	15.21	1.97	7.80	2.45	0.82	0.00	
TOTALS (%)	27.96												37.82				3.27
05-2 Helgafell Traverse																	
Counts (2238) 20x mag	651	280	167	244	27	0	0	131	52	106	250	25	71	177	57	0	2238
% material	29.09	12.51	7.46	10.90	1.21	0.00	0.00	5.24	2.32	4.74	11.17	1.12	3.17	7.91	2.55	0.00	
TOTALS (%)	41.60												22.52				10.46
05-2 Helgafell Traverse																	
Counts (2088) 20x mag	443	0	194	328	43	0	0	47	144	156	403	32	83	187	28	0	2088
% material	21.22	0.00	9.29	15.71	2.06	0.00	0.00	2.15	6.90	7.47	19.30	1.53	3.98	8.96	1.34	0.00	
TOTALS (%)	21.22												39.18				10.30
09-2 Helgafell Traverse																	
Counts (2183) 20x mag	513	0	185	854	12	2	0	0	29	101	222	29	186	50	0	0	2183
% material	23.50	0.00	8.47	39.12	0.55	0.09	0.00	0.00	1.33	4.63	10.17	1.33	8.52	2.29	0.00	0.00	
TOTALS (%)	23.50												25.97				2.29
11-2 Helgafell Traverse																	
Counts (622) 10x mag	276	0	61	55	12	3	0	0	69	6	59	10	20	39	12	0	622
% material	44.37	0.00	9.81	8.84	1.93	0.48	0.00	0.00	11.09	0.96	9.49	1.61	3.22	6.27	1.93	0.00	
TOTALS (%)	44.37												26.37				8.20
11-2 Helgafell Traverse																	
Counts (1775) 20x mag	512	0	152	386	0	2	9	0	66	91	238	55	125	81	58	0	1775
% material	28.85	0.00	8.56	21.75	0.00	0.11	0.51	0.00	3.72	5.13	13.41	3.10	7.04	4.56	3.27	0.00	
TOTALS (%)	28.85												32.39				7.83
Helgafell Average (%)	29.16	2.09	8.88	19.08	1.18	0.11	0.37	1.48	5.69	4.50	13.12	1.78	5.62	5.41	1.65	0.00	
20-2 Wells Gray Traverse																	
Counts (1471) 20x mag	754	0	114	56	0	169	0	30	39	33	64	15	49	148	0	0	1471
% material	51.26	0.00	7.75	3.81	0.00	11.49	0.00	2.04	2.65	2.24	4.35	1.02	3.33	10.06	0.00	0.00	
TOTALS (%)	51.26												13.60				10.06
21a-2 Wells Gray Traverse																	
Counts (2119) 20x mag	855	46	434	53	25	296	0	71	0	0	0	0	12	183	112	32	2119
% material	40.35	2.17	20.48	2.50	1.18	13.97	0.00	3.35	0.00	0.00	0.00	0.00	0.57	8.64	5.29	1.51	
TOTALS (%)	42.52												0.57				15.43
21a-2 Wells Gray Traverse																	
Counts (2095) 20x mag	557	247	295	181	19	128	71	207	0	0	37	2	9	292	44	6	2095
% material	26.59	11.79	14.08	8.64	0.91	6.11	3.39	9.88	0.00	0.00	1.77	0.10	0.43	13.94	2.10	0.29	
TOTALS (%)	38.38												2.29				16.32
21a-3 Wells Gray Traverse																	
Counts (2248) 20x mag	844	174	362	190	0	286	79	20	4	0	34	0	0	180	59	16	2248
% material	37.54	7.74	16.10	8.45	0.00	12.72	3.51	0.89	0.18	0.00	1.51	0.00	0.00	8.01	2.62	0.71	
TOTALS (%)	45.28												1.69				11.34
21b-3 Wells Gray Traverse																	
Counts (2180) 20x mag	747	90	299	163	0	371	72	28	5	18	51	10	53	162	94	17	2180
% material	34.27	4.13	13.72	7.48	0.00	17.02	3.30	1.28	0.23	0.83	2.34	0.46	2.43	7.43	4.31	0.78	
TOTALS (%)	38.39												6.28				12.52
Wells Gray Average (%)	38.00	5.17	14.43	6.18	0.42	12.26	2.04	3.49	0.61	0.61	1.99	0.31	1.35	9.61	2.86	0.66	

B.4 Glass-palagonite traverse for Helgafell (sample #03-2) by EMPA (wt.%). Distance between 39 spot analyses ~ 0.99 μm , with a total distance of 37.58 μm .

Spot	SiO2	TiO2	Al2O3	FeO	MnO	MgO	CaO	Na2O	K2O	P2O5	F	Cl	Total	Distance (μ)
1	0.06	0.02	0.05	0.17	-0.03	-0.01	0.03	0	0	0	-0.05	0.82	1.15	0
2	0.39	0.03	0.3	0.2	0	0.05	0.05	0	0	0.01	-0.02	0.88	1.91	0.99
3	0.81	0.03	0.9	0.25	0	0.05	0.09	0	0.01	-0.02	0.02	0.71	2.87	1.98
4	1.95	0.06	1.75	0.68	-0.02	0.22	0.22	0.01	0.02	0.02	-0.07	0.51	5.45	2.97
5	4.76	0.31	5.19	1.38	-0.02	0.36	1.18	0.04	0.11	0.04	-0.02	0.88	14.24	3.95
6	6.36	0.19	5.76	2.69	0	0.59	0.93	0.04	0.09	0.05	-0.07	1.01	17.7	4.95
7	16.63	0.45	11.93	4.09	0.02	1.64	1.68	0.09	0.19	0.06	0	0.59	37.38	5.93
8	27.83	0.6	14.51	10.21	0.16	3.61	3.83	0.09	0.23	0.09	-0.03	0.33	61.47	6.92
9	36.37	1.47	13.59	11.81	0.13	5.84	7.44	0.12	0.16	0.09	0.14	0.16	77.3	7.91
10	40.76	2.08	12.46	13.98	0.15	8.2	9.77	0.15	0.1	0.22	0.01	0.12	87.99	8.9
11	44.34	2.89	12.53	15.54	0.15	10.83	10.46	0.27	0.08	0.17	-0.09	0.07	97.32	9.89
12	43.32	2.87	13.1	17.18	0.12	5.18	7.28	0.17	0.24	0.09	0.06	0.07	89.69	10.88
13	36.9	2.98	13.48	17.05	0.05	3.02	7.6	0.39	0.3	0.18	-0.02	0.06	82.01	11.87
14	44.23	2.1	15.23	13.31	0.15	5.66	10.43	1.06	0.28	0.28	0.12	0.04	92.9	12.85
15	46.89	1.78	15.02	13.44	0.21	7.19	11.65	1.25	0.24	0.21	0.04	0.04	97.97	13.84
16	47.92	1.77	15.16	11.34	0.2	8.55	12.43	1.21	0.17	0.25	0.15	0.04	99.18	14.83
17	47.88	1.88	15.18	10.79	0.18	9.15	12.17	1.53	0.14	0.26	-0.09	0.03	99.19	15.82
18	48.34	1.84	15.3	10.64	0.16	9.34	12.3	1.47	0.13	0.3	-0.06	0.03	99.84	16.81
19	47.97	1.95	14.56	10.24	0.12	9.49	13.01	1.04	0.14	0.22	-0.01	0.04	98.78	17.8
20	48.68	1.89	15.34	9.94	0.15	9.26	12.92	1.5	0.1	0.28	-0.18	0.02	100.08	18.79
21	49.16	1.85	15.04	10.99	0.19	8.91	12.29	1.25	0.14	0.26	-0.02	0.05	100.13	19.78
22	48.94	1.87	14.89	13.57	0.22	7.59	11.98	1.1	0.27	0.23	-0.04	0.06	100.74	20.77
23	48.06	1.79	14.74	13.93	0.15	7.23	11.42	1.94	0.29	0.23	0.1	0.08	99.95	21.75
24	48.8	1.79	15.22	12.14	0.17	8.24	11.94	1.36	0.26	0.24	0.09	0.03	100.28	22.74
25	48.75	1.95	15.18	11.71	0.23	9.92	11.83	1.01	0.26	0.24	-0.02	0.02	101.1	23.73
26	49.03	1.75	15.19	12.07	0.15	7.45	11.8	1.67	0.26	0.22	0.03	0.08	99.7	24.72
27	48.35	1.83	14.96	12.47	0.16	7.7	11.61	1.82	0.21	0.22	-0.11	0.05	99.37	25.71
28	40.77	1.8	13.09	10.98	0.2	6.39	9.08	1.58	0.21	0.19	0.13	0.18	84.6	26.7
29	23.35	1.99	9.63	9.22	0.07	3.5	4.05	0.66	0.18	0.15	0.16	0.42	53.39	27.69
31	18.36	2.61	9.87	8.38	0.04	0.51	1.84	0.15	0.24	0.09	0.08	0.58	42.76	28.68
31	27.05	3.87	14.64	10.04	0.01	0.62	2.3	0.18	0.33	0.17	0	0.95	60.14	29.67
32	34.22	4.8	16.83	13.85	0	0.95	3.45	0.15	0.51	0.2	0.04	0.56	75.54	30.65
33	32.97	3.76	9.43	15.84	0.04	1.48	4.43	0.09	0.55	0.19	-0.09	0.4	69.18	31.64
34	41.83	2.97	13.6	17.19	0.07	2.37	4.41	0.07	0.55	0.09	0.02	0.23	83.38	32.63
35	35.66	1.11	9.14	16.62	0.12	4.97	3.68	0.07	0.53	0.09	0.05	0.23	72.28	33.62
36	43.64	1.06	13.8	14.81	0.06	5.26	3.11	0.08	0.4	0.06	0.04	0.22	82.54	34.61
37	40.11	0.7	11.5	14.84	0.09	6.9	2.94	0.08	0.66	0.05	-0.02	0.26	78.14	35.6
38	43.77	0.51	13.91	14.06	0.12	6.81	2.7	0.12	0.53	0.08	0.09	0.41	83.12	36.59
39	23.56	0.36	9.83	10.42	0.02	5.13	1.24	0.14	0.42	0.08	0.07	0.79	52.06	37.58

B.5 Glass-Palagonite traverse for Wells Gray (sample #21a-2) by EMPA (wt.%). Distance between 32 spot analyses ~0.99 μm , with a total distance of 30.53 μm .

Spot	SiO2	TiO2	Al2O3	FeO	MnO	MgO	CaO	Na2O	K2O	P2O5	F	Cl	Total	Distance (μ)
1	0.04	0.02	0.00	0.19	-0.01	0.00	0.03	0.00	0.00	0.00	-0.03	0.99	1.23	0
2	0.06	0.02	0.00	0.17	0.00	0.02	0.31	0.01	0.01	0.00	0.06	0.76	1.42	0.98
3	0.81	0.03	0.17	0.33	0.01	0.07	1.87	0.04	0.04	0.00	0.03	0.57	3.98	1.97
4	3.08	0.07	0.72	0.78	0.01	0.18	6.80	0.07	0.16	0.07	0.01	0.53	12.48	2.95
5	2.46	0.05	0.79	0.71	0.00	1.43	27.13	0.32	0.12	0.39	0.11	0.38	33.89	3.94
6	9.41	0.12	3.12	2.23	0.01	1.99	30.78	0.54	0.34	0.41	0.01	0.30	49.26	4.92
7	23.60	0.35	7.31	8.49	0.12	2.09	16.20	0.63	1.06	0.39	0.08	0.30	60.62	5.91
8	40.37	0.60	12.87	16.69	0.72	2.06	2.90	0.78	1.87	0.18	0.06	0.15	79.24	6.89
9	45.07	0.80	14.98	19.71	1.59	2.01	1.43	0.74	1.93	0.14	0.10	0.13	88.62	7.88
10	45.42	0.82	15.30	19.99	1.16	1.96	1.05	0.61	2.12	0.11	-0.04	0.08	88.58	8.86
11	48.54	0.85	16.55	18.36	0.08	2.07	0.84	0.49	1.88	0.14	0.08	0.04	89.91	9.85
12	46.76	1.00	15.30	17.75	0.01	2.19	0.92	0.71	2.10	0.16	-0.07	0.08	86.93	10.83
13	48.41	1.23	14.38	18.69	0.05	2.14	0.97	0.66	1.77	0.18	-0.02	0.07	88.54	11.82
14	46.68	2.09	13.55	17.90	0.12	3.80	1.04	0.65	1.90	0.14	-0.05	0.05	87.84	12.8
15	46.72	3.52	13.87	17.86	0.06	5.01	1.27	0.61	1.65	0.16	0.20	0.05	90.98	13.79
16	44.28	5.77	12.94	16.43	0.08	4.28	1.69	1.01	1.35	0.16	-0.09	0.10	88.00	14.77
17	43.34	7.02	12.47	13.41	0.03	1.21	1.99	1.04	0.99	0.23	0.05	0.33	82.10	15.76
18	39.51	5.75	11.43	11.21	0.04	0.86	1.80	1.23	0.78	0.21	0.12	0.50	73.44	16.74
19	36.13	3.04	12.30	9.35	0.04	1.19	1.43	1.08	0.88	0.09	-0.03	0.44	65.94	17.73
20	28.13	1.85	9.92	7.29	0.05	1.16	1.71	1.02	0.75	0.07	-0.02	0.65	52.59	18.71
21	23.85	1.30	8.18	5.53	0.05	1.76	3.54	1.16	0.54	0.11	0.08	0.77	46.88	19.7
22	38.06	1.80	12.17	9.21	0.18	4.31	8.12	2.32	0.78	0.30	0.16	0.35	77.75	20.68
23	47.47	2.17	14.76	11.81	0.17	5.79	10.48	1.85	0.90	0.41	0.06	0.07	95.93	21.67
24	49.63	2.22	15.30	11.86	0.14	5.97	10.65	1.69	0.95	0.41	0.02	0.05	98.89	22.65
25	49.65	2.22	15.27	11.89	0.17	5.97	10.75	1.27	0.93	0.48	0.00	0.05	98.63	23.64
26	49.82	2.17	15.42	11.87	0.14	5.92	10.68	1.43	0.94	0.46	0.02	0.06	98.93	24.62
27	49.93	2.25	15.32	12.07	0.17	6.02	10.68	1.08	0.95	0.44	-0.09	0.04	98.85	25.6
28	50.40	2.25	15.53	12.03	0.22	6.00	10.75	1.01	0.95	0.44	0.12	0.05	99.75	26.59
29	50.16	2.29	15.42	12.02	0.17	5.97	10.87	1.00	0.92	0.44	0.12	0.04	99.40	27.57
30	50.38	2.24	15.49	12.12	0.18	5.97	10.80	1.60	0.95	0.46	0.03	0.06	100.28	28.56
31	49.74	2.20	15.34	11.80	0.19	6.02	10.73	2.51	0.96	0.44	0.03	0.05	100.01	29.54
32	48.03	2.10	15.30	11.64	0.19	6.00	10.58	2.84	0.92	0.41	0.04	0.10	98.16	30.53

B.6 Error bar calculations for ratio plots to test immobility of trace elements (Nb, Y, La, Nd, Zr, Th, Sc and Ta) in Helgafell (HG) and Wells Gray (WG) for use in mass balance isocon diagrams. Error based on precision. Calculation formula shown in List of Equations (pg. xiii); taken from Ragland (1989).

Analysis No.	X-value Nb/Y = Q	X-error Nb/Y ± Error	Y-value La/Nd = Q	Y-error La/Nd ± Error		Analysis No.	X-value Zr/Th = Q	X-error Zr/Th ± Error	Y-value Sc/Ta = Q	Y-error Sc/Ta ± Error	
HG Glass:						HG Glass:					
03-2C2-2G	0.61963	0.00327	0.65568	0.00412		03-2C2-2G	184.10	19.68	72.72	8.40	
03-2C2-3G	0.62944	0.00330	0.66722	0.00416		03-2C2-3G	254.09	36.45	66.97	7.86	
03-2C2-4G	0.64497	0.00340	0.64917	0.00415		03-2C2-4G	162.75	16.61	77.92	11.04	
03-2C2-6G	0.61891	0.00338	0.60166	0.00369		03-2C2-6G	309.52	61.22	65.58	8.35	
11-2C1-3G	0.55892	0.00331	0.85523	0.00612		11-2C1-3G	118.79	8.74	75.21	10.86	
11-2C1-4G	0.60416	0.00312	0.76465	0.00514		11-2C1-4G	208.52	22.29	76.89	10.31	
11-2C1-5G	0.53043	0.00307	0.62945	0.00391		11-2C1-5G	179.19	19.16	65.81	7.97	
11-2C1-6G	0.57043	0.00317	0.57597	0.00384		11-2C1-6G	182.70	19.08	63.11	7.18	
05-2-C1-1G	0.49000	0.00270	0.64013	0.00412		05-2-C1-1G	256.73	34.93	76.05	8.92	
05-2-C1-3G	0.49440	0.00285	0.63653	0.00453		05-2-C1-3G	272.37	39.20	71.60	8.54	
05-2-C1-4G	0.41310	0.00266	0.68838	0.00508		05-2-C1-4G	302.29	47.79	78.73	9.86	
05-2-C1-6G	0.54403	0.00292	0.67542	0.00473		05-2-C1-6G	235.50	31.10	86.42	12.98	
09-2-C1-1G	0.55828	0.00268	0.72052	0.00416		09-2-C1-1G	198.68	20.27	69.87	10.09	
09-2-C1-2G	0.54727	0.00287	0.65139	0.00375		09-2-C1-2G	193.91	19.79	80.38	10.06	
09-2-C1-3G	0.52358	0.00272	0.61422	0.00392		09-2-C1-3G	210.71	23.08	101.27	15.85	
09-2-C1-4G	0.59686	0.00300	0.65253	0.00407		09-2-C1-4G	158.94	13.72	97.09	16.20	
09-2-C1-5G	0.47017	0.00274	0.65954	0.00446		09-2-C1-5G	144.84	11.41	80.26	10.39	
WG Glass:						WG Glass:					
20-2-C1-1G	1.20000	0.00471	0.97595	0.00327		20-2-C1-1G	69.11	1.80	26.38	2.04	
20-2-C1-2G	1.13311	0.00415	0.83725	0.00256		20-2-C1-2G	67.39	1.57	31.35	2.48	
20-2-C1-3G	1.16945	0.00435	0.81239	0.00245		20-2-C1-3G	81.09	2.30	25.85	1.67	
20-2-C1-5G	1.05713	0.00345	0.87798	0.00260		20-2-C1-5G	82.25	2.11	31.11	2.23	
21a-2-C1-4G	1.23333	0.00506	0.83368	0.00282		21a-2-C1-4G	78.22	2.51	25.05	1.78	
21a-2-C1-6G	1.23401	0.00512	0.83685	0.00281		21a-2-C1-6G	74.14	2.18	27.77	2.11	
21a-2-C1-1G	1.09451	0.00423	0.83685	0.00262		21a-2-C1-1G	70.43	1.78	22.03	1.40	
21a-2-C1-3G	1.17717	0.00437	0.98758	0.00304		21a-2-C1-3G	85.38	2.49	24.28	1.52	
21a-3-C1-2G	1.06521	0.00369	0.85605	0.00247		21a-3-C1-2G	87.38	2.42	27.54	1.85	
21a-3-C2-4G	1.29118	0.00519	0.86318	0.00292		21a-3-C2-4G	76.65	2.31	30.29	2.74	
21a-3-C2-5G	1.20820	0.00474	0.82103	0.00273		21a-3-C2-5G	61.51	1.48	23.60	1.64	
21a-3-C2-6G	1.21450	0.00461	0.86278	0.00253		21a-3-C2-6G	70.64	1.72	23.82	1.50	
21b-3-C1-1G	1.08807	0.00397	0.88511	0.00279		21b-3-C1-1G	67.58	1.53	28.93	2.17	
21b-3-C1-2G	1.08436	0.00403	0.79066	0.00235		21b-3-C1-2G	72.17	1.71	26.17	1.80	
21b-3-C3-5G	1.08850	0.00404	0.92116	0.00295		21b-3-C3-5G	87.53	2.71	29.51	2.26	
21b-3-C3-6G	1.08056	0.00387	0.79383	0.00225		21b-3-C3-6G	69.81	1.62	29.28	1.91	
HG Palagonite:						HG Palagonite:					
03-2C2-2P	0.62059	0.00331	0.65059	0.00454		03-2C2-2P	178.27	15.70	45.23	3.54	
03-2C2-3P	0.64142	0.00453	0.67543	0.00576		03-2C2-3P	207.17	28.02	60.40	7.82	
03-2C2-4P	0.51800	0.00388	0.67031	0.00500		03-2C2-4P	118.96	9.71	64.56	9.32	
03-2C2-6P	0.41994	0.00379	0.76387	0.00621		03-2C2-6P	187.49	22.75	86.02	13.75	
11-2C1-3P	0.50578	0.00427	0.57781	0.00616		11-2C1-3P	488.90	186.03	86.71	18.61	
11-2C1-4P	0.21248	0.01036				11-2C1-4P			0.00	0.00	
11-2C1-5P	0.50331	0.00627	0.64991	0.00895		11-2C1-5P	110.56	13.79	40.38	5.42	
11-2C1-6P	0.22571	0.00358	0.88363	0.00713		11-2C1-6P	836.47	441.85	37.12	4.65	
05-2-C1-1P	0.55623	0.00256	1.00749	0.00741		05-2-C1-1P	175.45	13.58		0.00	
05-2-C1-3P	0.51230	0.00283	0.54295	0.00312		05-2-C1-3P	459.69	129.00	82.02	11.85	
05-2-C1-4P	0.43078	0.00286	0.75704	0.00615		05-2-C1-4P	165.62	15.82	41.28	3.30	
05-2-C1-6P	0.43446	0.00253	0.73277	0.00483		05-2-C1-6P	222.06	29.33	61.95	7.27	
09-2-C1-3P	0.51193	0.00398	0.71938	0.00612		09-2-C1-3P			67.40	8.73	
09-2-C1-4P	0.46938	0.00330	0.76532	0.00686		09-2-C1-4P	120.27	9.15	107.72	22.47	
09-2-C1-5P	0.46966	0.00335	0.40491	0.00307		09-2-C1-5P	459.00	137.39	59.02	6.82	
WG Palagonite:						WG Palagonite:					
20-2-C1-1P	1.24132	0.00567	0.90345	0.00389		20-2-C1-1P					
20-2-C1-2P	1.32342	0.00317	0.95538	0.00179		20-2-C1-2P	110.14	2.33	19.62	0.95	
20-2-C1-3P	1.18264	0.00447	1.02222	0.00359		20-2-C1-3P	58.77	1.15	12.19	0.60	
20-2-C1-5P	1.04700	0.00254	0.81509	0.00145		20-2-C1-5P	69.09	0.87	17.79	0.61	
21a-2-C1-4P	0.81246	0.00455	0.89801	0.00329		21a-2-C1-4P	49.01	1.06	54.47	7.72	
21a-2-C1-6P	1.74170	0.02099	1.16489	0.01707		21a-2-C1-6P	118.60	5.49	57.24	10.49	
21a-2-C1-1P	1.21771	0.00835				21a-2-C1-1P					
21a-2-C1-3P	1.31011	0.00494	0.95725	0.00359		21a-2-C1-3P	79.41	1.83	13.41	0.73	
21a-3-C1-2P	0.51976	0.00197	0.77088	0.00172		21a-3-C1-2P					
21a-3-C2-4P	1.21681	0.00484	0.83106	0.00322		21a-3-C2-4P	69.84	1.52	14.02	0.64	
21a-3-C2-5P	1.48605	0.00791	0.81132	0.00535		21a-3-C2-5P	114.21	4.14	48.91	5.48	
21a-3-C2-6P	2.60750	0.01957	0.92488	0.00701		21a-3-C2-6P	157.83	8.75			
21b-3-C1-1P	1.07826	0.00351	0.87117	0.00233		21b-3-C1-1P	95.81	2.34	18.94	1.00	
21b-3-C1-2P	1.15712	0.00379	0.86951	0.00254		21b-3-C1-2P	125.11	4.10	19.96	1.42	
21b-3-C3-5P	0.85786	0.00426				21b-3-C3-5P	61.54	1.85	0.00	0.00	
21b-3-C3-6P	1.21158	0.00670	1.47989	0.01073		21b-3-C3-6P					

B.8 Major element (%) mass transfer using isocon diagrams (isocon = slope of regression line) for two data sets with different assumptions for water. Data set 1: anhydrous glass, water in palagonite assumed from low EMP totals. Data set 2: hydrated glass matching the water in palagonite (assumed from low EMP totals).

Data Set Assumption	Sample No.	Glass-Palagonite Pair	Slope (Isocon)	SiO ₂	TiO ₂	Al ₂ O ₃	FeO	MnO	MgO	CaO	Na ₂ O	K ₂ O
Helgafell Basalt 1:												
Data set 1	03-2 ICE	2P	1.0932	-37.2	-51.5	-60.4	13.4	-44.0	-45.0	-80.0	-98.4	-1.0
Data set 2		2P	1.0932	-1.7	-22.2	-37.8	76.5	-10.6	-14.0	-68.7	-97.4	71.1
Data set 1	03-2 ICE	3P	0.8429	-42.2	91.8	-49.7	38.8	-40.6	-67.4	-59.9	-97.9	-32.9
Data set 2		3P	0.8429	7.3	255.7	-7.4	159.4	0.2	-39.8	-24.8	-96.0	26.9
Data set 1	03-2 ICE	4P	0.8795	-36.9	23.1	-38.8	20.2	1.7	-61.2	-34.7	-87.2	107.0
Data set 2		4P	0.8795	4.3	105.9	2.7	98.9	71.3	-36.3	9.2	-78.2	217.1
Data set 1	03-2 ICE	6P	0.9708	-29.2	28.8	-44.4	5.0	-42.7	-55.1	-30.2	-89.5	45.2
Data set 2		6P	0.9708	3.5	81.3	-19.2	53.7	-14.7	-32.9	1.1	-85.4	106.1
Data set 1	11-2 ICE	3P	0.7874	-13.2	56.5	-38.0	40.0	-68.0	-23.9	-56.7		-59.3
Data set 2		3P	0.7874	32.9	139.5	-5.2	114.2	-51.1	16.4	-33.8	-100.0	-37.8
Data set 1	11-2 ICE	4P	0.6377	3.7	-24.2	7.2	76.3	-33.7	19.8	-61.9	-99.1	21.6
Data set 2		4P	0.6377	56.4	14.3	61.6	165.8	-0.1	80.6	-42.5	-98.7	83.4
Data set 1	11-2 ICE	5P	0.5280	-5.9	78.2	-22.0	89.0	-63.7	0.6	-32.6	-93.6	-0.1
Data set 2		5P	0.5280	77.3	235.7	47.0	256.1	-31.6	89.6	27.0	-88.0	88.2
Data set 1	11-2 ICE	6P	0.8109	-14.1	113.3	-12.4	25.9	-70.8	-31.8	-64.1	-98.6	-24.4
Data set 2		6P	0.8109	25.6	212.0	28.1	84.2	-57.3	-0.2	-47.4	-98.0	10.6
Helgafell Basalt 2:												
Data set 1	05-2 ICE	1P	1.1724	-15.5	-30.3	-16.7	-18.6	-29.6	-18.8	-76.1	-99.2	-74.0
Data set 2		1P	1.1724	-2.6	-19.7	-4.0	-6.2	-18.9	-6.5	-72.5	-99.1	-70.0
Data set 1	05-2 ICE	3P	0.8999	7.2	52.1	3.0	1.7	-51.1	-24.8	-56.3	-95.5	-17.5
Data set 2		3P	0.8999	27.0	80.2	22.1	20.5	-42.1	-10.9	-48.2	-94.7	-2.3
Data set 1	05-2 ICE	4P	0.8903	5.2	15.2	8.0	-6.8	63.7	-15.7	-63.7	-94.5	-23.6
Data set 2		4P	0.8903	28.6	40.8	32.1	14.0	100.2	3.0	-55.6	-93.2	-6.6
Data set 1	05-2 ICE	6P	0.9486	4.5	-32.5	-0.3	-10.9	-65.2	-1.2	-69.8		-34.0
Data set 2		6P	0.9486	23.9	-20.0	18.2	5.6	-58.7	17.1	-64.3	-100.0	-21.8
Data set 1	09-2 ICE	3P	0.7339	-11.0	46.4	-16.9	30.4	-25.8	-22.0	-24.8	-86.6	8.5
Data set 2		3P	0.7339	34.6	121.4	25.7	97.1	12.2	17.9	13.7	-79.7	64.0
Data set 1	09-2 ICE	4P	0.8570	-15.5	39.5	-13.5	17.0	8.1	-24.3	-32.4	-83.1	-2.2
Data set 2		4P	0.8570	15.1	89.9	17.8	59.3	47.2	3.1	-7.9	-76.9	33.2
Data set 1	09-2 ICE	5P	0.8365	-5.8	64.2	-23.3	15.1	-57.9	-52.7	-31.7	-83.3	14.8
Data set 2		5P	0.8365	29.7	126.1	5.6	58.5	-42.1	-34.9	-5.9	-77.0	58.0
Wells Gray:												
Data set 1	20-2 WG	1P	0.9965	-3.4	-25.4	25.0	20.2	-106.2	-65.1	-82.4	-99.7	-43.9
Data set 2		1P	0.9965	11.3	-14.0	44.1	38.6	-107.1	-59.8	-79.7	-99.7	-35.3
Data set 1	20-2 WG	2P	1.7410	-44.2	-62.5	-27.9	-33.9	-86.8	-78.7	-88.9	-98.2	-41.7
Data set 2		2P	1.7410	-36.3	-57.2	-17.7	-24.5	-84.9	-75.6	-87.3	-98.0	-33.4
Data set 1	20-2 WG	3P	1.0221	-8.0	-33.8	26.5	-0.1	-73.8	-67.9	-81.9	-98.6	-5.8
Data set 2		3P	1.0221	8.8	-21.7	49.6	18.2	-69.0	-62.1	-78.6	-98.4	11.4
Data set 1	20-2 WG	5P	1.6740	-42.7	-57.3	-25.2	-31.0	-96.7	-78.9	-89.1	-99.3	-43.6
Data set 2		5P	1.6740	-33.8	-50.6	-13.5	-20.2	-96.1	-75.6	-87.4	-99.1	-34.7
Data set 1	21a-2 WG	4P	0.9263	-2.5	-43.6	4.2	55.9	-74.3	-68.4	-88.8	-48.2	86.2
Data set 2		4P	0.9263	16.4	-32.7	24.4	86.2	-69.4	-62.2	-86.6	-38.2	122.3
Data set 1	21a-2 WG	6P	0.9386	-6.4	-63.0	-3.8	14.8	-28.5	-71.0	-90.1	-78.7	78.1
Data set 2		6P	0.9386	23.9	-51.1	27.3	51.9	-5.3	-61.7	-86.9	-71.8	135.7
Data set 1	21a-2 WG	1P	1.0525	-10.5	-12.4	-11.4	-16.2	-106.0	-68.9	-81.0	-64.5	40.2
Data set 2		1P	1.0525	12.4	10.0	11.4	5.3	-107.5	-60.9	-76.2	-55.4	76.1
Data set 1	21a-2 WG	3P	1.1325	-42.6	-77.6	-29.0	-45.3	-2.6	-66.7	-93.3	-75.5	18.1
Data set 2		3P	1.1325	-0.3	-61.0	23.5	-4.9	69.4	-42.1	-88.3	-57.4	105.3
Data set 1	21a-3 WG	2P	1.0835	-8.5	21.6	-25.2	-50.9	-84.7	-89.8	-90.4	-92.1	-32.4
Data set 2		2P										
Data set 1	21a-3 WG	4P	1.2204	-21.1	54.0	-36.7	7.2	-11.9	-22.9	-91.5	-89.1	27.3
Data set 2		4P										
Data set 1	21a-3 WG	5P	1.1760	-23.1	64.0	-32.1	-13.1	-88.7	-78.2	-90.4	-80.0	12.4
Data set 2		5P										
Data set 1	21a-3 WG	6P	0.9488	-0.4	65.2	-14.7	57.0	-33.3	-2.7	-90.7	-76.7	103.6
Data set 2		6P										
Data set 1	21b-3 WG	1P	1.2871	-26.7	-69.4	-29.3	-11.8	-94.4	-68.4	-87.3	-94.3	-3.3
Data set 2		1P										
Data set 1	21b-3 WG	2P	1.2213	-21.2	-53.3	-29.1	6.3	-70.7	-58.6	-88.1	-93.5	10.3
Data set 2		2P										
Data set 1	21b-3 WG	5P	0.7849	12.7	20.0	19.7	74.0	-85.8	-27.0	-78.8	-64.5	139.7
Data set 2		5P										
Data set 1	21b-3 WG	6P	0.7442	32.8	-22.3	44.7	37.2	-81.9	-44.2	-64.3	-87.1	34.1
Data set 2		6P										

Appendix C Historical Review Summary

C.1 Characteristics of high-temperature, hydrothermal alteration vs. low-temperature, burial-diagenesis alteration.

High-Temp, Primary Palagonite (Schiffman et al., 2000) / Hydrothermal Palagonite (Pauly et al., 2011; Jakobsson and Moore, 1986)	Low-Temp, Secondary Palagonite OR Pedogenic Weathered Tephra (Schiffman et al., 2000) / Burial-diagenetic Palagonite (Pauly et al., 2011)
<p>Characteristics: Higher rate of alteration during/directly after eruption due to hot fluids; highly porous. Thinner, less developed rinds and few zeolites. Extent of palagonitization is lower due to shorter duration & high amt. of water (Pauley et al., 2011).</p>	<p>Characteristics: Thick, smooth, less porous palagonitized rinds low in water and high in REE's (Pauly et al., 2011).</p>
<p>Environment: Seafloor volcanism, phreatomagmatic and subglacial volcanism (Pauly et al., 2011).</p>	<p>Environment: Submarine volcanoclastics (Pauly et al., 2011), subaerial weathering and soil formation (Schiffman et al., 2000).</p>
<p>Kilauea caldera, HI: palagonite only found adjacent to caldera-bounding faults/steam vents (Schiffman et al., 2000).</p>	<p>Kilauea caldera, HI: low temp; no palagonitization. Pedogenic alteration of tephra: dependent on precipitation and soil acidity (Schiffman et al., 2000).</p>
<p>Tephra alteration products: On Surtsey, between 25-120°C (Jakobsson and Moore, 1986): Opal, calcite, anhydrite, gypsum, chabazite, analcite, phillipsite, tobermorite, xonotlite, smectite (nontronite). Fresh/young – possibly more zeolites.</p>	<p>Tephra alteration products: Alteration mainly takes place in last stages of cooling of lava and/or after it (Bonatti, 1965); due to glass forming from rapidly cooling melt at temp. several hundreds of degrees lower than melt temperature at the moment of effusion. Fe-montmorillonite smectite, low-temp (Hein et al., 1979).</p>
<p>Characteristics: Consolidated and cemented.</p> <p>Temperature: Island of Surtsey (Jakobsson and Moore, 1986): 40-60°C = 0.5-1 $\mu\text{m}/\text{yr}$ palagonite growth rate 80°C = 75-80% palagonitized 100°C = 3 $\mu\text{m}/\text{yr}$ palagonite growth rate 120°C = 100% palagonitized</p>	<p>Characteristics: Pedogenic weathered tephra (in contrast to palagonitized tephra): Non-consolidated to poorly consolidated Minerals unattached to the parent glass Only found in arid regimes Dissolution and desilication of tephra develops opal and clays May contain smectite as a component of pedogenic clay; also containing kaolinite and opal (Schiffman et al., 2000).</p>

C.2 Minerals and Materials Associated with Palagonitization (Hay and Iijima, 1968; Jakobsson and Moore, 1986; Jercinovic et al., 1990; Thorseth et al., 1991; Stroncik and Schmincke, 2001; Walton and Schiffman, 2003; Schiffman et al., 2000; Webmineral.com, 2015).

Mineral Name	Chemical Formula	Physical, Chemical, Optical Properties
Magnetite	Chemical Formula: Fe_3O_4 Empirical Formula: $\text{Fe}^{2+}\text{Fe}^{3+}_2\text{O}_4$	Opaque; Isometric
Hematite	Fe_2O_3 iron(III) oxide; $\text{Fe}^{3+}_2\text{O}_3$	Uniaxial; Equant
Calcite	CaCO_3	Early mineral to form at any depth; cement.
Montmorillonite * smectite	$(\text{Na},\text{Ca})_{0.3}(\text{Al},\text{Mg})_2(\text{Si}_4\text{O}_{10})(\text{OH})\cdot n\text{H}_2\text{O}$	Phyllosilicate sheets. Potassium, iron, and other cations are common substitutes; 2:1 swelling clay mineral; grows in pores.
Beidellite * smectite	$(\text{Na}_{0.5}\text{Al}_2(\text{Si},\text{Al})_4\text{O}_{10})(\text{OH})_2\cdot n\text{H}_2\text{O}$	Phyllosilicate sheets. 2:1 clay.
Fe-saponite * smectite	$\text{Ca}_{0.25}(\text{Mg},\text{Fe})_3((\text{Si},\text{Al})_4\text{O}_{10})(\text{OH})_2\cdot n(\text{H}_2\text{O})$	Fe-Mg-rich clay Soluble in sulfuric acid.
Nontronite *smectite (Fe)	$\text{Na}_{0.3}\text{Fe}^{3+}_2\text{Si}_3\text{AlO}_{10}(\text{OH})_2\cdot 4(\text{H}_2\text{O})$	Primary clay species of palagonite (at 25-150 °C). Can replace olivine edges.
Phillipsite *zeolite	$(\text{Na},\text{K},\text{Ca})_{1-2}(\text{Si},\text{Al})_8\text{O}_{16}\cdot 6(\text{H}_2\text{O})$	Potassic; less silicic; above and below sea level (at 25-°150 C). Biaxial. Tends to grow larger below sea level.
Chabazite *zeolite	$(\text{Ca},\text{Na}_2,\text{K}_2,\text{Mg})\text{Al}_2\text{Si}_4\text{O}_{12}\cdot 6\text{H}_2\text{O}$	Calcic; Commonly occurs in voids; overgrows phillipsite. 68–92 °C (0-4 m depth in drill hole).
Analcime *zeolite	$\text{Na}_2(\text{Al}_2\text{Si}_4\text{O}_{12})\cdot 2\text{H}_2\text{O}$	Late-stage replacing of early zeolites. Vesicle walls/seams; 55-75°C; isotropic, colourless PPL
Gismondine *zeolite	$\text{CaAl}_2\text{Si}_2\text{O}_8\cdot 4(\text{H}_2\text{O})$	Hydrated aluminosilicate forms colorless, bipyramidal crystals of orthorhombic symmetry.
Illite *mica clay	$(\text{K},\text{H}_3\text{O})(\text{Al},\text{Mg},\text{Fe})_2(\text{Si},\text{Al})_4\text{O}_{10}(\text{OH})_2(\text{H}_2\text{O})$	Alkali-rich; High ion substitution.
Goethite	$\text{Fe}^{3+}\text{O}(\text{OH})$	Usually zoned; Crystalline-poor; spherical bodies or irregular form.
Tobermorite	$\text{Ca}_5\text{Si}_6\text{O}_{16}(\text{OH})_2\cdot 4\text{H}_2\text{O}$	Found as cement or in vesicles; 25-150 °C; negative relief, weak birefringence.
Opal	$\text{SiO}_2\cdot n(\text{H}_2\text{O})$	Amorphous silica; 6-10% water.
Halite	NaCl	Salt; isotropic.
Xonotlite	Hydrated calcium silicate, similar to tobermorite	Found 125.4 m depth in drill hole, 147 °C.
Anydrite	Anhydrous calcium sulfate, CaSO_4 .	Abundant deep in drill hole (cool sea water precipitates sulfate); 24–149 °C.
Gypsum	Calcium sulfate dehydrate, $\text{CaSO}_4\cdot 2\text{H}_2\text{O}$	Low relief.

C.3 Scientific analytical methods used to study palagonitization.

Optical petrology	Peacock (1926); Jakobsson and Moore (1986); Stroncik & Schmincke (2001); Pauly et al. (2011)	Texture, mineralogy in thin section
SEM-EDS, Scanning electron microscopy	Jercinovic (1990); (Thorseth 1991)	For porosity, texture
RL-FTIR, Reflected Light Infrared Spectroscopy	Pauly et al. (2011)	Absorbance due to total water in glass & palagonite
XRD, X-ray diffractometer	Jercinovic (1990); Stroncik & Schmincke (2001); Bonatti (1965); Thorseth (1991); Schiffman (2000); Jakobsson and Moore (1986).	Secondary minerals. XRD reveals authigenic smectite cement and minerals, TEM diffractions on grains; analysis of clay-size fraction
EMPA, Electron microprobe	Pauly et al. (2011); Stroncik and Schmincke, (2001); Thorseth (1991); Jakobsson and Moore (1986).	Major element geochemistry, using standards
LA-ICP-MS, Laser Ablation Mass Spectrometry	Pauly et al. (2011).	Trace element geochemistry, using standards
Fluorescence microscopy	Thorseth (1991).	For porosity, texture
EMPA traverses	Pauly et al. (2011); Thorseth (1991); Jercinovic et al. (1990).	Across glass-palagonite material.
Compact Reconnaissance Imaging Spectrometer for Mars (CRISM)	Ackiss et al. (2016, 2017)	Mineral signatures on Mars identified by spectral absorption bands.
AFM (Atomic-force microscopy)	Stroncik and Schmincke (2001).	Reveals structures at the nanoscale, for variability in degree of aging in palagonite.
Fission track dating	Hekinian and Hoffert (1975).	Palagonitization rate estimates.
Whole-rock chemical analyses	Jakobsson and Moore (1986).	X-ray and wet-chemical methods